UNIVERSITY OF CALIFORNIA

SANTA CRUZ

SYNTHESIS AND METROLOGY OF CONDUCTING CARBON NANOTUBE ASSEMBLIES

A dissertation submitted in partial satisfaction of the
requirements for the degree of

DOCTOR OF PHILOSOPHY

in

ELECTRICAL ENGINEERING

by

Timothy Jay Longson

March 2013

The Dissertation of Timothy Jay Longson
is approved:

_____

Professor Claire Gu, Chair

_____

Professor Michael Isaacson

_____

Dr. Brett Cruden

_____

Tyrus Miller
Vice Provost and Dean of Graduate Studies

Table of Contents

List of Figures

xiii

xiv

List of Tables

Abstract

Synthesis and metrology of conducting carbon nanotube assemblies

by

Timothy Jay Longson

Since its discovery, the carbon nanotube (CNT) has been proposed as one of the ultimate materials for its electrical, thermal and mechanical properties due to its incredibly strong sp^2 bonds, low defect density, and large aspect ratio. Many experimental results on individual CNTs have confirmed these outstanding theoretically predicted properties. However, scaling these properties to the macroscopic regime has proved to be challenging. This work focused on the synthesis and measurement of highly conducting, macroscopic, CNT assemblies. Scaling up the synthesis of vertically aligned multiwalled CNT (MWNT) forests was investigated through the development of a large, 100mm, wafer scale, cold wall chemical vapor deposition chamber. In addition to the synthesis, two distinct CNT assemblies have been investigated. A linear morphology where CNTs are strung in series for electrical transport (CNT wires) and a massively parallel 2D array of vertically aligned CNTs for Thermal Interface Material (TIM) applications.

Poymer-CNT wire composites have been fabricated by developing a coaxial CNT core-polymer shell electrospinning technique. The core-shell interactions in this system have been studied by way of Hansen's solubility parameters. The most well defined CNT core was achieved using a core solvent that is semi-immiscible with the shell solution, yet still a solvent of the shell polymer. Electrical characterization of the

resulting CNT core has shown a two orders of magnitude increase in conductivity over traditional, homogeneously mixed, electrospun CNT wires.

A number of vertically aligned MWNT assemblies were studied for their thermal interface properties. Double-sided Silicon substrate (MWNT-Si-MWNT) TIM assemblies were characterized using a DC, 1D reference bar, thermal measurement technique. While attempts to control MWNT density via a micelle template technique produced only 'spaghetti like' CNTs, sputter deposited catalyst provided stark variations in array density. Relevant array morphologies such as density, height, and crystallinity were studied in conjunction with their thermal performance. A Euler buckling model was used to identify the transition between increasing and decreasing resistance with density over array height, these two regimes are explained by way of contact analysis.

Self catalyzing Fecralloy substrate MWNT TIMs were studied in a similar vein to the Silicon based assemblies. This substrate was investigated because of its malleability, ease of CNT synthesis and increased CNT adhesion. The growth behavior was studied with respect to the array morphologies, i.e. array height, density, crystallinity, and diameter, while the contact resistance was evaluated using a DC, 1D reference bar technique. The best performing samples were found to have a factor of two increase over their Si counterparts. Temperature dependent thermal measurements offer insight into the interfacial phonon conduction physics and are found to agree with other temperature dependent studies, suggesting inelastic scattering at the MWNT-Cu interface. Due to the challenges associated with deliberately controlling a single array morphology, a statistical approach was used for identifying the influences of the multivariate array

morphology on contact resistance. Showing the strongest correlation with array height, following a $R \sim L^{-0.5}$. Several models were investigated to help explain this behavior, although little insight is gained over the empirical relations.

To better characterize these MWNT TIM assemblies two experimental techniques were developed. A transient 3ω thermal measurement technique was adapted to characterize the thermal performance of CNT TIMs, offering insight into the limiting resistance in a mulilayer material stack. The MWNT-growth substrate interface was found to dominate in the Si samples while the MWNT-opposing substrate interface dominated in the Fecralloy samples. These measurements strongly supported the DC thermal measurements and the qualitative observations of substrate adhesion. Additionally, a new technique for observing nano sized contacts was established by viewing contact loading through an electron transparent membrane, imaged under an SEM. The contrast mechanism is explained by a voltage contrast phenomenon developed by trapped charges at the interface. The resolution limits have been studied by way of electron beam interactions and the use of Monte Carlo simulations, showing nanometer resolution with appropriate experimental conditions. The real MWNT contact area was found to be less than $1/100^{th}$ the apparent contact area even at moderate pressures and the number of contacting CNTs is approximately $1/10^{th}$ the total number of CNTs. These results confirm experimental measurement values for van der Waals adhesion strengths and thermal interface resistance.

Acknowledgments

This is an interesting section to write because I feel like it should somehow reflect my experience over the past five years, which as it turns out is not a trivial task... Obviously the people I interacted with, in and around the lab, had a strong influence on my experience.

One such experience that jumps to mind happened early in my research when working on the electrospinning apparatus. I was unsure if I was producing any fibers so began exploring the influence of the substrate (Silicon) position in fiber collection. I wanted to move the substrate very close to the needle tip that had the high (15kVDC) source attached to it. Fearful of electric shock, I naively asked my lab-mate, Ranadeep, if the Si he gave me was conductive - he didn't think so. To be *extra* careful I held the Si with a pair of pliers with insulating handles and rubber gloves. This should give me plenty of insulation from the high voltage source, I thought.. With the Si about a centimeter away from the needle tip I saw an arc jump across from the needle to the Si and simultaneously felt the shock in my hand and my foot, literally grounding the source. Luckily the supply could only source two microamps and I had set it even lower than this. I immediately went back to tell Ranadeep who proceeded to join me in the lab to investigate things further. Within moments of arriving Ranadeep promptly shocked himself! At which point we both decided we'd done enough lab work for the day and went to get coffee.

While this story isn't particularly flattering for either of us, it captures some

of the essence of my research experience. In addition to getting us out of the lab for the day, it likely strengthened our relationship, taught me a thing or two about safety, and certainly highlights the value in making mistakes. Being in the lab and experimenting is really just that, experimenting. Without the freedom to experiment, and make the occasional mistake, I'm fairly certain I wouldn't have wanted to complete my dissertation. This freedom and opportunity to explore different aspects of the project is really what I have to thank all of my advisors for most. First and foremost I'd like to thank Dr. Cruden who was always willing to answer questions or offer guidance without dictating any particular path. I'd also like to thank my school advisor Professor Gu, who was supportive and gave me similar autonomy. I'd also like to thank Dr. Kashani, Dr. Zhao, and Dr. Maddocks who all provided stimulating discussions, advice and guidance towards the thermal interface work.

Of course my lab-mates are the ones I interacted with on a daily basis and were those who made being at NASA fun. Mostly I'd like to thanks Ranadeep, who despite my unflattering story was a continual source of inspiration. As he said, "even if only one tenth of our ideas worked we would have been "rich and famous"." I'd also like to thank the rest of Cruden's crew, Sarah, Dmitry and Hiro. A special thanks to all of Cattien's group who were particularly supportive towards the end of my research, they include Setha, Jeremy, Bryan, Jovi and Darrell.

Additionally I'd like to thank all of my family (Janet, Tony and Tom) who probably received the most of my complaints, while understanding the least about what I was actually doing. This also applies to my pseudo-family-in-laws who I was fortunate

enough to spend time with after meeting my lovely, talented and brilliant girlfriend Molly. While offering a significant distraction, she also kept me on task during events that may have set me off course.

Chapter 1

Introduction

1.1 Why carbon?

Carbon is the only material to have allotropes in all three dimensions (0D C_{60}, 1D CNT, 2D Graphene, 3D Diamond) [1]. It is the basic element in all known life forms, the second most abundant element by mass in the human body, and it is the fourth most abundant element by mass in the universe. Entire undergraduate classes are devoted to the study of chemical bonding to carbon. So the obvious question arises, "why carbon?".

Carbon owes its unique abilities to its atomic number, 6, and the implications this number has on its electronic configuration, $1s^2 2s^2 2p^2$. The inner $1s^2$ electrons are strongly bound and do not contribute to bonding. However, all four electrons in the second orbital are relatively weakly bound. Additionally the energy difference between the upper $2p$ and lower $2s$ energy levels is small compared to the C-C chemical bond.

As a result, the wave functions of these four electrons can mix, changing the occupation of the $2s$ and $2p$, both increasing the binding strength and number of configurations C can obtain with neighboring atoms. Carbon's ability to exhibit sp^n hybridization distinguishes it from the other remarkable group 14 elements.

1.1.1 Hybridization

sp hybrids

This form of hybridization is characteristic of molecules with alternating single and triple bonds such as alkynes. The $2s$ orbital mixes with one of the three $2p$ orbital, forming two sp orbitals and two unchanged $2p$ orbitals. Figure 1.1 illustrates this mixing, resulting in a linear hybridized atom. In triple bonds such as ethylene, the three bonds are formed by the $sp-sp$ overlap between adjacent carbon atoms, forming a strong σ bond, and two weaker π bonds formed by p-p overlap. A synthetically controversial, 1D, carbon allotrope called carbyne would have such a structure and may posses a number of outstanding physical properties [2, 3].

sp^3 hybrids

Here the $2s$ orbital mixes with all three $2p$ orbitals forming four sp^3 hybridized orbitals. This hybridization results in a tetrahedral configuration which, in addition to a number of organic molecules, can lead to the formation of a 3D carbon allotrope, diamond. Due to the strong σ bonds in all directions, diamond forms an isotropic, cubic structure with a high band gap of 5.3eV. These strong σ bonds give diamond a very high phonon

2
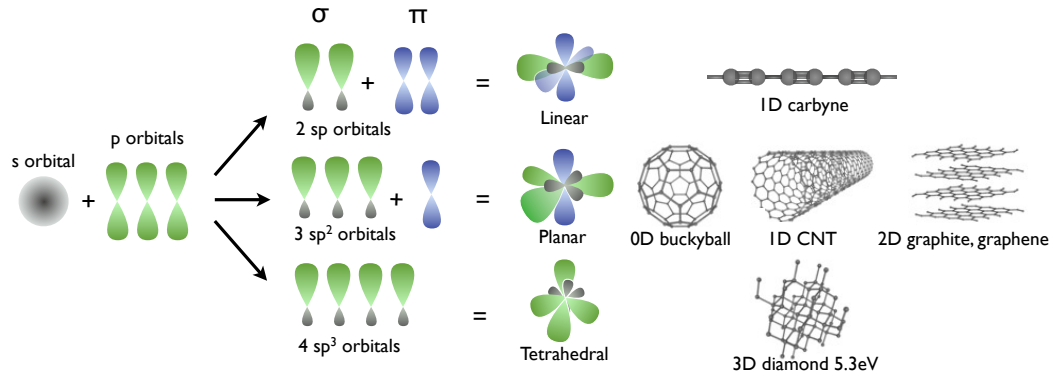
Figure 1.1: Hybridization diagram, showing sp, sp^2 and sp^3 hybridization and the resulting allotropes.

conduction making it one of the most thermally conductive materials. Its extremely high strength and melting point add to its unique properties.

sp^2 hybrids

sp^2 hybridization requires the $2s$ orbital to mix with two $2p$ orbitals forming three sp^2 hybridized orbitals and one remaining $2p$ orbital. This results in a planar structure, able to form three strong σ bonds in the same plane and one remaining π bond perpendicular to the σ bonds. This hybridization forms the most common type of carbon allotrope, graphite. In this configuration, all C atoms form σ bonds with adjacent C atoms along the same plane, while the π bond protrude perpendicularly to the plane, forming a 2D hexagonal structure. Graphite is the result of stacking such structures, giving the allotrope extreme strength along the a-axis, in the σ bond plane, but very weak strength along the c-axis, the direction perpendicular to the σ bonds. This is what leads to

graphites brittle nature, making it useful as a lubricant and in pencils. Interestingly this hybridization is also able to form localized planar arrangements in nano configurations such as the polyhedra 0D, fullerenes, and in the cylindrical and conical morphologies of 1D carbon nanotubes CNTs and carbon nanofibers CNFs.

It is also interesting to note the vast differences between the allotropes. Diamond is clear, an insulator and incredibly strong, yet graphite is black, an electrical conductor, and very brittle. Amorphos carbon is another ubiquitous form of carbon and is a mixture of sp^2 and sp^3 hybridized carbon. Some short-range order can be observed, although it lacks any long-range order.

1.2 sp^2 configurations

1.2.1 3D graphite and 2D graphene

3D graphite is the naturally forming allotrope of sp^2 hybridizied carbon. Graphite is formed by the ABAB stacking of hexagonal sheets of covalently bonded carbon atoms. A single sheet, one atom thick, is known as graphene [4]. While this material has been discussed as early as the 1960s, it was previously thought to be unstable at room temperature. The interest in this material has only recently flourished as a result of the ability to easily produce it, using a simple exfoliation technique discovered by Novoselov et al. in 2004 [4]. Since then, graphene has received similar attention as Carbon Nanotubes (CNTs) did after their discovery in the early 1990s, due to their similarly amazing properties. Its most notable properties include its electrical, thermal and mechanical

properties. The electron transport measurements have shown exceptionally high electron mobilities at room temperature, reaching values as high as $15{,}000 \ \mathrm{cm}^2\mathrm{V}^{-1}\mathrm{s}^{-1}$ and showing little dependence on temperature [5]. Their thermal conductivity is equally impressive with values measured as high as $5300 \pm 480 \ \mathrm{Wm}^{-1}\mathrm{K}^{-1}$ [6] and is shown to be phonon dominated transport.

Graphene's amazing properties are derived from its 2D crystal structure. Figure 1.2 shows the unit cell and associated Brillouin zone of graphene, where $\mathbf{a}_1$ and $\mathbf{a}_2$ are the unit vectors in real space, and $\mathbf{b}_1$ and $\mathbf{b}_2$ are the reciprocal lattice vectors defined as:

$$
\begin{aligned}
\mathbf{a}_1 &= \left(\frac{\sqrt{3}}{2}a, \frac{a}{2} \right), \quad \mathbf{a}_2 = \left(\frac{\sqrt{3}}{2}a, -\frac{a}{2} \right) \\
\mathbf{b}_1 &= \left(\frac{2\pi}{\sqrt{3}}a, \frac{2\pi}{a} \right), \quad \mathbf{b}_2 = \left(\frac{2\pi}{\sqrt{3}}a, -\frac{2\pi}{a} \right)
\end{aligned}
\tag{1.1}
$$

where the lattice constant $a = |\mathbf{a}_1| = |\mathbf{a}_2| = 1.42 \times \sqrt{3} = 2.46 \text{Å}$. Similarly the reciprocal space lattice constant is $|\mathbf{b}_1| = |\mathbf{a}_2| = 4\pi/\sqrt{3}a$. The first Brillouin zone is selected as the shaded hexagon in Figure 1.2, which also shows the points of high symmetry, Γ, M, K. These points of high symmetry are important in regard to the electronic properties, which are discussed in Section 1.3. The c-axis layer separation in graphite is 3.35Å, much larger than the nearest neighbor atom separation within the benzene ring of 1.42Å.
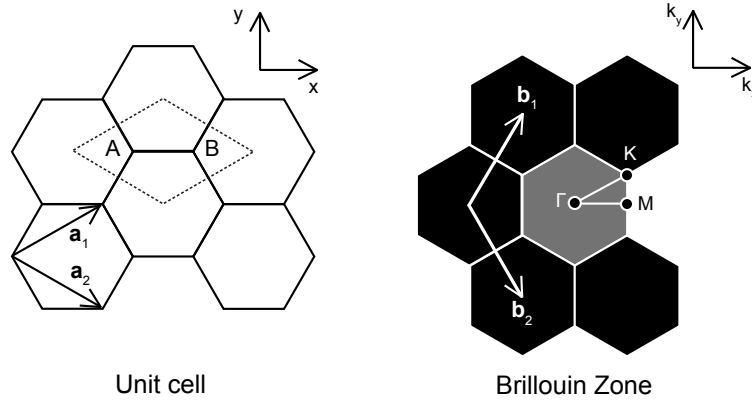
Figure 1.2: Left, diagram of graphen's unit cell, enclosed by the dotted line. 'A' and 'B' denote the two atoms in the unit cell, while $\mathbf{a}_1$ and $\mathbf{a}_2$ denote the unit vectors in real space. Right shows graphene's Brillouin zone, within the gray shaded hexagon. $\mathbf{b}_1$ and $\mathbf{b}_2$ are the unit vectors in reciprocal space, while Γ, M, and K are the points of high symmetry.

1.2.2 0D buckyball or fullerene

The 0D allotropes of carbon are known as FullerenesC_{60}, buckyball, buckminsterfullerene or fullerene, named after Buckminster Fuller for his work with geodesic domes.

The 0D allotropes of carbon are known as Fullerenes, although this class of allotrope is also often generally referred to as buckyball, buckminsterfullerene, or C_{60}. The name Fullerene is derived from Buckminster Fuller for his work with geodesic domes. While C_{60} (containing 60 carbon atoms) is one of the more stable conformations, others such as C_{70} are often created [7]. C_{60} is interesting because of its high stability, which

can be attributed to its cage-like, truncated icosahedron structure, resembling a soccer ball. It contains twenty hexagons and twelve pentagons (no pentagons share a vertex), where each vertex in the polygons contains a C atom and each edge has a bond. It has a diameter of 0.71nm and has become the larges matter to have shown wave-particle duality.

1.2.3   1D carbon nanotubes and carbon nanofibers

There are a variety of 1D carbon nano-structures (CNS) ranging from Single Walled Carbon Nanotubes (SWNT or SWCNT), Multi-walled Carbon Nanotubes (MWNT or MWCNT), Carbon Nanofibers (CNF), and Amorphous CNFs, each with dramatically different structures and differing physical properties [8]. However, all of these structures are sometimes mis-categorized as Carbon Nanotubes (CNTs). Nanotubes fundamentally differ from Nanofibers in that they are completely hollow, whereas CNFs may have periodic breaks in the tubular structure (i.e. bamboo CNFs) or no hollow section at all.

SWNTs have the simplest structure of the CNSs and are composed of a single sheet of graphene rolled into a cylinder. Due to this simplicity and their high purity, they are often used for fundamental physical research. MWNTs are composed of a series of SWNTs nested inside one another. Often researchers will distinguish double-walled CNTs (DWNTs) from MWNTs due to their properties approaching that of SWNTs. MWNTs tend to be easier to fabricate and as a result have found their way into a number of application, where the unique electrical properties of the SWNT are not

7

required. CNFs contain a stacked conical structure or a mixture of stacked cones and tubes. This discontinuity of the hexagonal crystal along the fiber axis dramatically decreases its properties over that of the SWNT and MWNT. A detailed discussion of their sysnthesis techniques is presented in Chapter 2.

SWNT structure

As previously alluded to, the SWNT has some unique characteristics over that of the MWNT, all of which can be related to its physical structure. The transport properties of the SWNT depend largely on the direction in which the graphene sheet is oriented relative to the tube axis. The following treatment is adapted from the work of Saito, Dresselhaus and Dresselhaus – for a more detailed explanation the reader is referred to their book [1]. The left side of Figure 1.3 illustrates the concept of chirality, showing the range of lattice orientations relative to the tube axis. The chiral vector $\mathbf{C}_h$ defines this orientation, the translational vector $\mathbf{T}$ is perpendicular to $\mathbf{C}_h$. The chiral vector is defined in terms of the unit vectors $\mathbf{a}_1$ and $\mathbf{a}_2$ by the following relation:

$$\mathbf{c}_h = n\mathbf{a}_1 + m\mathbf{a}_2 \equiv (n, m), \quad (n, m \text{ are integers}, 0 \leq |m| \leq n). \tag{1.2}$$

The Translational vector $\mathbf{T}$ is the second defining vector used to describe the SWNT unit cell. It is parallel to the SWNT tube axis and perpendicular to the chiral vector. As a result it can also be defined in terms of the unit vectors, $\mathbf{a}_1$ and $\mathbf{a}_2$ as:

$$\mathbf{T} = t_1\mathbf{a}_1 + t_2\mathbf{a}_2 \equiv (t_1, t_2), \quad (\text{where } t_1, t_2 \text{ are integers}) \tag{1.3}$$

Unit cell

Brillouin zone
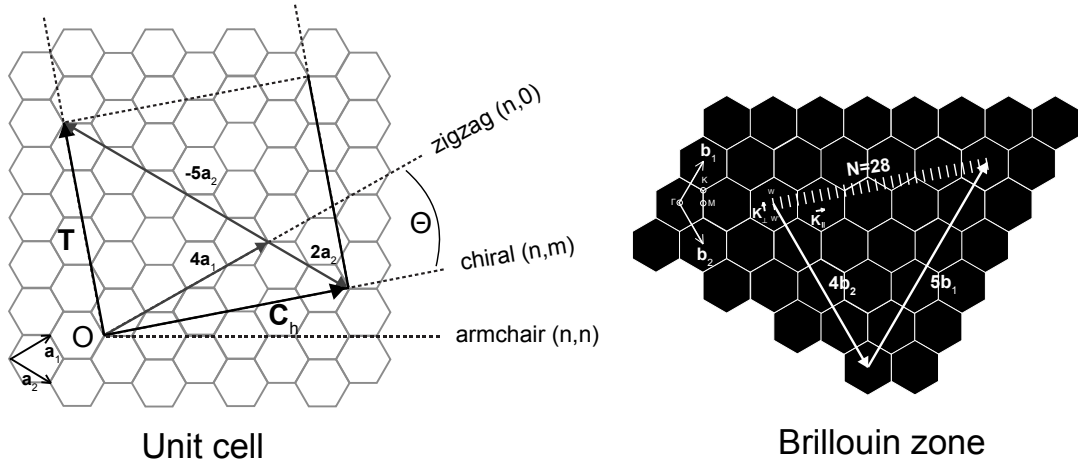
Figure 1.3: Left, hexagonal lattice and unit cell of SWNT and its defining vectors including the chiral vector $\mathbf{C}_h$ and the translational vector $\mathbf{T}$, which is parallel to the tube axis. The specific chirality represented by $\mathbf{C}_h$ is (4,2). Right, shows the reciprocal space and Brillouin zone with the associated reciprocal space vectors $\mathbf{K}_\parallel$ and $\mathbf{K}_\perp$. $\mathbf{K}_\parallel$ is parallel to the first Brillouin zone is represented by the line segment WW'. There are 28 k vectors represented by the N=28 line segments, $\mathbf{K}_\parallel = (4\mathbf{b}_1 - 2\mathbf{b}_2)/28$, and $\mathbf{K}_\perp = (5\mathbf{b}_1 + 4\mathbf{b}_2)/28$.

$\mathbf{T}$ corresponds to the first lattice point in the graphene sheet, which is intersected by the line perpendicular to $\mathbf{C}_h$. Using $\mathbf{C}_h \cdot \mathbf{T} = 0$, $\mathbf{a}_1 \cdot \mathbf{a}_2 = a^2/2$ and the definition of the chiral vector, Eqn. 1.2, one can arrive at an expression for $\mathbf{t}_1$ and $\mathbf{t}_2$ as:

$$t_1 = \frac{2m + n}{d_R}, \quad t_2 = -\frac{2n + m}{d_R} \tag{1.4}$$

9

where d_R is the greatest common denominator the two numerators in the set of equations above. In the example of the (4,2) SWNT in Figure 1.3, $d_R = 2$, $\mathbf{T} = $ (4,-5). The components for both translational and chiral vectors are illustrated on the figure and in this particular case both vectors coincidentally have an $\mathbf{a}_1$ component of 4.

The unit cell for the SWNT is defined by the area encompassed by $\mathbf{C}_h$ and $\mathbf{T}$. The range of chiralities are restricted from zigzag (n,0) to armchair at (n,n). This nomenclature is derived from the profile of the cross-section generated from these two chiral vectors. The circumference of the tube is equal to the magnitude of the chiral vector and hence its diameter, d_t, is related by:

$$d_t = |\mathbf{C}_h|/\pi = \sqrt{\mathbf{C}_h \cdot \mathbf{C}_h}/\pi = a\sqrt{n^2 + m^2 + nm}/\pi \qquad (1.5)$$

Conversely the diameter of the SWNT will define its chiral vector. This eludes to the potential for selecting chirality based on catalyst diameter. The diameter and chiral vector can only take on discrete values due to the periodic boundary condition that must be met for a continuous bond around the circumference of the tube. The chiral angle θ, depicted in the left side of Figure 1.3, is defined as the angle between the chiral vector and unit vector $\mathbf{a}_1$. The chiral angle can take on values between 0 and 30°, due to the hexagonal symmetry of the lattice. Hence for zigzag, $\theta = 0°$, while for armchar $\theta = 30°$.

Given that the unit cell is defined as the area spanned by $\mathbf{C}_h$ and $\mathbf{T}$, and knowing that there are two carbon atoms per area of a hexagon, one can derive the number of carbon atoms in the unit cell by:

$$2N = 2\frac{|\mathbf{C}_h \times \mathbf{T}|}{|\mathbf{a}_1 \times \mathbf{a}_2|} \tag{1.6}$$

Given that the $2p$ electrons are most free to contribute to conduction, knowing the number of electrons per unit cell is critical to understanding the transport properties.

Brillouin zone for SWNT

To work with the Brillouin zone we must first define the reciprocal lattice vectors $\mathbf{K}_{\parallel}$, parallel to the SWNT axis and $\mathbf{K}_{\perp}$ in the circumferential direction. Since the SWNT is effectively 1D, only $\mathbf{K}_{\parallel}$ is a reciprocal lattice vector, while $\mathbf{K}_{\perp}$ has discrete k values in the direction of $\mathbf{C}_h$. The reciprocal lattice vectors are defined using Eqn. 1.4, 1.6 and the following relationships:

$$\mathbf{C}_h \cdot \mathbf{K}_{\perp} = 2\pi, \quad \mathbf{C}_h \cdot \mathbf{K}_{\parallel} = 0$$
$$\mathbf{T} \cdot \mathbf{K}_{\perp} = 0, \qquad \mathbf{T} \cdot \mathbf{K}_{\parallel} = 2\pi \tag{1.7}$$

which results in the expression for $\mathbf{K}_{\parallel}$ and $\mathbf{K}_{\perp}$:

$$\mathbf{K}_{\perp} = \frac{1}{N}(-t_2\mathbf{b}_1 + t_1\mathbf{b}_2), \quad \mathbf{K}_{\parallel} = \frac{1}{N}(m\mathbf{b}_1 - n\mathbf{b}_2) \tag{1.8}$$

The vectors are illustrated for the working example of a (4,2) SWNT, on the right side of Figure 1.3. Here the first Brillioun zone is represented by the WW' line segment, which is parallel to $\mathbf{K}_{\parallel}$.

It can be shown that there are no common divisors for t_1 and t_2 resulting in N discrete wave numbers for $\mu\mathbf{K}_{\perp}$ where $\mu = 1, 2,...,$N-1. This is illustrated on the figure by

11

the N=28 parallel line segments. However, due to the symmetry of the two dimensional graphite lattice, two wave vectors which differ by $N\mathbf{K}_\perp$ should be equivalent. Since the length of the nanotube is effectively infinite (i.e. aspect ratios $> 10^4$), and there is translational symmetry of $\mathbf{T}$, there will be continuous wave vectors in the direction of $\mathbf{K}_\parallel$. The continuous nature of the $\mathbf{K}_\parallel$ and quantized nature of $\mathbf{K}_\perp$ are what gives rise to the nanotubes distinct one-dimensional energy dispersion relations.

1.3 Electronic properties of SWNTs

The electronic structure of the SWNT is basically a subset of that for graphene. Due to the 1D nature of the SWNT, the wave vectors are parallel to the tube axis and discretized, as discussed in the previous section. This leads to 1D energy dispersions, which are effectively cross sections of the energy dispersion for graphene.

Energy dispersion relation of graphene

In graphene, the electrons that contribute to sp^2 bonding are tightly bound to each-other in the plane of the sheet, while the remaining 2p orbital, perpendicular to the sheet, is unchanged and most able to contribute to electron transport. The electron band structure for graphene can be approximated by a tight binding calculation for the π electrons. The electron dispersion relation for graphene has been plotted in Figure 1.4, extending over the Brillouin zone. In the 3D plot the upper half of the energy dispersion curve represents the π^* energy, anti-bonding band, while the lower half describes the π energy bonding band. The two electrons per unit cell occupy the lower, π band. The
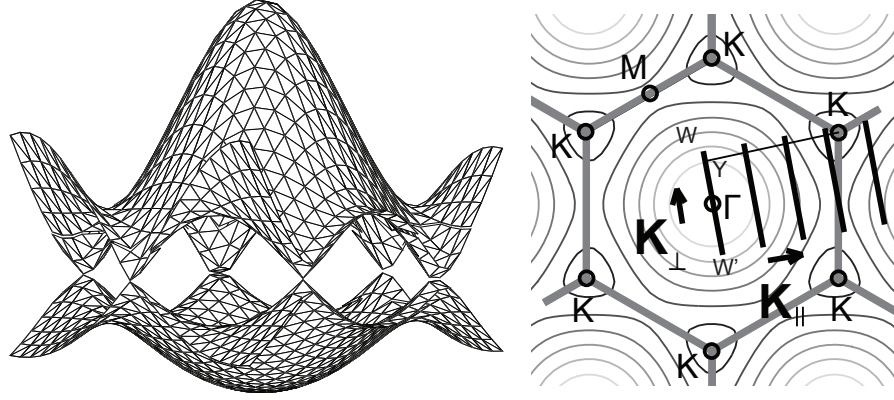
Figure 1.4: 3D energy dispersion relation for graphene over the Brillouin zone, the K points of high symmetry have a degenerate energy gap. Right, 2D contour plot of graphene's energy dispersion relation with overlaid (4,2) SWNT wave vectors and cutting lines for generating 1D dispersion relations of the SWNT (not all N=28 cutting lines are shown and not all elements are to scale).

upper and lower energy bands are degenerate at the K points of symmetry, through which the Fermi energy passes. These points of degeneracy lead to graphite being a semimetal.

Energy dispersion relation of SWNT

The N pairs of 1D energy dispersion relations for the SWNT are generated by the cross sectioning of graphene's 2D energy dispersion relation by the cutting lines described by the two wave vectors and illustrated in the Brillouin zone of Figure 1.3. A more zoomed in view of these cutting lines for the same (4,2) SWNT, overlaid on-top of the contour lines for graphen's π^* anti-bonding energy dispersion is illustrated in Figure 1.4.

13
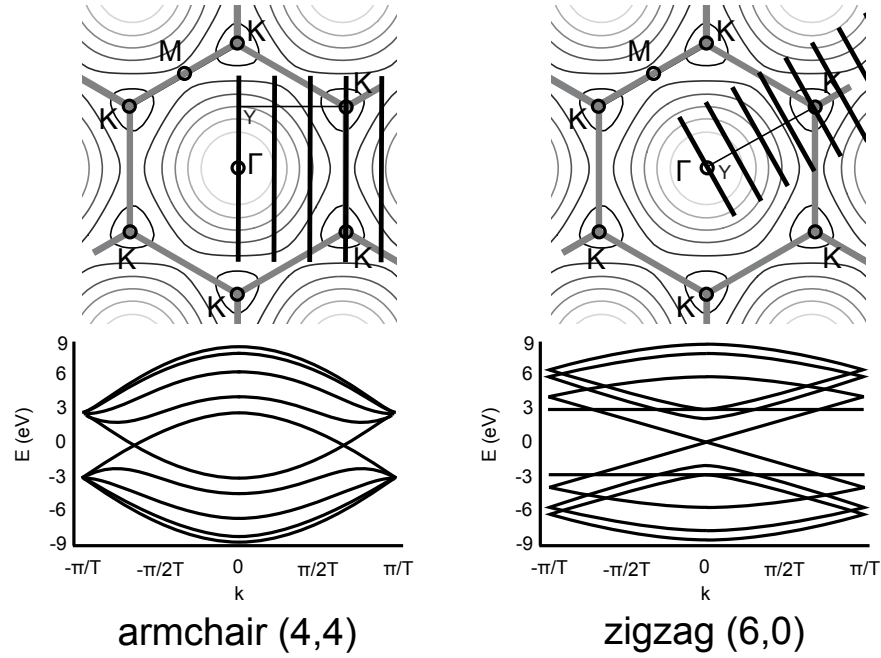
Figure 1.5: Brillouin zone and dispersion relations for two different metallic SWNTs. Showing the cutting lines intersecting the point of degeneracy, causing a zero band gap and metallic behavior.

Similar cutting line overlays are presented in Figure 1.5, along with their associated 1D energy dispersions. In each Figure, only a subset of the cutting lines are presented, those contained within the Brillouin zone. The electronic nature of the SWNT is governed by the way in which these cutting lines intersect graphene's energy bands. The SWNT behaves metallically if the cutting lines intersect the K degenerate points in graphene's energy band, and semiconducting otherwise.

The two illustrations in Figure 1.5 describe metallic SWNTs, while that in 1.4 is semiconducting. The condition for metallic behavior requires that the length of the
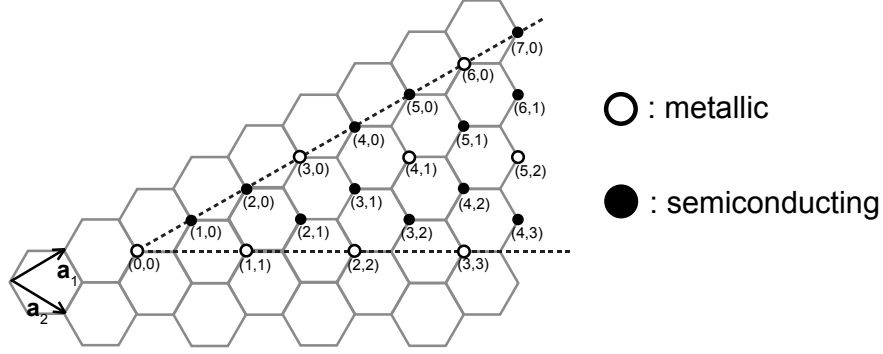
Figure 1.6: Oscillating metallic and semiconducting behavior based on chiral vector $\mathbf{C}_h$, plotted with respect to the hexagonal lattice.

perpendicular $Y\vec{K}$ to the cutting line be an even multiple of $\mathbf{K}_\perp$, so that one of the cutting lines falls on the K point of degeneracy. The equation describing $Y\vec{K}$ is:

$$Y\vec{K} = \frac{2n+m}{3}\mathbf{K}_\perp \tag{1.9}$$

Resulting in the conditions:

$$\text{metalic}: (2n+3)/3 = \text{integer}$$
$$\tag{1.10}$$
$$\text{semiconducting}: (2n+3)/3 \neq \text{integer}$$

This suggests that given a totally random distribution of SWNTs, one third will be metallic, while the remaining will be semiconducting.

SWNT energy gap

As expected, the Density of States (DOS) can be shown to have a non-zero value for

15

energies at the Fermi level E_F located at E=0 for metallic SWNTs, but a value of zero for semiconducting SWNTs. The DOS also shows singularities (van Hove peaks) characteristic of 1D materials. These van Hove singularities result in unique optical properties, which can be used to identify the SWNT chirality using optical spectroscopy. The energy gap for semiconducting SWNTs has been shown to be depend upon the inverse of the their diameter, d_t, and independently to their chirality [1]:

$$E_g = \frac{|t|a_{C\text{-}C}}{d_t}, \tag{1.11}$$

where $a_{C\text{-}C}$ is the nearest neighbor C-C distance on a graphene sheet, $1.44\mathring{A}$, $|t|$ is the nearest neighbor C-C tight binding overlap energy, taken as 3.13 eV for graphite but closer to 2.5 eV for 2D graphene. An interesting observation from this is that for diameters larger than $\sim$1.4nm, the bandgap is smaller than the thermal energy T. This, in addition to the fact that statistically, one third of the SWNTs are metallic, suggests that all MWNTs should behave metallically.

Quantum transport in 1D wire

At low temperatures the conductance of the SWNT is ballistic, i.e. electrons can flow without scattering. This is an effect of quantum confinement, where electrons are only free to move (and scatter) in one direction. This results in a length independent quantum resistance and the ability for electrons to behave as waves, manifesting interference phenomena.

In a traditional bulk material, the resistance is governed by its intrinsic resis-

tivity, ρ and the dimensions of the material:

$$R = \rho \frac{L}{A}, \tag{1.12}$$

where A is the cross sectional area of the wire. Likewise, its conductance is the inverse

of its resistance. For the bulk material, ρ is independent of the material shape or upon

the applied voltage. However, when the dimensions of the wire's cross section shrink,

approaching that of the electron's characteristic lengths (electron mean free path, Fermi

wavelngth, and phase-relaxation length), the resistivity becomes quantized:

$$R = \frac{h}{2q^2} \cdot \frac{1}{M} = R_0 \cdot \frac{1}{\mathcal{T}M}, \tag{1.13}$$

where h is Plank's constant, q is the charge of an electron, M is the number of modes in

the wire, and $\mathcal{T}$ is the transmission probability following a scattering event. R_0 is known

as the quantized resistance and is approximately equal to 12.9kΩ or more precisely

$h/(2q^2)$. In the ballistic limit, there are no scattering events and so the conductance

scales with the number of modes M. This is a fascinating discovery, that even for a

ballistic conductor there is an associated resistance, although it does not scale with the

wire length.

The quantum resistance is a result of the wire contact to the macroscopic

drain. The drain has an ideally infinite number of modes and electrons all of which are

at equilibrium, while the quantum wire has a small number of modes with electrons not

in equilibrium. This requires a redistribution of current among the modes, resulting in

what can be thought of as a contact resistance.

For a non-ideal quantum wire, scattering events can occur, introducing the transmission probability coefficient $\mathcal{T}$ and associated reflection probability $\mathcal{R} = (1 - \mathcal{T})$. A scattering site has the ability to reverse the direction of the electron or change its phase. If the interference effects during scattering are neglected, one can examine a series of $i = 1, .., N$ scatting events to arrive at a length dependence on resistance. For N identical scattering events in series, the total transmission coefficient will be [1]:

$$\frac{\mathcal{R}}{\mathcal{T}} = N \frac{\mathcal{R}_i}{\mathcal{T}_i} \Rightarrow \mathcal{T} = \frac{\mathcal{T}_i}{N(1 - \mathcal{T}_i) + 1} \tag{1.14}$$

and assuming there are λ scattering events per unit length, i.e. $N = \lambda L$ and defining a characteristic length $L_0 = \mathcal{T}/\lambda(1 - \mathcal{T})$, the transmission coefficient then becomes:

$$\mathcal{T} = \frac{\mathcal{T}_i}{\lambda L(1 - \mathcal{T}_i) + \mathcal{T}_i} = \frac{L_0}{L + L_0} \tag{1.15}$$

substituting this into the equation for quantum resistance, Eqn. 1.13, reveals a familiar length dependent relation:

$$R = R_0 \frac{1}{M} \left(1 + \frac{L}{L_0} \right), \tag{1.16}$$

Similarly the dependence on area at the macroscopic scale can be rationalized at the quantum level by the number of current carrying modes in the wire:

$$M \approx \frac{k_F^2}{4\pi} A, \tag{1.17}$$

18

where k_F^2 is the Fermi wavevector. Resulting in the combination of these dimensional elements:

$$R = R_C + R_B = \frac{4\pi R_0}{k_F^2 L_0}\left(\frac{L_0}{A} + \frac{L}{A}\right) = \frac{\rho L_0}{A} + \frac{\rho L}{A} \qquad (1.18)$$

This quantum contact resistance is hidden in large systems where the bulk resistance and other forms of contact resistance dominate the system.

1.4 Phonon conduction of SWNTs

Due to the low mass of Carbon, yet its incredibly high bond strength in the hexagonal lattice, the SWNT is very stiff leading to an exceptionally high speed of sound. This stiffness is also the reason why CNTs have been found to have thermal conductivities rivaling that of Diamond. As a result of this, thermal conduction is dominated by phonons, opposed to electrons, in all CNTs, regardless of their metallic or semiconducting behavior. This section briefly describes the method for calculating the phonon dispersion energies and corresponding density of states followed by a summary of experimental work performed to validate the fundamental physics behind their thermal properties.

Phonon dispersion in graphene

A very similar parallel to that between the electronic properties of graphene and the SWNT can be drawn with regard to the thermal analysis. The dispersion relation for phonons in graphene can be used along with the zone folding techniques described in

sections 1.2.3 and 1.3 to evaluate the SWNTs thermal properties. The phonon dispersion for graphene is calculated using a simple spring approximation for the inter-atomic forces within the lattice, which is valid for small atomic displacements. A simple system of equations of motion can be constructed for a few nearest neighboring atoms. Due to the oscillatory dynamics of the system, a Fourier transform can be used to decouple the system. The normal modes of the system and its dispersion relation can then be determined.

Since there are two carbon atoms in the graphene unit cell, six degrees of freedom must be considered. To accurately describe its dynamics, the interaction of the fourth nearest neighbors must be considered. Values for the force constants are not known a priori but rather are obtained by fitting the phonon dispersion relations over the Brillouin zone as determined experimentally from inelastic neutron scattering or electron energy loss spectroscopy. A simple approximation of the phonon dispersion relation is depicted in Figure 1.7. A noteworthy aspect of this dispersion relation is that the lowest energy, out-of-phase acoustic mode (ZO) has a k^2 relation around the Γ point, while the other two acoustic modes have a more common linear dependence. The remaining three higher energy modes are optical modes and are Raman active, making them very useful in the characterization of the graphitic material.

From the developed phonon dispersion relations, the phonon density of states can be evaluated as a function of frequency. A larger density of states corresponds to a flat region in the phonon dispersion relation as shown for that of graphene in 1.7.
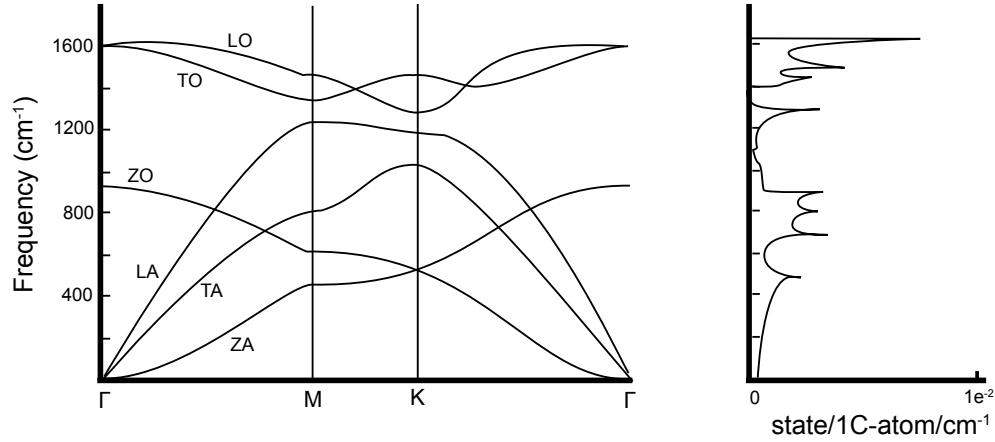
Figure 1.7: Phonon dispersion relation for graphene and associated phonon density of states adapted from [9].

Phonon dispersion relation in a SWNT

Very similarly to that performed in the electronic energy dispersion relation of SWNT (Sec. 1.3), the 1D phonon dispersion relations for a SWNT can be approximated by cross sectioning the 2D phonon dispersion relation for graphene. A more thorough investigation of this method can be found in *Physical Properties of Carbon Nanotubes* [1], the details of which will not be discussed here, although the overall implications of the results are.

Since there are three phonon dispersion relations per atom in graphene and 2N atoms in the SWNT unit cell, there are then 6N SWNT phonon modes per SWNT, which can all be folded into a single Brillouin zone. Several of these may be degenerate leading to fewer than 6N distinct vibrational degrees of freedom. Unfortunately the zone folding method does not accurately predict the 1D dispersion relations for all SWNTs,

particularly at low frequencies. An example of this is the out-of-plane tangential acoustic mode for graphene (ZA), which when rolled into a tube produces a radial breathing mode with non-zero frequency. To solve this problem the 3D dynamical matrix must be solved directly.

There are two distinct differences as a result of rolling the graphene sheet into a tube. The first is that the out-of-phase acoustic mode in graphene translates to a non-zero radial breathing mode in the SWNT. This means that all lower energy modes are linear with k, making the phonon density of states (PDOS) go to zero as the frequency approaches zero, while the PDOS for graphene is finite as $\omega \to 0$. In addition to this there are low energy singularities in the SWNT density of states similar to the van Hove peaks in the electronic density of states. These differences are most notable at low temperatures.

SWNT heat capacity and thermal conductivity

The unique structure of the SWNT is apparent at low temperature by observing the phonon heat capacity C_{ph}. The phonon contribution to heat capacity can be calculated using the phonon density of states. At low temperatures the heat capacity is dominated by the low energy acoustic phonon modes, their behavior as $\omega \to 0$ and $k \to 0$ dictate the behavior of the heat capacity. Since the out-of-plane acoustic mode in the SWNT, showing a k^2 dependence, was shifted to higher energies with respect to that of graphene, the low temperature dependence of C_{ph} will be linear. However, for graphite, MWNTs, and ropes of SWNTs, there is coupling between adjacent graphene sheets, generating low

energy dispersions along the direction normal to the a-axis. Due to their low energies, all of their states can be occupied at relatively low temperatures (T > 50° K), making their moderate temperature behavior effectively the same as 2D graphene. At temperatures below $\sim$ 50K these inter-planar ZA modes become significant causing $C_{ph} \propto T^2$.

Similarly to the heat capacity, the low temperature thermal conductivity can reveal information about the material dimensionally and shape of the low energy phonon dispersion relations. The phonon contribution to thermal conductivity can be expressed in terms of the heat capacity C, group velocity v_z and relaxation time τ [10]:

$$\kappa_{zz} = \sum C v_z^2 \tau \tag{1.19}$$

where κ_{zz} is the diagonal of the thermal conductivity tensor. The group velocity v can be determined from the slope of the acoustic dispersion relations. In highly crystalline materials, at high temperatures, the phonon relaxation time τ is dominated by phonon-phonon Umklapp scattering. At low temperatures inelastic phonon scattering dominates and is a result of boundaries or defects leading to a constant τ. For low crystalline materials such as MWNTs, this inelastic phonon scattering may dominate, obscuring the Umklapp scattering.

1.5 Overview of next generation wiring

The use of CNTs has been largely hindered by the ability to scale up these traits to the macroscopic world. One proposed macroscopic architecture is the CNT wire

also known as the *armchair quantum wire* from the developments of Rice universities *armchair project* [11].

The goal of this approach is to produce a tightly packed bundle of CNTs, possibly SWNTs with preferentially metallic (hence the name *armchair*) tubes, continuous in length, forming a macroscopic wire whose mechanical and electrical properties exceed that of existing wires. Solving this engineering challenge is important to the aerospace field, where weight and strength are of major concern, and in the energy field, where increasing demands will be placed on the electrical grid as our energy consumption increases and power sources are more distant. Several research groups have made large strides towards this effort, the most significant of which are summarized in the following paragraphs. The challenge is difficult due to the CNTs size. Traditional manipulation techniques are insufficient and the van der Waals forces at this scale are strong, making de-agglomeration and realignment of the CNTs difficult. A review of the experimentally measured mechanical properties are summarized in table 1.1.

Table 1.1: Mechanical properties of CNTs

Material	Young's Modulus (GPa)	Tensile Strength (GPa)	Specific Strength (kN-m/kg)
SWNT [12]	30	1002	20,000
MWNT [13]	800-900	150	56,000
Steel [14]	200	0.2	254

Dry spinning

The name 'dry spinning' suggests that no liquid solution is used to disperse and aid in alignment and wire formation. Within this domain there are two distinct and notable methods developed. The first is an alignment and fiber forming process performed in-situ to the growth, while the second is a post production method.

The direct vapor phase spinning method is based on the Floating Catalyst synthesis technique described in Section 2.2.2.1. During growth Ya-Li Li and others noticed that the CNTs would often self assemble into long wires, sometimes extending the entire length of the furnace. Li et al. extended upon this and found that it was possible to make continuous wires by mechanically drawing the CNTs from the "aerogel" state within the furnace [15]. The "aerogel" state is described as having the consistency of "elastic smoke", where the CNTs have enough interactions to be mechanically stretched. Li reports "the key requirements for continuous spinning are the rapid production of high-purity nanotubes to form an aerogel (19) in the furnace hot zone and the forcible removal of the product from the reaction zone by continuous windup". Li and others have also been able to make CNT sheets using this method. Both the sheets and the wires show great promise both in terms of their mechanical and electrical properties, see Table 1.2 below for a summary of these properties. Recently a company, *nanocorp*, has started the process of trying to commercialize this technique for large-scale wire production.

This spinning technique is in some sense very similar to the direct vapor phase spinning technique described above. This method takes advantage of the Van der Waals

interaction between CNTs to be able to mechanically stretch and align the CNT forests into coherent wires and sheets. Rather than spinning wires from the "aerogel" state, the wires are spun from a vertically aligned forest of CNTs grown on a flat substrate using the CVD method as described in Section 2.2.2.3. Once vertically arranged in a CNT forest, researchers have been able to pluck a few tubes from one edge of the array, using a needle or scotch tape, and slowly drag them away. As these initial tubes are drawn away others are carried with them, causing what can be described as a side-by-side telescoping effect. As a fiber is pulled away it can be simultaneously twisted, in the process increasing strength. Zheng et al. have been able to make fibers and sheets with high tensile strengths and moduli but even more impressive specific strengths and stiffness due to their incredibly low density [16], [17], [18], see Table 1.2. Although the physical properties of these fibers are quite impressive, there is still concern about the scalability of this technique. While researchers have been able to grow vertically aligned forests up to the wafer scale, this still presents an ultimate limit to the length of the fibers formed using this technique.

Wet spinning

Wet spinning is a traditional technique used to make polymeric fibers. The polymers are dissolved into an appropriate solvent then extruded though a spinneret that is submerged in a coagulation bath. As the polymer solution comes in contact with the coagulant it precipitates from the solution and solidifies. This basic concept has been used to develop two very different CNT fibers as described below.

Lars M. Ericson et al. at Rice university used super acids to disperse high concentrations of CNTs which are then wet spun into coagulation baths of water, creating some very interesting fibers [19]. The 102% sulfuric acid is able to disperse relatively high concentrations of CNTs, around 4% wt., by surrounding the individual tubes with acid anions. This mixture can be maintained if kept fastidiously dry. The solution is then extruded through a small orifice and left to drop a few feet into a coagulation bath of water. Once the super acid solution hits the water it reacts creating needle-like crystal solvates that they refer to as "SWNT alewives". Once the solution reacts the fiber is formed and can be drawn from the coagulation bath onto a spinning drum. This method allows for continuous spinning of fiber of nearly any length. Despite this good process-ability the tensile strengths achieved were only 116±10 MPa. Although the conductivities were quite high, 5×10^5 S/m, they're still two orders of magnitude lower than copper, 6.3×10^7 S/m. This method seems quite promising and may be improved though better alignment of the SWNTs.

Brigitte Vigolo et al. have wet spun similar SWNT fibers as Ericson but by using a completely different nanotube solution and coagulation bath [20]. Here the SWNT solution is based off of a simple aqueous solution with a surfactant, SDS, for better dispersion and de-clumping of the nanotubes. The coagulation bath was a 5% wt. 70k MW polyvinylalcohol (PVA) solution in water. Vigolo speculates that because the PVA is amphiphilic it displaces some of the SDS attached to the SWNTs. However, in contrast to SDS, PVA doesn't provide a suitable CNT dispersant, allowing the Van der Waals interaction between tubes to elevate, creating a cohesive fiber. Although the

fibers produced using this method are physically much less impressive than the ones produced using the super acid technique, this method does have the advantage of being much safer and easy to experiment with.

Homogenous electrospinning

Electrospinning is similar to traditional textile dry spinning but creates much finer, typically nano scale, fibers. This process involves suitably viscoelastic solutions, i.e. polymer solutions, as the fiber material, which is simultaneously stretched and dried by the application of a large electric field. Although plain CNT solutions do not posses the viscoelastic property required for electrospinning, many different homogenous CNT/polymer solutions do. The application of this technique to CNT/polymer composites has seen much attention because of its unique ability to well align the CNTs along the axis of the resulting ultra-fine fiber. Although the physical properties of these CNT/polymer electrospun composite fibers do not rival those from other techniques previously mentioned.

1.6 Overview of CNT thermal interface materials (TIMs)

As previously discussed, due to its high crystallinity (low defects) and high bond strength, CNTs posses some of the highest thermal conductivities of any material. This along with their ability to conform to nanoscale surface features makes them an attractive material for thermal interface management. Thermal interface management is becoming an increasing limiting factor in the progression (i.e. miniaturization and

Table 1.2: Summary of experimental macroscopic CNT wire production.

Method	CNT type	Alignment FWHM	Electrical σ (Ω^{-1} m^{-1})	Tensile Strength (GPa)	Modulus (GPa)
Vapor phase [15]	SW-MW	11°	8.3 x 10^5	0.1 - 10	-
Aligned forest [16]	MW	-	3 x 10^4	1.35-3.35	100 - 263
Super acid [19]	SW	31°	5 x 10^5	0.116	120 $\pm$ 10
PVA coagulation [20]	SW	$50° - 65°$	3 x 10^3	-	9 - 40

speed increase) of electronics. The International Technology Roadmap for Semiconductors (ITRS) identifies thermal management, specifically TIMs and heat-sinks, to be likely bottlenecks in next generation electronics. This section briefly describes some of the work done in applying CNTs to the thermal interface problem. A more general description of the thermal interface problem and some of the work done in this field is presented in Chapter 4.

Unaligned CNT mixtures

Early attempts to make CNT based TIMs involved simply mixing CNTs with greases. This followed the general method for making traditional TIMs by incorporation of a fraction of highly conducting particles into a low conductivity, viscous liquid. This is a "filling" type of TIM whereby it is able to move freely towards voids between

the two conductors, effectively increasing the area of conduction. This method was expected to show great improvements with only a slight fraction of filler, above the percolation threshold for conduction. However, while this method does show some promise, it doesn't approach the levels originally expected. For example, Liu et al. found that with a 3.8% wt. loading of a mixture of SWNTs and MWNTs into a silicone elastomer, they were able to achieve a 65% increase in conductivity [21]. Biercuk et al. observed slightly more favorable results with the incorporation of only 1% SWNTs into industrial epoxy, showing a 125% increase in conductivity at room temperature. Much of the reason for these poor enhancements are a result of the uniaxial properties of the CNT. Homogenous mixing of the CNTs leads to randomly, or even partially horizontally oriented CNTs depending on the deposition technique, which decreases the effective thermal conductivity. CNTs oriented normally to the conducting surfaces are better suited for thermal conduction.

Aligned CNT forests

Aligned CNT forests have shown much more promising results over that of their unaligned counterpart, producing contact resistances that are competitive with state of the art TIMs [22]. These architectures typically have no additional filler material, composed purely of CNTs grown on a substrate using the chemical vapor deposition technique discussed in Section 2.2.2.3. In addition to being aligned in the direction of heat flow, each nanotube spans the gap between the two surfaces. However, these improvements are somewhat detracted by the fact that this TIM is of the 'interrupting' type. 'interrupt-

single-sided: double-sided:

Dry contacts
~12mm²K/W

Opposite sides of foil
~12mm²K/W

Bonded free ends
~1mm²K/W

CNT to CNT
~4mm²K/W

Filled with grease or PCM
~5mm²K/W
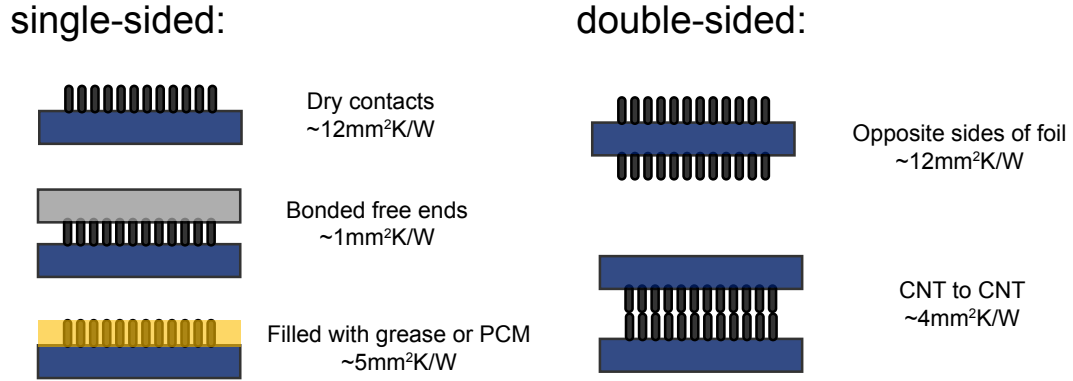
Figure 1.8: Vertically aligned CNT TIM assemblies.

ing' TIMs break the original contact between the conductors, creating at least two new contacts each with hopefully less than half the resistance of the original contact. A more detailed explanation of the TIM types are discussed in Section 4.1.

Dry single-sided interface: Much of the pioneering work with vertically aligned CNT arrays (VACNT) was done using simple single-sided samples. Here the CNTs are grown on one side of a substrate, while the contribution from the opposite side is either subtracted using another reference TIM or is intrinsically unnecessary to the thermal measurement technique. This type of VACNT assembly is referred to as a single-sided interface assembly and is the most commonly studied in the literature. An illustration of this, along with the other vertically aligned assemblies, is shown in Figure 1.8. In this case the CNTs are 'dry adhered' to a mating substrate, without any additional material to aid the contact. The CNT tips make van der Waals contacts to the opposing substrate and are found by most research groups to be the dominant source of resistance

31

around 10-30 mm^{2}K/W [22, 23]. The growth ends are assumed to have good chemically bonded contacts giving them a much lower resistance on the order of 1-2 mm^{2}K/W, while the bulk resistance of the CNTs is of similar magnitude. Figure 1.9 plots a review of the single-sided dry interface measurements performed by Fisher's group [24, 25, 26], showing an increase in performance over time and an improvement when switching from a DC to AC thermal measurement technique. While these results are competitive with existing technologies, the desire to further decrease the contact resistance has lead to the development of a number of alterations to this basic assembly.

VACNTs + grease or PCM: An obvious next step in development of the VACNT TIM is to observe the effect of adding some other existing TIM to the CNT forest. Similarly to the unaligned CNT mixtures, the grease or phase change material (PCM) is expected to increase the effective contact area near the tips of the CNTs, in turn decreasing the contact resistance at the opposing substrate. This method does in fact decrease the overall resistance by a little less than a factor of two in some cases [27, 25].

Bonded tips: Attempts to further decrease the CNT-opposing substrate interface resistance have lead to investigations into permanently bonding CNT tips to the opposing substrate using thermo-compression techniques [22, 28, 29]. This technique has shown the strongest improvement, with bonded contact resistance approaching that of the growth end contact, sim1mm^{2}K/W [22]. This method does however require considerably more work, including deposition of thin metal films on the tips of the CNTs and a thermo-compression step. Additionally, once established, the contact cannot be
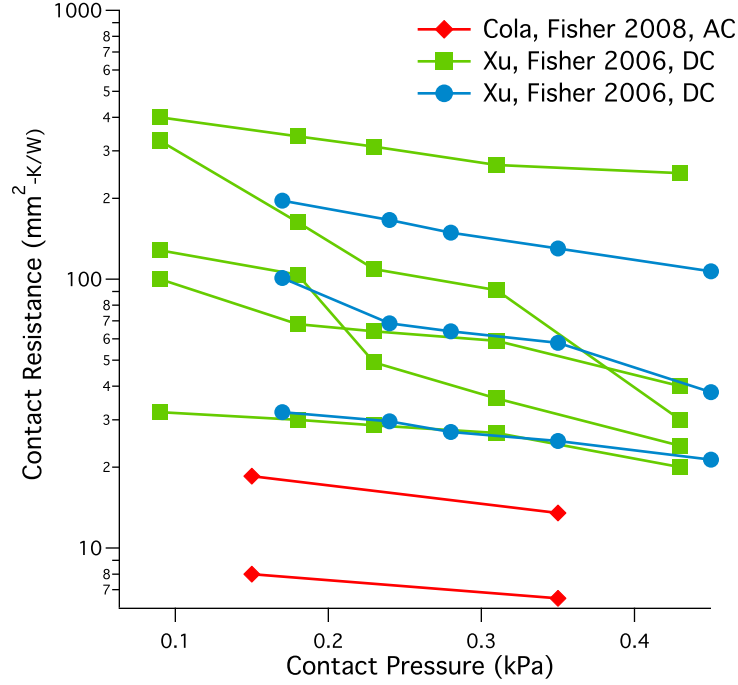
Figure 1.9: Review of single-sided CNT TIM interface resistances from Fisher's group [24, 25, 26]. DC refers to the steady state, 1D reference bar thermal measurement method, while AC refers to the transient photo-acoustic thermal measurement.

irreversibly broken.

Double-sided foils: As a more practical implementation, one which can be inserted into an existing system, work into double-sided VACNTs on foil substrates have been pursued. On initial inspection, one would imagine that these assemblies would simply be double the resistance of the single-sided plus any bulk contributions from the foil itself. However, due to the flexibility of the foil, there has been some thought that it may help the CNTs conform to the surface, especially if the surface is non-ideal,

33

containing high surface roughness or waviness. Indeed, some of these studies have shown promising results where the double-sided foil performs similarly well to single-sided samples [30, 31].

Opposing CNT to CNT contacts: The last morphology studied is that of two opposing CNT arrays. As with the single-sided assembly, the growth interface is likely to have a relatively low resistance for both arrays. This suggests that, in order to improve the performance over the single-sided assembly, the CNT to CNT interface resistance must perform better than the CNT to opposing substrate resistance. This interface is likely to perform better due to the fact that the acoustic mismatch between interfaces should be zero, since the two surfaces are composed of the same material, and due to the fact that the both sides of the interface can deform with equal compressibility, reducing the effective modulus of the interface [32]. Indeed these assemblies have been shown to have a reduced resistance over the single-sided counterparts. However, this benefit comes at the cost of needing to be grown directly on the target surface (i.e. not a drop-in-place solution), which is often not possible or feasible due to the constraints on the growth process, in particular the high temperatures experienced during growth. The bonding techniques described earlier may be a way to mitigate these difficulties, although again it requires additional processing steps.

In addition to the different morphologies, there are also a number of thermal measurement techniques and subtle nuances in the measurement method. As a result

there are vast differences in the results being published. Even thermal measurements taken using the same technique with a reference standard may deviate considerably from one lab to the next. This variation in metrology has hindered much of the progress in the field.

1.7 Dissertation overview

The work presented here focuses on scaling up the remarkable transport properties of the CNT to the macroscopic scale. This effort is pursued in three facets; (1) scaling the synthesis, (2) developing methods to produce massively serialized chains of CNTs for their electrical transport, and (3), the bulk of the thesis, focuses on developing and characterizing assemblies of parallel 2D arrays of vertically aligned CNTs for their thermal interface applications.

Chapter 2 gives an overview of the synthesis techniques followed by an in depth discussion of the design, construction and testing of a custom made, large scale, chemical vapor deposition chamber for MWNT synthesis. Chapter 3 describes the investigation into a new technique for developing macroscopic CNT wires by way of a coaxial electrospinning technique. Chpater 4 introduces the hurdles associated with thermal interfaces and describes the fundamental problems associated with them. It also discusses the design and development of the 1D reference bar thermal measurement system, used extensively throughout chapters 5 and 6. Chapter 5 investigates the thermal interface properties of MWNTs grown on Silicon substrates, finding that the thermal resistance

follows two regimes that can be differentiated with the critical buckling pressure of the forest. Chapter 6 investigates the thermal properties of self catalyzing Fecralloy substrates for their use as thermal interface materials (TIMs). The growth behavior is studied by way of the array morphologies, which are then used to rationalize the thermal contact resistance of these samples. Chapter 7 describes the theory and experimental implementation of a transient thermal measurement system based on the 3ω method. This system is then used to characterize a few samples on both Silicon substrates and Fecralloy substrates, offering insight into the dominant source of resistance in these two growth substrates. Finally Chapter 8 presents a new technique for characterizing nanoscale contact dynamics using a modified approach based on environmental SEM. This technique is used to study the real contact area of a MWNT forest, the results of which validate other van der Waals adhesion and thermal interface studies. The conclusion summarizes the work here and offers some suggestions for future work.

Chapter 2

CNT synthesis

2.1 Introduction

This section describes an overview of the CNT synthesis techniques, their advantages and disadvantages, and their defining characteristics. The method largely used in this study was the atmospheric pressure, thermal CVD method due to its versatility and simplicity. A more detailed discussion of this technique and a summary of some of the results from this chamber serve as one of the motivating factors in the development of a large scale, 4 inch wafer CVD system discussed in the second half of this chapter. The design criteria for the large scale CVD chamber was to maximize growth uniformity across a 4 inch diameter wafer. With this in mind, analysis of an existing hot-plate, cold wall, thermal CVD system helped identified some critical aspects to improve uniformity. A custom heated shower-head gas delivery system and dual zone hot-plate were made. A number of challenges faced during the initial testing of the system are discussed,

followed by results showing good uniformity across the substrate.

2.2 Background

Over the past two decades, considerable effort has been placed on refining, expanding and understanding the methods of synthesizing CNTs. Broadly speaking the methods can be broken up into two categories, physical and chemical techniques. Physical methods rely on high energies to release the carbon atoms from the precursor, while chemical methods catalytically decompose the precursor. In addition to the materials and resources needed for each technique, the overall product greatly influences the method selection, when building a new reactor. The synthesis method will affect the products quality, composition, and configuration. More detail into the advantages and disadvantages of each synthesis technique is presented in the following subsections.

2.2.1 Physical methods

2.2.1.1 Arc discharge

Arc discharge growth was the first method used that conclusively produced MWNTs. Iijima was using this method to produce C_{60} when he observed the MWNT [33]. This method was later shown to produce SWNTs by introducing catalytic metals such as Fe, Co, Ni into the carbon precursor. This method relies on the evaporation of C atoms by an inert gas (He, Ar) plasma at low pressures. The plasma is generated by high currents ($\sim$100A) passing across two carbon electrodes placed end to end and can

generate temperatures in excess of 3000°C. The carbon vaporizes from the anode and condenses in the form of MWNT, SWNT, C_{60} and amorphous carbon on the cathode. Higher concentrations of a given species can be controlled through processing conditions such as pressure, temperature or the concentrations of catalytic additives to the precursor. This method appears to produce the highest quality CNTs, possibly due to the high temperature annealing effect [34], although the quality comes at the cost of needing high energy and the post production purification. The CNT growth is also somewhat chaotic, with bundles of tubes only slightly aligned to the flow of current. Although this method is simple, inexpensive and can produce very high quality SWNTs, its low yield, post-process purification and non-scalable nature has fueled the search for other techniques.

2.2.1.2 Laser Ablation

Like arc discharge, laser Ablation relies on the evaporation of a carbon target. The method was developed in 1995 by Guo et al. [35]. The method uses a pulsed or continuous laser aimed at a carbon target, contained in a high temperature furnace ($\sim$1200°C) filled with an inert atmosphere (Ar, He). As the target evaporates, the gaseous carbon flows down stream through the furnace to a cooled Cu collector where the carbon condenses into a CNT mat composed of ropes or bundles of tubes and other carbon nanomaterials. The configuration of the tubes grown using this method is similar to that of the arc discharge method, yet the yield of CNTs to other carbon species is slightly higher. Similarly to the arc discharge method, this technique requires some

post-process purification, although the fraction of nanomaterial species can be slightly controlled through processing conditions.

2.2.2 Chemical methods

Chemical methods can be further subdivided into substrate based chemical vapor deposition (CVD) and floating catalyst or aerosol techniques.

2.2.2.1 Floating catalyst

The floating catalyst or aerosol method is a thermally driven process similar to that of CVD, though in this case the catalyst is in an aerosol rather than deposited onto a substrate. What makes it noteworthy in this context is its growth configuration. The tubes are grown in the aerosol phase, which opens up interesting possibilities for collecting them as they're growing. This method is also potentially continuous, both the precursor and catalyst can be continuously fed into one end of the furnace while CNTs are drawn out the other end. This is particularly attractive for making wires of "infinite" length. Li et al. extended upon this and found that it was possible to make continuous wires by mechanically drawing the CNTs from the "aerogel" state within the furnace [15]. The continuous nature of this method and the ability to make relatively high quality materials without post-production purification make it appealing for its use in mass production of CNTs.

2.2.2.2 Flame synthesis

As its name suggests, the flame synthesis method is used to form SWNTs in a controlled flame environment. The method is aimed at creating SWNTs from very inexpensive materials and lower energy sources [36]. A two stage flame arrangement is used to exploit the emission of metal aerosols during combustion of cheap hydrocarbons. The first stage combusts the raw materials forming metal aerosols and carbon exhaust, while the second flame releases the C atoms to form CNTs from the floating metal catalyst by a method similar to the floating catalyst technique. While potentially more scalable and cheaper to produce, this method produces low purity CNTs with a significant amount of catalyst and soot, requiring further purification for many applications.

2.2.2.3 Substrate supported catalyst CVD

Substrate supported catalyst CVD has gained widespread use and attention due to the highly pure and aligned products. The CNTs align themselves perpendicular to the substrate during growth, making them attractive for a number of applications including Thermal Interface Matierals (TIMs) [22], field emission electrodes [37], and building blocks for MEMS switches [38], to name a few. Additionally the growth areas can be trivially controlled by lithographically patterning the catalyst, further increasing the utility of this technique.

The CVD method is broken up into two distinct parts, yet can be accomplished seamlessly by the natural ramping of the furnace. The first step involves catalyst preparation. Heating is used to transform the (typically carbide forming) transition metals

from thin-films (characteristic of their deposition process), into nano-islands. This process is a form of Ostwald ripening [39]. This is followed by heating the reactor to a suitable growth temperature and flowing a, typically low molecular weight hydrocarbon, precursor into the reaction zone. Dissociation of the hydrocarbon by pyrolysis is usually aided by the catalyst. The dissociated carbon atoms are then thought to dissolve into the catalyst, and upon saturation the CNT forms as precipitate [40]. This basic process is illustrated on the left side of Figure 2.1.
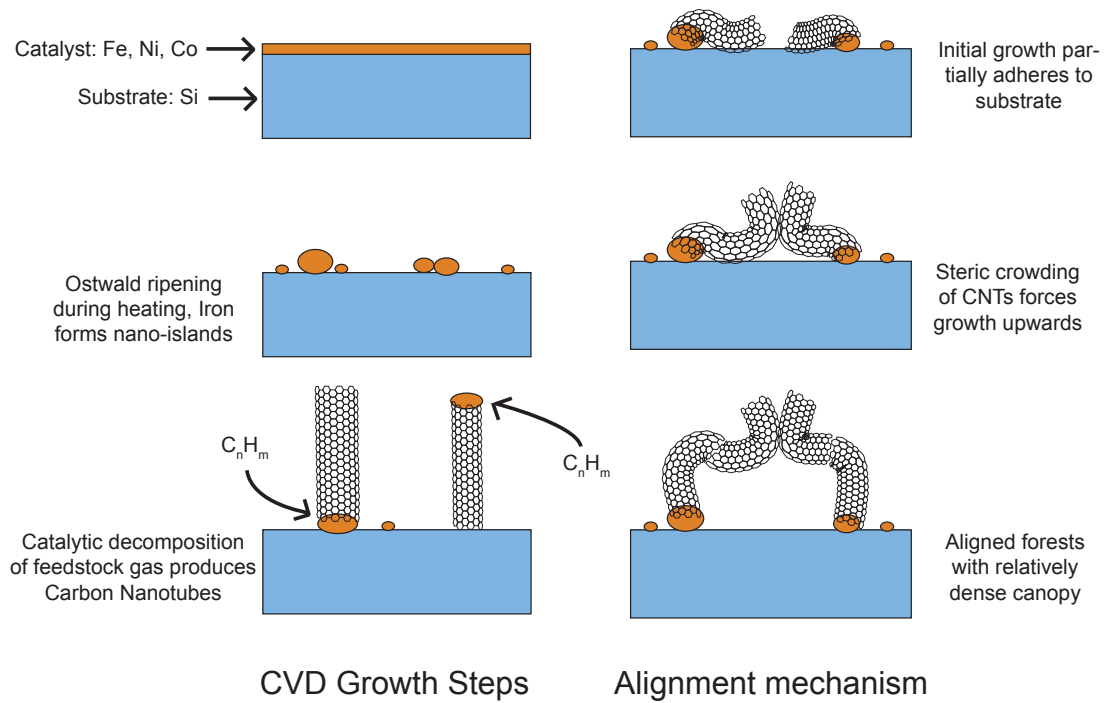
Figure 2.1: Substrate supported catalyst CVD growth and alignment mechanisms.

As the CNT extends out of the catalyst, the catalyst can either remain adhered to the substrate or can be lifted from the surface, this is referred to as 'root' and 'tip'

growth respectively and is as illustrated in the bottom left element of Figure 2.1. In either growth mechanism, the CNTs align themselves perpendicularly to the growth substrate. This is thought to occur as a result of a densification of CNT material early in the growth process resulting in steric crowding of the CNTs along the substrate forcing them to grow vertically [41]. This alignment mechanism is illustrated on the right side of Figure 2.1.

The basic process described above is known as thermal CVD and is the most common CNT synthesis technique, although slight variants have become popular. In particular, Plasma Enhanced CVD (PECVD) is often used, where a glow discharge is generated in the reactor to facilitate or alter growth [42]. The plasma is believed to aid in the dissociation of the precursor, although in many cases it is also likely to increase the substrate temperature through ion bombardment. The plasma may also facilitate in aligned growth through the generation of an electric field. This observation has resulted in the study of Electric field assisted CVD in which the ansiotropic polarizability of the CNT is leveraged to aid in alignment.

2.3 Atmospheric pressure thermal CVD

Due to the overwhelming simplicity and versatility of the substrate supported catalyst CVD method, it has become the preferred method for most labs performing CNT research. Much of the work presented here made use of such a system. A simple overview of the atmospheric thermal CVD system used in this research will be discussed

along with an overview of the results from this system. Advantages and disadvantages of this system will be discussed and serves as the motivation for the implementation of a custom furnace in the following section (Sect. 2.4).
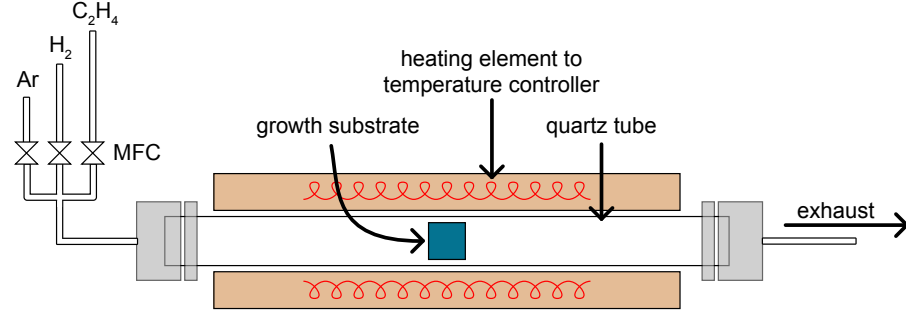
Figure 2.2: Diagram of atmospheric thermal CVD tube furnace.

Figure 2.2 illustrates the simplicity of the atmospheric thermal CVD setup, which can be constructed from all 'off-the-shelf' products. Its main components consist of the furnace, often a quartz tube furnace with integrated temperature controller, the mass flow controllers for gas regulation and the feedstock and carrier gasses (Ar, H_2, and hydrocarbon, e.g. C_2H_4).

Despite the relative simplicity of this system, it is able to provide a good platform for small scale experiments. Figure 2.3 illustrates the long term stability of this system, plotting growth rate for two batches of samples grown with excess of two months between them and under heavy use from multiple users during this timeframe. Such a system does however suffer from a few pitfalls, mostly related to the precise consistency between samples. Figure 2.4 illustrates the inconsistency between sample
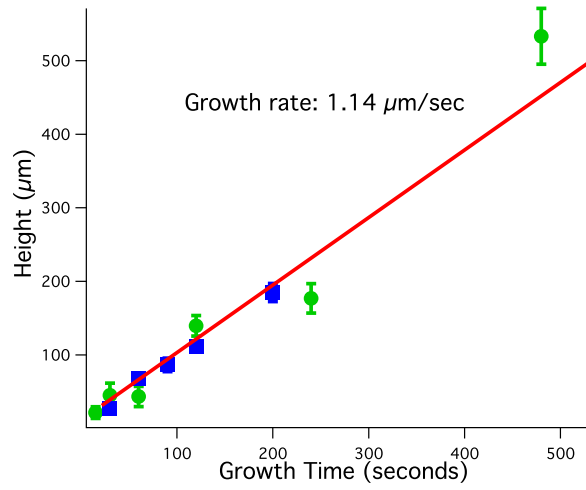
Figure 2.3: Plot of atmospheric thermal CVD, MWNT growth rate on Silicon substrate using 10nm Al buffer layer and 2.5nm Fe, grown at $750°C$. Blue and green data are separated by over six months showing long term stability.

using identical growth conditions. This figure plots four measurable quantities related to the array; height, density, MWNT diameter, and the Raman disorder to graphitic band ratio (D/G ratio), offering a metric to quantify the crystallinity of the CNTs. From these plots it is clear that while the diameter varies little, all points lie within the standard deviation of the others – the height, density and D/G ratio vary considerably. Unfortunately placing multiple samples in the same chamber does not circumvent this problem and is often made worse by such efforts. Additionally the space in the chamber is limited, the diameter of the system used here was just under 2cm, leaving little room for splitting a single growth substrate into multiple samples for testing or for producing a large area thermal interface material. The consistency and ability to grow multiple

45

samples simultaneously motivated the development of a custom cold-wall, hot-plate CVD chamber described in the next section 2.4.
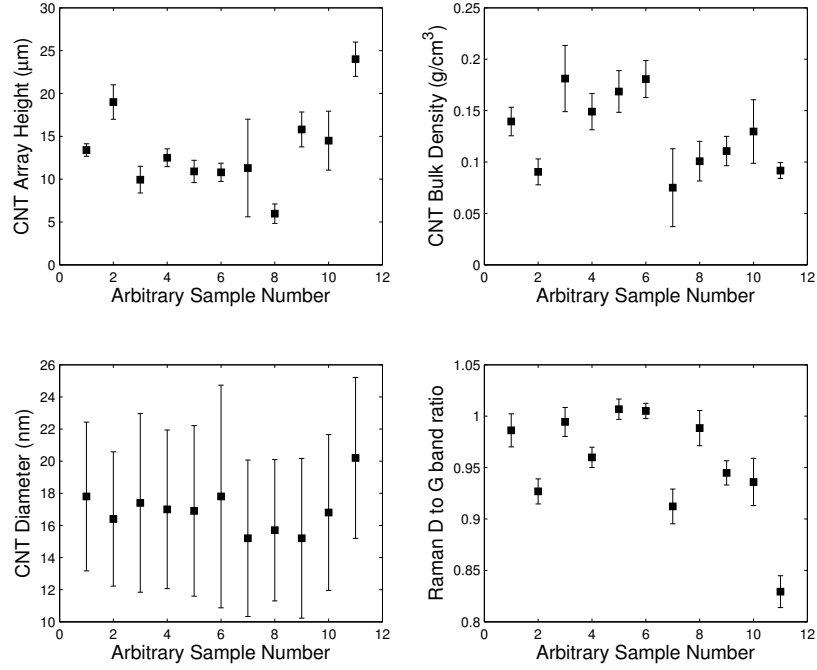
Figure 2.4: Four plots showing the sample growth consistency for the atmospheric thermal CVD chamber.

2.4 Design, construction and testing of large scale thermal CVD reactor

2.4.1 Motivation

A substantial motivation for designing and constructing a custom made CVD chamber was aimed at improving reproducibility between samples for better control over future experiments. In addition to this there was some interest in commercializing such a growth process, requiring larger scale production of CNT arrays to reduce manufacturing costs and to accommodate versatile industrial applications.

2.4.2 Design

Two basic design constraints were placed on the chamber. The size was specified to have a 100mm diameter, consistent with 4 inch wafers commonly used in pilot production and the conformity across this area should be maximized.

Given these constraints, investigations into existing systems were made. Interestingly there is little literature on the design of large scale CVD chambers for CNT synthesis. As a result, investigations into a smaller, existing systems were made. In particular, tests were performed on smaller scale, 60mm diameter hot-plate, cold-wall, CVD chamber designed for experimental scale CNT synthesis. This experimental system was used extensively by Ranadeep Bhowmick who used it to study MWNT growth kinetics [40].

A basic diagram of the chamber under investigation is presented in Figure 2.5A.
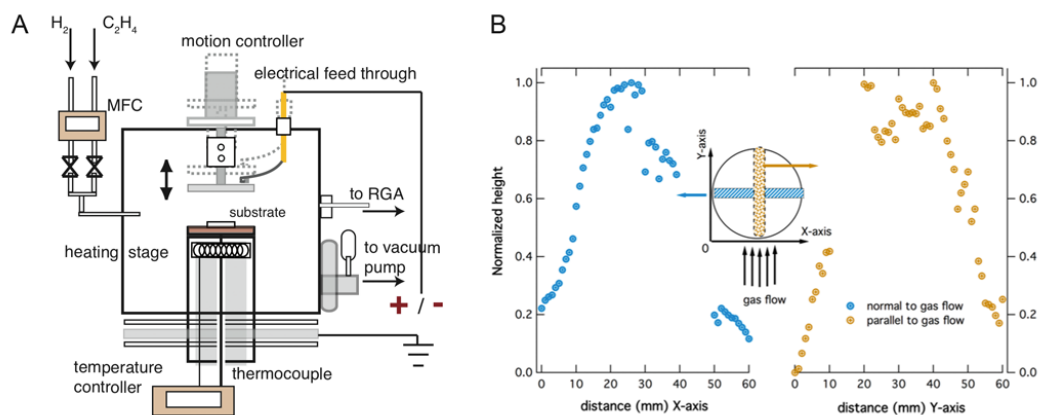
Figure 2.5: 60mm diameter CVD system used in testing.

It contained a single heating element that spanned the entire width of the hot-plate, had gas fed from one side of the chamber, parallel to the hot-plate surface, and had the exhaust on the opposite side as the gas inlet, as illustrated in the diagram. In addition to this it had a variable distance plate suspended over the hot-plate. Originally designed for plasma enhanced CVD then later adapted for electric field enhanced growth tests, it was found that this plate served as a heat reflector and was integral to achieving good CNT growth. The hot-plate design, gas flow, and heat reflection were all suspected to have strong effects on the substrate temperature and hence the CNT growth uniformity.

Characterization of the small 60mm diameter chamber was performed by analyzing the resulting CNT growth height as a function of radius along the hot-plate. This was done both perpendicularly and parallel to the gas flow, the plots of which are presented in Figure 2.5B. This information was gathered by growing on several $1cm^2$ silicon substrates placed radially along the hot-plate, then cleaving the samples after

48

growth and imaging the cross sections using the SEM. While the plots are somewhat sporadic, probably due to the chaotic cleaving process, there is clearly a large difference in CNT height between the edges of the hot-plate and the center. This roughly follows a normal distribution and can be fit such that the height for growth perpendicular to gas flow is centered 5.4mm from the center with a one σ width of 18mm. Similarly, the height for growth parallel to gas flow is centered 1.9mm from the center, towards the exhaust, with a one σ width of 24.4mm. While both growth directions are not centered and have similar spread ($\sim$20mm), the direction parallel to gas flow is clearly influenced by the cool gas entering the chamber, reducing the growth height in this region to nanometer lengths. The additional 80% variation on the other three extremes of the measurement are believed to be due to substrate temperature uniformity, as determined by the thermal edge loss.

Clearly there is a $\sim$20mm sweet spot in the center of the hot-plate, where the growth is fairly uniform before the CNT hight starts drastically dropping. In terms of area, it suggests that only 1/10th of the hot-plate produces uniform growth. This is fine for a small scale experimental setup but needed to be addressed for a larger system. To address these temperature uniformity issues, careful attention was placed on the-hot-plate and shower-head design. An overview of the system level design is presented followed by detail surrounding each subsystem.

2.4.2.1 System-level

The overall system is designed largely around commercially available components. There are however, a few custom designed and fabricated parts – in particular the hot-plate and shower-head that will be discussed in more detail in the following sections. Figure 2.6 diagrams the system level design. The chamber is composed of a four port, 10 inch flange vacuum chamber. As can be seen in Figure 2.6, the gas flow is controlled by mass flow controllers. It mixes in the lines and enters the chamber through the inlet at the top. It then flows through the heated shower-head impinging on the substrate and reacting with the catalyst. The substrate is heated through the dual zone hot-plate. The residual gas flows out the exhaust. The entire operation of the chamber is controlled via computer automation. The discussion of the design and progress has been broken up into five subsystems, following the flow of gas through the system.

2.4.2.2 Gas/feedstock injection

There are three primary gases used for the CNT growth. Argon (Ar) is used as an inert gas for purging the system and maintaining a chemically inactive environment during heating and cooling of the chamber. Hydrogen (H_2) is used both before growing to reduce the catalyst and during growth as a carrier gas. Ethylene (C_2H_4) is the precursor, providing the carbon for the CNTs. It is only used once the desired temperature has been reached and the duration of its use largely controls the height of the CNT forest. All three gases are connected to Mass Flow Controllers (MFC) to precisely
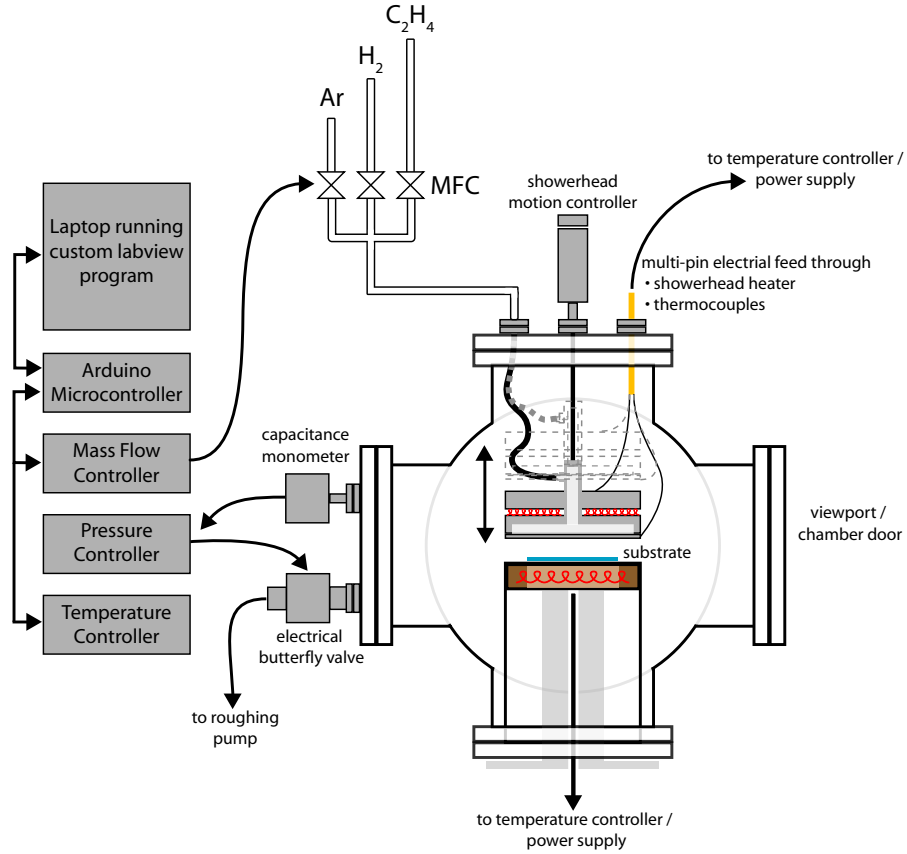
Figure 2.6: System level design of large scale CVD chamber.

control the amount of each gas. The MFCs are connected to a controller box where the flow for each gas can be set and monitored. This controller box is also connected to a PC, which is able to turn the gasses on and off and set and read the flow for each gas. After the gas passes the MFCs, all three gas lines are combined into a single line which enters the CVD chamber.
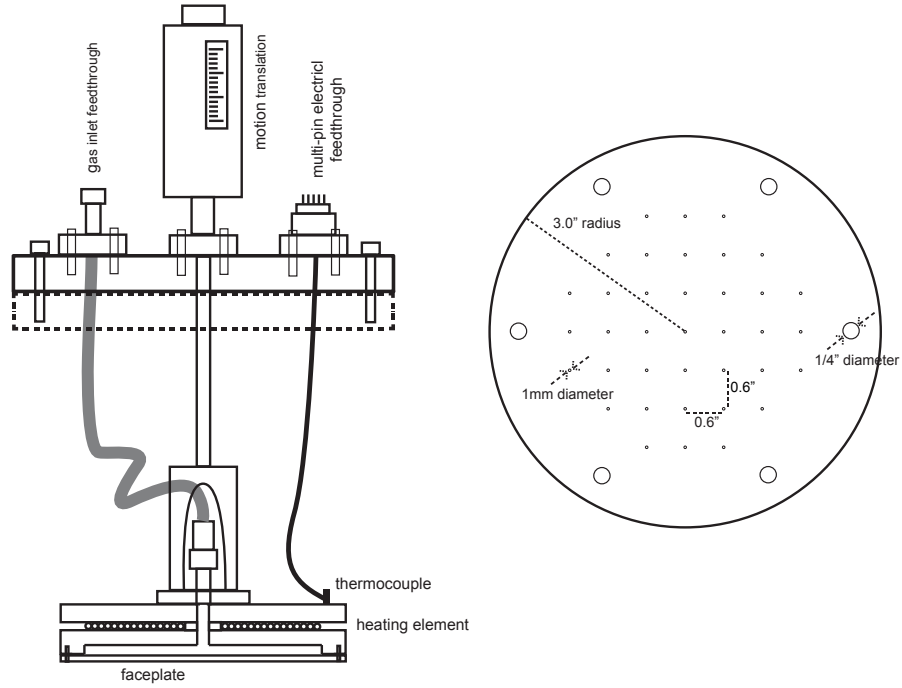
Figure 2.7: Diagram of top flange assembly on left and faceplate design on right.

2.4.2.3 Shower-head (gas distribution, gas preheating, and heat reflector)

Once the gas enters the chamber, it is fed to the custom made shower-head. Figure 2.7 illustrates the top flange assembly including the shower-head and faceplate design. Following this illustration, the gas is fed to the center of the shower-head via a flexible stainless steel tube, which allows the shower-head to move up and down via the linear translator connected between the shower-head and the top flange. Controlling the distance between the shower-head and the substrate is suspected to alter the growth performance.

The shower-head is heated via Joule heating of a NiCr wire insulated using

ceramic beads. The wire is wound between the two main disks that makeup the shower-head. The maximum target temperature of the shower-head is 500°C. The heater is controlled by an Omega CN616 temperature controller, the output of which is fed through a variable transformer to control the peak voltage on the heating coil. The temperature on the shower-head is sensed through a thermocouple attached to the surface of the top disk. Both the thermocouple leads and power leads are connected through the top flange to a multi-pin electrical feedthrough.

The gas flows down the center shaft of the shower-head and into a cavity between the bottom stainless steel disk and the faceplate. The faceplate has a rectangular grid of 37, 1mm diameter, holes drilled with a 15mm pitch. Once the gas exits the shower-head it is free to impinge upon the sample and hot-plate.

2.4.2.4   Hot-plate

Due to the suspected strong temperature profile of the 60mm, single element hot-plate design, the new design was chosen to have two heating elements and a surface that extends beyond the desired growth area. Due to the size constraints of commercial vacuum chambers, a 10" flange chamber was chosen to house the equipment. This further constrained the hot-plate area to a 6 inch diameter, leaving a little over an inch on either side of the hot-plate.

The hot-plate consists of a cylindrical enclosure made from 316 stainless steel connected to the bottom flange, see Figure 2.8. The heating element is not within the chamber itself but is placed at the top of the cylinder on the side exposed to air. The

heating element is made from a ceramic alumina bisque, which prevents the coiled heater from short circuiting, the schematic of which is also in Figure 2.8. An attempt was made to keep the power per unit area emitted from the heater constant. This calculation along with the calculation for power required to reach the desired temperature is presented in the appendix A.1.

The ceramic heater holds two heating elements, one which encapsulates the center area of the 10cm diameter wafer and the other which extends the remaining area from a radius of 5cm to 12.5cm. These two heating elements are controlled by the same Omega CN616 temperature controller and also have two variable transformers in series with the controller to control the maximum voltage that the coils will receive. There are holes drilled through the alumina bisque to allow thermocouples through to the underside of the SS hot-plate. The temperature controller is also controlled via the PC so that the entire process can be automated. Initial tests lead to short circuiting from the heating element popping out of the ceramic and making contact to the metal container. This problem was solved by adding a thin electrically insulating alumina mesh between the heating elements and the top metal plate.

After reacting with the catalyst on the substrate, the gas flows down around the edge of the hot-plate supporting cylinder and out through three ports on the bottom flange towards the exhaust.
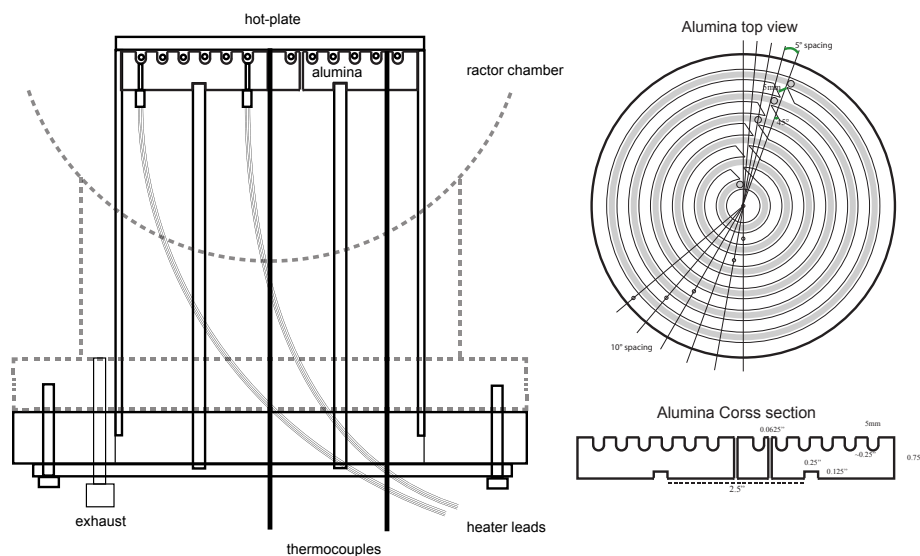
Figure 2.8: Diagram of bottom flange assembly and alumina ceramic heater.

2.4.2.5   Exhaust

The exhaust removes any used or unused gas and particulates out of the chamber. It was originally designed to use a passive exhaust system, relying on the injection of new gas to push out the exhausted gas, though after some consideration it seemed as though a roughing vacuum pump was necessary. While this chamber is designed to operate near atmospheric pressures, a roughing pump may greatly reduce the purging time and reduce the risk of H_2 combusting with any residual oxygen due to poor purging. The evacuation of residual oxygen is of serious concern because the lower and upper flammability limits are 4% and 75% respectively and the autoignition temperature is 500°C, which matches the regime in which the chamber will be operating. Between the chamber exhaust and the roughing pump is an electronic butterfly valve. This valve is

controlled by an MKS 651C which monitors the pressure from a capacitive monometer and adjusts the valve accordingly.

2.4.2.6   Computer automation

Custom circuits and software were designed to automate the mass flow and temperature controllers on the chamber. This was expected to produce more uniform and consistent results, enabling users to hone in on the ideal growth conditions more quickly. A custom interface and control using LabVIEW was implemented and tested on the atmospheric pressure, thermal CVD system prior to use on this large system. This software allows the user to set up custom waveforms to control the flow rates of each of the process gasses and the temperature on each of the heaters with respect to time. The entire growth process is automated requiring little or no intervention from the user during growth. Once setup the user can hit go and the entire process will be carried out including cooling.

2.4.3   Construction and calibration

The hot-plate, alumina bisque, and shower-head were all machined by third party companies using the designs specified previously. The remaining equipment was purchased from MKS instruments, MDC vacuum, Omega Engineering, McMaster Carr, and Swagelok. These items were assembled and careful calibration of the chamber ensued. An image of the entire system near completion is shown in Figure 2.9.

Before any growth was attempted, a broad calibration of the gas flow and

heating elements was performed. The goal of the temperature calibration was to verify the ability to achieve the desired set-points. Initial tests revealed that the heaters were all designed to output less power then they needed to quickly ascend to their set-points. The resistance of both hot-plate heaters were nearly halved to 20 ohms, allowing us to reach the limit of their current consumption given our voltage supply limit. The shower-head heater resistance had initially been miss-calculated and was also rectified to 26.4 ohms. Additional calibration of the PID system was performed to minimize the rise time and overshoot of the heaters during ramping.

The gas flow was controlled through the mass flow controllers (MFCs) that are connected to the MKS 247 readout, which is then connected to the computer via a microcontroller. Calibration needed to be performed at both the MKS readout and at the microcontroller/computer. The MKS readout required calibration due to the difference in gas between that used and the original calibration gas used for the MFCs. This calibration was performed by sealing the chamber, and measuring the change in pressure vs time for a given flow rate. Using the ideal gas law ($PV = NRT$), the actual flow was determined. This was first performed using a previously calibrated instrument, verifying future measurements. In addition to this calibration, the digitization of the flow rate was non-linear and needed to be corrected for in software.

2.4.4 Modifications and repair

Following preliminary tests, a number of issues presented themselves, requiring several modifications and repairs. Broadly speaking these issues can be lumped into two
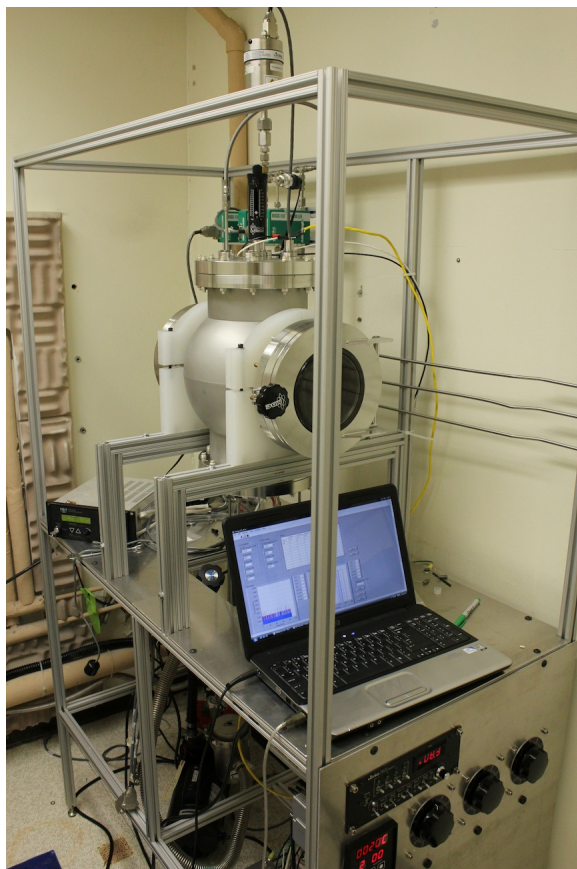
Figure 2.9: Image of large CVD chamber near completion.

categories; heating issues and problems with carbonaceous buildup.

2.4.4.1   Carbonaceous buildup - passivation of stainless steel

A great deal of the components used in the chamber were constructed from stainless steel (SS). Prior to fabricating these parts it was known that the SS would present some problem due to its Iron content. This iron would no doubt act as catalyst for the decomposition of ethylene, producing soot or other carbonaceous materials.

58

However, the small chamber studied earlier also contained many SS parts, which didn't appear to present a major problem. Other materials were considered but rejected due to the temperature with which they needed to withstand. As such, the design continued with predominately SS parts for the hot-plate and shower-head. This however, quickly presented a major problem. Within a few growths large amounts of amorphous carbon or other carbonaceous materials began building up on the shower-head, faceplate nozzles (to the extent of clogging them) , and hot-plate. This presented a major problem in the reproducibility of results in the system. The shower-head faceplate, which appears most susceptible to this buildup, was removed and a thin (40nm) Chromium layer was applied to mask out the Iron in the stainless steel, making the surface less catalytic. When the faceplate was removed for the Cr deposition it was revealed that the same, if not more, carbonaceous material had built up on the top-side of the faceplate, inside of the shower-head. This was concerning because it wasnt clear whether the application of Cr would remove the problem. The carbon could have been decomposing within the shower-head or could have been decomposing near the hotplate then diffusing back through the nozzles into the shower-head. To determine which case was more likely, some simple diffusion calculations were performed. A mass balance between the diffusing species and the flow of input gas through the nozzles was calculated. It was found that for the given configuration, a minuscule fraction would work its way back through the nozzles. It was also found that the flow could be significantly decreased (by a factor of 10) without much effect on the backwards diffusion of these species.

While the application of Cr did appear to reduce the amount of carbonaceous

59
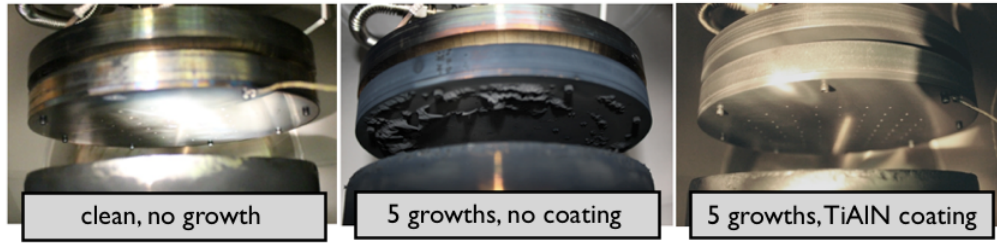
Figure 2.10: Carbonaceous buildup before and after TiAlN passivation layer.

buildup, it appeared as though further steps needed to be taken. Attempts were made to operate the shower-head at a reduced temperature or completely unheated but this resulted in very poor CNT growth. This is most likely due to the decreased temperature at the hot-plate. Further efforts to passivate the iron in the stainless steel were needed. Physical vapor deposition of Titanium Aluminum Nitride presented the most promising method for masking out the iron while able to withstand such high operating temperatures. The shower-head and hot-plate were coated. The coating almost completely removed the problem. The left most image in Figure 2.10 shows the shower-head and hot-plate before growth, the middle image shows the carbonaceous buildup on the uncoated stainless steel after 5 growths, and the right most image shows the TiAlN coated stainless steel after 5 growths with nearly no signs of carbon deposits.

2.4.4.2 Heating

Heating of the system was by far the largest problem encountered. The problems mostly centered around not having enough power and not being able to accurately determine the substrate temperature. Despite initial miscalculations regarding

the heater power, the heaters were not powerful enough to reach the desired set-point temperature of 750°C. FIgure 2.11 illustrates the problem by plotting the temperatures at various points around the chamber, as illustrated in the diagram on the left side of the figure, during a ramping cycle. While the back side of the hot-plate would reach temperatures approaching the set-point, the top of the hot-plate is likely a couple of hundred degrees less. This top temperature measurement, 'TC3' on the figure, was measured by a point contact thermocouple resting on the top surface. Due to the loose contact this measurement may be less than what the sample is really experiencing, but gives a rough idea of the conditions. The two plots on the right of Figure 2.11 show different chamber conditions, the middle plot shows two different flow rates of Ar during ramping, 200 and 400 sccm, while the far right plot shows the effect of the shower-head to hot-plate spacing on the temperature profiles. To help with this problem of insufficient heat, several approaches were tested.

To help relieve the power draw on the second zone, an additional guard heater was added to the sidewall of the heater plate column. It was assumed that much of the heat from the hot-plate guard heater was being lost to conduction down the side walls of the hot-plate column. The second guard heater consisted of a high temperature heater tape, wrapped around a stainless steel cylinder with a slit cut in one side. The slit allowed adjustment of the diameter of this cylinder to fit snuggly inside the hot-plate heater column, offering good thermal coupling. This heater was integrated into the computer controlled software and was able to reach a temperature of 400°C. However it quickly became apparent that this added guard heater was not solving the problem.
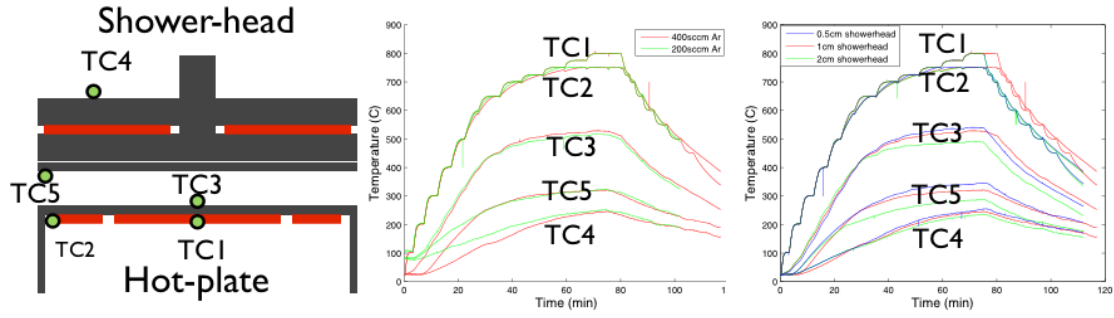
Figure 2.11: In-situ temperature measurements of shower-head and hot-plate at multiple locations as depicted in the diagram on the left. The two plots on the right show the five temperature measurements during ramping of the chamber under different operating conditions, highlighting the influence of the shower-head/hot-plate spacing and gas flow rates on heat loss.

The primary guard heater was not able to reach a higher temperature with the second guard heater at 400C. This caused the entire chamber to heat up with little or no effect on the hot-plate. This suggests that the initial assumption, that the heat loss was primarily due to conduction, was incorrect. Upon reconsideration it seems much more likely that, given the high temperatures, the main source of heat loss is due to radiation. This heater was subsequently removed.

The second approach to solving the guard heater temperature problem was to decrease the radiative heat loss. Given that the thermal radiative power is $P = \epsilon \sigma A T^4$, where ϵ is the emissivity, σ is the Stefan-Boltzmann constant, A is the area, and T is the temperature difference between objects, it is clear that there is at least a couple of ways to modify the heat loss. The emissivity of the hot elements and the surrounding cold

elements can be changed to some degree. Lower emissivity surfaces will make the hot elements radiate less and will make the cold surfaces absorb less. This became tangibly evident after coating the hot-plate and shower-head materials with TiAlN as discussed above, increasing their emissivity, which lowered the max temperature on the guard heater from 740C to 710C. Future efforts may involve applying an additional thin layer of highly reflective material to these surfaces to reduce the emissivity. The next obvious variable to play with is the difference in temperature between emitting and absorbing surfaces. The shower-head offers a great radiation shield to the hot-plate. Increasing the temperature of this element should reduce the power loss from the hot-plate. The addition of highly reflective shielding material in areas that are not already shielded is another valuable approach. Because we are limited with the materials that can be put into the chamber due to purity, cleanliness, heat tolerance, vacuum tolerance, and chemical reactivity (see Section 2.4.4.1 Carbonaceous Buildup, passivation of stainless steel), its much easier to address the issue from outside the chamber first.

It was observed that much of the radiation energy could be emitted from the back-side of the heating element, which is conveniently outside of the chamber. A multi-layer insulation (MLI) consisting of 8 alternating layers of 100mill Stainless Steel and fiberglass bound together by staples and NiCr wire was fabricated to slip inside of the heater column between the hot-plate cylinder and the heating element standoff. This effort had some improvement but wasn't as significant as expected.

Besides the radiation shielding mentioned above, the heating element was changed to increase its surface area, in turn, increasing its radiative power output.

Based off the technical data from Omega and the resistance of the previous heating element, it is calculated to have an area of $0.0118m^2$. New, higher gauge NiCr wire was purchased, which offers a smaller resistance per unit length. The change in the wire gauge and resistance per unit length lead to an increase in total surface area, at the cost of increasing electrical power to reach a desired temperature. The length of the coil was chosen to offer the maximum current deliverable to it, limited by the variac to 10A at 120VAC. This resulted in a total surface area of $0.0147m^2$ and, according to the datasheet, a maximum temperature between the range of 875C and 1100C. This element was installed and preliminary results show that it is able to reach the desired set-point at 75% of its maximum voltage (56% of its maximum power).

The shower-head contributes a great deal to the maximum achievable temperature of the hot-plate. This is most likely due to its radiative shielding attribute. Some preliminary tests show that not heating the shower-head results in terrible, short and discontinuous growth, despite the hot-plate reaching its 750C set-point. This heater was similarly underpowered much like the guard heater. As such it too was operating too close to its maximum tolerance. The maximum achievable temperature on the back side, away from the hot-plate was 280C while the front faceplate facing the hot-plate could reach nearly 350C. This lower power and large heat capacity of the shower-head lead to very long ramping periods. In an attempt to decrease this heating time, the shower-head was ramped at low pressure, which ultimately lead to the NiCr wire blowing out. It's believed that a localized plasma was created between the NiCr wire and the grounded shower-head body. This probably lead to local arcing resulting in superheat-
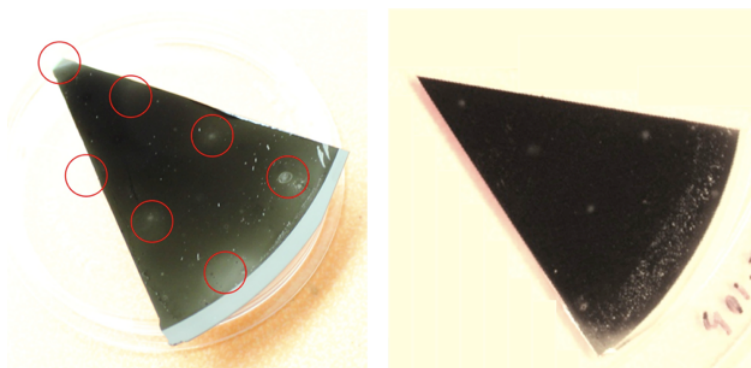
Figure 2.12: Wedge of 4 inch wafer with CNTs grown on it. The images are intentionally overexposed to highlight the spots of reduced growth. The left images shows the growth with a 1m/s flow through the shower-head, reducing the growth near the nozzles, while the right image shows the growth after the number of nozzles were doubled, decreasing the flow to 0.5m/s, resulting in better uniformity.

ing and melting of the NiCr wire. Operating this heater at low pressure was a mistake for two reasons, the heating element would reach a much higher temperature because of the reduced convective loss and the arc potential would reach nearly a minimum at such pressures. This heater presents a major challenge because of its exposure to the inside of the chamber, for example, carbon deposits are likely to cause it to eventually short circuit to the shower-head body. Additional engineering hurdles may present themselves for continuous sustained operation. However, within the timeframe of these experiments no further complications associated with this shower-head were observed. Future work may benefit from using a smaller, lower heat capacity shower-head with more powerful, fully encapsulated heaters.

Irregular heating has also been observed as a result of the shower-head flow. Initial tests show that the flow from the shower-head nozzles, particularly the center nozzle, which is directly in line with the gas inlet, causes a decrease in growth around these points, see Figure 2.12. This is likely due to increased cooling from the incoming gas. It was calculated that the flow of gas is 1m/s through these nozzles. Raising the shower-head is likely to reduce this localized cooling, although it has also been shown to reduce the overall temperature on the surface of the substrate (Fig. 2.11). Reducing the flow or changing the number of nozzles, their pitch or diameter may also be solutions to this problem. To mitigate this problem the number of nozzles was doubled, decreasing the flow rate by half and a molybdenum baffle was placed over the gas inlet to further disperse the gas within the shower-head. Subsequent growths show that these additions have solved much of these problems. Figure 2.12 shows the growth before and after nozzle modifications.

2.4.5 Testing and validation

Once the initial rounds of system debugging was performed and the system began functioning near the desired specifications, a more detailed study of the growth uniformity was performed. To evaluate the growth uniformity, a number of samples were prepared along the length of the hot-plate radius. These samples were grown using a varying ratio of ethylene to hydrogen during the growth step, while all other growth conditions were held constant. The resulting samples were analyzed along their length using both Raman spectroscopy to determine their disorder to graphitic band

66
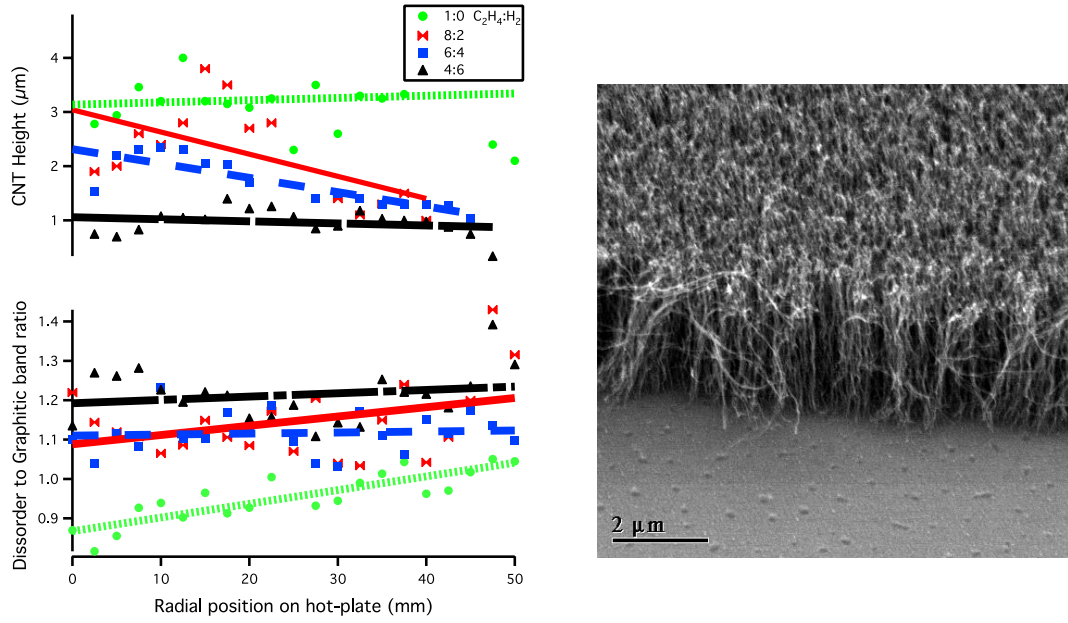
Figure 2.13: Evaluation of MWNT growth performance from large scale chamber. Left plots the array height and Raman D/G band ratio as a function of radial position along the hot-plate for a range of ethylene to hydrogen flow ratios. Right image shows a typical side view of the forest, imaged using the SEM.

ratio (D/G ratio, a metric for the CNTs quality or crystallinity) and using a Scanning Electron Microscope (SEM) to determine their height. These results are plotted in Figure 2.13.

From the plot in Figure 2.13 it's clear the the growth is fairly uniform both in terms of array height and crystallinity. There is some scatter in the data but general trend shows a constant or linear dependence on radial position. Furthermore the CNT height matches that of the Raman, samples with less height have more disorder. Ad-
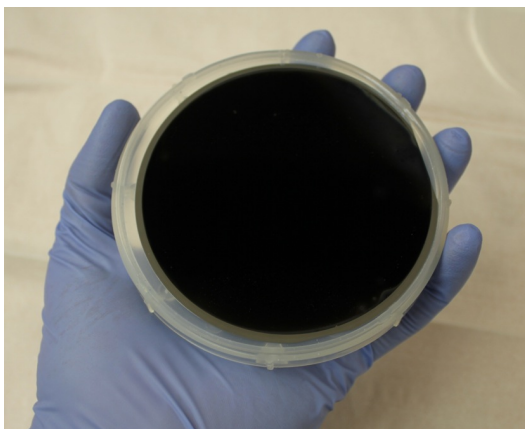
Figure 2.14: Picture of 4 inch wafer fully covered with CNTs grown using the chamber described in this work.

ditionally samples grown with less ethylene are shorter and more disordered, indicating that the amount of precursor may be the limiting factor in array height. Increasing the chamber pressure and the flow rate may increase the growth rate. However, these experiments only scratch the surface of the growth dynamics in such a system. Further experiments must be performed to fully understand the influence of precursor to carrier gas ratio and

2.4.6 Conclusions

A four inch diameter, pilot production scale CVD chamber for CNT growth was designed and built from the ground up. The main design optimization was placed on highly uniform height and quality across the growth area. Initial tests were performed on an experimental scale hot-plate CVD chamber to identify potential design flaws. A

custom design was implemented based on a dual zone hot-plate and heated shower-head. A number of implementation obstacles were mitigated, resulting in a well functioning system capable of producing highly uniform CNT growth across a four inch wafer. However, the growth rate is very low but has been identified to be a combination of the limited precursor gas used in the experiments and a lower than expected hot-plate surface temperature.

Such a growth chamber is ideally suited for growing single-sided MWNT thermal interface materials. CNT TIMs were the target application for the products of this chamber and are discussed in more detail in chapters 4 - 8. However, its output can also be used for a number of other purposes. While not relying on the intrinsic alignment of the CVD process, growth from such a chamber can be used for fiber making. The challenge of fiber making, specifically for its electrical conduction is addressed in the following chapter, chapter 3.

Chapter 3

Micron sized CNT wires via a coaxial electrospinning technique

CNT based wires hold promise to offer unparalleled electrical and mechanical properties over traditional bulk materials. These exceptional electrical properties may be necessary in the near future given the energy issues confronting the growing demands of the Earth. While individual CNTs posses such remarkable properties, fabricating a continuous, macroscopic wire remains elusive. Both the scale up of CNT production (as discussed in chapter 2) and the development of better fiber making techniques is required. The following chapter addresses a new approach to CNT wire making using a coaxial electrospinning technique.

3.1 Introduction

The research presented here aims to tackle the CNT wiring problem using a coaxial electrospinning technique. Due to its small diameter, constricting nature and electric/flow-filed orientation, coaxial electrospinning may produce tightly packed, well aligned CNT bundles. These bundles may then be woven into larger macroscopic twines and ropes. While other groups have made progress with electrospinning homogeneous polymer-CNT composites, the electrical [43], [44] and mechanical [45], [46] properties of these fibers are still many orders of magnitude lower than that of individual CNTs. Liu et. al. serendipitously made SWNT core-polymer shell nanofibers using a homogenous electrospinning technique [47]. While it is not clear whether their results produce continuous and repeatable coaxial structures, their Raman results show an increase in the 236 cm^{-1} RBM peak which eludes to a compressive stress induced by the constricting shell. This, along with the generally superb alignment of CNTs within electrospun fibers [46], [48] motivated the investigation of the coaxial electrospinning technique.

This work investigates the feasibility of creating continuous CNT core-polymer shell fibers using a coaxial electrospinning approach. In order to better understand and design this system, a detailed study of the polymer-free core solution interaction with the shell solution is presented by way of the Hansen solubility parameters. This interaction is a critical variable in coaxial electrospinning that had not previously been explored. A variety of morphologies were observed for the different core-shell solubility regimes and the challenges in their accurate characterization are addressed. Finally, electrical

characterization of individual MWNT cores were performed and their conductivities are compared to those of existing MWNT fibers.

3.2 Experiment setup

3.2.1 Materials

Multiwalled carbon nanotubes (MWNT) were purchased from Cheap Tubes Inc. with an inner diameter of 5-10nm, an outer diameter of 20-40nm and a length of 0.5-2μm. Poly(methyl methacrylate) (MW $\sim$ 996,000), sodium dodecyl sulfate (SDS), along with all of the organic solvents used in this research were purchased from Sigma-Aldrich. None of the materials underwent further purification. The MWNT solutions were initially sonicated in a Cole-palmer 8893 for one hour. Before spinning, 15 minutes of additional sonication were performed to re-disperse agglomerated MWNTs. The polymer solutions were prepared and sonicated for one hour then left at room temperature for three days to fully dissolve. For imaging and Raman spectroscopy, the samples were spun onto n-type Silicon, while for electrical characterization the samples were spun onto glass slides with thermally evaporated aluminum contact pads.

3.2.2 Electrospinning equipment

Electrospinning was performed in ambient room conditions using a home made dual syringe pump based on the deposition tool from the Cornell university *fab@home* project [49]. A custom coaxial needle was made for each experiment that consisted of

a shell capillary with OD=2.4mm, ID=1.6mm and a core capillary with OD=0.84mm, ID~0.66mm. The core capillary protruded from the shell by 0.2 - 0.6mm to facilitate entrainment of the core as demonstrated by Reznik et. al. [50], as seen in Figure 3.1. All fibers were spun with a spinneret to collector distance of 20cm using a variable, high voltage DC source, Spellman EPM15P30. The voltage source was limited to 15KVDC, though the voltage was finely tuned, between 5-8KVDC, during spinning to match the extrusion rate from the syringe pump. The ratio of flow rates between the core and shell was maintained throughout the experiments with the shell flowing five times that of the core, though the absolute value of these flows could not be maintained due to variations in solution parameters. In particular, more volatile solutions had to be spun at higher flow rates to maintain a stable Taylor cone. The shell flow varied between 1-3ml/h.

3.2.3 Characterization equipment

Raman spectroscopy was performed on a Renishaw spectrometer with a HeNe 632.8 nm laser. Optical imaging was performed using a Leica DMLM microscope. Scanning electron micrographs were taken at Stanford nanocharacterization lab using an FEI SL30 Sirion SEM with an FEG source. Electrical measurements were performed on a Desert Cryogenics TTP4 probe station using custom made electrochemically etched Tungsten probe tips, as described elsewhere [51], and an HP semiconductor parameter analyzer, 4156B. Aluminum contact pads were thermally evaporated using a BOC Edwards Auto 306 thermal evaporator through various sized TEM grids as hard masks.
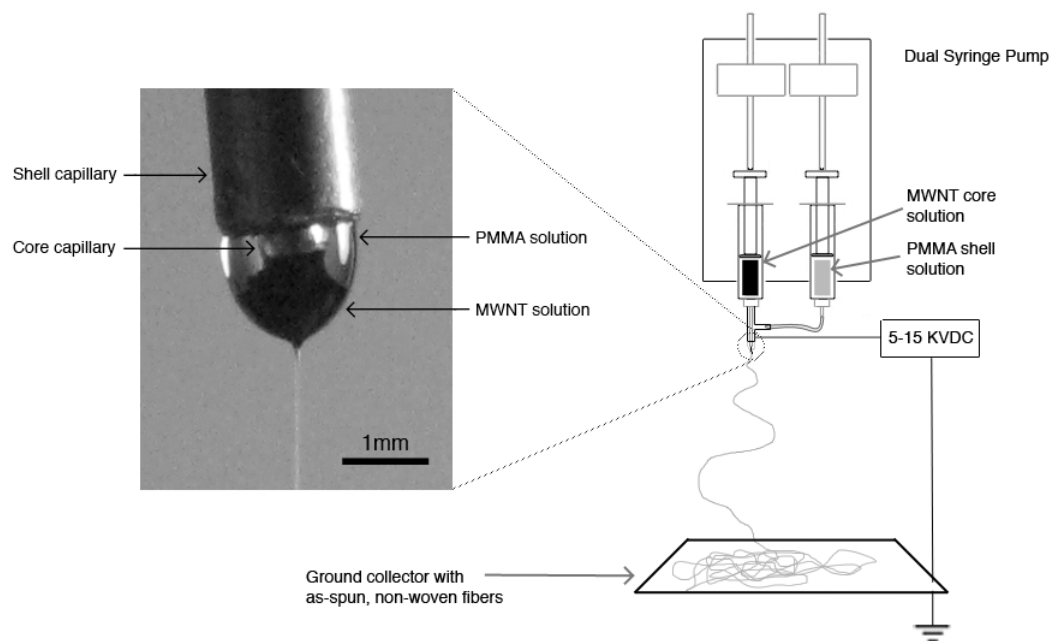
Figure 3.1: Coaxial needle with Taylor cone composed of PMMA shell and MWNT core solutions

3.3 Results and discussion

3.3.1 Experiment space / solution properties / morphology

The field of coaxial electrospinning is still fairly new and due to the large number of variables involved, is still poorly understood. Despite the proposed advantages of coaxially electrospinning a CNT core-polymer shell fiber, there are many obstacles in achieving such a morphology. There are two critical challenges in this endeavor. The first is the lack of viscoelasticity of the CNT core. Much of the past work with coaxial electrospinning has been done with pairs of solutions which are both independently

electrospinnable, facilitating the production of a clean core-shell morphology. Here the shell is being relied upon to act as a guide for the non-electrospinnable core. Many other research groups have used this technique to electrospin other non-electrospinnable polymers, though few have used completely polymer free core solutions. Song et. al. were successful in coaxially electrospinning a core composed of FePt nanoparticles dispersed in hexane with a PCL/2,2,2-triuoroethanol shell [52]. While fairly well defined core-shell structures were presented in this work, the longest continuous core length was reported to be 3μm, suggesting aspect ratios on the order of 100:1 for their 20 - 50nm core diameters. A more detailed study of the core-shell interaction needs to be investigated to produce truly continuous non-viscoeleastic cores. The second difficulty with the CNT core is the problem of effectively dispersing the CNTs. Even in an ideal solvent, only a fraction of a weight percent of CNTs can be effectively dispersed. This poor dispersibility presents three problems. The first being the total mass of the solvent relative to the CNT. With such a small CNT fraction, it is difficult to produce a tightly bundled CNT core without voids left behind by the evaporating core solvent. The second problem is that CNTs may agglomerate on length scales comparable to core diameter during the course of electrospinning, disrupting the continuity of the fiber structure. The third problem with the dispersibility is the restrictions it imposes upon the choice of core solvent. The interaction between the core and shell solvent plays a very important role in the final fiber morphology and ultimately governs whether or not the solutions can even be electrospun.

Out of all the variables involved in coaxial electrospinning, the most critical
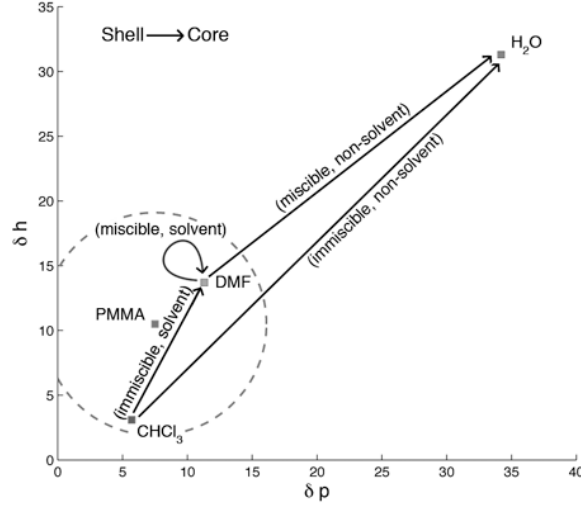
Figure 3.2: Hansen solubility parameters of core-shell solvent pairs in four miscibility-solvency regimes, data from [53]

appear to be the mixing interactions of the two (core, shell) solutions. The core solution interaction with the shell's polymer and solvent can be described by four fundamental solution combinations. These combinations are characterized by the interaction between the core's solvent with the shell's solvent and polymer. The two solvents may be miscible or immiscible, while the shell polymer may or may not be soluble in the core solvent. In this work, we refer to these four possibilities as miscible-nonsolvent, immiscible-nonsolvent, miscible-solvent, or immiscible-solvent. These terms are applied qualitatively, considering that miscibility and solubility may be considered to occur to varying degrees depending on relative concentrations. These relationships are well described by the general Hildebrand solubility parameter and the more specific Hansen solubility parameters.

Hildebrand is noted for much of the pioneering work in the study of quantifying solubility [54]. This was done by using the square root of the cohesive energy, the amount of energy required to vaporize a quantity of solvent after the onset of boiling (eqn. 3.1).

$$\delta = \sqrt{\frac{\Delta H - RT}{V}} \tag{3.1}$$

While Hildebrand was able to fairly accurately predict solubility between solvents by their proximity in δ, this method fell short with particular pairs of solvents such as nitromethane and ethanol. Hansen and others aimed to solve this problem by breaking Hildebrand's solubility parameter up into more representative components [54]. Hansen did this by dividing it up into δ_d, the (atomic) London dispersion force, δ_p, the (molecular) permanent dipole forces, and δ_h, the (molecular) hydrogen bonding component. These components are additive in energy, making the Hilebrand parameter equal to the square root of the sum of the squares of the Hansen components (eqn. 3.2).

$$\delta = \sqrt{\delta_d^2 + \delta_p^2 + \delta_h^2} \tag{3.2}$$

The method for determining the components of the Hansen solubility parameter is out of the scope of this paper, more information can be found in Hansen's book [54]. Their use is straightforward, based on solubility proximity, as with Hildebrand's solubility parameter. Similarly to the solvency between two solvents, the solvency between a solvent and a polymer can also be assessed using these parameters. The solubility parameters of polymers cannot be measured directly as in the case of volatile solvents but must be

dissolved in a variety of solvents to determine these values. After dissolving the polymer in a range of solvents and doubling the dispersion parameter scale, a "solubility sphere" can be roughly assigned to the volume encompassing the three solubility components, with an "interaction radius", R. If the Hansen parameters of a solvent or solvent mix lie within the solubility sphere, it is likely that they will dissolve the polymer. This can be graphically assessed or calculated via equation 3.3, where R is the interaction radius and subscripts 1 and 2 represent the solvent and polymer respectively.

$$R \geq \sqrt{4(\delta_{d1} + \delta_{d2})^2 + (\delta_{p1} + \delta_{p2})^2 + (\delta_{h1} + \delta_{h2})^2} \qquad (3.3)$$

The solubility parameters and interaction radii of many common solvents and polymers have already been determined and are readily available [53], [54]. All of the Hansen values used for this research were taken from the book *Properties of Polymers* [53].

Using the polar and hydrogen components of the Hansen solubility parameter, neglecting the relatively weak London dispersion component, the four core-shell interaction regimes can be graphically represented as in figure 3.2. This graph diagrams the interaction of four specific pairs of solvents that were investigated. The lines connect the solvent pairs, while the arrow marks which is the core. The addition of MWNTs and the surfactant, SDS, presumably alters the exact hydrogen and polar component of the solubility parameter but this was neglected for simplicity. Table 3.1 presents a more exhaustive list of the solutions explored and their representative morphologies.

A surprisingly large number of morphologies were observed throughout the

78
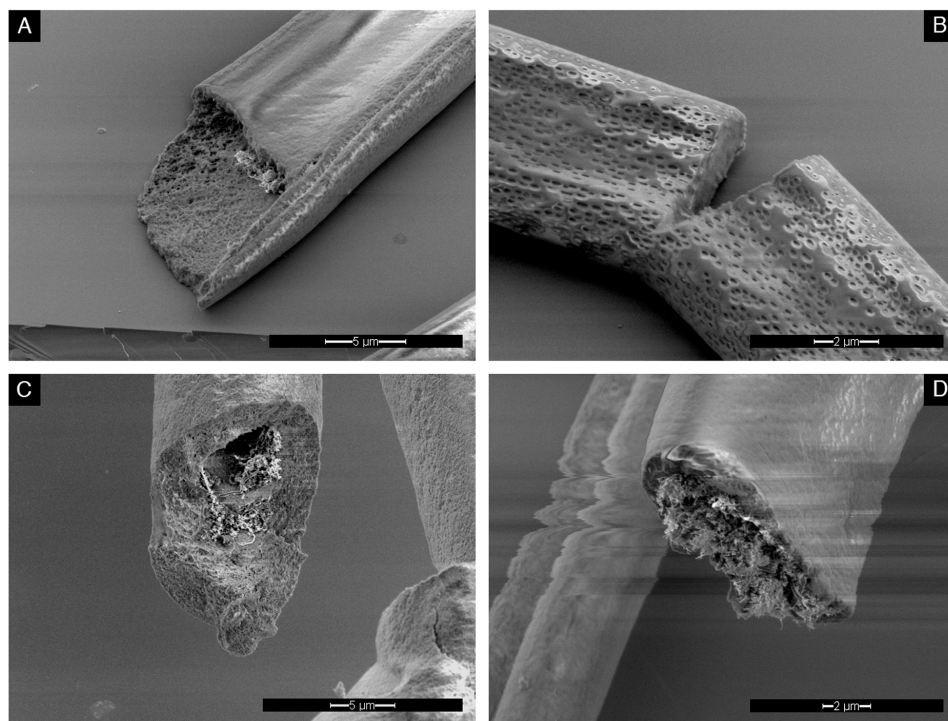
Figure 3.3: SEM Images of Various Fiber Morphologies, (A) Collapsed hollow core with a small MWNT bundle protruding, (B) Porous shell, (C) Hollow core with MWNTs decorating side wall , (D) Solid MWNT core in ribbon shaped fiber. Striations in image caused by charge accumulation induced by the electron beam.

course of this research. Figure 3.3 highlights a few of particular interest. Figure 3.3(a) shows how several samples exhibited a collapsed core or dumbbell cross-section. This is the result of a void forming from the evaporating core solvent which then collapses due to a differential in atmospheric pressure. The Young's modulus of such collapsed tube walls can be determined from their images, as demonstrated by Yarin et al. [55]. These morphologies, collapsed core and dumbbell, are generally described in table 3.1 as

79

fiber Artifacts. Figure 3.3(b) shows a porous shell fiber which is caused by evaporation of the highly volatile shell solvent, chloroform. Bognitzki et. al. saw similar behavior in PLLA/dichloromethane fibers, which they attributed to the rapid phase separation during electrospinning, creating solvent rich regions that transformed into pores [56]. Figure 3.3(c) shows a hollow core that has retained its cylindrical structure with a few scattered MWNT bundles decorating the inner side walls of the tube. Figure 3.3(d) has a fairly well defined MWNT core protruding from the PMMA shell, with an elliptical cross-section, in table 3.1 this is described as Bundled Core (BC). The striations in the image are a result local charging on the fiber deflecting the electron beam during imaging. These SEM images present the basic set of morphologies that were identified as in table 3.1. While many variations on these morphologies were observed, they can be generalized to these four basic groups, hollow core, bundled core, porous shell, and fiber artifacts. The wide variation in morphologies illustrates the great impact that the core-shell solution interactions have on the final fiber shape.

3.3.2 Miscible-nonsolvent

The miscible-nonsolvent pair of DMF/water was not able to be electrospun as the solvents mixed upon contact, causing the PMMA in the shell to precipitate out of the H_2O/DMF mixture. This resulted in a coagulated, non-spinnable solution at the needle tip. This result was not unexpected and similar effects are expected for other miscible-nonsolvent pairs so no other combinations were investigated.

Regime	Shell		Core		Morphology
	Conc.	Solvent	Conc.	Solvent	
miscible-nonsolvent	10%	DMF	0.5%	2%SDS/H_2O	Coagulated
immiscible-nonsolvent	14%	$CHCl_3$	0.5%	2%SDS/H_2O	HC, PS
	14%	DMF	0.5%	2%SDS/IPA	HC, BC
	14%	DMF	0.2%	(MeOH:DMF)	BC, few HC
miscible-solvent	6-16%	DMF	0.1-0.75%	DMF	HC, BC, A
immiscible-solvent	14%	($CHCl_3$/DMF)	0.5%	DMF	HC, BC, A
	14%	(Toul./DMF)	0.5%	DMF	sparse BC
	14%	(MIBK/DMF)	0.5%	DMF	HC, BC, PS, A

Table 3.1: Coaxial Solution Pairs; morphology abbreviations: HC-Hollow Core (Voids), BC-Bundled Core, PS-Porous Shell, A-Artifacts
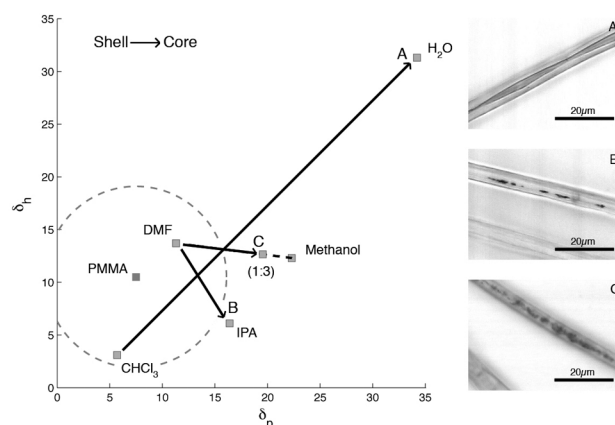
Figure 3.4: Hansen solubility graph of immiscible-nonsolvent core-shell solution pairs, insets: (A) shell 14% PMMA/CHCL$_3$ core 0.5% MWNT/2% SDS/H$_2$O, (B) shell 14% PMMA/DMF core 0.5% MWNT/2% SDS/IPA, (C) shell 14% PMMA/DMF core 0.2% /(Methanol:DMF)

3.3.3 Immiscible-nonsolvent

Figure 3.4 plots the three solution pairs tested in this regime using the hydrogen and polar components of the Hansen solubility parameter. The insets of this figure are optical micrographs showing the characteristic morphologies. The immiscible-nonsolvent combinations were expected to create the most well defined core-shell structures as others have argued that the nonsolvency of the core will create a solid interface between the core and shell due to local precipitation of the shell polymer [57]. For the most immiscible pair, water / chloroform, this was clearly evident as nearly all of the fibers had hollow cores, see Figure 3.4 inset A., though very few MWNT bundles were found within these hollow cores possibly due to a poor dispersion of MWNTs in the

core solution. The other two pairs of solutions in this regime, DMF / IPA and DMF / methanol, showed similar results but with fewer hollow cores and more apparent MWNT bundles, 3.4 insets B and C respectively, though none produced the ideal morphology.

3.3.4 Miscible-solvent

The simplest type of miscible-solvent pair is one where the shell and core share the same solvent. Given that DMF is the best solvent for dispersing CNTs [58] and it is also a good solvent for PMMA, it was used for the tests in this regime. This pair of solutions produced reasonably well defined coaxial structures with few voids (Fig. 3.5). The production of core-shell morphologies in this regime may be attributed to the lower mobility and or immiscibility of the PMMA and MWNTs rather than the solvents. MWNTs have similar aspect ratios to polymers, as such, they are not free, in the sense of a liquid solvent, and cannot mix freely to contribute to a larger entropy change. Due to the quality of these structures, they were used for the subsequent electrical measurements (Sect. 3.3.6.1). Although there were well defined sections of MWNT cores in these fibers, there were also scattered and mixed MWNTs in other sections and regions with fiber artifacts. The fiber artifact appear as a dark line under optical microscope and may be mistaken as MWNT cores without closer examination. Figure 3.5 clearly demonstrates the utility of Raman spectroscopy in identifying the presence of MWNTs within the core and discarding artifacts. The four Raman spectra in this plot correspond to those taken in the center of the four fibers imaged to the left of the spectra. The presence of MWNTs in the top two samples is characterized by the first-order

Raman graphitic, G, peak at $\sim 1582 \text{cm}^{-1}$, its disordered, D, peak at $\sim 1350 \text{cm}^{-1}$ caused by second-order single-phonon scattering, and its G' or 2D band at $\sim 2700 \text{cm}^{-1}$ caused by second-order double-phonon scattering [59]. The third sample confirms the presence of the core artifact by the absence of MWNTs in the Raman spectra. The artifacts observed in these fibers are attributed to the core collapse as in Figure 3.3.A. The fourth spectrum of a pure PMMA fiber formed by ordinary (non-coaxial) electrospinning serves as a reference for the other peaks. These are all attributed to the PMMA [60], except for that between 900 - 1000cm^{-1} caused by the silicon substrate [61].

In this regime, variables such as flow rate, spinneret to collector distance, and shell viscosity were investigated to determine their role in core entrainment. No conclusive results were obtained from the flow rate or the collector to spinneret distance tests. Varying the shell concentration and hence its viscosity did however show notable influence on the fiber morphology. As others have noted [62], [63], increasing the concentration of the polymer solution generally leads to increased fiber diameter, which in the case of the coaxially spun fibers also leads to an increase in voids and MWNT clumping with shell concentrations above 14% wt. Figure 3.3.C shows a fiber from the limit of this study, 16%PMMA/DMF shell, 0.5%MWNT/DMF core, that has a very large outer diameter and a well defined hollow core with some MWNTs lining the inner wall of the shell. Varying the core concentration also clearly has an effect the core morphology. Above 0.5% wt. MWNT/DMF the core became significantly more clumpy leading to shorter continuous sections of core and voids adjacent to the MWNT bundles. This is due to increased MWNT agglomeration rather than a change in solution viscosity.
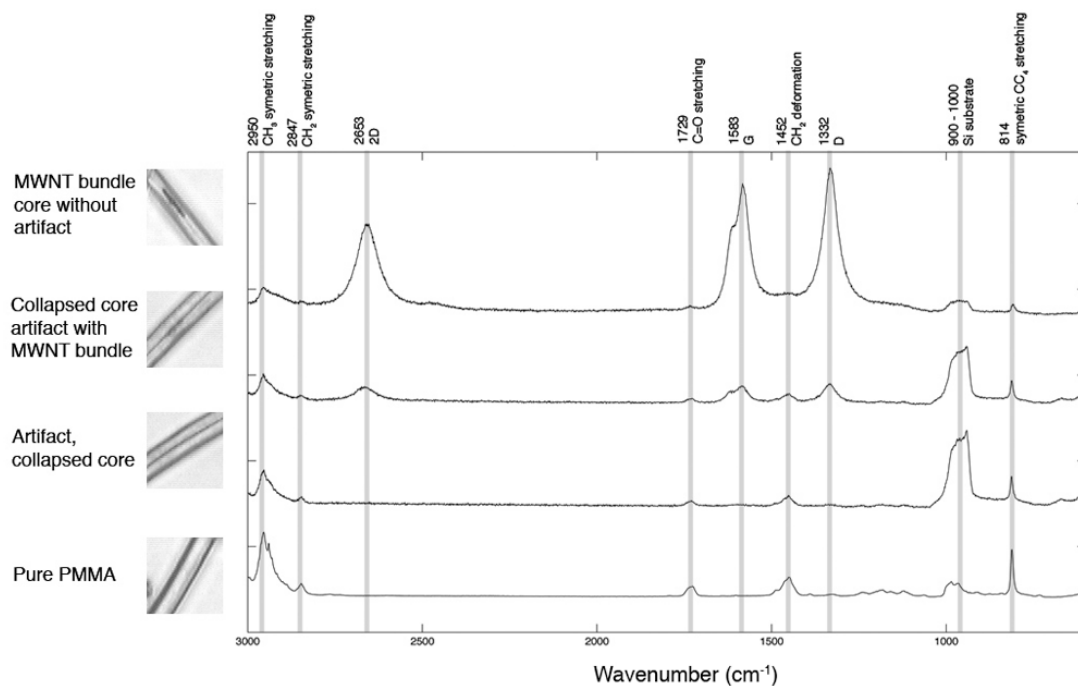
Figure 3.5: Raman spectra of MWNT core in PMMA fiber Vs. fiber artifact, 632nm excitation. PMMA peak assignment from [60]

3.3.5 Immiscible-solvent

The solvent-immiscible solution pair was speculated to be the optimal regime for producing densely packed MWNT cores. While the core and shell won't mix because of the immiscibility, a solid interface between the two shouldn't form because of the mutual solvency of the polymer, allowing the shell to continue to narrow, compressing the core as the core solvent evaporates. Though this approach seems promising, finding an immiscible pair that are also both reasonable solvents of PMMA and where the core solvent suitably disperses the MWNTs is a challenge. Because DMF was the

best candidate for the core solvent it was used throughout this set of experiments. A variety of shell solvents and solvent mixtures were explored as depicted in Figure 3.6. Though the miscibility of these solvent pairs was not known, the assumption that "like dissolves like" guided the choice of solvents to opposite extremes of the PMMA solubility sphere. Unfortunately, this study didn't show the trend that was postulated. Surprisingly, there was much variation within even a single solubility line such as that for the Chloroform:DMF shell solution mixtures. A slight trend observed in these samples was an increase in the quality of the core for shell solvent mixtures close to the center of the PMMA solubility sphere. Though there were many examples of hollow cores, the fraction of fibers with hollow cores was significantly less than in the immiscible-nonsolvent regime, which supports the theory that the formation of a solid interface facilitates the core-shell morphology. The insets on Figure 3.6 present a cross-section of the fiber morphologies observed, inset A shows well defined bundling, inset B shows hollow cores, and inset C presents a collapsed fiber with few MWNT bundles.

3.3.6   Shell removal

Selective shell removal is important both for electrical characterization and to estimate the MWNT alignment. The most obvious approach is to use traditional photolithography techniques, or in the case of PMMA, electron beam lithography. Preliminary tests were performed using an industrial electron beam source, though due to the short lengths of the MWNT cores and the turbulent development bath, no exposed MWNT bundles were observed. A more straightforward approach to remove the shell,
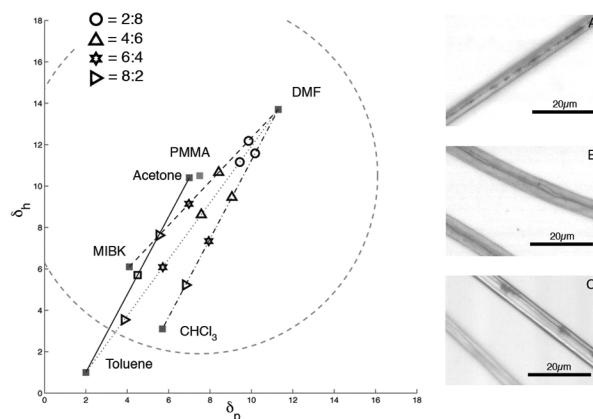
Figure 3.6: Hansen solubility graph of immiscible-solvent core-shell solution pairs, insets: (A) shell 14% PMMA/(CHCL$_3$:DMF) 6:4 core 0.5% MWNT/DMF, (B) shell 14% PMMA/ (CHCL$_3$:DMF) 4:6 core 0.5% MWNT/DMF, (C) shell 14% PMMA/ (MIBK:DMF) 6:4 core 0.5% MWNT/DMF

although not selectively, is to simply burn it off. Figure 3.7.A shows a fiber in the middle of thermal decomposition where the shell has begun melting while the MWNT bundle remains intact. Another method for selectively removing the shell was found by illuminating the fiber with the Raman laser at high power ($\sim$1 mW/μm^2). Absorption of the Raman laser by the MWNTs and subsequent conversion to thermal energy melts the surrounding PMMA. This only worked in regions that contained well defined MWNT bundled cores. Figure 3.7.B shows a point in the fiber where the PMMA has been melted around a well defined MWNT bundle. Similar optothermal transduction in SWNTs is well known [64], [65]. While this technique for selectively exposing the core for electrical characterization was promising, it often resulted in complete breaking of
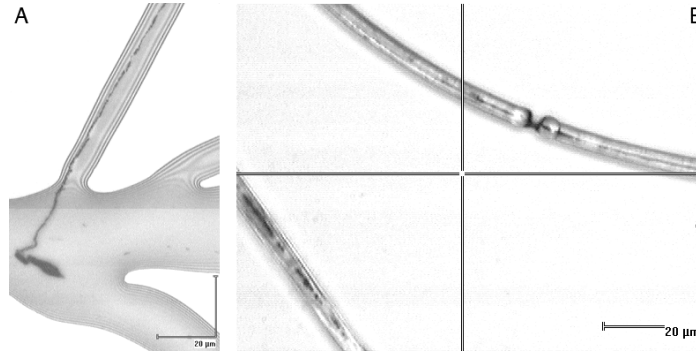
Figure 3.7: Optical micrographs of shell removal, (A) partial reflow of shell around MWNT bundle, (B) Selective melting of shell around MWNT bundle via 632nm HeNe laser

the fiber which prohibited direct probing.

3.3.6.1 Electrical Characterization

Two point electrical measurements were performed on thermally decomposed 10% PMMA/DMF shell, 0.5% MWNT/DMF core fibers. The fibers were spun onto a glass slide substrate. The shell was removed by heating in air to $450°$ for one hour. 400nm thick Aluminum contact pads were then thermally evaporated over the MWNT bundles using a TEM grid as a shadow mask. By chance, many of the MWNT bundles bridged adjacent contact pads allowing electrical measurements to be made. Because of the short length of the MWNT bundles only two probe measurements were performed, neglecting contributions to contact resistance. Figure 3.8 shows the linear behavior of a typical IV curve produced though one of the bundles, the inset shows a bundle bridging two Al contact pads. Figure 3.9 plots the calculated conductivities for a few
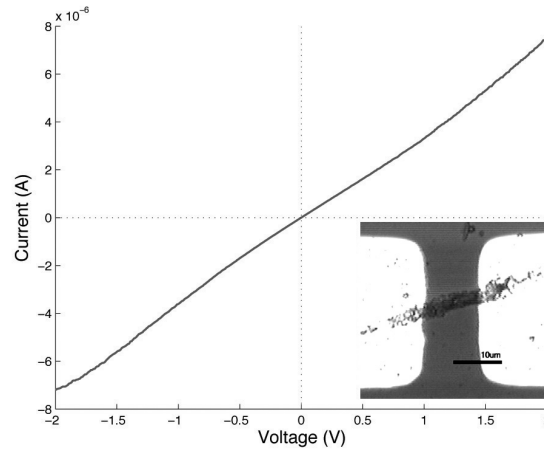
Figure 3.8: I-V curve of MWNT bundle, inset optical image of MWNT bundle bridging two Al contact pads

bundles versus their diameter. The variation in conductivity is within the confidence of the measurement rather than indicating dependence on diameter. For the conductivity calculations the bundles were assumed to have semicircular cross-sections and uniform edges, the radius of which was estimated via optical microscopy. Subsequent SEM images (e.g. Fig. 3.3.D) suggest that the assumption of a semicircular wire morphology may have been an overestimate of the actual mass of the bundles, resulting in very conservative estimates of the bundle conductivities. This, along with the undetermined contact resistance suggest much higher conductivities than reported. Even though these numbers represent an underestimate of the actual fiber conductivity, the conductivities of these short segments are on average two orders of magnitude greater than those reported for MWNT/polymer electrospun composite fibers [43]. However, these conductivities are still many orders of magnitude lower than the theoretical values and

even several orders below what other groups have achieved using alternate fiber making approaches [19], [16]. The obvious explanations for these lower conductivities are poor continuity, low density, and poor alignment. To gain a quantitative understanding of one of these factors, the MWNT alignment within the bundle was measured using image analysis of a high resolution SEM image of one of the thermally decomposed fibers. The full width half maximum of the Gaussian fit was quite large at $92.3°$. This poor alignment could be a result of the polymer removal step, where polymer reflows before burning, which may reshape the MWNT bundle. Whether or not this occurs would require assessment of the alignment of the bundle while it's still encased in the polymer shell.
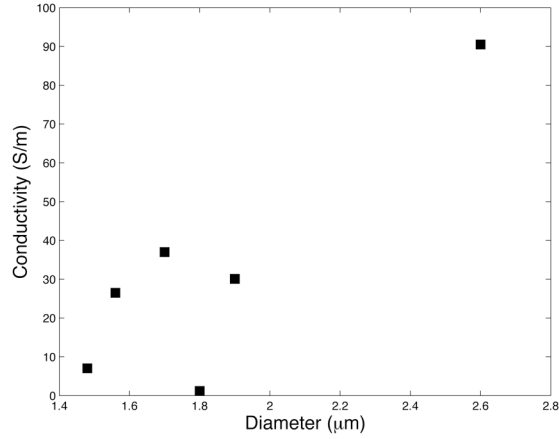
Figure 3.9: Conductivity Vs. diameter of MWNT bundles

3.4   Conclusions

MWNT shell-PMMA core, micron sized, composite fibers were prepared via a coaxial electrospinning technique. Two point electrical measurements were performed on short segments of MWNT cores following thermal degradation of the shell, showing conductivities up to two orders of magnitude higher than homogeneous MWNT/polymer composite fibers. The interaction of the polymer free core on the shell was investigated through the use of the Hansen's solubility parameters with the goal of promoting alignment, packing density, and continuity of the core.

Four core shell solution interaction regimes were explored based on their miscibility and the core solutions solvency of the shell polymer. Miscible solutions with a PMMA nonsolvent core lead to coagulation of the Taylor cone, preventing any electrospinning. Immiscible-nonsolvent solution pairs resulted in the most well defined core-shell interface. While the core shell structure is well defined, this interface is formed early in the spinning process, before the core solvent has completely evaporated, causing many hollow regions. This regime may be useful for creating hollow tubes or well defined polymer-polymer coaxial fibers but for our purposes, the formation of this interface prevented further constriction, bundling, and alignment of the MWNT core. Surprisingly miscible-solvent pairs created reasonably well defined coaxial fibers with many bundled MWNT cores. This shows the importance of the MWNTs in altering the miscibility of the core solution. While this regime did produce well bundled cores with few voids, it also produced many fiber artifacts that impeded accurate characterization

of the MWNT core. Immiscible-solvent pairs produced the best bundled cores, though this regime had the most variation in fiber morphology, producing hollow cores, bundled cores, porous shells, and other fiber artifacts. The factors influencing the production of these undesirable morphologies in this regime are not clear, though there does appear to be a trend in those that impact the well bundled core. The number of bundled cores increased as the shell solvent approached the center of the PMMA solubility sphere. An ideally suited shell solvent for the polymer along with a semi-miscible, semi-solvent core solution, one which lies on the fringe of the PMMA solubility sphere, is expected to produce the best results.

Although the ultimate fiber morphology was not achieved, there is still promise for increased nanotube alignment and packing density with decreased fiber diameter. The ultimate limiting factor to this technique and other solution based CNT fiber making techniques appears to be the quality of the CNT dispersion. It is speculated that the continuity and alignment of the MWNT core could be drastically increased if a suitable CNT dispersion in the ones to tens of a weight percent were achieved.

While other CNT wire making techniques are producing fibers with properties approaching that of bulk materials

While other groups have developed wires whose properties approach that of bulk materials - with potential room for improvement. It's unlikely that a coaxial electrospinning approach will produce materials that surpass those of other wetspinning techniques. However, such an electrospinning approach may be useful in developing more highly functional materials such as optoelectronics or ultracapacitors, in which an

internal electrical conductor is required.

Chapter 4

Problem of thermal interface and 1-D reference bar TIM characterization

CNTs are aptly suited as a wire material due to their high electrical conductivity, high current density and amazing strength. Similarly CNTs are well suited to TIM applications due to their high thermal conductivity, small size and mechanical compliance. When arranged in a vertically aligned forest, individual CNTs can deform to a rough mating surface, creating a high surface area of contact and hence a low thermal contact resistance. The following chapter discusses the fundamental problem, the physics behind thermal interfaces, reviews existing Thermal Interface Materials (TIMs), and gives a treatment of the most commonly used thermal interface testing device, the 1D reference bar method.

4.1 Problem of thermal interfaces resistance

4.1.1 Motivation

Thermal management is becoming increasingly important to a number of fields, in particular the ever expanding microelectronics industries. The international Technological Roadmap for Semiconductors (ITRS) identifies thermal management, specifically TIMs and heat-sinks, to be likely bottlenecks in next generation electronics [66]. This is a result of the continualy shrinking dimensions, increasing density and increasing speed of transistors in integrated circuits (IC). The following equation describes the power dissipated by a CMOS transistor, illustrating the increasing power density problem:

$$P = CV^2 f \tag{4.1}$$

where C is the capacitance of the transistor; largely the gate capacitance although wire, drain and source capacitance also contribute. V is the operating voltage, and f is the switching frequency. While the capacitance would appear to drop as the transistors shrink due to decreasing gate area, the dielectric separator distance is also decreasing, thereby increasing the capacitance. There are fundamental limits to the voltage scaling associated with the silicon band gap and room temperature thermal energy, so arbitrarily lowering the voltage is not a viable means to mitigate the power dissipation problem. Clearly, the frequency increases the current and hence power increases linearly. Not all transistors in the IC switch during each period of the chip frequency, although average loads can be ascribed to each functional block of the chip. All of this, along with the
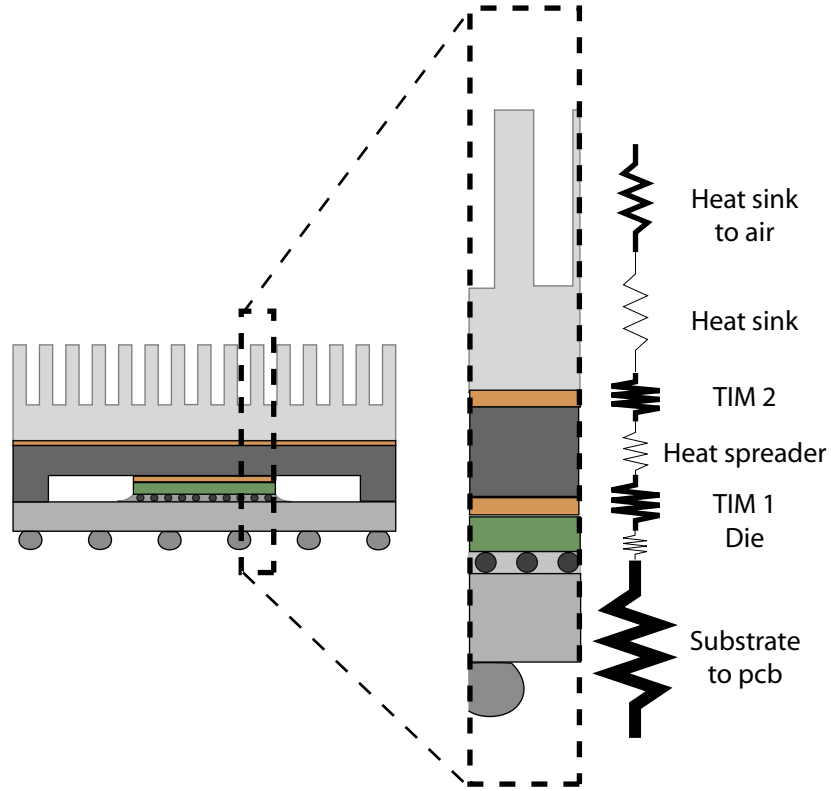
Figure 4.1: Illustration of cross section of chip/heat-sink assembly with associated thermal resistance model. The magnitude of the resistors are roughly reflected by their line width.

increasing density of transistors leads to an increase in power density that's needed to be dissipated as heat. ITRS predicts that by the year 2020 both 'Cost-performance' and 'High-performance' single-chip packages will need to dissipate over 1 W/mm^2 [66].

Figure 4.1 illustrates a cross section of a typical chip package and heat-sink assembly along with the associated layers and thermal resistances. The magnitude of the resistance of each layer is reflected by the stroke width of the resistor symbol.

As illustrated, the thermal interface materials represent a major portion of the overall resistance. Very little heat is dissipated through the substrate and out the printed circuit board (PCB), most of the heat must pass through the TIMs and heat-sink.

4.1.2   Fundamental problem: contact resistance

In order to reduce the thermal contact resistance it is first important to understand what causes this resistance. No matter how flat or smooth a surface may appear, there are always imperfections that cause contacting surfaces to have a significantly reduced area of contact. For dry metallic surfaces this contact area is usually a 1 to 2% of the nominal contact area [67]. Figure 4.2A) illustrates this problem for two contacting surfaces at the microscopic scale. For dry surfaces in a vacuum, i.e. no filler material in the voids, only conduction at the contact points contributes to heat transfer. Conduction and convection across the voids is not present and radiative heat flux is proportional to $(T_{hot}^4 - T_{cold}^4)$, as a result it only becomes significant at high temperatures (Fig 4.2C).

Heat transfer at only a few spots separated by a large distance forces the heat flow lines to be restricted, flowing through a few points. This phenomena is known as constriction and spreading resistance. The two resistances are mathematically equivalent. However, constriction refers to the heat flow towards a constriction point, while spreading refers to heat flow away from a constriction point. These two terms are sometimes both referred to as constriction resistance. The constriction resistance is governed by the geometry of the contacts, their distribution and the thermal conductivity of the
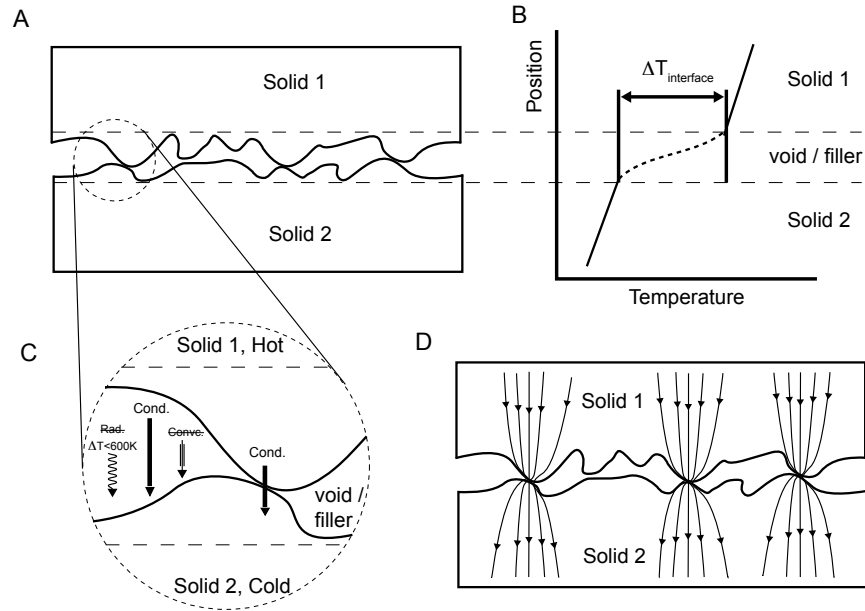
Figure 4.2: Diagram showing the fundamental problems of contact resistance. A) shows the problem of contact area, surfaces that appear flat may be very rough at the microscopic scale, limiting the contact area to only a few percent of the nominal area. B) Plots the temperature as a function of position across the contact, showing an abrupt jump near the interface. C) A close up view of the two solids in contact, only conduction through the contact is a significant form of heat transfer. D) Illustrates constriction and spreading resistance towards and away from the point contacts.

two materials. The smaller the area fraction between the contact spot and the area between contacts, the more significant constriction resistance becomes. The concept of constriction and spreading resistance are illustrated in Figure 4.2D where the heat flow lines are sketched and shown to converge towards the three constriction points.

In addition to constriction and spreading resistance there is a third resistance associated with a contact, known as the mismatch, Kapitza, or interfacial thermal resistance [68]. This resistance is present for any two dissimilar materials in contact, even provided perfect contact without any voids. The resistance is a result of the difference in electronic and vibrational modes within the two materials. As an energy carrier attempts to traverse the interface, it has a probability of transmission or scattering depending on the available energy states. The transmission probability is particularly poor for two materials with differing dominant conduction carrier types, i.e. phonons and electrons. The highest mismatch resistance measured is between bismuth and hydrogen terminated diamond, with very low and high Debye temperatures respectively. This resistance was found to be $0.11\text{mm}^2\text{K/W}$ [69]. Conversely, the lowest mismatch resistance was found between aluminum and copper with a value of 2.5e-4 $\text{mm}^2\text{K/W}$ [70]. These resistances are orders of magnitude smaller than the total thermal impedance of a state of the art TIM, $\sim 10\text{mm}^2\text{K/W}$.

The combination of all resistances associated with a contact, leads to a temperature drop across the contact, ΔT for a given heat flux, Q/A through the joint. The contact resistance is calculated from the preceding terms by:

99

$$R = \frac{A\Delta T}{Q} \quad \left(\frac{m^2\text{-}K}{W}\right) \tag{4.2}$$

A diagram of the contact resistance between two hypothetical conductors is shown in Figure 4.2B. Unlike thermal conductivity, which is expressed in terms of Fourier's law:

$$\kappa = \frac{Ql}{A\Delta T} \quad \left(\frac{W}{m\text{-}K}\right), \tag{4.3}$$

the thermal resistance is not an intrinsic property of the materials, rather it is dependent upon contact pressure, surface roughness, and deformation mechanics [67]. These experimental and material preparation sensitivities, along with the inherent difficulty in thermal measurement [71], makes evaluation and comparison of TIMs performance quite challenging.

4.1.3 Prior work

To mitigate the temperature drop associated with contact resistance, researchers have developed two fundamentally different types of TIMs, 'filling' and 'interrupting' types. Figure 4.3 illustrates the the two types of TIMs and shows their simplified thermal circuit models. The filling type aim to increase the area of contact by inserting a new, highly conformable, liquid or gel material between the two conductors. Ideally it only fills the voids left behind after contact between the two solids is established. Since the filled voids now conduct through the new filler medium, the new contact resistance should be the parallel combination of the original bare contact resistance and the new filler resistance:
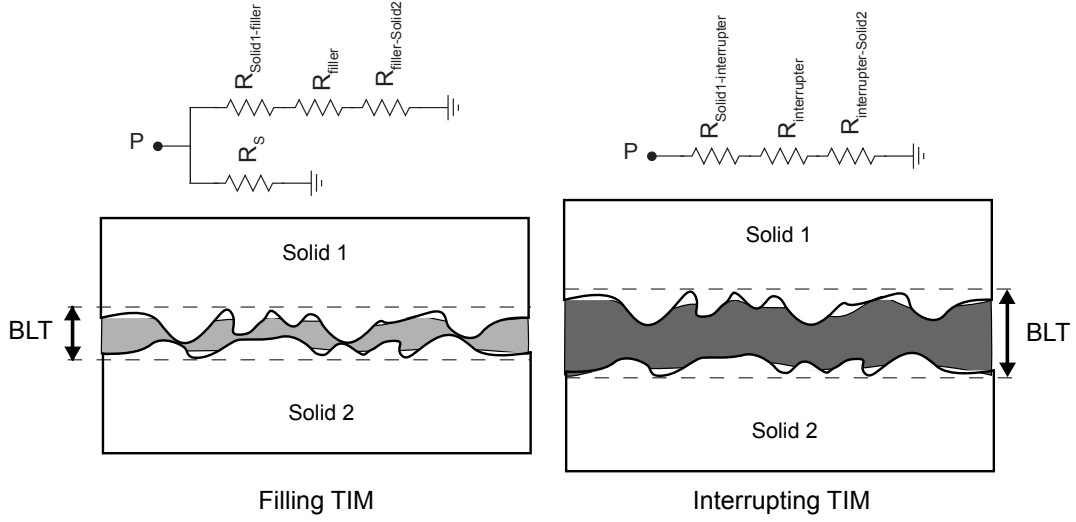
Figure 4.3: Diagram of filler and interrupter type TIMs and their associated thermal circuit models.

$$R_c = \left(R_s^{-1} + R_f^{-1} \right)^{-1}, \tag{4.4}$$

where R_c is the overall contact resistance, R_s is the original bare contact resistance of the solids, and R_g is the contribution from the grease or filler material. The filler resistance is composed of the bulk resistance, equal to the Bond Line Thickness (BLT) gap divided by the thermal conductivity of the filler BLT/κ_f, plus the two contacts between the filler and the solids. However, this simple model is not quite accurate as the additional filler will alleviate some of the constriction resistance compared to that of the bare contact – in other words R_s will not be identical to the original reference measurement, but for many cases it will be close.

101

The interrupting TIM completely breaks the original bare metal contact, replacing it with two new contacts as illustrated in Figure 4.3. This has the effect of simplifying the circuit model as there is no longer a contribution from the bare metal contact. This along with the typically thicker bond line thicknesses associated with interrupting TIMs means that in order to be competitive with filler TIMs, the interrupting type needs to have lower bulk and contact resistances. However, due to the increased BLT the interrupter type may be able to make better contact to surfaces that are severely non-parallel or bowed.

4.1.3.1 Traditional TIMs

There are a number of different commercially available TIMs, each with its pros and cons. Table 4.1 presents a broad summary of the different TIM categories along with their general traits. κ_{bulk} refers to the bulk thermal conductivity of the TIM, while the 'conformal' column describes its ability to conform to uneven surfaces, thus minimizing void volume and increasing contact area. The migration of the material, often referred to as 'pump-out' is the tendency of filler TIMs to migrate out of the joint over the course of thermal cycling. This is generally less of a concern for interrupting type TIMs and adhesives. The stress column denotes mechanical stress and is a significant problem for TIMs that cure or set such as the adhesives or metal bonding. Over the course of thermal cycling and mechanical vibrations, these rigid TIMs can crack or delaminate from the contacting surfaces, causing an abrupt jump in the thermal resistance. All of these traits should be weighed in the selection of a TIM for its desired application.

Table 4.1: Commercial TIM summary, general rating based on positive, neutral, and negative assessment

TIM	Type	High κ_{bulk}	Conformal	Low migration	Low stress
grease	filler	0	+	-	+
PCM	filler	-	+	0	+
pads/gels	interrupter	0	-	+	+
adhesives	filler	+	+	+	-
soft metals	interrupter	+	0	+	-

4.1.3.2 CNT TIMs

Some specific implementations of CNT TIMs were discussed in the introduction, section 1.6. However, there are still many gaps in the knowledge of what governs their performance. In particular, there is a large void in the correlation between array properties such as height, density, alignment, diameter, and crystallinity, to the thermal performance of the CNT forest. Additionally a further understanding of the dry contact, van der Waals interface, is needed since this appears to be the limiting factor in these TIMs. Deeper understanding of the mechanical behavior of these forests is likely to aid in the understanding of the TIM problem as compressibility relates to real contact area, which should largely influence the contact resistance.

Cola et al. made large strides towards the effort of correlating array morphology to the thermal performance [32]. They are the only group to form a comprehensive

103

model describing the contact mechanics of the CNT interface and relating it to the observed thermal properties. Their model does however make a few assumptions about the mechanics, in particular the characteristics of the compressive modulus, which are not universally supported in the literature. Additionally they fail to close the loop on this system by measuring the mechanical and thermal properties simultaneously. They do conclude that the thermal contact is dominated by the CNT tips through van der Waals contacts, that the overall resistance is dependent upon the real contact area, and that maximizing this area is a function of the compressibility and density. Furthermore, compressibility is a function of density, suggesting that some optimized combination of these parameters is needed to maximize contact area.

Liu et al. performed a nice study on the effect of density and, to a lesser extent, height on the array's thermal performance [72]. While only presenting a subset of the possible array morphologies, they conclude that there is an ideal height near $50 \mu m$ and that the resistance decreases with decreasing density until the CNTs can no longer support a vertical structure. This supports Cola's conclusion that array compressibility, which increases with decreasing density, plays a vital role in creating a high performance CNT TIM.

There has recently been developments in the mechanical characterization of CNT forests, which may aid in the optimization of future CNT TIM performance. Goodson's group has begun correlating the array modulus to alignment and density [73]. As well as developing new and facile, non-destructive techniques for measuring the in-plane modulus [74, 75]. Ultimately the array morphologies need to be related to the

contact dynamics, compressibility and contact area, which then can be related to the thermal resistance. This is currently a arduous task due to the difficulty in controlling array morphologies, the time consuming nature of many of these measurements, and the total lack of ability to measure real contact area. Ultimately the processing and metrology techniques need to improve to the required systematic study.

4.2   1-D reference bar TIM characterization

4.2.1   Background

There are a number of standardized methods for thermal testing, although the 1D reference bar method, also known as the ASTM D5470 has gained significant attention. Much of this attention is related to its apparent simple design and operation. It has become the *de facto* standard for TIM testing both in research and industry, yet the standard was not originally developed for TIM testing. Originally developed to measure the thermal conductivity of homogeneous or composite thermally conductive materials, it sought to remove contact resistance as this could be misinterpreted as an increase in conductivity. This was achieved by applying a large compressive force (3MPa), and if necessary, measuring a number of samples of different thickness so that the contribution of the contact could be removed. Clearly not the intention of TIM testing, which specifically seeks the contact resistance, the ASTM D5470 standard is often slightly modified for variable pressure measurements. Operating at lower pressures is necessary for the accurate characterization of TIMs whose final operating environment is likely to be in

the hundreds of kilopascal range rather than megapascals as the standard requires. The close simulate of this measurement technique to the final operating environment of the TIM, is another reason for its mass adoption.

The 1D reference bars simplicity may have actually hindered the field. Its simplicity encourages the creation of custom homebuilt instruments, which inflates variations in results between labs. Additional sources of variation include surface preparation (flatness, parallelism, surface contamination), ambient atmosphere, and stray heat loss. These tend to become more pronounced as the TIMs performance increases and the total resistance of the sample drops. These along with a general lack of standard for calibration make the accurate evaluation of TIMs challenging.

The following sections describes the overall method, fabrication, and testing of a custom built 1D reference bar thermal measurement. In addition to the variable pressure modification to the ASTM standard, this system is also capable of measuring samples under high vacuum and down into the cryogenic regime. Both of these features are necessary for evaluating the TIMs for high performance aerospace applications.

4.2.2 Principle of operation

The 1D reference bar method relies on one dimensional heat conduction through two reference bars, compressed on either side of the sample under investigation. The temperature gradient in the reference bars can be used in conjunction with Fourier's law:

$$\vec{q}_z = -\kappa \frac{dT}{dz}, \tag{4.5}$$

where the thermal conductivity κ can be verified or otherwise established, to extrapolate the temperatures at the sample-reference bars interfaces. The basic apparatus and a plot of the characteristic measurements are shown in Figure 4.4. This approach is only valid assuming there is no heat loss in the radial direction (i.e. 1D heat conduction). For measurements performed in air, there is usually a guard heater covering one or both reference bars. However, this complicates things somewhat as the guard heater temperatures must be chosen to appropriately suppress radial heat flow. This is a steady state or DC technique opposed to a transient or AC technique, requiring that the whole system reach equilibrium before measurements are performed. Depending on the thermal mass of the reference bars and the thermal conductivity of the sample, this time to equilibrate can be quite long.

From a single measurement, one determines the overall joint contact resistance, including the two interface resistances and the bulk resistance, as discussed for interrupting type TIMs in section 4.1.3. From a series of measurements with different sample thicknesses, one can isolate the sum of the two contacts and the bulk conductivity by examining the resistance as a function of sample thickness. The joint resistance R_j is given by $BLT \cdot \kappa_{sample}^{-1} + R_c$, where BLT is the sample thickness, κ_{sample} is the bulk conductivity of the sample and R_c is the sum of the two contact resistances. This means that the y-intercept of the resistance versus thickness plot is the contribution from the contacts, while the slope is the inverse of its bulk conductivity. This of course

107
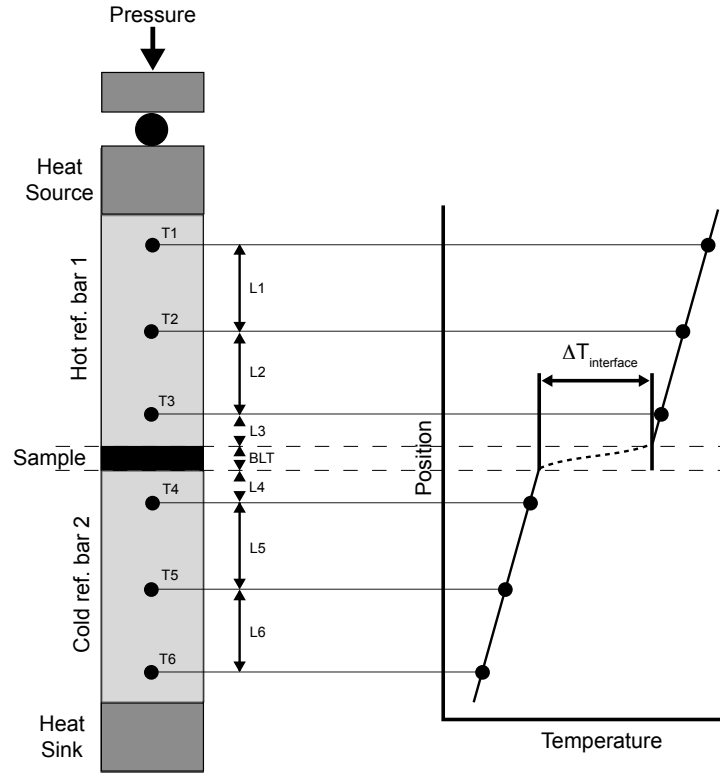
Figure 4.4: Diagram of 1D reference bar apparatus. The relative size of the sample is enlarge for illustrative purposes.

only works if the contact resistances stay roughly the same for all measured thicknesses and that the material under investigation adheres to Fourier's law. It is possible that, for very short, highly crystalline, CNTs measured at low temperatures, Fourier's law may not be obeyed as the phonon transport begins to behave ballistically rather than diffusively. However, this is only likely to occur for very short, sub micron CNT lengths, whose thermal conductivity would likely be too high to ascertain by this technique.

4.2.3   Experimental apparatus

The system used in the subsequent studies was designed, built, and operated at the university of Wisconsin-Madison, by Dr. Jim Maddocks. Much time and effort went into the iterative calibration and refinement of the system to ensure accurate measurements. The overall system is very similar to that presented in Figure 4.4. The cold block is mounted directly onto a pulse tube cryocooler allowing the temperature to be adjusted between $70°K < T < 300°K$ by adjusting the compressor stroke and or adding heat to the cold block. There are four type E thermocouples mounted to the surface of each reference block. The reference blocks are made from 0.5"x0.5", $161mm^2$, oxygen free high conductivity (OFHC) copper. The top reference bar is heated via a joule heater wound around another segment of copper. A ball bearing is placed between the heater and the pressure applying clamp to both reduce heat loss and to aid in the alignment of the two sample interfaces. Initial tests suggested some heat loss through the ball bearing so a guard heater was included above the ball bearing and its temperature was set to that of the experimental heater, maintaining $\Delta T = 0$ across the ball bearing.

Pressure is applied to the top reference bar via a pair of compression springs sheathed over supporting OHFC copper rods. Similar use of springs has been shown to produce little variation in pressure over a wide range of temperatures [76]. These springs are tightened via a pair of compression nuts and they collectively push down on a pressure plate that rests on the guard heater. The pressure from these springs was calibrated prior to sample measurement and can be controlled by the number of

turns on the nuts following initial contact. The initial design incorporated a bond line thickness monitor, although due to the difficulties in operating the BLT monitor under vacuum, this data was not collected for most samples. Due to the freedom in the top reference bar, supported on top of a ball bearing to aid in alignment, an alignment jig was used to load the samples.

Unlike the room temperature measurements, those performed at reduced temperature also suffer from positive heat flux into the experimental apparatus from the bell jar or outside sources. To minimize these heat sources, mutilayer aluminized Mylar insulation was added to reduce radiative heat transfer. Additional parasitic heating can flow through the thermocouple wires, creating a falsely elevated temperature. To mitigate this, type E thermocouples were used, which have highly alloyed, low thermal conductivity leads. These leads were also wrapped around supporting copper rods, grounded to the cryocooler. The entire system is contained within a vacuum bell jar capable of maintaining base pressures between $1 \times 10^{-4} - 5 \times 10^{-5}$ torr depending on the temperature of the cryocooler. With no load, the cryocooler can reach a base temperature of 45°K and can sink 10W at 95°K.

4.2.4 Measurement procedure

A typical 1D reference bar measurement is plotted in Figure 4.5. A fairly small power is applied to the top reference bar, while the base of the bottom bar is kept at a constant temperature. This establishes a temperature gradient in each reference bar as shown in the figure. The slope can be used to determine or verify the thermal
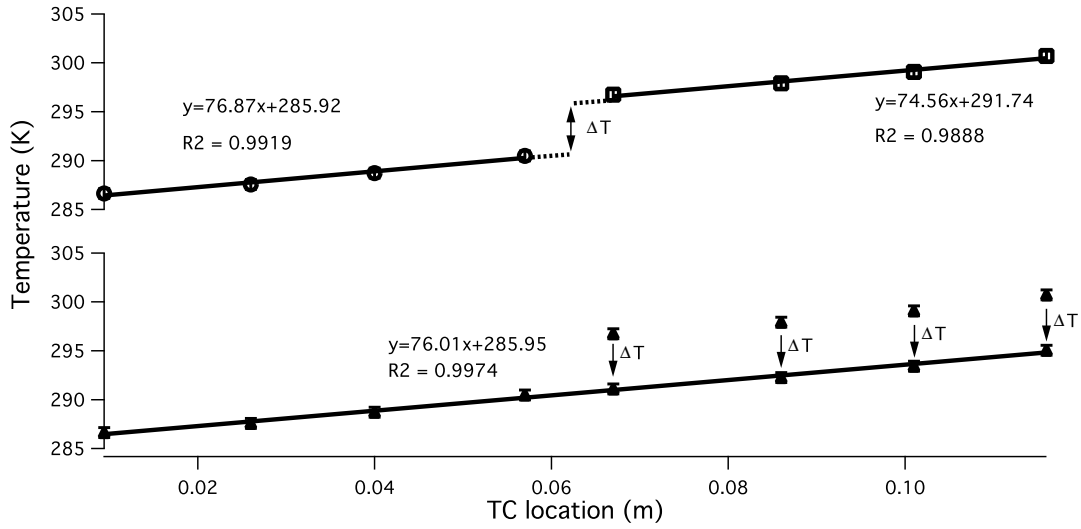
Figure 4.5: Example of 1D reference bar measurement of bare copper interface, showing two fitting methods. The top fits a line to each reference bar separately, calculating ΔT across the interface after fitting. The bottom method fits a single line to both bars, adjusting ΔT as a fit parameter.

conductivity of the reference bar material. The gradient in the reference bars is linear and in good agreement with the documented values for OHFC copper. The offset between the two gradients is a result of the junction resistance. Two separate lines can be fit to each reference bar and the temperature drop calculated from the difference between these lines. Alternatively, a single line can be fit to the entire dataset with the temperature drop used as another fit parameter. A third, slight variation of the second method, uses a calculated gradient based on the known conductivity of the reference bars, fitting only the y-intercept and the junction temperature offset. The fundamental difference in these three calculation methods is the way in which ΔT is established,

whether it is integrated into the data fitting or calculated after the fitting routine. Both

of these fitting methods are presented in Figure 4.5 and would ideally lead to the same

result. However, there is a 3% variation between the slopes of the two reference bars

in the first method and the ΔT varies from $5.82°$K to $5.65°$K between the first and

second routine respectively. Since both reference bars were cut from the same stock, it

is assumed that there is little variation in the bulk conductivity between the hot and

cold block. For this reason, the method incorporating ΔT into the fitting routine was

used. The problem can be cast into matrix form using the following set of equations:

$$A\beta = Y, \quad \beta = (A^T A)^{-1} A^T Y, \tag{4.6}$$

where A is the dynamics matrix, β are the fit parameters, and Y is the measured thermal

data:

$$
A = \begin{bmatrix}
x_{ref\text{-}bar1_1} & 1 & 0 \\
x_{ref\text{-}bar1_2} & 1 & 0 \\
\vdots & \vdots & \vdots \\
x_{ref\text{-}bar1_n} & 1 & 0 \\
x_{ref\text{-}bar2_1} & 1 & 1 \\
x_{ref\text{-}bar2_2} & 1 & 1 \\
\vdots & \vdots & \vdots \\
x_{ref\text{-}bar2_n} & 1 & 1
\end{bmatrix}
\quad
\beta = \begin{bmatrix} m \\ b \\ \Delta T \end{bmatrix}
\quad
Y = \begin{bmatrix}
y_{ref\text{-}bar1_1} \\
y_{ref\text{-}bar1_2} \\
\vdots \\
y_{ref\text{-}bar1_n} \\
y_{ref\text{-}bar2_1} \\
y_{ref\text{-}bar2_2} \\
\vdots \\
y_{ref\text{-}bar2_n}
\end{bmatrix}
$$

where $x_{ref\text{-}ba1_i}$ and $x_{ref\text{-}ba2_i}$ are the position of thermocouples i in reference bar 1 and

2 respectively, while $y_{ref-ba1_i}$ and $y_{ref-ba2_i}$ are the corresponding temperature measurements. m, b, and ΔT are the fit parameters for the slope, y-intercept and junction temperature respectively.

While the method of data analysis had some influence of the final results, the surface quality of the copper blocks was found to have a much stronger influence. As a result, each surface was polished by hand using 8000 grit sand paper prior to each measurement. This dependence was probably due to the formation of a thin oxide layer on the copper surface. A short, fine grit polish is enough to remove this oxide. Over time this may cause curvature across each surface, although this is expected to be a very slow process due to the fine grit of the polish.

4.2.5   Error analysis

Uncertainty propagation through an arbitrary function, F, can be performed by taking the norm of the linearized projections of each variable uncertainty, δX_i onto the function:

$$\delta F = \left[\sum_i \left(\frac{\partial F}{\partial X_i} \delta X_i \right)^2 \right]^{1/2} \tag{4.7}$$

This assumes independent variables and that the function is fairly linear, i.e. δX_i is small compared to its partial derivative. This is akin to estimating the sensitivity of F to changes in measured values X_i. By summing all of these functional sensitivities to the potential error in the measurements, δX_i, the error in the function, δF, can be established. This general technique is used to propagate the error from the measurements

113

through to the calculated results.

While there are a number of intermediate calculations that require uncertainty propagation using this technique, the ultimate goal is to establish the error associated with the thermal contact resistance. Unfortunately the error estimates of the measured value ΔT, in Equation 4.2 is not as straight forward as it is for Q and A. The error in ΔT is determined by the data fitting routine and differs slightly between the different routines discussed previously. For the case where ΔT is a fit parameter, the error associated with the fit parameters can be determined using the unbiased estimates of the fit parameters σ_{β_k} from [77]:

$$\sigma_{\beta_k} = \sqrt{((A^T A)_{k,k})^{-1} \frac{SSE}{n-p}}, \tag{4.8}$$

where A is the dynamics matrix, or heat flux matrix defined above (Eqn. 4.2.4), n is the number of measured data points and p is the number of fit parameters. The sum of squared errors, SSE, can be computed using the minimized solution from Equation 4.6 and the following eqution:

$$SSE = \beta^T A^T A \beta - 2y^T A \beta + y^T y \tag{4.9}$$

From the example in Figure 4.5, this technique produces a standard deviation of $\sigma = 0.34°$K. Comparing this with the deviation of ΔT between the two fitting routines $(0.17°$K$)$ suggests that this error estimation is an accurate reflection of the uncertainty. The other relevant uncertainties are estimated directly.

114

4.2.6 Measurements validation, Cu-Cu bare interfaces

Initial validation involved checking the thermal conductivity of the reference bar materials, the value of which is well known, particularly at room temperature. As discussed previously, this is done by measuring the relevant quantities and using Fourier's law (Eqn. 4.5) to establish a measured thermal conductivity. While this verifies the intrinsic properties of the measurement setup, there is still a large uncertainty in the evaluation of the contact resistance, which is highly sensitive to reference bar alignment, surface roughness, flatness and overall surface preparation. However, validating the contact resistance is non-trivial and is a challenge that has not been fully addressed by the research community.

Since there is no well defined reference material used for TIM measurement validation, the resistance of bare Cu-Cu interfaces was used. Unfortunately the bare Cu-Cu interfaces suffer from the same calibration problems as other TIMs. In particular, there are a number of experimental variables such as surface preparation and ambient conditions that deeply influence the overall junction resistance. As a result, a number of measurements were made using the same surface preparation but with varying ambient conditions (different pressures) and the results are compared against other documented literature values for Cu-Cu interfaces. These results are summarized in Table 4.2.

The bare Cu-Cu results are consistent with the range of values found in the literature for similar operating conditions. However, there is a reasonable variation between measurements. This is likely attributed to variations in the contact between

Table 4.2: Bare Cu-Cu contact resistance validation.

Pressure (MPa)	Surface preparation	Gap condition	Resistance (mm^{2}K/W)	Reference
0.985	600 grit	760 torr air	107	This work
0.985	600 grit	760 torr air	78	This work
0.985	600 grit	4.6e-4 torr	289	This work
0.985	600 grit	6.4e-4 torr	184	This work
0.985	600 grit	4.2e-4 torr	187	This work
3.82	1.65 μm	vacuum	200 - 500	[76]
~0.97	R$_{RMS}$ 0.55 μm	vacuum	~134	[78]
~0.96	R$_{RMS}$ 0.55 μm	1500 torr Ar	~79	[78]
~0.96	R$_{RMS}$ 0.55 μm	1500 torr N$_2$	~60.6	[78]

experiments either in alignment or surface preparation. This prompted an investigation into reference bar alignment and the creation of the previously mentioned alignment jig to ensure proper alignment during sample loading.

Chapter 5

CNT array TIMs on silicon substrates

5.1 Introduction

The bulk of the past experimental research in the CNT TIM field has used Silicon as a growth substrate. This is likely due to its ubiquity in the microelectronics field, its widespread use as a substrate for CNT growth, its high thermal conductivity (149 W/m-K at room temperature) and its atomically smooth surface. Nearly every research group studying this subject has focused on the use of the silicon substrate [22, 79, 23]. As a result of the plethora of data, a series of studies using Silicon as a substrate was pursued.

In an attempt to control the MWNT forest density, two approaches to catalyst preparation were investigated. A micelle template technique is shown to have good control over the catalyst density, although the resulting MWNT growth was insufficiently aligned for TIM testing. Sputter deposited catalyst was shown to result in the formation

of dense particles distributions with less controlled catalyst density. However, this catalyst preparation produced more suitable VACNT for TIM testing. A TIM statistical variation study was performed for sputtered catalyst grown MWNTs, showing relatively poor results compared to that found in the literature. This motivated a more in depth study of the array morphologies influencing the thermal resistance. Finally a simple Euler buckling model is used to explain the relationship between array morphology and thermal resistance.

5.2 Experimental techniques

5.2.1 Catalyst preparation by block co-polymer micelle templates

Micelles have been used for a number of years to create periodic arrays of nanoparticles. This is performed by using diblock copolymers to form micelles and subsequent loading of the micelles with metal salts. The technique has been successfully applied to the formation of gold nanoparticles for ZnO nanowire growth, deposition of ZnO nanoclusters for optical devices, and even as a masking technique for nano lithography. It has recently been applied to Fe nanoparticles formation for CNT synthesis [80, 81, 82].

Block copolymers are a facile approach to synthesize micelles with highly customized properties. In order to generate micelles the block copolymers must be amphiphilic, where one half of the chain is hydrophobic while the other half is hydrophilic. Typically micelles are formed in aqueous solutions and a result, the forces driving their

formation are those of the hydrophobic attraction at the hydrophobic tail-water interface. This force may be characterized as an interfacial tension, encouraging the hydrophobic tails to minimize their surface energies. These forces are balanced by the hydrophilic head-group repulsions due to their complex electrostatic, and/or steric interactions between adjacent headgroups. Together these forces create a minimum energy, which along with geometric packing considerations determines the preferred self-assembled shape. These amphiphiles can form into well defined structures such as cylindrical or spherical micelles, bilayers, or other three dimensional networks. A detailed explanation of these force balancing equations along with criteria for the formation of particular morphologies is described in Israelachvili's book, *Intermolecular and Surface Forces* [83]. The micelles formed in this study are referred to as reverse micelles because they are synthesized in a non-polar solvent, thus forming an inverted structure to those synthesized in aqueous solutions. However, similar force principles apply except in reverse.

The choice of diblock copolymer and specifically the chain lengths of the A and B segments deeply affects the morphology of the micelle and hence the resulting nanoparticles. For the reverse micelle case, the polar group length determines the nanoparticle size, while the non-polar group length governs the particle-to-particle spacing. Additionally there is a range of polar and non-polar chain lengths that satisfy the energy and geometric constraints for micelle generation, as discussed by Israelachvili [83]. Besides the head chain length, the size of the particle can also be controlled by the loading fraction of the micelle. However, the upper bound of this technique is saturation
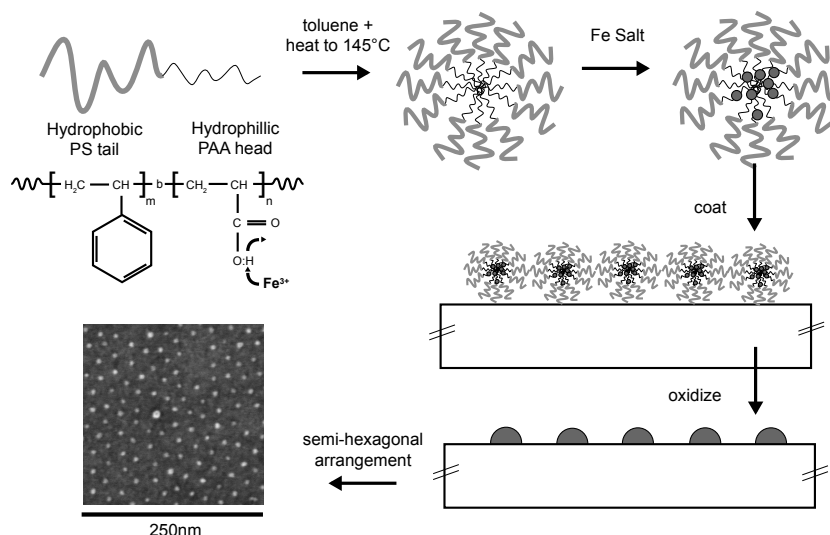
Figure 5.1: Procedural diagram to synthesize Fe nanoparticles via a block copolymer micelle template method.

limited. The saturation limit depends on the charge ratio of the head group monomer and salts used. In addition to modifying the tail length, the spacing between particles or the particle areal density can be modified in at least three other ways. The addition of a small fraction of homopolymer, matching that of the tail group, can increase the particle spacing [84]. In a similar vane, one can influence the particle spacing by changing the solution concentration and or application method to the substrate [82]. Due to its simplicity, the latter two methods were investigated in this study, the results of which are presented in the experimental section below.

The micelles formed here are very similar to those reported by Bennett and Liu [81, 82]. They are formed using polystyrene-poly(acrylic acid) (PS-PAA) diblock copolymer loaded with ironchloride (FeCl$_3$) salt. Two different molecular weights were

used with 15k:3.6k g/mole (PS:PAA) and another at 15k:4.3k g/mole, both purchased from Polymer Source, Inc. The polymer was dissolved in toluene with a concentration of 12 mg/mL and left to stir overnight. Further conversion to the micelle phase requires heating the solution to 145° for 20 minutes then cool to room temperature. Both Li and Bennett reported cloudiness prior to this step suggesting a mixture of cylindrical and spherical micelles [82, 84]. $FeCl_3$ was then added to the solution with 3:1 PAA monomer to Fe mole ratio. This reflects the charge ratio of the acrylic acid monomer to iron cation and should fully saturate the micelle. This step required very careful measurements (small $FeCl_3$ mass) and a speedy introduction into the solution as the $FeCl_3$ behaved hygroscopically, quickly absorbing water from the ambient air. This water may work its way into the finial micelles altering their size or shape. After the addition of the iron salt, the solution was mixed for an additional 6 hours. The solution was then decanted and diluted to a range of concentrations. The micelles can be deposited onto substrates via either spin or dip casting. Both techniques capable of producing monolayer or multilayer micelle films, depending on application variables. Attempts to dip cast proved to be unsuccessful, while spin casting was more effective. Spin casting was performed on silicon substrates with a range of spin speeds. Solutions were filtered through 200nm pore size, syringe filters during the spin casting procedure to remove any large particles. The solution was only cast at the final spin speed as the solvent quickly evaporates even at low spin speeds, producing potentially thicker films. Producing well dispersed films over $1cm^2$ substrates proved quite challenging. Additionally, surface tension originating at the substrate corners formed edge beads,

increasing the micelles in these regions. Uniform layer thickness requires removal of these edge beads through substrate cropping. Following micelle deposition, the organic material was burned off by heating in air at 400°C for 2 hours, leaving only iron oxide nanoparticles. Figure 5.1 presents a diagram of this process.

5.2.2 Sputter deposited catalyst

Thin film deposition of transition metals are the preferred and most common method for CNT catalyst preparation. Thin films are generated by the evaporation or sputtering of metals onto the substrate. Upon heating, these thin films coalesce into nano-particles through Ostwald ripening. This process is described in section 2.2.2.3. While physical vapor deposition techniques produce high quality, repeatable film quality, that can be lithographically patterned, they are poorly suited to forming nanoparticles with mono-dispersed diameters and quantifiable areal densities. Both the diameter distribution and areal density are coupled to the film thickness and annealing conditions. Changing either the annealing conditions or film thickness is likely to alter both the diameters and density, making it difficult to isolate a single variable for study. Additionally, sputter deposition requires the use of a high vacuum. Establishing this vacuum is a time consuming process, making liquid deposition potentially favorable for mass production. However, compared to the processing requirements and results produced using the micelle technique, sputter deposited catalyst is trivially easy and very consistent.

For sputter deposited catalyst, silicon substrates are prepared using standard solvent cleaning techniques. No oxide removal step is used, suggesting a thin SiO_2 layer

on the Si surface. The desired metal layers are deposited onto the substrate using a South Bay Technologies IBS/e. Typical layer stack includes a 10nm Aluminum buffer layer used to diminish diffusion of the subsequent layer into the substrate and to aid in the iron oxide reduction process. This layer is followed by the catalyst layer, typically 2.5nm Fe. All growth was performed using the quartz tube furnace described in Chapter 2.3.

5.3 Results

5.3.1 Characterizing micelle template Fe catalyst and resulting MWNT growth

Characterization of the catalyst particles

Characterization of the micelle generated iron oxide particles was mainly performed using a Hitachi S-4800 scanning electron microscope (SEM) in secondary electron imaging mode. Imaging was quite challenging due to the small particle size and was facilitated by minimizing the working distance. Resulting images were analyzed using *ImageJ* to determine particle size and distribution. Attempts were made to characterize the iron oxide nanoparticles with an atomic force microscope, although no clear images were formed. The micelle film, prior to removal of the organic material, was characterized using an ellipsometer to determine fillm thickness and index of refraction. The index of refraction varied around 1.6, near that of polystyrene.

Figure 5.2 shows four different SEM images of the resulting iron oxide nanopar-
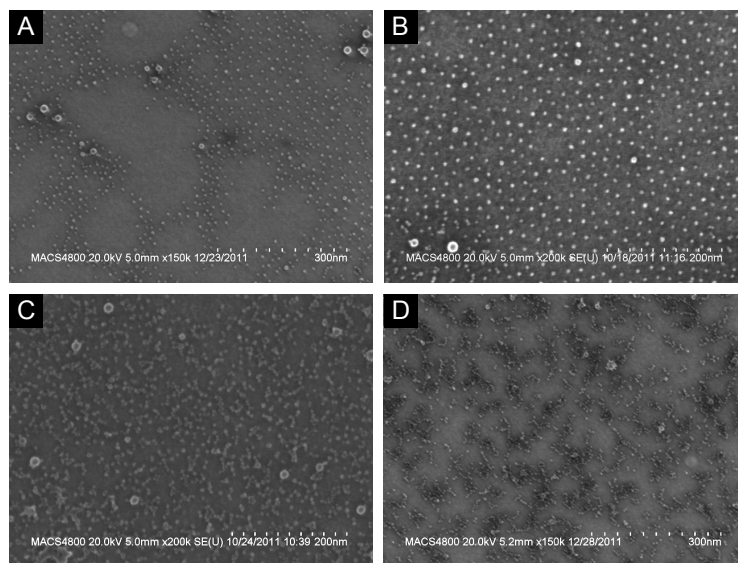
Figure 5.2: SEM images showing different micelle array morphologies. (A) incomplete coverage, (B) monolayer coverage, (C) multi-layer, (D) multi-layer clumping. Presence of larger, suspected vesicle, particles in each morphology.

ticle arrays generated using the micelle template technique. These images capture the representative morphologies observed in the range of experiments. Subfigure (A) shows incomplete, patchy coverage. This can result from either a too dilute solution or excessive spin speed during micelle deposition. Subfigure (B) shows a well dispersed monolayer, forming the characteristic semi-hexagonal packing array. Image (C) shows a multi-layer film. Multilayer films can be produced either using a high solution concentration, a low spin speed, or a combination of the two. When oxidized the iron oxide nanoparticles in these muli-layer micelles fall to the substrate forming less organized arrays compared to those of the monolayer. (D) shows the results from very
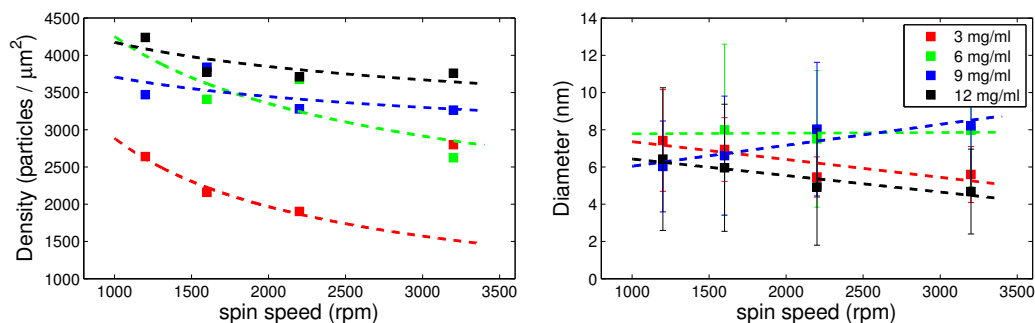
Figure 5.3: Plots summarizing iron oxide particle density and diameters from micelle experiments with 15k:4.3k molecular weight PS-PAA.

thick multi-layer micelle films, with a high degree of clumping between particles. This clumping or coalescing behavior may be early steps in the Oswald ripening process. In addition to the small 4-8nm particles, characteristic of the micelles, there were larger particles, 10 - 20nm, in every prepared solution. These larger particles are suspected to either be monolayer vesicles or swelled micelles due to the presence of water.

Control of catalyst density

A series of experiments using the 15k:4.3k molecular weight copolymer was performed in an attempt to control the density. A number of dilutions from a single stock solution were mixed. These solutions were spun cast onto 1cm^2 substrates and analyzed using the aforementioned techniques. The results are presented in Figure 5.3.

As expected, lower spin speed and higher solution concentration lead to more dense catalyst coverage. For very low solution concentrations, below 3mg/ml, the films are discontinuous and patchy regardless of the spin speed. Similarly, for spin speeds be-

low 1200rpm the catalyst coverage is discontinuous. This range of data is not presented in Figure 5.3 due to difficulties in its characterization as a result of its discontinuity. Solutions with a concentration of 3mg/ml produce self-assembled monolayer films at all spin speeds with very well-ordered quasi-hexagonal catalyst spacing. All higher concentrations produce multilayer films, distinguished by loss of the quasi-hexagonal spacing. At higher concentrations and lower spin speeds these individual catalyst particles begin clumping together. However, in all cases the catalyst diameter maintains a fairly narrow and well defined distribution of 6.65 ± 1.18 nm. Using this technique it was possible to tune the catalyst density between 2×10^{11} and 5×10^{11} particles/cm^2 – a range similar to what others have reported and successfully grown VACNTs from in the literature [72].

Characterization of MWNTs grown from micelle catalysts

A 10nm Al buffer layer beneath the iron is typically used to help promote CNT growth by limiting Fe diffusion into the substrate and helping reduce the iron oxide. This Al layer readily oxidizes and is presumed to be some form of aluminum oxide. Sputtered Al films resulted in grainy surface that prohibited the accurate characterization of the iron oxide nanoparticles. To overcome this problem, atomic layer deposition (ALD) was employed to apply an atomically smooth Alumina (Al_2O_3) layer to the Si substrate prior to the application of the loaded micelles. These Alumina layers have been shown to promote CNT growth in very similar ways to sputtered Al. The micelle template iron oxide nanoparticle arrays were applied to the ALD alumina, then characterized

126

using the SEM, followed by growth of CNTs using the quartz tube furnace described in Chapter 2.3 and subsequent characterization of the CNTs.

For the growth experiments the spin speed was held constant at 1600rpm, as this speed was found to produce the most uniform films, and only the solution concentration was varied. Figure 5.4 shows a summary of the growth results from these micelle generated iron oxide nanoparticles on ALD aluminia. Subfigures (A-D) show SEM images of the CNT growth from a range of micelle solution concentrations, while subfigure (E) plots histograms of the iron oxide particle diameter and resulting MWNT diameter. These catalyst particles produced a surprisingly low MWNT yield. For example, the monolayer micelle film in subfigure (A) produced roughly 10 CNTs/μm^2, with an initial $\sim$ 2000 catalyst particles/μm^2, this corresponds to a catalyst activity of 0.5%. This catalyst activity appears to increase slightly with increasing catalyst density.

Another interesting outcome is that the mean diameter of the CNTs is significantly larger than that of the micelles. The histogram of one such example, shown in Figure 5.4(E), reveals that the mean CNT diameter is nearly three times that of the mean catalyst diameter.

While this may be an artifact of the imaging technique, charging of CNTs had been shown to alter their perceived diameter in EM imaging [85], one may speculate that the variation in diamater CNTs and catalyst could be part of the cause for the remarkably low catalyst activity. It's possible that only larger catalyst particles are actively growing CNTs. In the more dense catalyst samples there may be increased clumping and Ostwald ripening leading to a larger number of large particles. This
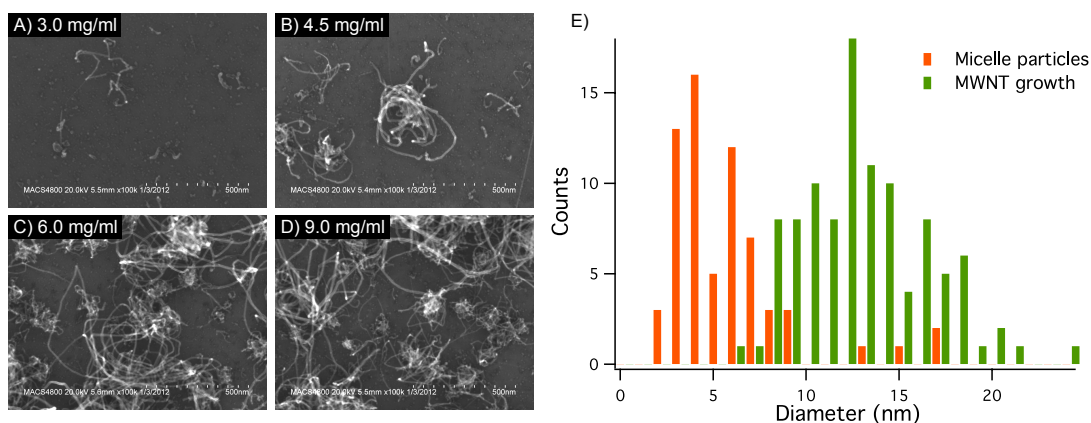
Figure 5.4: Summary of CNT growth from micelle template synthesized Fe nanoparticle arrays. (A-D) show SEM micrographs of the growth for various micelle solution concentrations all spun cast at 1600rpm. (E) plots two histograms of Fe particle and MWNT diameters from the same sample.

could help explain the increased growth in these more catalyst dense samples. Similar results have been found by Bennett and others who find that there is a catalyst particle "size window" in which the catalyst activity is highest [81]. Future work should use PAA chain length to control the catalyst diameter and observe its affect on catalytic activity. Regardless of the particle densities investigated here, none produced vertically aligned MWNT forests. As a result no thermal interface tests were performed.
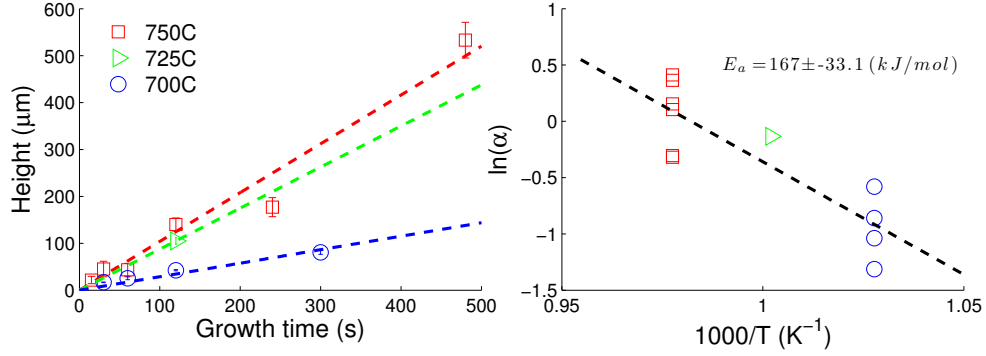
Figure 5.5: Pair of plots showing the growth rates for MWNTs grown on Si. The left plot shows array height versus growth time for three different growth temperatures while the right subfigure is an Arrhenius plot with the natural log of growth rate versus inverse temperature. The slope of this plot normalized by the universal gas constant gives the activation energy E_a to be 166.6±33.1 kJ/mole.

5.3.2 Characterization of MWNT forests from sputter deposited Fe films

Several array characteristics were observed in an attempt to identify the morphologies that correspond best with low thermal interface resistance. CNT height and diameter were observed directly using an SEM. Height was determined by scratching the surface and observing the CNT array at a 45° angle, which can then be used with the measured height to calculate the true normal height. Array density was calculated using mass difference, before and after growth, and using the forest volume, area measured macroscopically using calipers and height from the SEM measurements as

129

discussed above. Since the density calculation relies on array height there is a covariance between these two terms. Future studies should identify an alternate method for density measurements to remove this covariance. Raman analysis was performed using a Renishaw NIR 780TF spectrometer with a 514nm Ar laser. The disorder to graphitic band ratio (D/G) was determined by fitting Lorentzian curves to the raw Raman spectra, computing the ratio of the areas under the D-band at 1350cm^{-1} and G-band at 1582cm^{-1}. Besides the forest area, whose uncertainty was evaluated by the precision of the calipers, the uncertainty of all other quantities were evaluated by performing multiple measurements followed by calculation of their mean and standard deviation.

Figure 5.5 shows two plots related to the growth rates of MWNTs on Silicon. The first plot on the left simply shows the MWNT array height versus growth time for three different growth temperatures. The slopes of the fit lines represent the growth rates found to be 1.04, 0.87, and 0.29 $\mu m/s$ for 750°C, 725°C and 700°C growth temperatures respectively. At some point in the growth time the height is expected to saturate due to catalyst poisoning, although this regime was not explored in this range of experiments. The plot on the right of Figure 5.5 is an Arrhenius plot, showing the natural log of the growth rates versus the inverse temperature. The slope of the resulting line when normalized by the universal gas constant gives the activation energy, $\text{E}_a = 167\pm33$ kJ/mol. Pal et al. found similar activation energies for CVD growth of MWNTs on Inconel substrates and attributed the growth kinetics to be bulk iron diffusion limited [86].

Figure 5.6 shows a pair of plots related to the crystallinity (D/G ratio) and
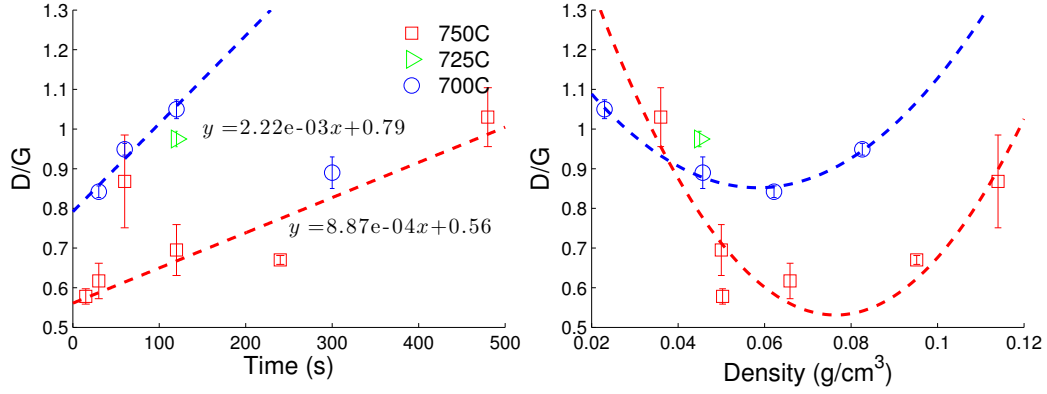
Figure 5.6: Pair of plots showing the Raman D to G ratio versus growth time and array density for the Si CNT growth at different temperatures. The D/G vs. time is fit with straight lines excluding the outlying points. The D/G vs. density is fit using a pair of parabolas.

array density. The left plot shows the D/G ratio as a function of growth time for the different growth temperatures. Besides an outlier in each data set, the D/G dependence on time is relatively linear. Intuitively, one might expect an increase in disordered carbon as more amorphous carbon is deposited with time. It also follows intuition that the lower temperature growth would be consistently more disordered, larger y-intercept, but it also appears to have a steeper slope. It may be possible that disordered sites along the CNT act as nucleation points for amorphous carbon deposition. Since a linear relationship between height and growth time was already established for this data set, one can conclude without plotting that the D/G is also linearly increasing with array height, although this may be a less insightful interpretation of the physical mechanisms behind the data.

The right plot in Figure 5.6 shows the D/G ratio plotted with respect to the array density. The data is fit with second order polynomials, although there is no clear physical rational for this dependence. Both growth temperatures show a similar parabolic tendency with a minima in disorder between 0.059 and 0.076 g/cm^3. The array density was also evaluated with respect to growth time and array height but didn't show any obvious trends.

5.3.3   Thermal contact resistance of MWNTs from sputtered Fe films

To avoid increasing measurement error by the need to subtract a reference measurement, all samples measured in this study were double-sided (i.e. CNTs grown on both sides of the silicon substrate). This approach does have the potential to increase error in other ways, the most obvious of which is the potential dis-congruity between growth on each side. However, error due to differences in array morphologies on the two opposing sides of a substrate are assumed to be small compared to that of using another TIM in the material stack. Additionally, since the substrate is rigid and relatively thick (0.5mm), substrate conformation will have little or no contribution to the contact resistance.

5.3.3.1   Statistical variation study

Initial tests were fairly rudimentary, with little characterization of the CNT films besides their thermal resistance. In addition to the 10nm of Al the samples in this data set also had a 10nm layer of Mo beneath the Al, thought to increase the

CNT adhesion, although there is no evidence to support this. The set of samples were prepared and measured as similarly to one another as possible. The samples had 10nm Mo, 10nm Al, 2.5nm Fe sputtered on each side of double sided polished 0.5mm thick Si. MWNT growth was carried out in a quartz tube furnace such that the sample was suspended on its edges and both surfaces were equally exposed to the gas and heat. The furnace was purged with Argon for 15 minutes with a flow of 530 sccm followed by purging of the Hydrogen line for 5 minutes at 270 sccm. The furnace temperature was ramped from room temperature to the final growth temperature in 17 minutes with H2 flowing at 135 sccm. Growth was initiated at the final temperature by flowing 135 sccm H2 as a carrier gas and 380 sccm Ethylene (C_2H_4) as its feedstock. The duration of growth was 10 minutes for all samples, followed by a 5 minute post growth anneal and purge in Ar at 530 sccm. The furnace was then let to cool to room temperature with Ar flowing until the furnace was sufficiently cool, 300°C. The samples were all tested using the 1D reference bar method presented in Section 4.2.4, although only three thermocouples were used for these measurements and no guard heater was present. The results of this study are presented in the Table 5.1, all resistances represent the full material stack.

While the sample preparation and measurement procedure were held nearly constant there was clearly much variation in their results. The thermal contact resistance mean and standard deviation between these eight samples was $260 \pm 59 \text{ mm}^2\text{K/W}$. This is roughly 10 times higher than what was expected from reports in the literature for similar materials and test methods [87, 24]. This prompted the obvious line of questions

Table 5.1: CNT-Si-CNT TIM statistical variation study. All data collected under high vacuum, with 0.947MPa contact pressure, under steady state conditions.

Sample	Average Temp (K)	Calculated Heat (W)	Conductance (W/K)	Resistance (mm^2K/W)
02-24-11A	294.29	4.69	0.573	282
02-24-11B	296.27	4.79	0.676	239
02-25-11A	293.64	4.35	0.558	289
02-25-11B	296.13	4.59	0.589	274
03-03-11A	293.05	4.76	0.795	203
03-03-11B	294.38	4.56	0.570	283
03-04-11A	295.25	4.46	0.456	354
03-04-11B	293.44	5.22	1.010	160

pertaining to the source of this discrepancy.

The samples did undergo a large degradation upon removal from the test apparatus. Large sections of the CNT forest became delaminated when removed from the copper blocks. This poor adhesion to the substrate may have been one such source for their order of magnitude increase in resistance over those reported in the literature. However, it is not clear whether the delamination occurred before or after the thermal measurement. Given the well documented bulk thermal conductivity of Si, the resistance contributed from the bulk substrate should only be 3.36 mm^2K/W. Unfortunately without any further information about the array morphology or more sophisticated thermal

measurements, one can only speculate where the dominant source of resistance originates. This prompted a more sophisticated approach to sample metrology prior to thermal characterization. A more rigorous characterization of sample morphologies is presented in the section below.

In addition to the need for increased array characterization, there was also some concern about the measurement accuracy of the 1D reference bar method. It was unclear whether the poor results were a consequence of the samples or the measurement technique. As a result, three aspects of the TIM testing was changed. To increase the accuracy of the measurement, a fourth thermocouple was placed in each reference bar. This, along with some other electrical noise corrections, reduced the uncertainty of the temperature measurements to $\pm0.2K$ and increased the accuracy of the temperature gradient. To reduce the potential for systematic error, a new set of heaters was made, including one experimental heater and one guard heater, both with built-in thermocouples. This allowed the zeroing of the ΔT across the ball bearing, ensuring that all heat from the experimental heater flows through the sample. The third modification was to change the method of data analysis. Rather than fitting both the thermal gradient in the copper bars and the ΔT across the sample (two covarying terms) the gradient was calculated from the (now corrected) heat flux and the line was best fit to the data using only ΔT across the sample and the y-intercept as a fit parameters.

While the samples from the previous 'statistical variation study' could not be re-measured following these corrections to the reference bar method, the parasitic heat loss in the previous measurements can be accounted for and the results adjusted

135
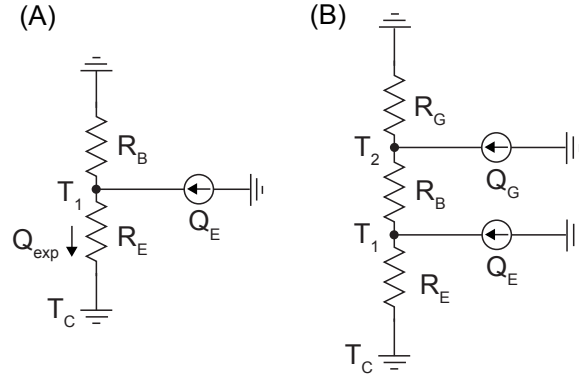
Figure 5.7: Thermal circuit model of 1D reference bar apparatus before (A) and after (B) the addition of a guard heater.

accordingly. To calculate the parasitic heat loss prior to the addition of the guard heater one can model the experimental apparatus before and after the addition of the guard heater as a thermal circuit, as illustrated in Figure 5.7. This along with a two measurements with the two new heaters, one can establish the lost heat without the guard heater.

The first measurement requires both the guard heater and experimental heater have power applied and for the temperatures at T_1 and T_2 be equal, such that $\Delta T_{1-2} = 0$. This means no heat flows through R_B, that all of the heat from the experimental heater flows through R_E, likewise all of the heat from the guard heater flows through R_G. From this the values of R_G and R_E are simply the temperature gradient measured across these elements divided by the heat flux through them:

$$R_E = \frac{T_C - T_1}{Q_E} \quad R_G = \frac{T_C - T_2}{Q_G},$$ (5.1)

136

Now the only unknown resistance is R_B, which can be determined by powering either one of the two heaters alone. For example, if power is applied to the guard heater, then the equivelent resistance is $R_{eq} = R_G \parallel (R_B + R_E) = (T_2\text{-}T_C)/Q_G$, allowing R_B to be solved directly knowing Q_G, T_2 and T_C. The resistance of the ball bearing and that of the experimental apparatus can then be substituted into the original apparatus circuit (Fig. 5.7A) to compute the real heat flux experienced by the experimental column, Q_{exp}.

Using this method, adjusted values for the data collected under the 'statistical variation study' was computed with the new fitting routine. The results from these corrected values are presented in table 5.2. As expected, less heat flowed through the sample than originally calculated, making the original values artificially high. While this correction makes the overall performance of these samples even worse, the variance between samples is slightly better. The mean and standard deviation from the corrected values are 340 ± 45 mm^{2}K/W. With this increased confidence in the measurement system, the attention was directed back towards the samples.

5.3.3.2 Morphological study

As the statistical variation study suggests, there is a need to understand what factors influence the thermal performance of these MWNT arrays. Fully understanding the morphological features of the arrays and their functional dependence on contact resistance will help optimize the CNT TIM performance. While a seemingly obvious endeavor, the work presented in the literature towards this effort has only scratched

Table 5.2: CNT-Si-CNT TIM statistical variation study with adjusted values to correct for parasitic heat loss through the top of the reference bar. All data collected under high vacuum, with 0.947MPa contact pressure, under steady state conditions.

Sample	Average Temp (K)	Calculated Heat (W)	Conductance (W/K)	Resistance (mm^2K/W)
02-24-11A	294.29	3.98	0.434	371
02-24-11B	296.27	3.97	0.483	334
02-25-11A	293.64	3.97	0.480	336
02-25-11B	296.13	3.97	0.461	350
03-03-11A	293.05	3.98	0.565	285
03-03-11B	294.38	4.02	0.467	345
03-04-11A	295.25	3.99	0.384	421
03-04-11B	293.44	3.98	0.575	280

the surface. Much of the experimental work presented in the literature deals with single, isolated samples without detailed morphology characterization. Fewer experimental works present some systematic study, although typically concerning either growth conditions or post growth treatment processes [26, 88, 89]. These studies fail to identify the underlying physical mechanisms for their observed trends. A few others have began correlating array morphologies to the resulting thermal contact resistance. Liu et al. performed a density dependent study using the same micelle template catalyst preparation technique presented above. They managing to hold other variables constant,

showing that the contact resistance decreased with decreasing density [72]. Amama et al. performed a CNT diameter dependent study using a dendrimere-assisted catalyst preparation technique. Here they found that the larger diameter CNTs tended to have more defects, as evident from Raman spectroscopy, leading to lower contact resistance. This, along with the conclusions of Amama et al. who related Young's modulus to defect density in CNFs [90], support the theory that the decreased resistance is a result of their forests increased mechanical compliance. This relationship between contact resistance and mechanical compliance can also be supported by Liu's density study. Cola et al. have made the largest strides towards developing a cohesive model relating the deformation mechanics of CNT arrays to their thermal performance [32]. Again in Cola's study, the mechanical compliance is identified as a key factor in the thermal performance. This study surmises that in order to minimize contact resistance, one must minimize array stiffness and maximize its density. However, stiffness increases with density, suggesting that there is some optimized combination of these parameters.

The reason for the limited scope of such studies relating array morphology to thermal resistance is the difficulty in isolating and monitoring a single morphology trait. Even if a process is identified as being able to control a single array variable, all relevant variables must be monitored to ensure there is no unintended variation. This can be time consuming, costly, and difficult. Additionally, the relevant array properties must be identified prior to any destructive measurements. These relevant array morphology traits may include, CNT height, diameter, density, alignment/waviness, crystallinity, surface roughness, modulus, substrate adhesion, and thermal contact resistance. Most

139
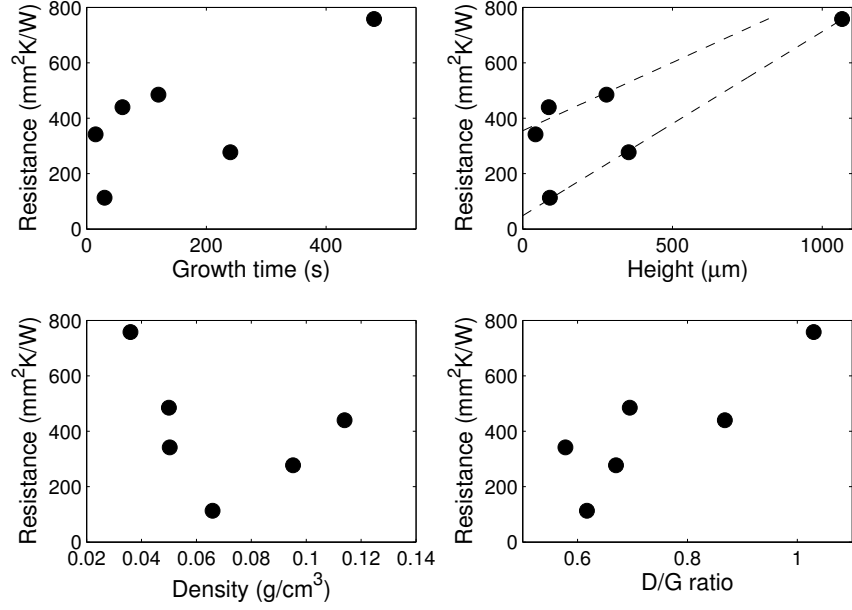
Figure 5.8: Thermal interface performance of double sided CNTs grown on Si versus various array parameters, i.e. growth time, array height, density and crystallinity.

methods for characterizing the last three items on the preceding list are destructive, or at least modify the array from its pristine condition.

For the following morphology study, emphasis was placed on array height, density, crystallinity and thermal resistance, the characterization methods for which are discussed in Section 5.3.2. Figure 5.8 plots these array morphologies as well as the growth time with the corresponding thermal resistance for the samples grown at 750°C. The growth time is suspected to correlate with resistance most by its correlation with array height, although it may also influence other factors such as crystallinity or density. The array height was measured for a single side of the double sided TIM. However, for

this analysis the array height has been doubled to reflect the entire thickness of the CNT forests. The total TIM thickness is roughly double the array height plus the thickness of the Si substrate (0.5mm), which is not reflected in the values presented in the first quadrant of Figure 5.8.

While arguments against the significance of bulk CNT thermal conductivity were just presented, for completeness the height versus interface resistance is analyzed in an attempt to see the impact of κ_{CNT}. Assuming bulk CNT resistance dominated, one would expect the resistance versus hight to follow a straight line with increasing slope, following Fourier's law. While the data doesn't support this simple analysis, one can interpret it as two data sets with different contact resistances (y-intercepts) but with similar bulk thermal resistance (slope). Two lines fitting the data divided in this scheme are presented in the plot. These lines correspond to a contact resistance and slope of 355 mm^{2}K/W and 2.03 W/mK for the top line and 48.2 mm^{2}K/W and 1.51 W/mK for the bottom line. While the bulk conductivities found here appear particularly low at first glance, they are within a commonly reported range. Even more confusing are their results compared to the exceptional bulk conductivity of a single MWNT, in the 2000-3000 W/mK range [91, 92]. However, this can be explained by the low array density which results in a much lower real contact area than the nominal contact area. This concept is discussed in detail in Chapter 8, showing that as little as 0.1% of the area may be in contact. With such a low area, the bulk conductivities found here can easily be justified with respect to those of single MWNTs. Similar analysis can be used to explain the high contact resistances found here, although much lower values have been
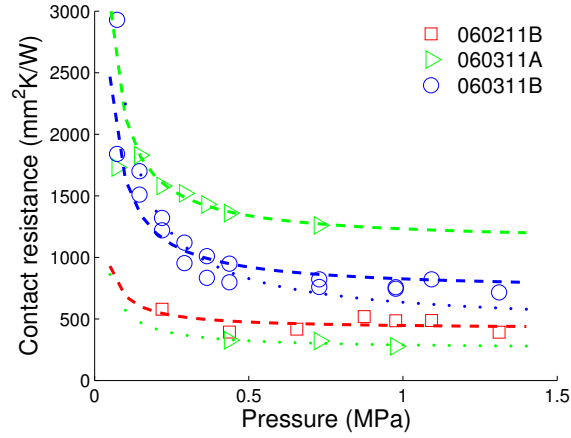
Figure 5.9: Thermal contact resistance as a function of contact pressure for three CNT-Si-CNT samples. Dashed lines show fit to increasing pressure, while dotted lines show fit to decreasing pressure

obtained in the literature for similar arrays. These lower bulk resistances are expected given the larger number of defects compared to single tube measurements, which are performed on relatively short segments.

The resistance plotted against array density in Figure 5.8 shows a 'V' shape. More detailed analysis of this trend, along with a proposed model based on simple Euler buckling is presented in the next Section 5.3.4. The resistance versus D/G ratio shows a vaguely linear relation where $R \propto D/G$. However, this relationship is the reverse to what other's have seen [90].

Pressure dependent measurements were performed on a few select samples, the results of which are plotted in Figure 5.9. All of these pressure dependent data sets are fit with power distributions, $R = aP^{-0.94} + b$, where the coefficients a and b

are fit parameters. The $P^{-0.94}$ dependence is typical of TIMs under elastic deformation [67]. Sample 060211B (red squares) is very linear suggesting that it is already in the 'saturation regime', which is characteristic of CNT TIMs [32], while the other two samples show a clear $\sim 1/P$ relation. Both 060311A (green triangles) and 060311B (blue circles) have data for loading and unloading curves. 060311B (blue circles), shows very similar results for both loading and unloading with a slight drop in resistance during unloading, suggesting some adhesion or plastic deformation. However, sample 060311A (green triangles) underwent a dramatic shift in its resistance at $\sim$0.98 MPa, which was maintained through the unloading cycle. This dramatic shift in resistance is likely due to a sudden increase in contact area. Perhaps there was some debris preventing the sample from establishing its full contact, which was crushed as the pressure was increased. Besides this one anomaly, the pressure dependent resistance behaves consistently with that reported for contacting surfaces. These forests show a saturation in their resistance pressure curve well below the standard measurement pressure chosen here as 0.98MPa. This confirms that the relatively low performance of these samples is not a result of the chosen measurement pressure but rather a fundamental aspect of the array.

5.3.4 Modeling contact resistance

A simple model for describing the contact resistance is developed around Euler buckling of CNTs and the assumption of point (circular disk) contacts. Assuming the CNTs behave as ideal rods, then the number of CNTs in contact with a surface can be predicted by the force or pressure exerted on the forest and hence exerted back from the

143
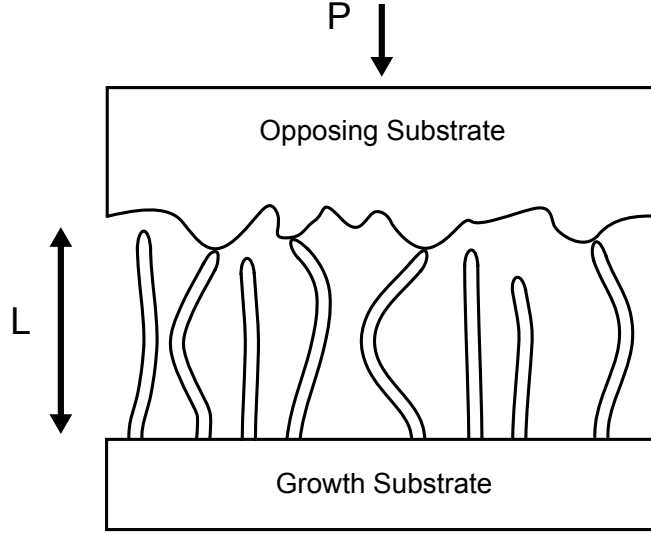
Figure 5.10: Diagram showing Euler buckling of a fraction of individual CNTs within a forest upon compression.

sum of CNTs that have undergone buckling. Figure 5.10 illustrates this idea, showing a few CNTs in contact with the opposing surface, undergoing buckling, while others CNTs are not in contact. Given the number of CNTs in contact, one can establish a simple description of the total joint resistance based on the contact area $(N\pi r^2)$, contact resistance $(R_{cont.})$ and the bulk thermal conductivity (κ):

$$R \approx \frac{1}{N\pi r^2}\left(R_{cont.} + \frac{L}{\kappa}\right), \tag{5.2}$$

Where r is the average radius of a CNT, and N is the number of CNTs in contact, determined by the following set of equations:

$$N = min(N_{tot.}, N_{buckled}) \tag{5.3}$$

$$N_{buckled} \approx \frac{P}{F_{Euler}} = \frac{4PL^2}{E\pi^3 r^4} \tag{5.4}$$

$$N_{tot.} \approx \frac{\rho_{forest}}{\rho_{graphite}\pi r^2} \tag{5.5}$$

Where the condition $N = N_{tot.}$ is supplied in the case that the applied pressure exceeds

the total buckling pressure, suggesting that all CNTs have buckled and that the forest

is undergoing further densification. In this case the total number of CNTs in contact is

calculated by the forest density, ρ_{forest}, in relation to the density of graphite, $\rho_{graphite}$

$= 2.25$g/cm^3, and the cross sectional area of the CNT, πr^2. The preceding equation for

the area of the CNT is assuming a solid core, which may be a suitable approximation

for large outer diameter CNTs with small inner diameters. Unfortunately neither inner

or outer diameter is known for these particular samples, although the outer diameter is

assumed to be close to that of the micelle produced catalyst growth, between 15-30nm.

Since the pressure is large ($\sim$1MPa), all the CNTs should be buckled and the forest

should be 'fully compressed'. This means $N_{buckling} > N_{tot.}$ and the resistance should

follow:

$$R \propto \frac{1}{\rho_{forest}} \quad \text{or} \quad R \propto \frac{L}{\rho_{forest}}, \tag{5.6}$$

depending on the magnitude of L/κ with respect to $R_{cont.}$. This is assuming $R_{cont.}$ and
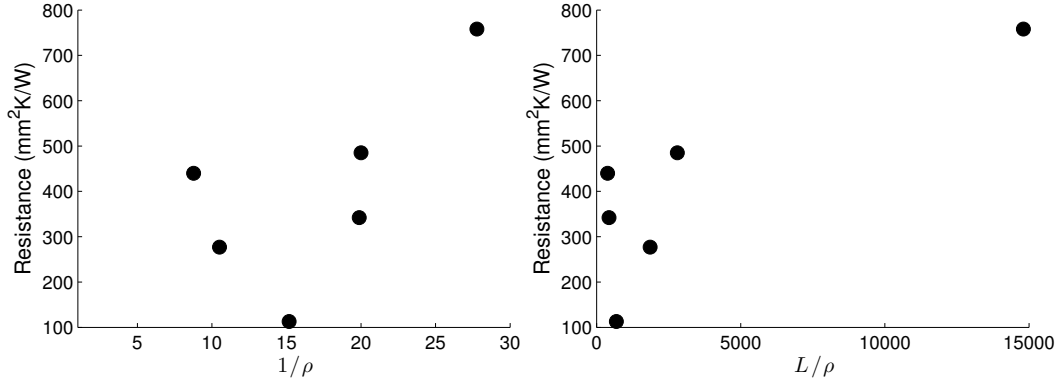
Figure 5.11: Plots of thermal resistance versus $1/\rho$ and versus L/ρ.

κ are constant between samples. To evaluate the likelihood that either variant of this model is accurate, two plots have been generated reflecting the relationships of Equation 5.6. These two plots are displayed in FIgure 5.11, unfortunately neither of which present a trend that would support the model.

Since the data doesn't follow the simple case, where the area scales as the density, an alternate interpretation was investigated, one in which the area scales as the compressibility of the forest. As a simple approximation for the compressibility of the forest, the Euler buckling force was multiplied by the total number of tubes:

$$P_{critical} = N_{tot.} \times F_{Euler} = \frac{E\pi^2}{4\rho_{graphite}} \cdot \rho_{forest} \left(\frac{r}{L}\right)^2 \tag{5.7}$$

For a constant radius this critical buckling pressure scales as $P_{critical} \propto \rho/L^2$. For the limited set of samples measured, $P_{critical}$ varies by roughly three orders of magnitude $(3.1 \times 10^{-5} - 2.6 \times 10^{-2}$ MPa). While the pressures of $P_{critical}$ are much less than the

146
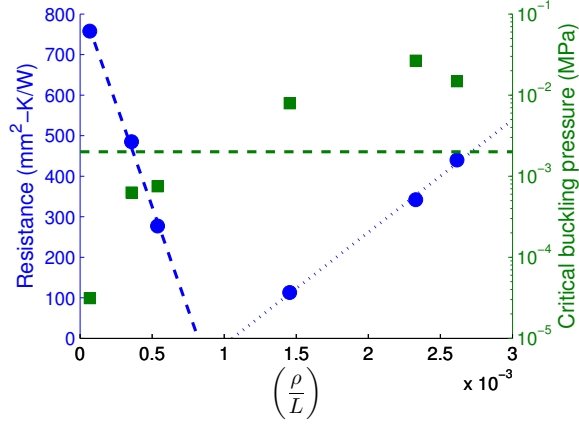
Figure 5.12: Plots of thermal resistance (blue circles) and critical buckling pressure (green squares) versus ρ/L. The dashed blue line shows resistance decreasing with ρ/L, while the dotted blue line shows resistance increasing with ρ/L. The dashed green line roughly signifies value of buckling pressure required for the transition.

applied pressure during measurement, it may still be used as an estimate of the stiffness of the sample. This critical buckling pressure was found to delineate between samples of increasing resistance with ρ/L and samples of decreasing resistance with ρ/L at a buckling pressure around 2e-3MPa. Figure 5.12 illustrates this relationship showing both resistance and the critical buckling pressure plotted with respect to ρ/L. While the decreasing resistance with respect to ρ/L can be easily rationalized and is explained by the model presented above (Eqn. 5.2), the trend with the increasing resistance is less obvious. The regime with increasing resistance with ρ/L can be rationalized by asserting that the contact area is determined by the material stiffness. If the resistance is determined by the real area of contact A_r, such that:

$$R = \frac{L}{\kappa A_r}, \tag{5.8}$$

and the real area of contact can be evaluated in terms of the contact dynamics:

$$A_r = A_{max} \left(\frac{d}{d_{max}} \right)^2, \tag{5.9}$$

Where d is the compression of the material, d_{max} is the compression at which full contact is established, and A_{max} is the maximum real contact area. The square in the ratio of compressions comes from the assumption that the contacts can be described as conical protrusions into a plane. The area of the cone then scales as πhs where h is the cone height and s is the length of the side, both of which scale linearly with the height, or protrusion depth, resulting in $\pi d^2 \frac{tan(\theta)}{cos(\theta)}$. The maximum real contact area can be calculated via the array porosity multiplied by the nominal contact area A:

$$A_{max} = A \frac{\rho_{forest}}{\rho_{CNT}} \tag{5.10}$$

Where ρ_{CNT} is that of an individual CNT, which can be approximated as that of graphite, $\rho_{graphite}$, as in equation 5.5. Assuming the compression is elastic and that the pressure is distributed across the entire film, one can calculate the displacement from the compressive modulus and the applied pressure since $E \equiv \Delta P/(\Delta L/L)$, it follows that for $d = \Delta L$:

$$\frac{d}{L} = E \frac{F}{A_{max}} = \frac{EPA}{A_{max}}, \tag{5.11}$$

by substituting the equation for A_{max} (Eqn. 5.10) into Equation 5.11, solving for the displacement, d, and substituting this result and Eqn. 5.10 into that for the real contact area A_r, (Eqn. 5.9)

$$A_r = A \left(\frac{LEP}{d_{max}} \right)^2 \left(\frac{\rho_{CNT}}{\rho_{forest}} \right) \tag{5.12}$$

This result can then be used with the original equation for the resistance (Eqn. 5.8) to arrive at:

$$R = \left(\frac{d_{max}}{EP} \right)^2 \frac{1}{\kappa A \rho_{CNT}} \frac{\rho_{forest}}{L}, \tag{5.13}$$

which has a ρ/L dependence. The original argument still holds for the cases with low buckling pressure, where the sample is expected to be fully compressed and $d \geq d_{max}$, suggesting that $A_r = A_{max}$. This means that Equation 5.12 simplifies to that of Eqn. 5.9 and the resistance becomes:

$$R = \frac{\rho_{CNT}}{A\kappa} \frac{L}{\rho_{forest}} \tag{5.14}$$

However, Equation 5.13 does not explain the nonzero intercept observed in the data of Figure 5.12. While this model can for the most part explain the behavior observed in this data, it must be interpreted with some degree of caution due to its application to a limited range of data. Ideally future studies would include the use of transient thermal characterization techniques such as the one discussed in Chapter 7, to distinguish the various contributions of resistance, along with more sophisticated

mechanical characterization tools such as that described in Chapter 8 to directly measure the real contact area.

5.4 Conclusion

This chapter discusses the MWNT growth on silicon substrates for thermal interface assemblies. Initial thermal characterization of poor morphologically characterized samples revealed a significant discrepancy between the literature results and those reported here. This prompted a detailed investigation into the 1D reference bar thermal measurement, resulting in several improvements to the overall accuracy and precision. The discrepancy also motivated a higher level of scrutiny of the CNT samples. In an attempt to control only MWNT density, a micelle template technique for accurately controlling the catalyst was pursued. While this catalyst preparation technique showed some promise, the resulting MWNTs were of too low density to form vertically aligned arrays. As a consequence, no thermal characterization was performed on these samples. In lieu of the micelle controlled density study, a number of array properties were characterized as a function of growth time and temperature for MWNTs grown from sputter deposited catalyst. These studies found dramatic changes in not only height but array density and crystallinity. While not showing a clear Fourier dependence on array hight, a more complex thermal model was developed to explain the measured resistance as a function of array height and density. Based on Euler buckling, the thermal model finds that below a critical buckling pressure, the thermal resistance decreases with ρ/L, while

above this threshold the resistance decreases with L/ρ. Several caveats along with the

limited data set, necessitates the further study to validate or reject this model.

Chapter 6

Self catalyzing Fecralloy foils for CNT TIMs

6.1 Introduction

While most of the work towards CNT TIMs have been performed on Silicon growth substrates, it is unlikely that a final product would use such a substrate. In addition to being rigid and brittle, silicon may not be the ideal substrate due to reasons of growth optimization or manufacturability. A few groups have begun expanding away from the Si substrates for CNT TIMs, although this work has been mostly limited to Al and Cu due to their higher bulk conductivity and malleability [89, 31, 30]. However, in most cases the contribution from the bulk thermal conductivity pales in comparison to that of the CNT contacts, making nearly any metal suitable for such a task. In terms of a manufacturing standpoint, selecting a metal that already contains the catalyst and the

ability to withstand the conditions for CNT growth may be much more favorable over the slight increase in thermal conductivity. Pal et al. have used a catalyst containing alloy (Inconel 600) to grow CNTs and study their thermal performance, although they also introduce additional catalyst via the CVD system [93]. It's unclear from their study how much of the growth is a result of the alloy and how much is from the aerosol catalyst. Using an additional Indium thermal interface material, Pal et al. were able to establish a linear relation between thermal resistance and array height, allowing them to extract bulk thermal conductivity of the forest to be 0.8W/mK and the zero-thickness interface resistance, comprising the sum of the CNT-Inconel and Indium-CNT resistances, to be 150 mm^2K/W. While these values are similar to early Si based CNT growth substrate TIMs with low clamping pressure [94], they are far from the values obtained from more recent studies [32]. While these results are not particularly impressive, as a first pass in the alloyed growth substrates, they are within a range that warrants further attention.

The increased CNT adhesion to such catalyst containing alloys, as reported by Talapatra et al. [95], is a strong motivation for their use in CNT TIMs. This growth substrate adhesion is suspected to reduce the resistance at the substrate-CNT root interface and will improve the longevity and re-use of such TIMs. CNT growth on other alloys, not yet used for TIMs, have reported similar increase in adhesion over that of Si. Stainless steel and other Ni,Fe,Cr alloys have been successfully demonstrated to grow CNTs with minimal surface pretreatment and without applying additional catalyst or buffer layers [96, 97, 98]. These advantages, along with the successful growth of CNTs on Fecralloy within our lab, motivated their study for thermal interface management.

153

Fecralloy ® (72.8% Fe / 22% Cr / 5% Al / 0.1% Y / 0.1% Z) is used, without additional catalyst or buffer layers and with minimal surface preparation, as a growth substrate for CNT TIMs. Very similar to stainless steel, this alloy is ubiquitous, cheap, ductile, machinable and mechanically stable. This study investigates the effects of growth parameters and substrate preconditioning on array morphologies. These array morphologies are then used to help identify factors that influence the thermal resistance of the CNT-metal-CNT TIM. A variety of thermal models are applied to the data in an attempt to correlate array morphology to thermal resistance. However, only simple empirical relations can be identified. The best performing Fecralloy based samples show nearly a factor of two decrease in thermal resistance over the best performing Si based samples studied in Chapter 5.

6.2 Experimental procedures

6.2.1 Sample preparation

Fecralloy foil, $50\mu m$ thick, was purchased from Goodfellow Corporation and cut into 18mm x 18mm squares. These were specifically chosen to be larger than the cross section of the 1D reference bar (12.7mm x 12.7mm) used in thermal measurements. These samples were polished by hand with emery paper containing successively finer grit. Following the polish, samples were cleaned using an ultrasonic bath and deionized water for two minutes. The samples were dried in a furnace at 50°C for five minutes prior to loading into the CVD chamber. Sample flatness was maintained throughout

the preparation process – any samples kinked or bent during polishing were discarded. All CNT growth was performed using atmospheric pressure thermal CVD, as described in Section 2.3.

MWNT growth was carried out in a quartz tube furnace such that the sample was suspended on its edges and both surfaces were equally exposed to the gas and heat. The furnace was purged with Argon for 15 minutes with a flow of 530 sccm followed by purging of the Hydrogen line for 5 minutes at 270 sccm. The furnace temperature was ramped from room temperature to the final growth temperature in approximately 17 minutes with H2 flowing at 135 sccm. Growth was initiated at the final temperature by flowing 135 sccm H2 as a carrier gas and 380 sccm Ethylene (C_2H_4) as its feedstock. The duration of growth varied between samples and was followed by a 5 minute post growth anneal and purge in Ar at 530 sccm. The furnace was then let to cool to room temperature with Ar flowing until the furnace was sufficiently cool to prevent CNTs from burning due to the presence of any oxygen, 300°C.

6.2.2   Characterization techniques

As discussed in Chapter 5, there are a number of array morphologies characteristics that may influence the samples thermal performance. Similarly to those studied in the case of the Si growth substrates, array height, density, crystallinity and CNT diameter were characterized in addition to the thermal resistance. These characterization techniques are the same as those described in Chapter 5, except for the addition of the CNT diameter distribution. One hundred individual CNTs diameters
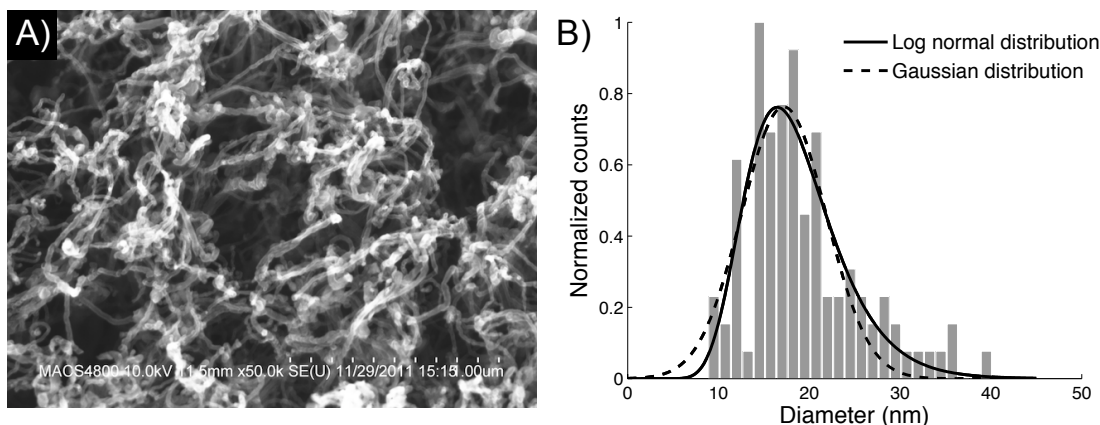
Figure 6.1: CNT diameter characterization via (A) high magnification SEM image of CNT tips and (B) histogram showing diameter distribution fit with log normal and Guassian distributions. .

were counted per sample using high magnification SEM images of the top of the forest. An example high resolution SEM image and the associated histogram of its diameters is presented in Figure 6.1. In addition to these standard set of characterization measurements performed on all samples, a few samples received additional characterization. The substrate surface roughness of a few samples was measured using an atomic force microscope. Attempts were made to characterize the surface roughness of the CNT tips, although only incomplete images were formed, likely due to the high compliance of the material.

6.3 Results

6.3.1 MWNT properties as a function of sample preparation and growth conditions

To understand the growth behavior of MWNTs on Fecralloy, a number of experiments were performed. In particular the implications of growth time, growth temperature and surface roughness were studied with respect to the array morphologies. This data is compared against a baseline dataset where all controllable variables are maintained, exposing the statistical variation between samples.

Statistical variation study

To better understand the variation in growth, eleven samples were prepared on Fecralloy using the same sample preparation and growth procedure. The resulting array morphologies were measured and are plotted in Figure 6.2. The sample variation is greater than the measurement error in all morphology traits except that of diameter. The mean and standard deviation are plotted as solid and dashed lines respectively. The mean and standard deviation of height, density, diameter and D/G ratio are 13.5 $\pm$ 4.9μm, 0.129 $\pm$ 0.038 g/cm^3, 16.9 $\pm$ 1.4nm, and 0.95 $\pm$ 0.053 respectively. These values provide a reference for comparing the results from other processing variations.

Growth time dependence

The duration of growth has one particularly obvious implication on the array. That is, that the array height is closely tied to the growth time, often linearly dependent up to
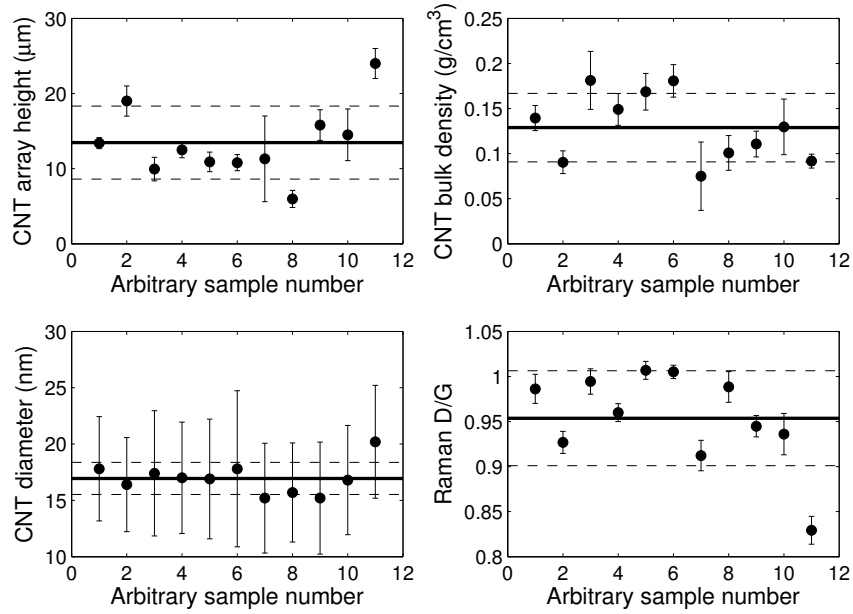
Figure 6.2: Four plots show the statistical variations of array height, density, Raman D/G ratio and CNT diameter for eleven samples with the same growth conditions, 700°C and 8000grit polish.

some saturation point. Given the height's importance in thermal interface performance, both in terms of the bulk resistivity and the mechanical compliance, it is important to know the growth rate. Besides the array height, there are other less obvious implications that growth duration has on the array morphologies. Figure 6.3 plots array height, bulk density, CNT diameter and Raman D/G ratios as a function of growth time for a number of Fecralloy samples grown at 700°C. The array heights were only measured for a single side of the double sided sample. The full sample thickness is roughly double the reported array height plus the $50 \mu m$ thick Fecralloy foil. The growth rate on Fecralloy

was notably (15x) slower than that on Si for the same growth temperature. It is fairly linear over the range of growth times measured, while the last point in the plot does have a reduced height, this is insufficient to claim the onset of saturation. A surprising outcome is that the density, diameter and D/G ratio all increase linearly with growth time. The most prominent of which is the D/G ratio, changing by over 60% over the range of experiments compared to the average measurement error of 1.8%. The three of these combined suggest a buildup of amorphous carbon along the walls of the CNTs as the growth time increases. This would cause all three array variables to increase over time. This amorphous carbon is likely to decrease the bulk thermal conductance due to increased scattering and phonon coupling to the less conductive amorphous carbon, although it may also decrease the resistance at the contact due to the increased contact area and reduced modulus. A more detailed study into the effect of amorphous carbon would be required to fully understand its implications.

Growth temperature dependence

The growth temperature has significant influence over a number of factors that can affect array morphology. This variable was initially investigated due to the proposed increase in crystallinity at higher growth temperatures. More crystalline MWNTs were thought to increase the bulk thermal conductivity of the forest, leading to better thermal performance. In addition to affecting the CNT crystallinity, the growth temperature may also influence a number of other factors including, the catalyst size distribution, the rate limiting step in the growth kinetics, the degree of amorphous carbon deposited,

159
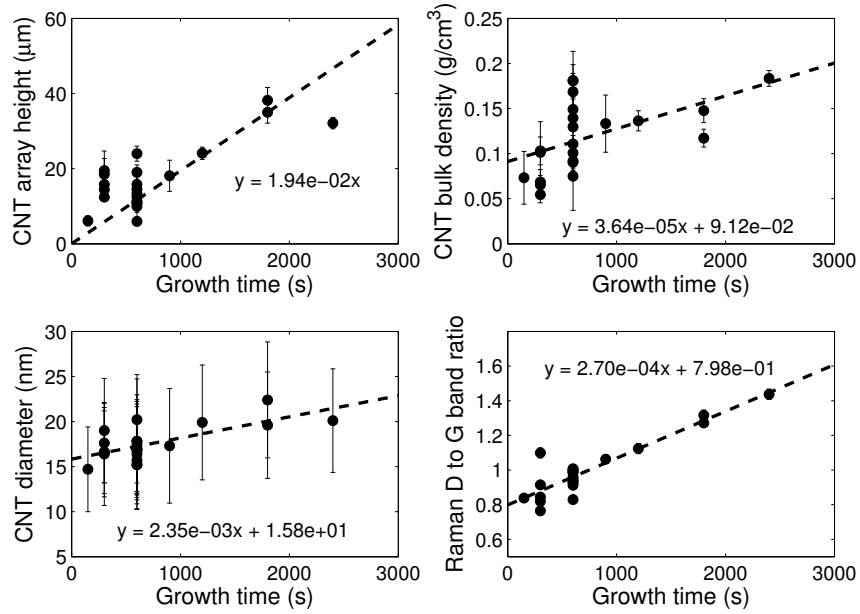
Figure 6.3: Four plots of array height, bulk density, diameter and Raman D/G ratios as a function of growth time for a number MWNT samples grown on Fecralloy at 700°C with 8000 grit polish. Array height is plotted for only one side of the double sided sample, full sample thickness is two times this plus $50\mu m$ for the foil substrate.

and may even change the phase of the precipitating carbon, transitioning from MWNTs to CNFs. Each of these could affect a number of array morphologies simultaneously. Further analysis of the samples such as Thermalgravimetric Analysis (TGA) and Transmission Electron Microscopy (TEM) should be able to identify these affects. However, in the current study these additional affects are not observed.

Figure 6.4 shows two plots relating growth temperature and time to array height. The left plot shows array height versus growth time for growth at 700C with
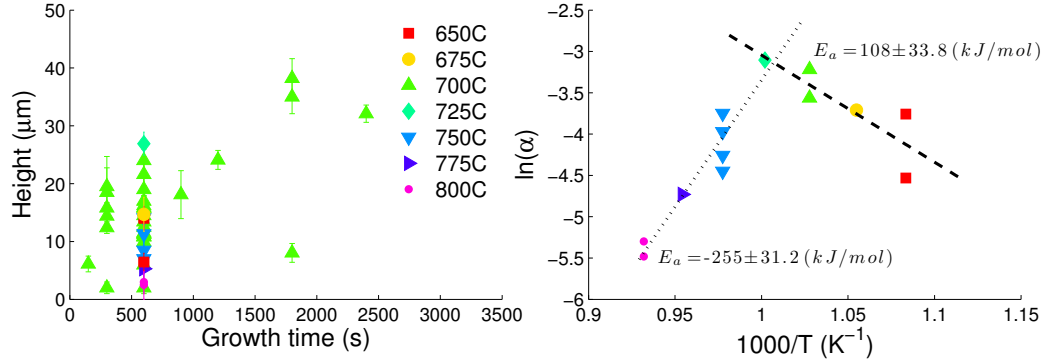
Figure 6.4: Pair of plots showing the growth rates for MWNTs grown on Fecralloy. The left plot shows array height versus growth time for growth at 700C with additional point measurements for different growth temperatures. The right subfigure is an Arrhenius plot with the natural log of growth rate versus inverse temperature. The slope of this plot normalized by the universal gas constant gives the activation energy E_a. Only a subset of the 700C samples were used in the Arrhenius plot due to variations in growth conditions over the course of the research. This plot shows two distinct regimes, of increasing and decreasing growth rate.

additional point measurements for different growth temperatures. On the right is an Arrhenius plot showing only a subset of the data from the left. The number of 700°C samples was reduced to only those measured specifically for the growth temperature study. The Arrhenius plot shows an initial increase in growth rate with temperature from 650°C to 725°C followed by a pronounced decrease in growth rate from 750-800°C. Since many of these growth rates were determined from single, 10min, growth periods, it is not possible to determine whether the growth rate is linear (steady state) during

161
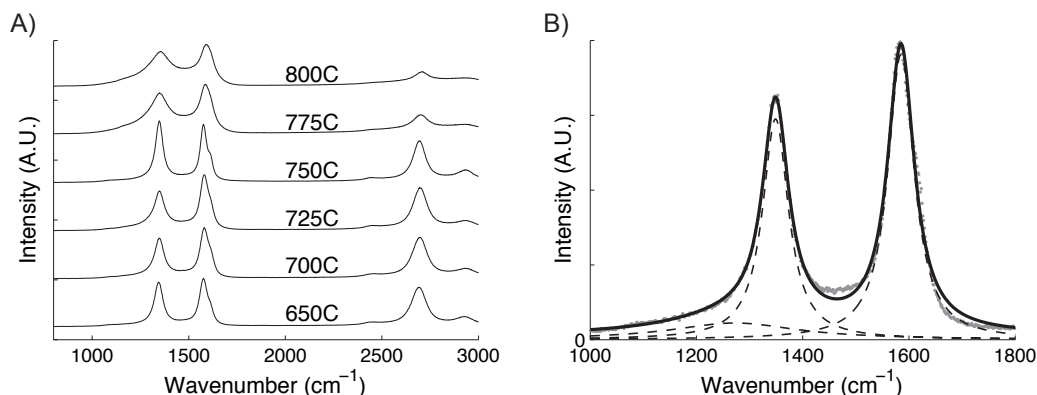
Figure 6.5: Raman spectra (A) from samples with different growth temperatures and (B) showing the Lorentzian curve fitting of the D and G peaks in a single spectra.

these regimes or whether they are in a transient, incubation or poisoning regime. While the exact cause for this diminished growth rate has not been determined, there are two hypotheses.

An energy like 255 kJ/mol is similar in magnitude to a chemical reaction, it is close to the C-C bond energy. To show negative energy suggests there is a parasitic reaction that is depleting carbon supply without growing CNTs. Amorphous carbon deposition, if it is the parasitic process, would likely also increase density without increasing height as observed in Figure 6.6. The other possibility is that the catalyst is pooling to larger diameter and lower density at higher temperature. Figure 6.6 seems to show this. This would increase the diameter and density, as observed. For constant mass deposition, greater density/diameter would result in decreased growth rate.

Figure 6.5 and quadrant four of Figure 6.6 summarize the Raman analysis

162

performed on the samples for the Fecralloy growth temperature study. Figure 6.5(A) plots several spectra gathered for a range of growth temperatures, all prepared with 1200 grit final polish. These spectra show the clear evolution of the D, G, and G' peaks at $\sim$1350, $\sim$1580, and $\sim$2700 cm^{-1} respectively. Figure 6.5(B) shows the Lorentzian curve fitting for a single spectra. For these samples a third peak has been added near 1270cm^{-1} to account for the shoulder in the D peak. The ratio of the area under the D and G band peaks for various spectra are plotted versus growth temperature in quadrant four of Figure 6.6. This shows a clear minima in disorder near 700°C with the D/G assuming a parabolic relationship with growth temperature.

This parabolic relationship can be understood by thinking about the reactions on either side of the minima. At temperatures below the minima, the increase in temperature will provide more ordered CNTs as the C bonding reactions go towards completion. However, at temperatures above the minima, both amorphous carbon deposition from parasitic reactions and an increased tube diameter, possibly favoring CNFs over CNTs, leads to a higher disorder. This rational is supported by the other observed quantities, i.e. diameter and density, which both follow the same basic trend. As the plots suggests this minima may be shifted slightly for higher polished substrates. However, the two surface preparations studied follow very similar trends.

Substrate surface roughness

Initially surface roughness was investigated because of the proposed decrease in contact resistance with decrease in roughness, the roughness of the array was thought to mimic
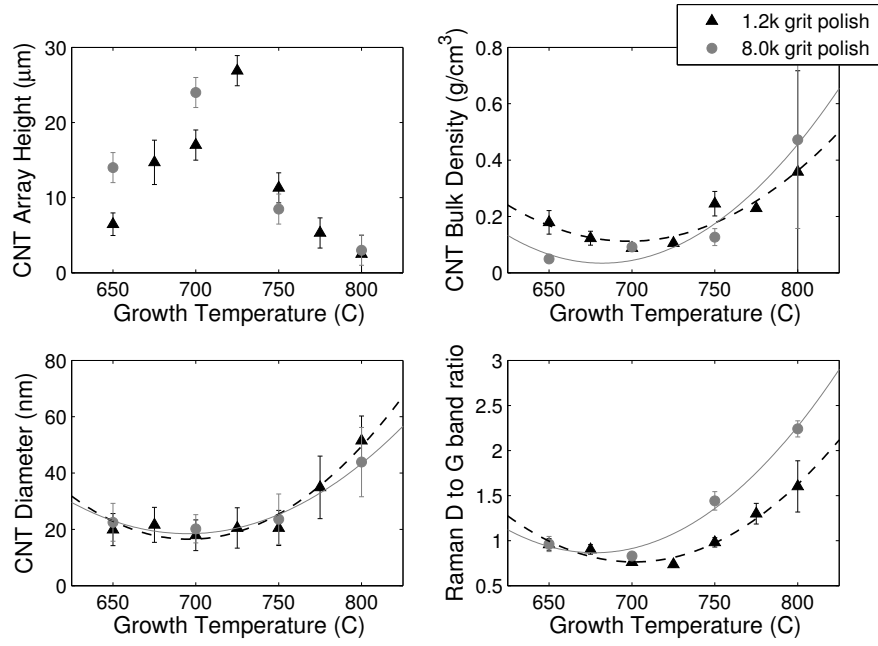
Figure 6.6: Influence of growth temperature on array morphology.

that of the substrate. However, after initial tests there didn't appear to be a strong
correlation. These tests were continued to higher surface roughness due to the claims
of Oye et. al. about decreasing array density with increasing roughness for CNT
growth on bulk Fecralloy [99]. Figure 6.7 shows four plots of root mean squared (RMS)
surface roughness versus CNT height, density, diameter and Raman D/G for five samples
prepared with 400, 600, 1200, 4000 and 8000 grit polishing. All of these samples were
grown at 700 C for 10 minutes using the standard growth recipe described in section
6.2.1. From the data in Figure 6.7 it is clear that in this case, substrate roughness
does not play a strong role in the final CNT morphology as claimed by Oye et. al. It
is likely that in the previous study there were large regions of the naturally forming

164
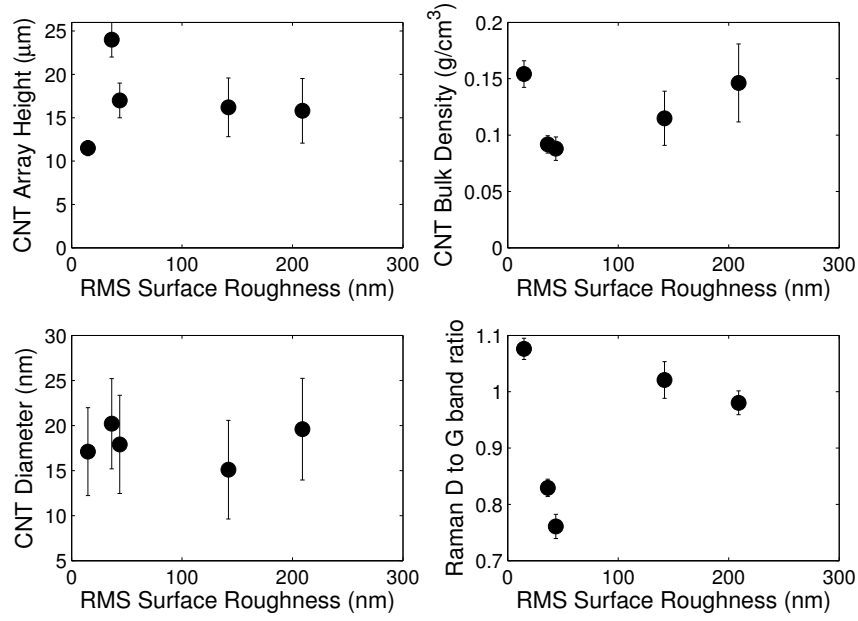
Figure 6.7: Influence of substrate surface roughness on array morphologies.

chromium oxide, Cr_2O_3, which were preventing CNT growth. The higher polishing of the substrate may have helped remove this layer, exposing fresh iron oxide to serve as a catalyst. While Masarapu et al. used a floating catalyst technique, they found growth sensitivity to similar substrate pretreatments. They found that the growth on 304 stainless steel was highly sensitive to pre-growth substrate etching, which they attributed to the removal of Cr_2O_3 and exposure of Fe_2O_3 observed by way of X-ray photoelectron spectroscopy (XPS) [100]. The observed lack of sensitivity to surface preparation in this study may be indicative of the complete removal of Cr_2O_3 for all polishing routines. It is likely that the variations seen here are within the statistical variations of the growth process.

165

6.3.2 Thermal interface resistance of MWNTs from Fecralloy foils

The thermal contact resistance of a number of double-sided Fecralloy grown samples were characterized via the 1D reference bar technique described in Chapter 4.2. A limited number of samples were measured as a function of additional variables such as contact pressure, interface temperature and substrate surface roughness. However, the bulk of the samples were analyzed using a fixed contact pressure of $\sim$0.97MPa and were performed at room temperature. All measurements were conducted under high (1×10^{-4} - 1×10^{-5}) torr vacuum. The aforementioned morphology traits are analyzed in conjunction with the thermal resistance data to identify array characteristics that lead to reduced resistance. The major trends are identified and their empirical relationships are presented.

Contact pressure

The pressure dependence on contact resistance for three Fecralloy samples is shown in Figure 6.8. Oddly the behavior of two of the three samples vastly contradicts the general trend for elastically deforming surfaces in contact [67] and that specifically found for CNT arrays [32], which generally follow an inverse pressure relationship. The contact resistance of CNT samples is generally found to decrease substantially with increasing pressure for a range of low pressures, 100-300kPa, then reach a saturation level for higher pressures, >300kPa. The first two datasets in Figure 6.8, ('071111a' and '071311a') show a contradictory increasing resistance with pressure. The last dataset in the figure ('092411a') is more congruent with the reported behavior in the literature and
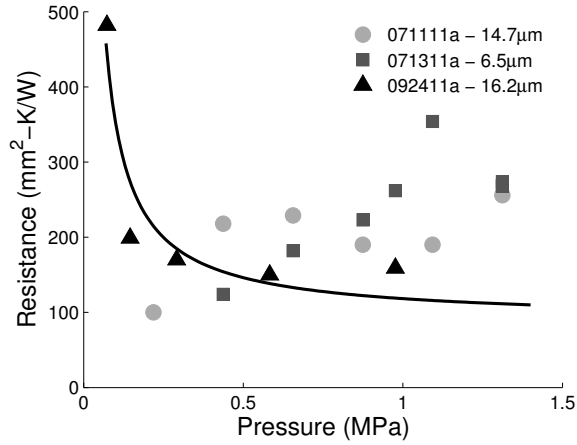
Figure 6.8: Plot of thermal contact resistance versus applied pressure for three Fecralloy grown CNT samples. The solid line fits the triangular data set for the '092411a' sample using a simple power relation, $R(P) = a \times P^{-0.94} + b$. the heights of the samples are close in value and are listed in the legend.

is fit with a simple power relation, $R(P) = a \times P^{-0.94} + b$. The saturation point of this last dataset occurs at a fairly low pressure - the nook in the curve is around 0.27MPa. It is possible that the range of pressure measurements in the other two datasets are insufficiently low to capture this trend and that the increase in resistance at much larger pressures is caused by a different mechanism. Perhaps higher pressures are disrupting the TIM, either through de-lamination of some CNTs or increased scattering from deforming CNTs. Ultimately this can not be ascertained without a more sophisticated thermal measurement technique, one capable of identifying the contributions from each interface. This concept along with more pressure dependent measurements are presented in Chapter 7.

Temperature-dependent contact resistance

While there are a number of applications that require room temperature thermal interface solutions, there are other more specialized applications that require good thermal interfaces at very low or high temperature. Both of these extremes are of interest to the aerospace community. TIMs are particularly interesting for cryogenic applications in which thermal resistance becomes an increasing hurdle. However, traditional TIMs become less ductile and more brittle at low temperature, making them ineffective conveyers of heat. Due to the CNTs high elasticity, the arrays ability to conform to nano-scale surfaces, and its high oxidation temperature, CNT TIMs may be applicable to both very cold and very hot heat transfer applications.

While there have been a number of research groups publishing experimental investigations into the thermal properties of isolated SWNTs, MWNTs, and CNFs [101, 91, 92, 102], the work on arrays has been less exhaustive. A few research groups have investigated some of the thermal properties of CNT forests at temperatures other than those in ambient conditions. Abot et al. measured the thermal conductivity of exceptionally long, millimeter scale, forests above room temperature, from 297-363°K [103]. Xie et al. measured the thermal diffusivity of MWNT forests and used this to calculate the thermal conductivity, for a range of temperatures above and below room temp., 218-473°K [104]. Hu et al. measured contact resistance, effective heat capacity and effective thermal conductivity of a MWNT array using a transient 3ω technique over a narrow range, near room temperature, 295-325°K [105]. However, none of the preceding studies focuses on the dominant source of resistance, $R_{contact}$,
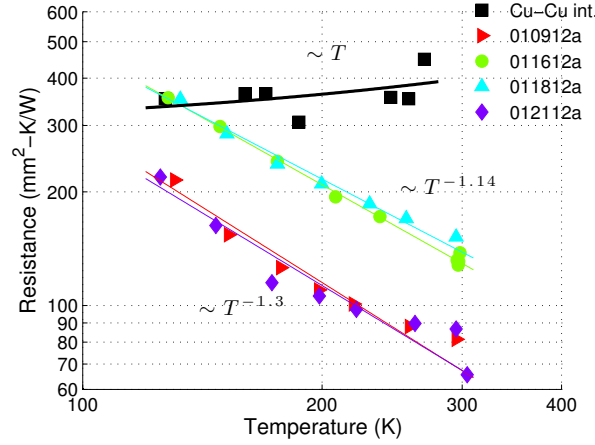
Figure 6.9: Plot of thermal contact resistance versus interface temperature for a number of Fecralloy samples and for bare Cu-Cu interface.

over a sufficiently vast range of temperatures. Panzer et al. began to approach this issue with their investigation into metallized SWNT forests. However, the metalization greatly reduces the contribution from the free end contacts resulting in the dominant source of resistance in their system to be that between the SWNTs and substrate [79]. Despite this, they measured the resistance at the metal-SWNT contact, the effective heat capacity, and the sum of resistances due to the bulk SWNT forest and the SWNT-substrate contact. Their measurements were performed over a range of 125-300°K, allowing them to investigate the phonon conduction physics of both the bulk material and the contact.

Information about the phonon transmittance at the interface can be captured by the temperature-dependent measurements. Figure 6.9 plots the temperature-dependence contact resistance for four Fecralloy-MWNT samples, and a bare Cu-Cu

169

reference over the range 150-300°K. bare Cu-Cu interface measured by Yu et al. at 3.82MPa showed a nearly linear decreasing relation with temperature [76] with values between 400-1100 mm^{2}K/W at 100K and 200-400 mm^{2}K/W at 300K. The relation found here for Cu-Cu interface is the inverse of that found by Yu et al. The square black data points in Figure 6.9 show the bare Cu-Cu contact resistance, which was found to increase slightly with temperature, where the black line fits the data with R(T) = 0.36T+291. In contrast all of the MWNT samples exhibit a resistance that is an inverse power relation with temperature. Assuming these measurements are dominated by the free end to opposing substrate contact resistance, then the temperature dependence of this contact agrees fairly well with that found by Panzer et al. for metal-SWNT interface resistance, $R_{met-SWNT} \sim T^{1.08}$. Panzer attributed this relationship to inelastic scattering at the metal-SWNT interface. Similar interfacial phonon conduction may be occurring here for the case of a free CNT tip to opposing substrate.

Substrate and mating contact surface roughness

Surface roughness has been identified as being a critical parameter in the resistance of metal contacts.

Madhusudana draws from the work of Mikic and Roca, to show the dependence of real contact area on surface roughness for elastically deforming materials. They found that for Gaussian distributed heights of spherically shaped asperities, the real to nominal contact area was inversely proportional to the mean absolute slope of the surface profile [67]. Implying that surface roughness is a significant factor in overall

contact conductance. Because of this, the surface roughness of both the Cu reference bars and that of the Fecralloy substrate were investigated in this brief study.

Table 6.1: Cu block surface roughness dependence on thermal contact resistance of single Fecralloy sample.

Surface prep. (grit size)	Equivalent polishing particle size (μm)	measurement order	Resistance ($\text{mm}^2\text{K/W}$)
600	15	1st	189
1200	9	2nd	118
8000	1	3rd	111

To evaluate the effect of surface roughness of the Cu reference bar blocks, the blocks were prepared with a number of different polishes and compared using a single sample. This was by no means a rigorous test, as the surface roughness was not measured post polishing and the sample performance is expected to degrade with successive measurements. In spite of this degradation in performance with successive measurements, a single sample was used because of the wide variability between samples. Only a single surface roughness measurement was performed using an AFM on a similarly prepared OHFC substrate using the 8000 grit - its RMS surface roughness was found to be 83.6 and 19.6nm in two different regions. Due to these two inconsistencies, this experiment is of a qualitative nature, although it is indicative of a clear dependence on measurement bar roughness. Table 6.1 summarizes the tests in which the Cu blocks were prepared with 600, 1200, and 8000 grit polish and used to measure the thermal

resistance of a MWNT-Fecralloy-MWNT sample. The MWNTs remained intact and attached to the substrate throughout the three measurements, although there was clear deformation of the forest after the compression of the initial measurement. The performance increase with decreasing surface roughness is significant from measurement 1 to 2, yet more modest from measurements 2 to 3. However, the fact that performance increases at all, in spite of the successive measurements, which likely degrades the sample, is indicative that the CNT TIMs perform better with smoother surfaces. This observation is supported by recent measurements by Chu et al. who found that the contact resistance for In bonded CNT tips to Cu drops from 7.1 to 0.5 mm^2K/W as the Cu RMS surface roughness decreased from 192nm to 5nm [106]. Due to this finding, all resulting measurements were performed with the Cu reference blocks polished using the 8000 grit polishing paper.

In a similar vein, the surface roughness of the Fecralloy substrate is expected to influence the roughness of the CNT forest canopy. With greater roughness leading to greater contact resistance. This along with its potential influence on array morphology as discussed above (Sec. 6.3.1) lead to this brief study. The results of which are summarized in Table 6.2.

Surprisingly there is not a strong correlation between substrate surface smoothness and contact resistance, unless the 4000 grit sample is removed. If this outlier is ignored than there is a clear ~2x increase in performance when transitioning from 600 to 1200 grit. Attempts were made to characterize the surface roughness of the CNT canopy using an AFM, although this proved challenging due to the soft, compliant na-

172

Table 6.2: Fecralloy growth substrate surface roughness dependence on thermal contact resistance in MWNT-Fecralloy-MWNT samples.

Surface prep. (grit size)	Equivalent polishing particle size (μm)	RMS surface roughness (nm)	Resistance (mm^{2}K/W)
400	30	142	159
600	15	209	140
1200	9	43.6	64.2
4000	3	14.8	296
8000	1	36.3	68.2

ture of the CNT tips. 8000 grit polish was chosen for all subsequent samples due to the perceived increase in consistency from using a higher polish.

Exploratory data analysis - array morphologies and thermal resistance

Due to the large variance in array morphology, rather than attempt to control a single array variable and study its isolated impact on resistance, a more simplistic statistical approach was taken. A large number of samples were made without a strong attempt to steer their morphologies and their properties were characterized, resulting in a multivariate dataset, from which exploratory data analysis can be performed. Figure 6.10 displays the five variable dataset in the form of a matrix of plots, showing the covariance of each pair of variables. There are five choose two, or ten, sets of covariance, which can

be displayed using only the strictly upper or strictly lower triangular matrix, making the data symmetric about the diagonal. The diagonal plots the univariate histograms, providing insight into each variable's distribution. The distribution of the MWNT diameter for example is very narrow, showing that there was little variation in this array morphology over the course of the experiments. As a result, it is unlikely that there will be much dependence upon this variable. This is indeed the case, when looking down column four (the diameter column) or across row four (the diameter row) the data is vertical and horizontal respectively, showing little or no dependence on diameter. This is not to say that the MWNT diameter doesn't influence these other array characteristics, only that the experiment space did not reveal these dependencies.

The other four array characteristics are a little less straight forward. The samples contain a reasonable distribution of values as depicted by the histograms along the diagonal. However, there is still only weak correlation between variable pairs. The pairs density-height, resistance-height, and D/G-density, visually have the strongest correlation after ignoring outliers. Density-height and resistance-height, both have either a negative power relationship or possibly a truncated quadratic. The D/G-density shows a positive linear relationship, although it is less strongly correlated after the removal of the two most outlying points. This D/G-density is contrary to the clearly quadratic relationship seen for the Silicon samples in Figure 5.6, although the range of densities is higher than those studied in the Si case, possibly spanning only the increasing half of the curve.

Because of the limited trends found in this analysis, other approaches involving

174
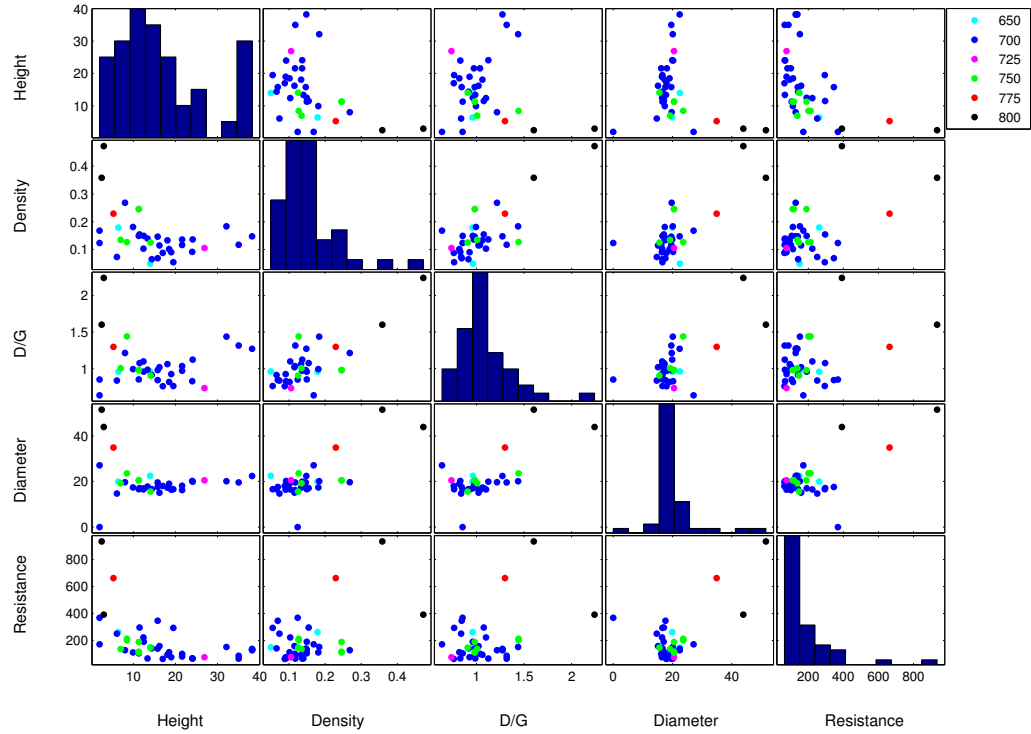
Figure 6.10: Fecralloy property matrix, plotting each measured array morphology against one-another. The different colors correspond to the growth temperatures in celsius as depicted in the legend. All thermal measurements were performed in vacuum, at room temperature and with an applied pressure of ∼0.97MPa.

the analysis of subsets of the data were also pursued. Figure 6.10 displays the growth temperature of the sample using the data marker color as depicted by the legend. Another example used the date of the sample growth as a metric to see if there were significant trends over the course of the study. However, these approaches provided little insight. The strongest functional dependence of contact resistance lay in the array

height.

Height dependence

Based on the previous exploratory data analysis, the array height was found to have the strongest impact on the contact resistance. Its relationship followed a negative dependence, found to match closest to a negative power law, $\sim H^{-0.5}$. This is unusual because it doesn't appear to follow Fourier's law, which was vaguely demonstrated with the MWNT growth on Silicon. While Fourier's law has been shown to be broken for very short SWNTs operating under a ballistic phonon conduction regime [107], this is not likely the case here due to the large array heights. Rather, this discrepancy is suspected to be a result of the array's mechanical behavior, in which the stiffness increases with decreasing array height. However, this does not follow standard Euler buckling, which scales as $\sim H^{-2}$. Figure 6.11 plots the height dependence for both the Fecralloy substrate and Silicon substrate growth, showing an apparent minima in resistance near 10-50μm. On the left hand side the Fecralloy follows the $\sim H^{-0.5}$ dependence, while on the right side the Silicon follows a linearly increasing $\sim H$ dependence. Attempts were made to have an increasing overlap between the two substrate types, although due to the vastly differing growth rates this was not sufficiently achieved. Attempts to model this behavior are discussed in the following section, although the character of this data is best described by this empirical relation.

176
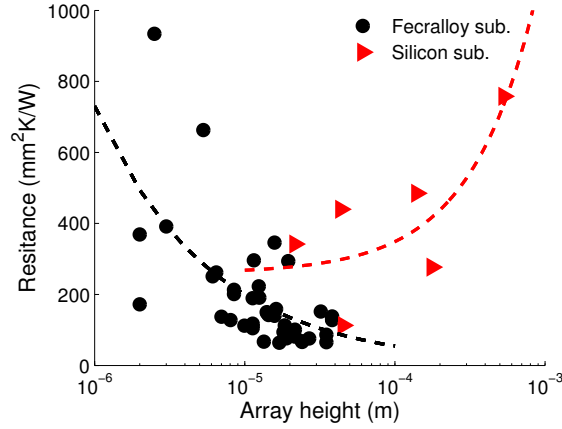
Figure 6.11: Plot of the influence of height on contact resistance for both Fecralloy substrate (black) and Silicon substrate (red) growth. The Fecralloy follows a $\sim H^{-0.56}$, while the Silicon follows a $\sim H$ dependence.

6.3.3 Modeling contact resistance

This section summarizes several attempts at modeling the contact resistance of the Fecralloy MWNT TIMs with respect to their array morphologies. The models used are the Euler buckling model described in Chapter 5, a height independent model based on Tong's MWNT compression studies, and Cola's model based on wool deformation theory. Unfortunately none of these models were found to adequately match the data.

Euler buckling model

As described previously in Chapter 5, the Euler buckling model is based off of the assumption that the MWNTs behave as ideal rods. As with the Silicon case, since the resistance was measured at high pressure ($\sim$1MPa), all of the CNTs should be buckled

177

and the forest should be 'fully compressed'. Under this model, this would suggest that $N_{buckkling} > N_{tot.}$ and the resistance should simplify to:

$$R \propto \frac{1}{\rho_{forest}} \quad or \quad R \propto \frac{L}{\rho_{forest}} \tag{6.1}$$
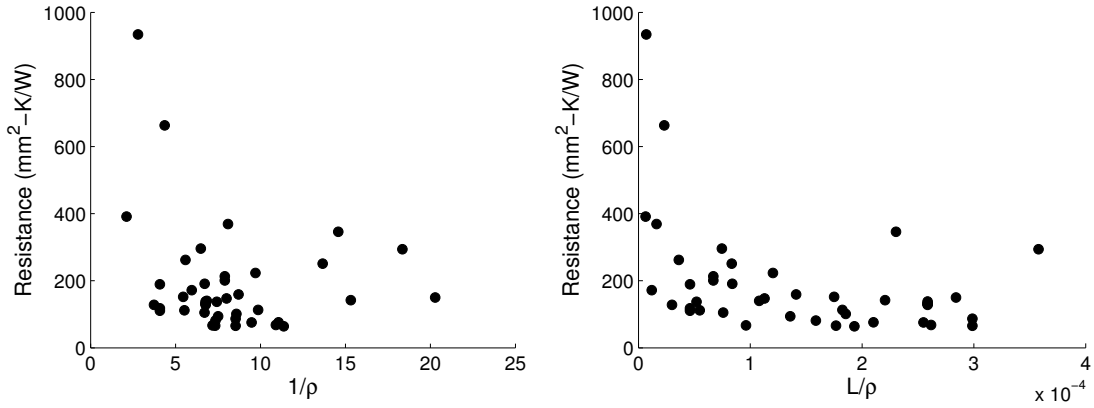
Figure 6.12: Euler buckling model assuming total buckling of forest, leading to $R \propto \rho^{-1}$ or $R \propto L\rho^{-1}$.

Figure 6.12 shows two plots assuming these relationships. However, the plots clearly don't show a linear relationship, suggesting the model is inadequate. This discrepancy was also observed in the Silicon data, which was re-interpreted by assuming the resistance scales with the real contact area, determined by the compressibility of the forest. As before, the compression can be related to the critical buckling pressure as defined as the total number of CNTs multiplied by the Euler buckling force of a single tube (Eqn. 5.7). Figure 6.13 illustrates this dependence, showing both the data from the Silicon substrate samples in Chapter 5 and the data from the Fecralloy samples. Unlike the

case of Silicon, there isn't a clear two regime distinction, only a roughly $R \propto (\rho/L)^{0.47}$ as shown by the blue dashed line in the figure. This agrees with the critical buckling pressure for all Fecralloy samples being above the transition point found for the Silicon samples (red dashed line). The origin of this $R \propto (\rho/L)^{0.47}$ relationship is unknown, although it could be explained using the model presented in Chapter 5. If the contact area scaled as the square root of the protrusion depth opposed to the protrusion depth squared, as was the case assuming conical protrusions in Chapter 5. However, such a geometry has not been found.
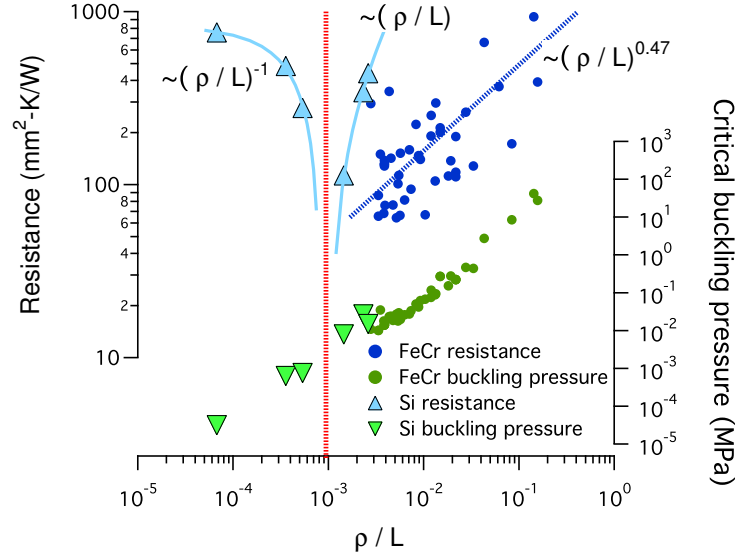
Figure 6.13: Thermal resistance (blue) and critical buckling pressure (green) data for both the Si samples presented in Chapter 5 and the Fecralloy samples plotted versus ρ/L. The blue dashed line is fit to the resistance data and follows a roughly $\sim (\rho/L)^{0.47}$ relationship.

Compression dependent contact

The idea of using the forest's resistance to compression as a means of evaluating its contact stimulated the investigation into other research into CNT mechanical studies. Tong et al. saw a height independent compressive modulus that they attributed to the forests waviness.

$$E_{comp} = \frac{2\pi^2 EI}{A_{CNT}\lambda^2} \approx \frac{\pi^2 Er^2}{2\lambda^2} = \frac{\pi^2 E}{2\rho_{graphite}} \cdot \frac{r^2 \rho_{forest}}{\lambda^2} \tag{6.2}$$

They found that in all of their cases the wavelength was nearly $12\mu m$, which they calculated. Unfortunately the compressive modulus nor the wavelength of the forests is known for the current study, although if the wavelength didn't change much between samples then one would expect to see a $R \propto r^2\rho$, where r is the CNT radius. Since radius doesn't change much between these samples this would scale simply with density. However, this is clearly not the case as seen in Figure 6.10.

This approach may not be adequate because Tong used only small stresses, in the KPa range, due to limitations in their loading device. Cao et al. and Maschmann et al. have performed CNT compression studies with large stresses applied and found the forest behaving as open-cell foams with three distinct regions of compression; Hookian at low stress strain with high modulus before any folding of the forest, plateau at medium stress strain with significant decrease in modulus - corresponding to the buckling of the open cell struts or folding in the case of CNT forests, and finally a densification region where the stiffness increases exponentially. Maschmann saw a height dependence (taller forests have increased yield stress but decreased onset of densification), which

he attributed to a change in relative density. However, this was not substantiated by density measurements, only an open-cell relation of density to strut thickness and length. The shortest array measured ($35\mu m$) didn't show a strong distinction between the first two regimes and did not appear to fold or accordion like the taller forests. This stress/strain behavior is similar to what Cola used in his model, discussed below.

Cola's wool deformation model

Cola et al. derived a model from the extension of wool fiber deformation where the thickness $t \propto P^{-1/3}$, where P is the pressure [32]. This is consistent with load displacement data in their analysis for short arrays. However, this is in contrast to the compression studies of Cao et al. and Maschmann et al. suggesting that Cola's model may only be valid for a limited array length or other array criteria.

Cola uses a slightly modified thickness-pressure relationship from the wool theory. Taking into account the 'incompressible thickness' of the forest and modifying the pressure to account for the volume fraction of CNTs and the contact width,

$$t = t' + (t_0 - t') \cdot \left(\frac{P_f}{\sigma_R} + 1\right)^{-1/3} \tag{6.3}$$

where $\sigma_R = c_1 \cdot E_b \cdot \phi^3$ is the compressibility of the forest. c_1 is a unitless fit parameter that takes on many of the array properties such as quality, alignment, etc. E_b is the average bending modulus of a single CNT assumed to be 100GPa and ϕ is the CNT volume ratio. The modified pressure to account for smaller than unity volume ratio and radial stiffness of the CNTs is:

$$P_f = \frac{P}{\phi \cdot \frac{a_x}{b_{cnt}}} \tag{6.4}$$

If $P_f \gg \sigma_R$ or $P \gg \sigma_R \cdot \phi \cdot \frac{\bar{a}_x}{b_{cnt}}$ then the forest is near its incompressible thickness t'.

Cola goes on to relate the real to apparent contact area ratio to the applied pressure and Bulk modulus by:

$$\frac{A_{r \cdot freeends}}{A} = \frac{2P}{B} \tag{6.5}$$

Using the definition of bulk modulus $B = -t \cdot (dP/dt)$, equation 6.3 and 6.5, Cola defines the contact area as a function of applied pressure:

$$\frac{A_{r \cdot freeends}}{A}(P) = \frac{2}{3} \cdot \phi \cdot \frac{\bar{a}_x}{b_{cnt}} \cdot \frac{P}{P + \sigma_R \cdot \phi \cdot \frac{\bar{a}_x}{b_{cnt}}} \cdot \left[\frac{t_0 - t'}{(\sqrt[3]{2} - 1) \cdot t' + t_0} \right] \tag{6.6}$$

The last term in this expression is shown to take on values between 0.5 and 1, suggesting that the contact area is mainly governed by the parameters ϕ and σ_R,

$$\frac{A_{r \cdot freeends}}{A} \propto \frac{1}{1 + \sigma_R \cdot \phi \cdot \frac{\bar{a}_x}{b_{cnt}} \cdot P^{-1}} = \frac{1}{1 + c_1 \cdot E_b \cdot \phi^4 \cdot \frac{\bar{a}_x}{b_{cnt}} \cdot P^{-1}} \tag{6.7}$$

Again, this suggests that contact area is not expected to increase if $P \gg \sigma_R \cdot \phi \cdot \frac{\bar{a}_x}{b_{cnt}}$.

Cola later rules out the growth substrate constriction resistance, the diffusive bulk resistance of the array, the CNT-opposing substrate ballistic resistance and its constriction

182

resistance, showing that their cumulative sum is still at least an order of magnitude lower than the measured values based on the nominal area predictions. He opts to describe the contacting surface as imperfect and ascribes a van der Waals resistance $R''_{vdW-CNT-OS}$ where,

$$R''_{GS-CNT-OS} \approx \frac{R''_{vdW-CNT-OS} \cdot A}{A_{r \cdot freeends}} \tag{6.8}$$

This seems reasonable especially given the good fit this model has to his data and the agreement between fit values of $R''_{vdW-CNT-OS}$ and those found through molecular dynamic simulations and more recent modified diffusive missmatch models [108]. The are however, other potential concerns related to the relatively high values of ϕ, the volume ratio, which are on average $\sim 5x$ larger than that measured for the Fecralloy samples here, and the assumption of the deformation behavior, which as previously mentioned is inconsistent with other studies. Regardless of these concerns, a simple analysis is pursued.

Since many of these array parameters are know for the Fecralloy samples, attempts were made to fit the data to Cola's model. Even though pressure data is only known for a couple of samples, one can assume the pressure at which the samples were measured is higher than the critical contact pressure that will be define as $P_{critical} = \sigma_R \cdot \phi \cdot \frac{\bar{a}_x}{b_{cnt}}$. This is supported by the previous pressure versus resistance plot, producing a $P_{critical} = 0.27$MPa, near the visually apparent nook in the curve. Suggesting that for the data measured here, a simplified model based on the asymptotic behavior of Cola's model can be used:

$$R''_{GS-CNT-OS} \propto \frac{3R''_{vdW-CNT-OS}}{2 \cdot \phi \cdot \frac{\bar{a}_x}{b_{cnt}} \cdot \left[\frac{t_0 - t'}{(\sqrt[3]{2}-1) \cdot t' + t_0} \right]} \qquad (6.9)$$

Unfortunately the 'incompressible thickness' of these samples is unknown so the last term in the denominator can not be used (of little consequence since it can only change by a factor of 2). $\frac{\bar{a}_x}{b_{cnt}}$ is defined in Chapter 8. ϕ is directly proportional to the bulk density ρ_{forest} by $\phi = \rho_{forest}/\rho_{graphite}$. The results of plotting resistance with respect to $(\phi \cdot \frac{\bar{a}_x}{b_{cnt}})^{-1}$ is shown in figure 6.14. Unfortunately, once again, this doesn't appear to give much insight into the physical rational for the change in resistance. However, again since the MWNT diameter isn't significantly changing this means that $\frac{\bar{a}_x}{b_{cnt}}$ is relatively constant and the functional dependence reduces to ϕ^{-1}, which is synonymous with ρ^{-1}.
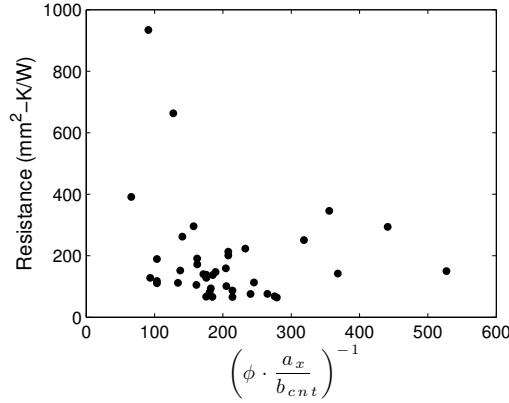
Figure 6.14: Contact resistance vs. $(\phi \cdot \frac{\bar{a}_x}{b_{cnt}})^{-1}$, attempting to fit the asymptotic behavior of Cola's model to the fecralloy data, this is pretty similar to the $1/\rho$ data plotted earlier, probably because there's not much change in the diameter and hence the value for $\frac{\bar{a}_x}{b_{cnt}}$.

6.4 Conclusion

Self catalyzing Fecralloy substrates are investigated as a growth substrate for MWNT TIMs. Fecralloy is used without any additional catalyst and with minimal surface preparation to grow double-sided MWNT TIM assemblies. The growth behavior is studied by way of the array morphologies, i.e. array height, density, crystallinity, and diameter distribution. The effect of growth temperature and time are used to observe the growth kinetics, showing a bimodal growth rate with temperature and an optimal growth rate at 725°C. In addition to array height, the density diameter and Raman D/G ratio are all found to increase linearly with growth time, suggesting a noticeable impact of amorphous carbon. The effect of substrate surface roughness is found to have little influence over the array morphologies as supported by a statistical variation study.

The contact resistance of dozens of such samples are evaluated using a DC, 1D reference bar, thermal conductivity measurement system. A few samples were used for pressure dependent and temperature dependent thermal resistance measurements. The temperature dependent measurements offer insight into the interfacial phonon conduction physics and are found to agree with other temperature dependent studies, suggesting inelastic scattering at the MWNT-Cu interface. Surface roughness of the Cu measurement bars is found to influence the contact resistance, while the substrate surface roughness is found to roughly half the resistance for increasing polish. Due to the challenges associated with deliberately controlling a single array morphology, a multivariate, statistical approach is used to observe the trends of contact resistance. The contact re-

sistance shows the strongest correlation with array height, following a $R \sim L^{-0.5}$, which contradicts Fourier's law. However, this is likely a result of the mechanical compliance rather than a ballistic conduction mechanism. Finally, several attempts were made at modeling the relationship between the measured array morphologies and the contact resistance. However, the modeling is relatively unsuccessful, forcing one to rely on the empirical relations found in the exploratory data analysis.

Chapter 7

3ω transient thermal spectroscopy of CNT TIMs

7.1 Introduction

Transient thermal measurement techniques are appealing due to their relative speed over DC methods, their reduced measurement error and their increased measurable quantities, including heat capacity and heat diffusion allowing depth resolution and characterization of multi-layer materials. However, transient techniques are typically more expensive, difficult to implement, difficult to analyze the resulting data, and may be more localized to a small area of the sample. Despite these tradeoffs, the transient techniques are deeply valuable in understanding the bottlenecks in thermal performance.

The 3ω measurement is a well established transient thermal characterization

technique. It requires little setup compared to other transient techniques such as thermoreflectance, yet can garner similar levels of detail about the sample under investigation. In particular, its ability to measure multi-layer materials and distinguish, interface resistance, bulk resistance, diffusivity and anisotropy for each layer makes this technique appealing for thermal interface measurements.

While the technique has been largely used to characterize uni-directional heat diffusion into a material stack, it has been extended to bi-directional heat diffusion for the characterization of liquid samples [109, 110, 111]. Similar bi-directional heat diffusion is necessary for the measurement of TIMs. Interestingly, however, despite the establishment of this experimental method very few research groups have used this method to characterize thermal interface materials, only one report is known to the authors, that of Hu et al. [105].

The following investigation discusses the physics driving the 3ω technique, details into its experimental implementation and application to thermal interface materials, explanation of the thermal model and data analysis, and the results for CNT TIMs.

7.2 Experimental impedance measurement

The 3ω thermal spectroscopic method relies on a micro-fabricated joule heater to simultaneously serve as both a heat source and temperature probe. The ability to probe the temperature is made possible by the temperature coefficient of resistivity

(TCR) of the joule heater, which when excited with a sinusoidal input current generates a voltage at three times the input frequency that is proportional to the temperature rise of the heater. By sweeping the excitation frequency, a thermal spectroscopic response is obtained of the materials surrounding the heater. This section describes the physical origin of the 3ω voltage, and details of the 3ω voltage measurement including common-mode cancellation of the 1ω voltage.

7.2.1 Origin of the 3ω voltage

The 3ω signal originates from the temperature coefficient of resistivity (TCR) of the heating element. A 1ω electrical current, $\mathbf{I}_{1\omega}$, leads to a 2ω power drop, $\mathbf{P}_{2\omega}$, and hence a 2ω temperature rise of the heater, $\mathbf{T}_{h,2\omega}$. Given the TCR of a joule heater, $\mathbf{T}_{h,2\omega}$ causes a 2ω resistance modulation, $\mathbf{R}_{h,2\omega}$. This 2ω resistance multiplied with the original 1ω current results in a 3ω voltage drop, $\mathbf{V}_{3\omega}$. Using this measurable 3ω voltage, one can calculate the $\mathbf{T}_{h,2\omega}$ temperature rise within the heater. The derivation of $\mathbf{V}_{3\omega}$ and the calculation of $\mathbf{T}_{2\omega}$ is presented in the following text.

Given a simple line heater that is driven with periodic current,

$$I(t) = I_0 \cos(\omega t) \tag{7.1}$$

The power delivered to the heater will be:

189

$$
\begin{aligned}
P(t) &= I(t)^2 \cdot R_h \\
&= (I_0 \cos(\omega t))^2 \cdot R_h \quad\quad\quad\quad\quad\quad\quad (7.2) \\
&= \left(\frac{I_0^2 R_h}{2}\right)_{DC} + \left(\frac{I_0^2 R_h \cos(2\omega t)}{2}\right)_{2\omega}
\end{aligned}
$$

Where R_h is the resistance of the heating element. Equation 7.2 shows that the power contains both a DC and 2ω component. Since the temperature rise in the heater is directly proportional to the heater power ($T_h(t) = Z_t \cdot P(t)$, where Z_t is the thermal impedance around the heater), the temperature rise in the heater also contains both a DC and 2ω component:

$$
T_h(t) = T_{h,DC} + T_{h,2\omega} \cos(2\omega t + \theta) \quad\quad\quad\quad\quad\quad\quad (7.3)
$$

Where T_h is the heater temperature, and θ is a phase shift with respect to the power oscillation. Assuming that the TCR of the heater is linear with T_h i.e. $R_h(T_h) = R_0(T_0)(1 + \alpha \Delta T)$, where R_h is the resistance of the heater and α is the temperature coefficient of resistance ($\alpha = \frac{1}{R_0}\frac{dR}{dT}$), then R_h will also contain both a DC and 2ω component:

$$
\begin{aligned}
R_h(t) &= R_0[1 + \alpha(T_{h,DC} + T_{h,2\omega}\cos(2\omega t + \theta))] \\
&= \left(R_0 + R_0\alpha T_{h,DC}\right)_{DC} + \left(R_0\alpha T_{h,2\omega}\cos(2\omega t + \theta)\right)_{2\omega}
\end{aligned}
\quad\quad (7.4)
$$

Given that voltage drop within a simple resistor follows Ohm's law, this 2ω resistance multiplied by the driving 1ω current will produce a 3ω voltage drop.

$$
\begin{aligned}
V_h(t) &= I(t) \cdot R_h(t) \\
&= I_0 \cos(\omega t)[R_0(1 + \alpha T_{h,DC}) + (R_0 \alpha T_{h,2\omega} \cos(2\omega t + \theta))] \\
&= \left(I_0 R_0 (1 + \alpha T_{h,DC}) \cos(\omega t) \right) + \left(\frac{I_0 R_0 \alpha T_{h,2\omega}}{2} \cos(\omega t + \theta) \right)_{1\omega} \\
&\quad + \left(\frac{I_0 R_0 \alpha T_{h,2\omega}}{2} \cos(3\omega t + \theta) \right)_{3\omega}
\end{aligned}
\tag{7.5}
$$

The first term in Equation 7.5 describes the 1ω voltage drop due to the DC resistance of the heater, while the second and third terms contain information about the 2ω temperature rise. The third term, modulated at 3ω, is detectible using a lock in amplifier. $V_{3\omega}$ is typically $\sim 1/1000\ V_{1\omega}$ due to the relatively small values of α for most metals. As a result, $V_{1\omega}$ needs to be filtered out for adequate detection of $V_{3\omega}$. Two common $V_{1\omega}$ filtering methods are discussed in section 7.2.2. After measuring $V_{3\omega}$, the modulated temperature rise can be computed by rearranging terms in Equation 7.5, resulting in:

$$
T_{2\omega} = \frac{2V_{3\omega}}{\alpha V_{1\omega}} = \frac{2R_0 V_{3\omega}}{V_{1\omega}} \frac{dR}{dT}
\tag{7.6}
$$

This temperature rise alone is often used for fitting a thermal model to the measured data. However, following Olson's lead, this temperature rise can be cast in terms of thermal impedance, offering a more intuitive data interpretation between samples [112]. A thermal corollary of Ohm's law produces the following equation:

$$
\mathbf{T}_h = \mathbf{Q} \cdot \mathbf{Z}
\tag{7.7}
$$

Where $\mathbf{Q}$ is the heat flux from the heater and $\mathbf{Z}$ is the thermal impedance of the

environment surrounding the heater. From this relation and that found in Equation 7.6, a new thermal impedance can be calculated in terms of the experimental conditions:

$$\hat{\mathbf{Z}}_j = \frac{4blR_0^2 V_{3\omega}}{V_{1\omega}^3} \frac{dR}{dT} \tag{7.8}$$

Where b and l are the half-width and length of the heater. The over-caret indicates an experimentally measured value, taken at one of the jth indexed frequencies. An additional correction can be made to this thermal impedance measurement, accounting for the thermal mass of the heater, although its effect is only significant at high frequencies and for thick heaters. Equation 7.8 represents the thermal surface impedance and is compared against a thermal model presented in 7.3 for data analysis.

7.2.2 $V_{1\omega}$ filtering techniques

Due to the comparably weak 3ω signal, typically $\sim V_{1\omega}/1000$, stemming from the small values of α in most metals, the $V_{1\omega}$ signal must be subtracted or filtered prior to $V_{3\omega}$ measurement. There are two common methods for filtering the $V_{1\omega}$ signal, methods referred to in this work as the differential amplifier (DA) technique and the Wheatstone bridge (WB) technique. Each technique has its advantages and disadvantages. Both of these techniques have been explored in this research and their specific implementation, results and tradeoffs will be discussed.

7.2.2.1   Differential amplifier filter

The differential amplifier is the more common $V_{1\omega}$ filtering mechanism. There are likely two reasons for this. First, this was the technique described in the pioneering work done by Cahill and others [113]. Secondly, this technique allows for easy computer controlling of the filter, enabling automatic tuning. This automatic tuning greatly simplifies temperature dependent thermal measurements due to the temperature dependence of the heater resistance. The 3ω method is aptly suited for such temperature dependent thermal measurements due to the inherent need to measure the TCR of the heater. The heater resistance R_h can be automatically measured during each tuning process. As a result, both the TCR and $V_{3\omega}(T)$ can be established in a single temperature sweep. It is advisable to minimize the source voltage when measuring the TCR to reduce the internal heating of the resistor. The notable disadvantages of this technique over that of the Wheatstone bridge are its complexity and potential introduction of signal distortion.

A simple schematic of the differential amplifier filter is presented in Figure 7.1. This circuit consists of passing the 1ω voltage through the heating element in series with a reference resistor (R_1). This will produce a small or negligible $V_{3\omega}$ relative to the heating element. Thus the signal generated from the reference resistor only contains a $V_{1\omega}$ component. The voltage drop across the two resistors can be detected using the instrumentation amplifiers. The output from the reference resistor is fed into a multiplying digital to analog converter (DAC), which is computer controlled, allowing
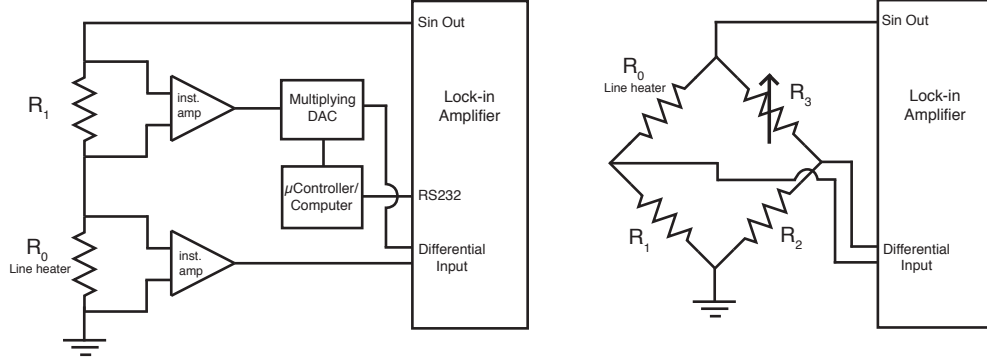
Figure 7.1: Schematics showing the two $V_{1\omega}$ filtering techniques. On the left is the differential amplifier method and on the right is the Wheatstone bridge.

the amplitude of this signal to be tuned to that from the heater signal. These two signals are fed into the differential inputs of a lock in amplifier. The computer can query the 1ω voltage from the lock-in amplifier providing a feedback loop to correct and auto-tune the multiplying DAC, to completely filter out $V_{1\omega}$. A vastly simplified, non-auto-tuning version of this circuit can be implemented, removing the multiplying DAC and computer and replacing the static reference resistor with a potentiometer. In this configuration $V_{1\omega}$ is filtered by manually adjusting the potentiometer.

The implementation of the DA circuit in this study used a precision 250Ω, USR 2-0808 reference resistor, two AD620 instrumentation amplifiers, an AD7541A multiplying DAC, output buffered by an AD744 high speed op-amp. The multiplying DAC was controlled via an ATMEGA128, *Arduino* compatible microcontroller, that used two RS232 serial ports, one to communicate with the SR850 lock-in amplifier and another to interface to a personal computer.

194

7.2.2.2 Wheatstone bridge filter

The Wheatstone bridge technique is relatively simple compared to the DA. It requires only passive elements, reducing build and debug time and decreasing signal distortion. However, the filter has to be manually tuned, making it less practical for temperature dependent measurements. The earliest reference found for using the WB technique for $V_{1\omega}$ filtering was written by Yamane et al. who describe how to convert the output from the balanced bridge, $v_{3\omega}$, to the correct $V_{3\omega}$ dropped across the heater, as [114]:

$$V_{3\omega} = \frac{(R_0 + R_1) \cdot (R_2 + R_3)}{R_1 \cdot (R_2 + R_3)} v_{3\omega} \qquad (7.9)$$

A basic circuit diagram of the WB can be seen in Figure 7.1. The potentiometer, R_3 controls the balancing of the bridge. The values of R_1, R_2 and the range of R_3 should be carefully considered to ensure proper balancing of the bridge and considering the power dissipation in the two halves. The bridge circuit could be converted into an active filter by replacing the manual potentiometer with a digital, computer controlled potentiometer. This would allow auto-tuning of the filter via a feedback loop between the lock-in amp to the computer and digital pot. However, this specific implementation was not investigated. Unless a buffer is applied to the output of the lock-in amp, it is critical to take the output impedance of the lock-in amp into effect when calculating the power and voltage drop in these elements. The results for both of these filters can be found in Section 7.5.1.

7.3 Thermal model and data analysis

7.3.1 Heat diffusion into semi-infinite substrate

Cahill is often credited for first describing the temperature rise within a flat line heater, placed on a simi-infinite substrate, undergoing periodic heating [115, 113]. However, Birge and Nagel performed similar measurements around the same time as Cahill [116, 109]. Birge described the temperature rise in terms of the one-dimensional or planar heat flow, as illustrated on the right side of Figure 7.2. This approximation is appropriate for high frequencies and large heater widths, where the thermal diffusion length, $\lambda \ll b$, the heater half width. The thermal diffusion length is defined as:

$$\lambda = |q|^{-1} = \left| \sqrt{\frac{\kappa}{i2\omega\rho c_p}} \right| = \left| \sqrt{\frac{\alpha}{i2\omega}} \right| \tag{7.10}$$

where q is the complex thermal wave number, κ is the thermal conductivity, ρ is density, c_p is the specific heat capacity, and α is the thermal diffusivity. In this regime, the temperature rise in the heater can be described by:

$$\delta T_h = \frac{P_0/2b}{\kappa q} = \frac{P_0/2b}{\sqrt{2\omega\rho c_p \kappa}} e^{-i\pi/4} = \frac{P_0/2b}{\sqrt{2\rho c_p \kappa}} \cdot \omega^{-1/2} \cdot e^{-i\pi/4} \tag{7.11}$$

Where P_0 is the applied power per unit length and $P_0/2b$ is the power per unit area. In this regime, only the product of thermal conductivity and heat capacity can be measured, although the data can be easily analyzed by measuring the slope of the log-log thermal spectroscopy plot as depicted in Figure 7.2.

Cahill solved the more general solution for the temperature rise in a finite
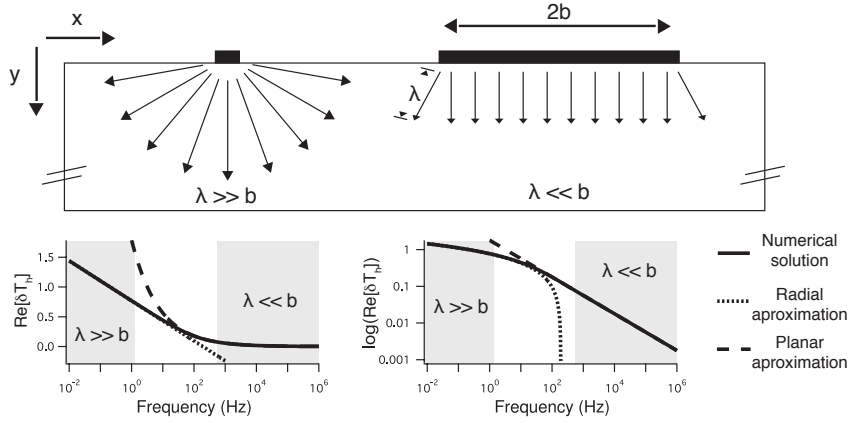
Figure 7.2: Illustration of the thermal penetration depth for two heater regimes, radial heat flow regime, where $\lambda \gg b$ and the planar or 1D heat flow regime, where $\lambda \ll b$. Below the illustration are two plots showing the thermal spectroscopic curves for a heater of width, $2b = 100\mu m$ placed on fused silica ($\kappa = 1.4W/m-K, \alpha = 9.5e^{-7}m^2/s$). These plots show the full numerical solution from eqn. 7.13, the radial approximation from eqn. 7.14 where $\Re[\delta T] \propto \log(2f)$ as seen in the plot on the left, and the 1D approximation (eqn. 7.11) where $\log(\Re[\delta T]) \propto \log(2f)$ shown in the plot on the right.

width heater. Taking the exact solution for an infinitely narrow line heater on the surface of an infinite half-volume, developed by Carslaw and Jaeger [117] and performing the superposition of a number of such lines to generate a heater between $-b$ and b, he arrived at the following expression for the complex temperature oscillation at the material surface:

$$\delta T(x, y = 0) = \frac{P_0}{\pi \kappa} \int_0^\infty \frac{\cos(kx)\sin(kb)}{kb(k^2 + q^2)^{1/2}} \, \mathrm{d}k \tag{7.12}$$

197

Where k is a dimensionless term of integration. Since the heater also serves as the sensor in the 3ω measurement, one would expect the temperature to vary slightly across the width of the heater. To account for this, the average of equation 7.12 is summed across its width, $-b$ to b, resulting in the final equation that describes the temperature fluctuation of the heater.

$$
\begin{aligned}
\delta T_h &= \frac{1}{2b} \int_{-b}^{b} \delta T(x, y = 0)\, \mathrm{d}x \\
&= \frac{P_0}{\pi\kappa} \int_0^\infty \frac{\sin^2(kb)}{(kb)^2 (k^2 + q^2)^{1/2}}\, \mathrm{d}k
\end{aligned}
\tag{7.13}
$$

Unfortunately, no analytical expression is known for equation 7.13. As such, it must be numerically computed to find the exact solution across all frequencies. Fortunately, there exists a radial heat flow approximation where $\lambda \gg b$ (Fig. 7.2), which, together with the 1D approximation, describes much of the thermal spectrum. In this case equation 7.13 reduces to:

$$
\delta T_h = -\frac{P_0}{2\pi\kappa} \ln(2\omega) - \frac{P_0}{2\pi\kappa} \ln\left(\frac{b^2}{\alpha}\right) - i\frac{P_0}{4\kappa} + \frac{\eta P_0}{\pi\kappa}
\tag{7.14}
$$

Where η is a constant with the value of 0.922... . This approximation greatly simplifies data analysis in this regime. As evident from the leading term in equation 7.14, the thermal conductivity of the substrate is now linearly proportional to the logarithm of twice the driving frequency, or put more simply, proportional to the logarithm of the heater temperature oscillation, as discussed in section 7.2.1. This method is often referred to as the 'slope' method, although this name is a little confusing since the 1D approximation can also be analyzed by its slope in the log-log space. Since these two

approximations solve different quantities (κ and $\kappa \cdot \rho c_p$), given a broad enough spectrum relative to the heater width, one can uniquely determine both the thermal conductivity and heat capacity, although this can also be done by fitting the full numerically computed solution.

In addition to the limitations in applicability of the two approximations, there are other limitations on both the full numerical solution and the approximations. As the section title suggests, these methods are only useful for determining the properties of semi-infiinite substrates. If the substrate is too thin, reflection of the thermal wave off the back surface will cause the heater temperature to diverge from the predictions of Equation 7.13. Luckily, semi-infinite is a relative term and in this case is compared to the thermal penetration depth, which is often small. The equations above only hold if the assumption of a semi-infinite substrate holds, where the substrate thickness, $d_s \ll \lambda$. In reality, the substrate thickness only has to be 5 times the thermal penetration depth $(d_s > 5\lambda)$ to maintain an error of less than 1%. In addition to the substrate thickness there are also limitations on the isotropy of the substrate and other, often neglected, effects such as heat capacitance and thermal boundary resistance of the heater. A detailed analysis of these effects was performed by Borca-Tasciuc et al. [118]. In spite of these limitations, the approximations have been extended to the measurement of thin films by subtracting the difference between the film on substrate and the substrate alone [119]. This difference method is appropriate for measurement of single-layer films, although for multi-layer film composites a more advanced formulation is needed.

7.3.2 Heat diffusion into multilayer, finite-thickness substrate systems

The ability to measure the thermal properties of multilayer systems is important for a number of reasons. This is particularly true for thermal interface material applications because, even in a simple system, there are thermal boundary and bulk resistances present. It is also critical for measuring electrically conductive materials, where additional insulation layers are needed to prevent the 3ω heater from shorting through the conductive material. In the present study, both of these challenges are present. There are thermal boundary resistances between the growth substrate and CNTs, R_{GS-CNT}, and between the CNT layer and mating or opposing substrate, R_{CNT-OS}. Additionally the CNT forest is highly electrically conductive so an added insulation layer is needed to isolate the 3ω heater from the CNTs. A number of groups have made significant progress in extending Cahill's heater temperature oscillation equation to account for such multilayer systems. A brief overview of this developing model and the algorithm used in this work are presented below.

A single-layer, semi-infinite substrate, anisotopic film formula to describe the temperature oscillation of a 3ω heater was first presented by Chen, et al. [120]. It was developed to observe the thermal properties of alloy-based superlattices using a pair of different width heaters to establish the film anisotropy. While their formula can be generalized to an arbitrary number of layers, the Chen presented a single-layer formula. Kim et al. present a multilayer, finite-thickness formula, although their formula assumes an isotropic media [121]. Borca-Tasciuc, Kumar and Chen establish a multilayer film-on-

finite/semi-infinite-substrate system with anisotropic thermophysical properties [118]. This solution appears to be the general form of that originally presented by Chen. This general formula is used to extensively study the approximated model presented earlier (eqn. 7.14) and establish more accurately its range of applicability. Olson more recently modified the formulation of Borca-Tasciuc et al., using the thermal corollary of Ohm's law (eqn. 7.7) and reversing the layer indexing to produce a generalized surface impedance analysis, capable of thermal conductivity, thermal heat capacity, conductivity anisotropy, and interlayer contact resistance for finite and semi-infinite substrates [112].

Olson describes a generalized surface impedance $\tilde{\mathbf{Z}}_j$ as a function of the excitation frequency, j, Equation 7.15a. It is distinguished from the measured surface impedance by an over-tilde and is obtained by integrating the layer transform

3D View Cross Section
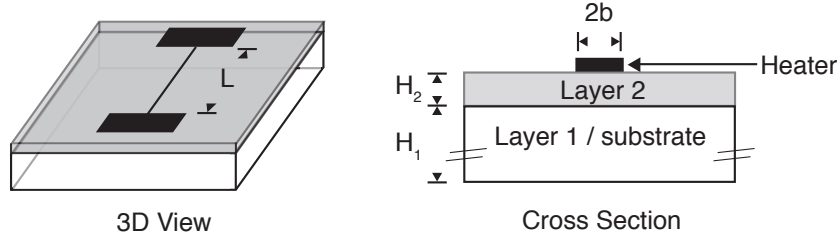
Figure 7.3: Diagram of multilayer material stack and thin film heater used for 3ω measurements.

impedance, $\mathbf{z}$, (eqn. 7.15b) with respect to the dimensionless transform variable, χ.

$$\tilde{\mathbf{Z}}_j = \frac{\delta T_h}{Q} = \frac{1}{\pi} \int_{-\infty}^{\infty} \frac{\sin^2(\chi)}{(\chi)^2} \tilde{\mathbf{z}}(\chi)_{N,j} \, \mathrm{d}\chi, \qquad j = 1, 2, ..., M. \tag{7.15a}$$

$$\mathbf{z}(\chi)_{n,j} = \frac{b}{\kappa_{y_n} \Phi(\chi)_{n,j}} \cdot \frac{\frac{\kappa_{y_n} \Phi(\chi)_{n,j}}{b} \tilde{\mathbf{z}}(\chi)_{n-1,j} - \tanh(\Phi(\chi)_{n,j} \frac{H_n}{b})}{1 - \frac{\kappa_{y_n} \Phi(\chi)_{n,j}}{b} \tilde{\mathbf{z}}(\chi)_{n-1,j} \cdot \tanh(\Phi(\chi)_{n,j} \frac{H_n}{b})}, \tag{7.15b}$$

$$n = 2, 3, ..., N, \qquad j = 1, 2, ..., M.$$

$$\Phi(\chi)_{n,j} = \sqrt{\psi_n \chi^2 + q^2 b^2}, \qquad n = 1, 2, ..., N, \qquad j = 1, 2, ..., M. \tag{7.15c}$$

$$\psi_n = \frac{\kappa_{x_n}}{\kappa_{y_n}}, \qquad n = 1, 2, ..., N. \tag{7.15d}$$

The layer transform impedance is evaluated recursively from the top layer, that which is in contact with the heater, N, down to the substrate, index number 1 (Fig. 7.3). The layer transform for the substrate (layer 1) is dependent upon the layer thickness

202

Table 7.1: 3ω substrate boundary conditions.

	Semi-infinite	Finite-adiabatic	Finite-isothermal
$\mathbf{z}(\chi)_{1,j}$	$\dfrac{-b}{\kappa_{y_1}\Phi(\chi)_{1,j}}$	$\dfrac{-b}{\kappa_{y_1}\tanh(\frac{1}{b}\Phi(\chi)_{1,j}H_1)\Phi(\chi)_{1,j}}$	$\dfrac{-b\cdot\tanh(\frac{1}{b}\Phi(\chi)_{1,j}H_1)}{\kappa_{y_1}\Phi(\chi)_{1,j}}$

and boundary conditions. The boundary conditions for semi-infinite, finite-adiabatic, and finite-isothermal have been derived from Ref. [118] and listed in table 7.1. Index n references the current layer, while index j references the frequency. As described previously, b is the heater half-width, κ is the thermal conductivity, H is the layer thickness, q is the complex thermal wave number (eqn. 7.10), and ψ is the anisotropy ratio (cross plane over in plane). Since the layer transform impedance is defined in essentially the same way as impedance, thermal boundary resistance can be easily introduced between layers by simple addition (eqn. 7.16).

$$\tilde{\mathbf{z}}(\chi)_{n,j} = \mathbf{z}(\chi)_{n,j} - R_n \tag{7.16}$$

Again, like the heater temperature oscillation defined by Cahill, Equation 7.15a has no closed form solution, as such it must be evaluated numerically. While the limits of integration are infinite, the argument quickly diminishes for $|\chi| > 4\pi$. A nonlinear least squares minimization algorithm can then be used to fit the desired layer attributes. A demonstration of the single path heat diffusion using Olson's method is presented in the SiO_2 substrate calibration section 7.5.2. However, in order to measure the thermal conductivity of a thermal interface material, a slightly more complex material stack is

proposed, which involves parallel paths of heat diffusion.

7.3.3   Parallel path heat diffusion

There are a few scenarios in which the simple multilayer geometry, with the heater placed at the top of the stack, is insufficient. The most commonly studied case is in the 3ω measurement of liquid samples [116, 109, 122, 110, 111, 123]. In this case the 3ω heater must be placed on a supporting substrate and either immersed in a liquid or liquid drops placed on top of the heater. This forms a sandwich of two different materials around the heater, resulting in two parallel paths for heat to diffuse. Due to the relatively simple material stack (the contact resistance between the two materials and the heater is assumed to be small, and the thickness of the sample is large, i.e. semi-infinite), previously researchers have analyzed these material stacks using a slight extension of either the planar or radial approximations discussed earlier (Equations 7.11 and 7.14 respectively). Equation 7.17 below demonstrates the extension of the planar approximation for such two sided samples, where subscript l denotes liquid and s denotes substrate.

$$\delta T_h = \frac{P_0/2b}{\sqrt{2\omega(c\rho)_s\kappa_s} + \sqrt{2\omega(c\rho)_l\kappa_l}}e^{-i\pi/4} \tag{7.17}$$

For such a system it is advisable to perform a reference or calibration measurement of the substrate alone prior to liquid measurements, thus the effects of the substrate can be accurately removed to calculate the liquid alone.

A similar method can be used for measuring the performance of thermal inter-

face materials, where the TIM needs to be brought into contact with 3ω heater rather than permanently adhered. If the heater is deposited directly onto the TIM, the contact resistance between the heater and the TIM will be artificially low, not accurately simulating its true application performance. To overcome this, the heater is deposited onto both a highly electrically and thermally insulating substrate, which the TIM can then be pressed up against as illustrated in Figure 7.4. For electrically conducting TIMs, as is the case with the CNTs forest, the heater must also be covered with a thin electrical insulator. Just as the liquid 3ω measurements, this produces two parallel paths for heat diffusion. However, unlike the liquid measurements, this system contains boundary resistances, multilayer stacks and may contain anisotropic materials and finite-thickness-substrates. These more complex features make data analysis more challenging. Although Hu et al. has analyzed the data from such a complex structure using a planar heat flow or 1D thermal model, due to the limitations this places on the heater width and or frequency range, we have opted to extend Olson's model for parallel path heat flow. Because Olson's method is already cast in terms of thermal impedance, it makes the adaptation of this method for parallel heat flow trivially easy.

$$\tilde{\mathbf{Z}}_j = \left(\frac{1}{\tilde{\mathbf{Z}}_{SiO2_j}} + \frac{1}{\tilde{\mathbf{Z}}_{sample_j}} \right)^{-1} \tag{7.18}$$

In this case the mating substrate is represented by a single layer, i.e. substrate only and was composed of 1mm thick of GE 124 Fused Silica, purchased from Ted Pella, Inc. and is modeled with an isothermal boundary. The second heat path is more complex. A $100nm$ thick sputter deposited SiO_2 film is deposited onto the top of the heater forming

205
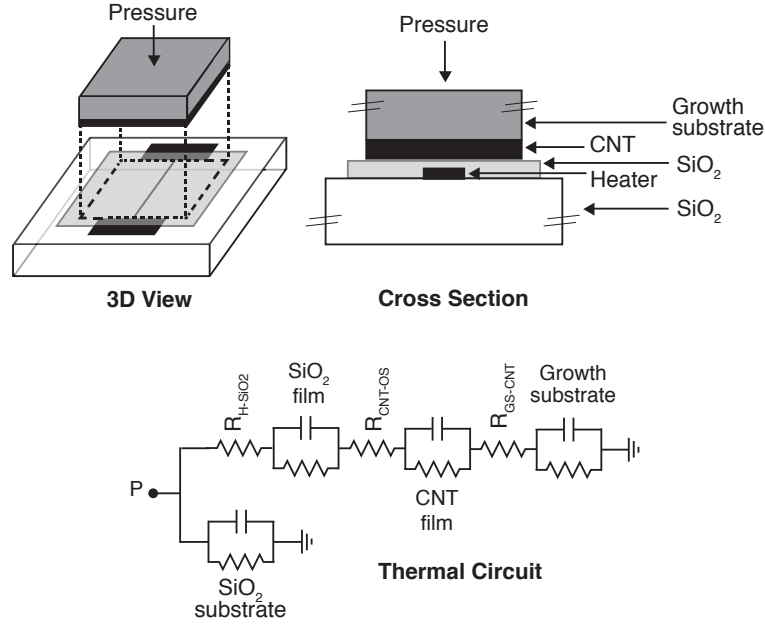
Figure 7.4: Diagram of multilayer, parallel heat path, material stack used for 3ω TIM measurement. The 3D view on the left shows the sample separated away from the mating substrate to expose the heater, while the cross section view shows the whole stack pressed together, sample, heater and mating substrate. The equivalent thermal circuit model schematically demonstrates the thermal stack showing two parallel paths for heat flow.

an electrical insulation layer, while still exposing the contact pads on either side (light gray layer in Fig. 7.4. The contact resistance between this film and the heater has been neglected due to the quality of the prepared film, this resistance is typically on the order of $1 \times 10^{-8} m^2 K/W$. Due to the limited thickness, the heat capacity may also be neglected and the whole film could be modeled as a single frequency independent

resistor as Hu et al. demonstrate [105]. This insulation layer is followed by the contact resistance of the free ends of the CNTs against the SiO$_2$ film, R_{CNT-OS}. This contact resistance represents the largest resistance in this leg of the circuit. This contact is in series with the CNT film impedance, represented by a parallel combination of bulk resistance and capacitance. This is in series with another contact resistance between the CNTs and the growth substrate, R_{GS-CNT}, which is generally accepted as being much smaller than the CNT-opposing substrate contact. This is followed finally by the thermal impedance of the growth substrate, that depending on thickness, material properties and thermal grounding may be regarded as semi-infinite, finite-adiabatic, or finite-isothermal. The equivalent thermal circuit diagram is shown in Figure 7.4.

7.3.4   Sensitivity study

Due to the complexity of the TIM thermal circuit and the layer parameters sensitivity to heater line width, a study of the fit parameters sensitivity is beneficial to understanding which parameters to fit and how to construct the experiment to extract the desired material properties. The following equation (eqn. 7.19a) represents a matrix of layer sensitivity coefficients, where each element is essentially a normalized gradient

of the given fit parameter.

$$\mathbf{D}_{k,j} = X_k \frac{\partial \tilde{\mathbf{Z}}_j}{\partial X_k}, \quad k = 1, 2, ... L_{DOF}, \quad j = 1, 2, ..., M. \tag{7.19a}$$

$$\frac{\partial \tilde{\mathbf{Z}}_j}{\partial X_n} = \frac{1}{\pi} \int_{-\infty}^{\infty} \frac{\sin^2(\chi)}{(\chi)^2} \frac{\tilde{\mathbf{z}}(\chi)_{N,j}}{\partial X_n} \, d\chi, \quad n = 1, 2, ..., N, \quad j = 1, 2, ..., M. \tag{7.19b}$$

$$\tag{7.19c}$$

Where X_n is one of the four fit parameters $(\kappa, \alpha, \psi, R_c)$ for the desired n^{th} layer. Additionally, k is the degree of freedom and j is the frequency value. The magnitude of a $\mathbf{D}$ element corresponds to the associated fit parameter sensitivity. Elements with larger values have more influence on the resulting fit, in other words the fit is more sensitive to elements with large values.

There are a number of experimental variables that deeply influence the quantities that can ultimately be measured using this technique. A sensitivity study such as this is important to understanding the limits of the parameter space before constructing an experiment. The experimental factors that influence the measurable quantities are, heater width, measurement frequency range, the thermo-physical properties of the sample, and the thermo-physical properties of the mating substrate. Often there are trade-offs in the quantities that can be measured. For instance, in the case of the CNT forest, in order to measure the relatively high bulk thermal conductivity there must either be a dramatically reduced interface resistance or the CNT layer must be large so that $R_{OS-CNT} \approx (\frac{l}{\kappa})_{CNT}$.

208

Below are two example sensitivity analyses. Each figure shows a plot for each layer in the material stack. The first example (Fig. 7.5) shows the sensitivity for both real and imaginary components (real solid line, imaginary dashed line) versus measurement frequency for a $22\mu m$ heater. This demonstrates the importance of the frequency range over which the measurements are performed. A general trend from this analysis is that the thermal diffusivity becomes more influential at higher frequencies as previously demonstrated in the 1D heat flow regime illustrated in 7.2. Another important note is that the contact resistance of the CNTs dominates all other CNT properties across the range of frequencies investigated. This fact prompted the next analysis in which the contact resistance is varied as the independent variable in the sensitivity analysis.

This second example (Fig. 7.6) shows the profound impact of the contact resistance between the CNT tips and the opposing substrate's SiO_2 thin film, R_{OS-CNT} for a $45\mu m$ heater. Here the contact resistance is varied and both the low frequency (1Hz) and high frequency (10kHz) response for the real part of each thermophysical property is plotted. Some notable aspects of this analysis is that the low frequency response is nearly dominated by this contact resistance for all reasonable resistance values $(\gtrsim 1e^{-6}m^2 K/W)$. This is a critical point to the remaining analysis because it demonstrates the limitation in measuring properties other than this contact resistance.

Of course the sensitivity analysis is not an exhaustive technique and can only offer some insight into the possible performance of the fitting procedure. It depends strongly on the point chosen for linearization and the degree of linearity around this

Table 7.2: Assumed values for linearization in sensitivity analysis. S1 and S2 are the two examples computed

	Layer	$\kappa(W/mK)$	$\alpha(m^2/s)$	ψ	Resistance (m^2K/W)	Height (m)
S1	Fecralloy	16.0	4.82e-06	1	5.00e-06	9.00e-04
	CNT	50	9.09e-05	1	2.00e-05	1.74e-05
	SiO2$_{film}$	1.40	9.50e-07	1	1.00e-07	2.50e-07
	SIO2$_{GE124}$	1.56	7.1e-07	1	0	1.00e-03
S2	Silicon	149	9.14e-05	1	1.00e-06	5.00e-04
	CNT	50	9.09e-05	1	variable	4.0e-06
	SiO2$_{film}$	1.40	9.50e-07	1	1.00e-07	1.00e-07
	SIO2$_{GE124}$	1.47	7.8e-07	1	0	1.00e-03
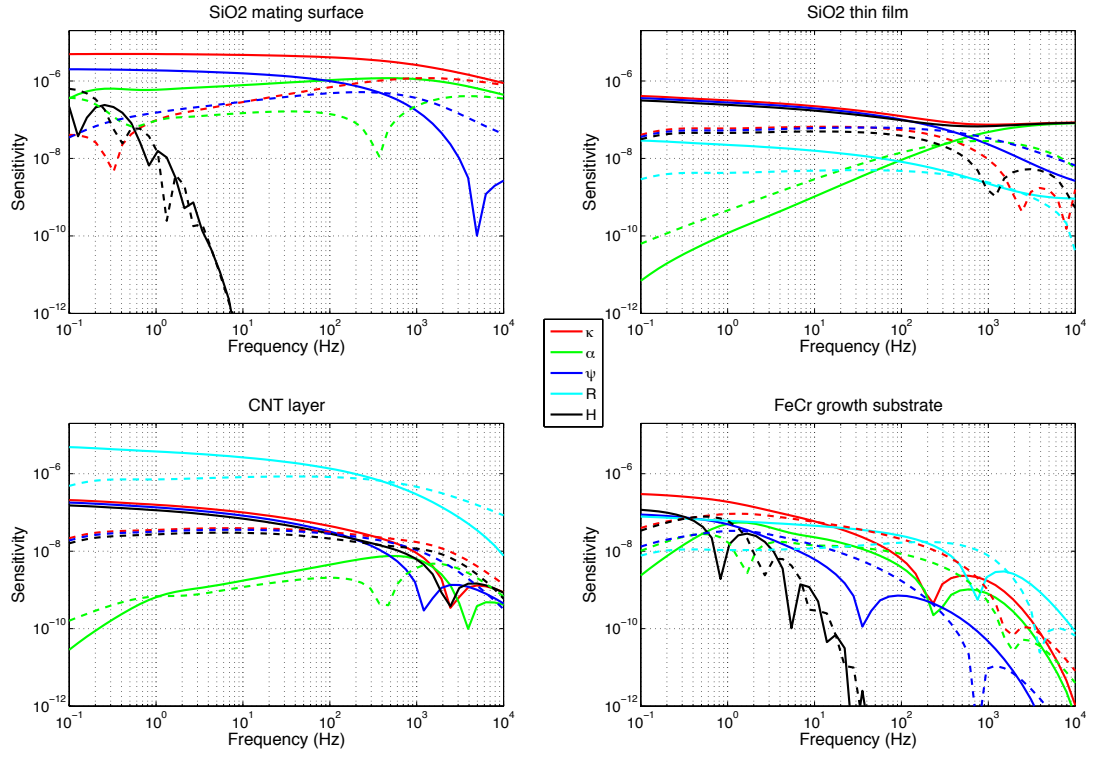
Figure 7.5: Sensitivity analysis as a function of excitation frequency. Calculations assume the point of linearlization described in Table 7.2 - S1. The solid lines represent the real part of the respective thermophysical property, while the dashed line represents the imaginary part. Both x and y scales are consistent between plots.

point.

7.3.5 Error analysis

Error estimation in fit parameters is arguably as important as the fit values. However, this analysis is often completely ignored in the 3ω data fitting or at best is partially explained but leaves the reader with ambiguities that can result in significant

211
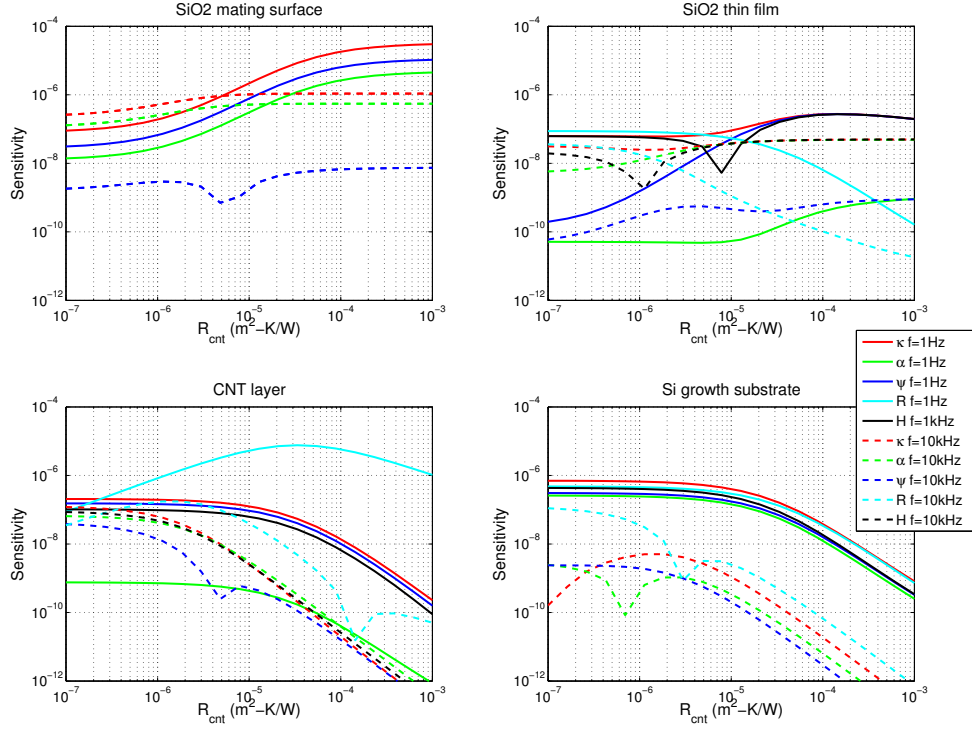
Figure 7.6: Sensitivity analysis as a function of opposing substrate - CNT contact resistance for $45\mu m$ heater. Calculations using the values given in Table 7.2 - S2.

variation in error estimates. In this section, the error analysis presented by other authors is discussed along with their pitfalls followed by an alternative approach aimed at addressing these issues.

Often estimation of the error associated with fit parameter coefficients is performed by linearizing around the the solution and calculating the error using the measured uncertainties [105, 124]. The measurement quantities include the electrical signals, $V_{3\omega}$, $V_{1\omega}$, $\frac{dR}{dT}$, R_0, and the heater dimensions b and l.

The error from $V_{3\omega}$ is estimated to be near 2% [105] and is largely suspected to be the dominant source of error. Future work should measure this directly using the Mean Average Deviation (MAD) function on contemporary lock-in amplifiers. All other measurement uncertainties are found to be less than 0.1%

From these uncertainties, the error associated with the measured surface thermal impedance, $\frac{\delta \hat{\mathbf{Z}}}{\hat{\mathbf{Z}}}$, can be established using simple uncertainty approximation principles applied to equation 7.8. From the surface thermal impedance uncertainty, the linearization around the fit solution and assuming the fit parameters are independent variables, one can find the error associated with any given fit parameter, X_k, using the following equation (eqn. 7.20).

$$\delta X_k = \sqrt{\left(\frac{\partial X_k}{\partial \hat{\mathbf{Z}}}\right)^2 \delta \hat{\mathbf{Z}}^2} \tag{7.20}$$

Where the reciprocal of the partial derivative of $\hat{\mathbf{Z}}$ with respect to X_k is determined following the fitting procedure using a numerical method.

This method falls short for two reasons. First is the assumption that the fit parameters are not covarying. The second problem is that this technique appears to evaluate the error for a single frequency. As previously demonstrated (Section 7.3.4) the sensitivity of each thermophysical property changes greatly with frequency, so evaluating the error based on this at a fixed frequency will not represent the true error. It may be more reasonable to assume a mean error for all fit frequencies, although this is not discussed in the literature.

To overcome these problems one can compute the unbiased estimates of the fit

213

parameters σ_{a_k} from [77]:

$$\sigma_{a_k} = \sqrt{(A_{k,k})^{-1} \frac{SSE}{N-L}} \tag{7.21}$$

Where SSE is the sum of squared errors, N is the number of data points, L is the total number of fit parameters and A is defined as:

$$A_{r,k} = \sum_{k=1}^{N} \frac{\partial f_k}{\partial a_r} \frac{\partial f_k}{\partial a_s} = J_{l,k} J_{k,l} = J^T J \tag{7.22}$$

Where J is the jacobian matrix defined as:

$$J_{k,l} = \frac{\partial f_k}{\partial a_l} \tag{7.23}$$

In this case the jacobian, is computed numerically using $Jacobianest.m$ - a community supplied matlab function for adaptive, robust, numerical differentiation. a_l is the lth fit parameter and f_k is a single measurement value, taken from re-indexed thermal surface impedance $\tilde{\mathbf{Z}}_\mathbf{j}$ such that each index, k, corresponds to a single real or imaginary value in a single curve, for the case of simultaneous fitting of multiple curves. For such a case with Q data sets, or curves, each containing M complex values, $k = 1, 2, ..., N$ where $N = 2MQ$.

This method for calculating the error associated with each fit parameter is more robust than those presented by other researchers performing 3ω analyses. It is evaluated across the entire set of fit data rather than at a single point and takes into account the covariance of the fit parameters.

The presented error analysis does however, fall short in one aspect. Uncertainty in certain measurements critical to the impedance calculation, such as the heater width, may not be accounted for, appearing as systematic errors in the final result. However, these additional measurements can be made with a high level of precision, removing the uncertainty given proper experimental practice.

7.3.6 Data fitting

Data fitting was performed using a custom written object oriented MATLAB® program, the code for which can be found in the appendix A.2.1. The code is designed to accept multiple data sets, i.e. curves, providing a higher level of constraint over fit parameters. This is particularly useful for measuring TIMs since typically a family of measurements are performed on the same sample, while varying only pressure. Depending on the TIM, this increase in pressure may manifest itself in changing different thermophysical properties, although in this study the assumption is that it is only varying the contact resistance of the CNTs to the mating substrate. The desired thermophysical are obtained by fitting the surface impedance oscillation data with the predicted impedance (Eq. 7.15a). The weighted, summed square of residuals, minimized during the data fitting is given by:

$$\chi^2(R_{cnt\text{-}gs}, R_{os\text{-}cnt}(P_1), R_{os\text{-}cnt}(P_2), ..., R_{os\text{-}cnt}(P_Q)) = \sum_j \left(\frac{\Re \hat{Z}_j - \Re \tilde{Z}_j}{\Re \sigma_{\hat{Z}_j}} + \frac{\Im \hat{Z}_j - \Im \tilde{Z}_j}{\Im \sigma_{\hat{Z}_j}} \right)$$

$$(7.24)$$

In the cases investigated in the results below, the focus was placed on the CNT

contact resitances, both at the growth end, $R_{cnt\text{-}gs}$, and at the free end to mating sub-strate, $R_{os\text{-}cnt}$. Other properties can be trivially fit, although due to their insensitivity, focus was placed on the contacts alone. The static thermophysical properties, i.e. those not fit, were taken from the suppliers data sheets in the case of sputtered SiO2, Si and Fecralloy and in the case of the MWNTs were taken as conservative estimates from those measured by Hu et al. [105].

The custom code is broken up into a few sections. The main program is named 'fitting3omega.m'. In addition to this main script, there is a 'measurement' class where the raw data for each 3ω measurement is stored; there is a 'heater' class where the definitions for each heater are stored; there is a 'layer' class which contains the information for each material layer in the stack; there is a 'material_stack' class, only containing static functions that assembles and generates the stacks, fit coefficient initial values, and bounds; and there is a 'fit_fn' class, only containing static functions that defines the fit methods and associated functions for error analysis etc.

7.4 Experiment setup

3ω heaters of various line widths were lithographically patterned onto GE 124 fused silica. The heaters were sputter deposited, using a 2nm Chromium adhesion layer followed by 100-150nm of Palladium. An additional 100nm of SiO_2 was sputtered on top of the heater to serve as an electrical insulation layer. The thermal coefficient of resistance (TCR) of each heater was measured by sweeping the ambient temperature

surrounding the heater between -20°C and 70°C, while simultaneously measuring the heater resistance. Vertically aligned multi-wall CNTs were grown on either Silicon or Fecralloy substrates using the CVD process and conditions described previously. CNT forest height was measured using a Hitachi S-4800 scanning electron microscope. The complete material stack and thermal model is illustrated in 7.4. The 3ω filtering electronics are described in section 7.2.2. Pressure is accurately applied to the sample using a custom made load-displacement mechanism. The load-displacement machine consisted of a linear translation stage with a linear stepper motor supported against the sample. An anchored pair of springs connecting to the translation stage increased the load on the sample as the motor stroke increased. The load of the springs was calibrated using a load cell prior to thermal measurements. An integrated Michelson's interferometer was intended to measure the film compression, although motor vibration was too severe to make accurate measurements.

7.5 Results and discussion

7.5.1 $V_{1\omega}$ filter performance

The two 1ω filter types discussed in section 7.2.2 were tested using the simple heater on glass, reference material. Tests were performed using both a $45\mu m$ and $250\mu m$ heaters. These two techniques showed very good agreement for low frequencies and match well to the thermal model (eqn. 7.15a). However, at high frequencies, roughly above 1kHz, the differential amplifier filter began veering from the expected values.
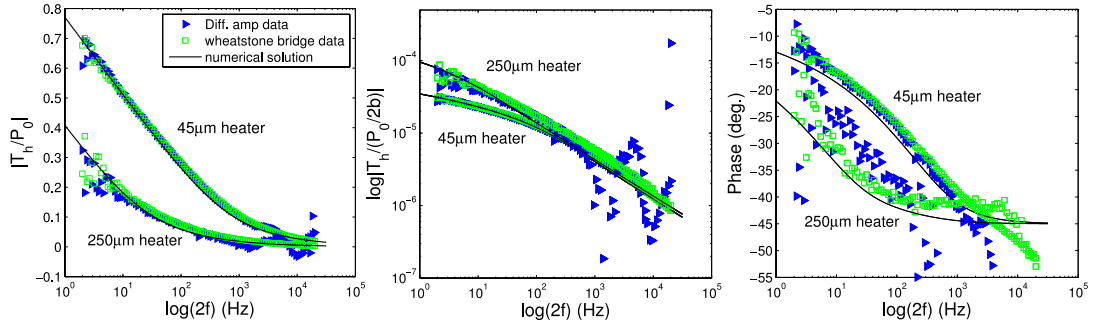
Figure 7.7: Plots showing the agreement between the $V_{1\omega}$ filtering techniques. The blue triangles show the results from the differential amplifier method, while the green squares are from the Wheatstone bridge. The black line shows the numerical computations from Equation 7.15a. These measurements were performed using two different heater widths on GE 124 fused silica. The left most and middle plot show the real part of the temperature fluctuation normalized to power per unit length and per unit area respectively. The right most plot phase shift in degrees.

This effect was more severe for the $250\mu m$ heater, although this is suspected to be a result of the different voltage drop across the wider heater rather than intrinsic to the heater width. Due to the desire to perform static temperature measurements, the exact cause of the distortion was not identified, and the Wheatstone bridge filter was used for all further measurements. A comparison between the 3ω measurements performed with the two filters is illustrated in Figure 7.7.
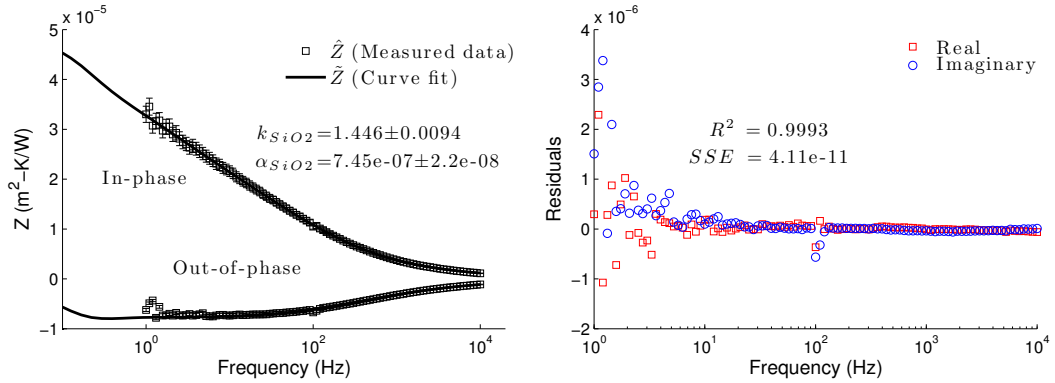
Figure 7.8: 3ω measurement of calibration slide using 45um heater.

7.5.2 Glass calibration measurements

Prior to any TIM measurement, verification of the basic principle was performed using a glass calibration slide composed of GE 124 fused silica. This calibration slide is later used as the opposing substrate in the parallel heat path 3ω measurements, so in addition to verification of the basic principle, this measurement also serves for subtracting the reference material in future TIM measurements. A number of heater line widths were produced and tested. Figure 7.8 plots the measured data, $\hat{\mathbf{Z}}$, and curve fit data, $\tilde{\mathbf{Z}}$, using Olson's data reduction techniques and its implementation described in 7.3.6. In this case only a single-isothermal-boundary layer was used to model the heat diffusion and two degrees of freedom were given to the fit procedure, κ_{SiO2} and α_{SiO2}. As seen in the Fig. 7.8, the curve fits well to both the real and imaginary data. At very low frequency the error increases dramatically, this is a result of lock-in amplifiers cut off frequency, which is set digitally. The found values for thermal conductivity and

219
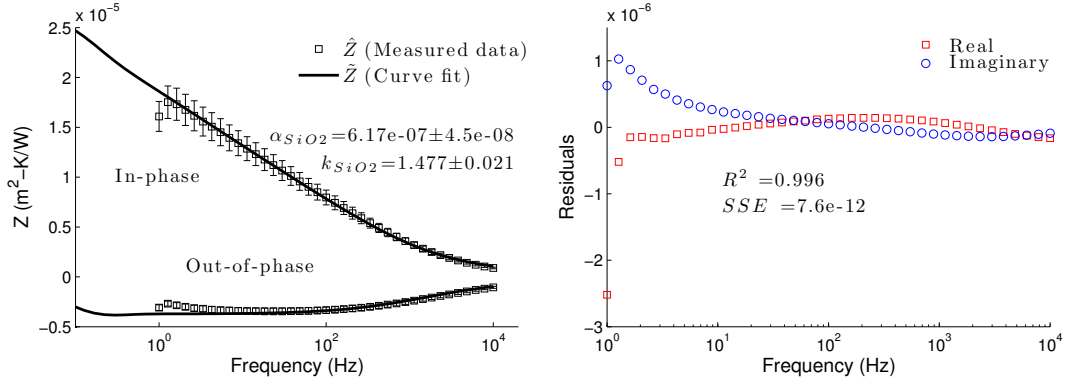
Figure 7.9: 3ω measurement of calibration slide using 22um heater.

diffusivity are listed in Table 7.3, along with those reported from a manufacturer. Interestingly however, the data fitting does not perform as well for the smaller, $22\mu m$, heater as demonstrated in Figure 7.9. The fits slight divergence from the data, especially at low frequencies and for the imaginary part, was not fully appreciated until future TIM fits were performed. This divergence turns out to be a major problem when more complex material stacks were used, more detail into this analysis is presented in section 7.5.4. However this divergence does not seem to be related to a poor thermal model but is more likely caused by some parasitic electrical elements.

Using the mean and standard deviation from the three 3ω measurements, there is a 1.8% thermal conductivity error between measurements and a 5.3% error relative to the suppliers value. Additionally the thermal diffusivity has a 40% error between measurements but only 7.3% error relative to the suppliers value. These errors give confidence to future measurements of unknown thermophysical properties.

Table 7.3: 3ω calibration measurements of GE 124 fused silica and its comparison to the supplier's datasheet.

Data source	κ (W/m-K)	α (m^2/s)
$22\mu m$ 3ω heater	1.477 ± 0.021	$6.17\mathrm{e}^{-7}\pm 4.5\mathrm{e}^{-8}$
$45\mu m$ 3ω heater	1.446 ± 0.009	$7.45\mathrm{e}^{-7}\pm 2.2\mathrm{e}^{-8}$
$250\mu m$ 3ω heater	1.499 ± 0.023	$1.28\mathrm{e}^{-6}\pm 6.2\mathrm{e}^{-8}$
3ω mean/deviation	1.474 ± 0.027	$8.8\mathrm{e}^{-7} \pm 3.5e^{-7}$
Supplier's datasheet	1.40	$9.50\mathrm{e}^{-7}$

7.5.3 MWNTs grown on Silicon

Several MWNT samples grown on silicon were used for the 3ω analysis. Unfortunately a number of heaters were inadequately insulated prior to sample measurement, resulting in short circuits when the electrically conducting CNTs were adhered for thermal measurement. As such, only one complete data set was captured for the CNT growth on Silicon. The sample used had a height of $4\mu m$, an area of 0.544 cm^2, a Raman D/G ratio of 1.24 ± 0.28 and was tested on a $45\mu m$ width, 7.777mm long heater and the applied power was 1.19mW.

Figure 7.10 shows an example of the collected 3ω data for a single applied pressure. This figure includes the fused silica reference measurement shown in black, along with its associated fit. The red data points are the experimentally measured values, comprising the thermal impedance of both the reference and sample, while the
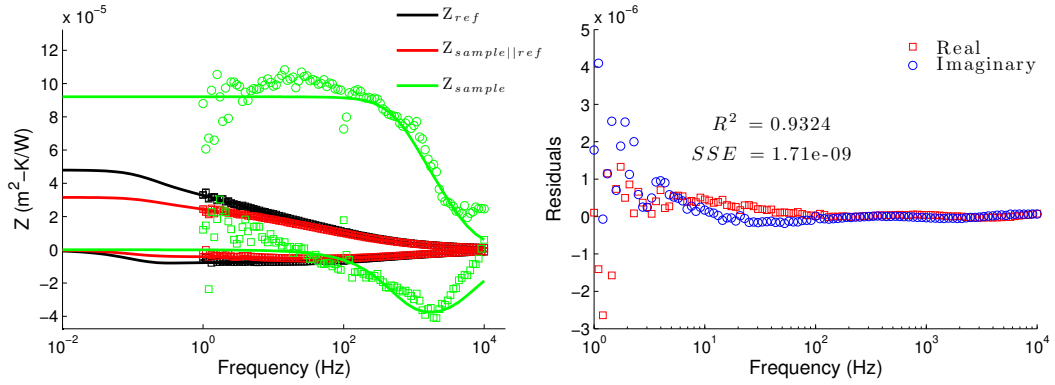
Figure 7.10: Example data fitting of a $4\mu m$ thick CNT forest sample grown on Silicon. The left plot shows the fits, while the right shows the residuals of the measured surface thermal impedance. On the left plot, the black points and curves show the reference fused silica sample, the red data shows the measured surface thermal impedance, reference in parallel with the sample, and the green curves show the calculated thermal impedance of the sample alone.

green data is calculated by subtracting the reference from the experimentally measured impedance, i.e. $Z_{sample} = (1/Z_{meas} - 1/Z_{ref})^{-1}$. The fitting function fits the experimentally measured thermal impedance, Z_{meas} opposed to the explicit sample impedance, the sample impedance is simply computed and displayed to illustrate the quality of the fit, as the reference impedance obscures much of the sample behavior in the experimental measurement. This figure shows that the quality of the fit is quite good. There is some divergence at very low frequency, particularly evident in the green 'sample' curve, although this behavior can not be modeled with the surface thermal impedance equa-

tion given the current set of constraints on the thermophysical properties. In particular the imaginary part of impedance should never rise above zero and the real part should not have a positive slope at low frequencies. If explained with the thermal model, this behavior would correspond to a negative thermal conductivity of the growth substrate. This behavior is described further in the results for the MWNTs grown on Fecralloy, in which this behavior is exacerbated.

Figure 7.11 shows the results from simultaneously fitting all the pressure curves from this sample. All of the static thermophysical properties used in the data fitting are presented in Table 7.4. The data is fit with a simple inverse pressure relationship, as expected for the resistance of contacting surfaces. Despite some scatter in the data, the curve fit intersects all but one of the areas spanned by the error bars, further validating the data. Interestingly, however, the contact at the growth end, $R_{cnt\text{-}gs}$ presents a significantly higher resistance than that of the free-end contact, $R_{os\text{-}cnt}$. This result is generally counterintuitive given the presumed chemical bonding of the CNTs to the substrate and opposes what other research groups are finding. However, this phenomena can be explained by the in-situ observations of surface contact dynamics, presented earlier (Chapter 8), whereby the tips making contact to the opposing substrate buckle creating a line of contact opposed to a single point contact. This of course is based on the assumption that the growth contact does not change with increasing pressure, which may not be completely accurate as both contacts may reduce in resistance with pressure. However, the mating contact is suspected to increase more dramatically. The fit curve suggests that at very high pressure $R_{os\text{-}cnt}$ approaches 5.6 mm^2K/W, which
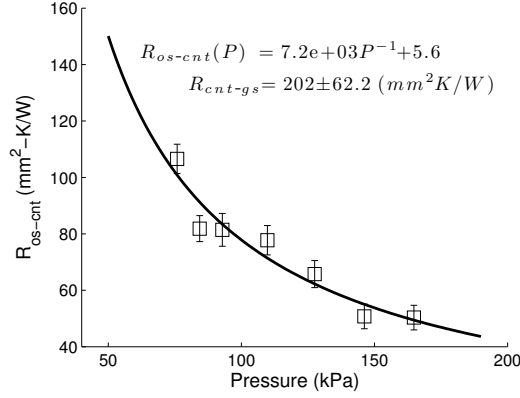
Figure 7.11: Pressure versus $R_{os\text{-}cnt}$ for $4\mu m$ thick MWNTs grown on silicon.

is exceptionally low, near the limit of free contacts resistance seen in CNT forests [32]. However, the performance should be evaluated over a larger pressure range before such lofty claims can be made. Of course the high performance of this contact is meaningless without the improvement of the growth substrate contact. As described elsewhere, improving the growth substrate contact resistance and its adhesion is what motivated the investigation of Fecralloy as a growth substrate. The results from the 3ω tests performed on Fecralloy growth substrates are presented next.

7.5.4 MWNTs grown on Fecralloy

A number of self-catalyzed MWNT samples grown on Fecralloy substrates were prepared for 3ω measurements. However, like those of the silicon substrate, many of the 3ω heaters began shorting or behaving oddly when the CNT samples were pressed against the reference material. The exact cause of this erratic behavior was not identified, although it is suspected to be a result of pin defects or other non-conformal defects

Table 7.4: Fitting conditions for MWNTs grown on Silicon. The bold entries are fit parameters free to adjust during the fitting routine.

	Layer	$\kappa(W/mK)$	$\alpha(m^2/s)$	ψ	Resistance (m^2K/W)	Height (m)
	Silicon	149	9.14e-05	1	**2.02e − 04**	5.00e-04
Sample	CNT_{4um}	50	9.09e-05	1	**varied**	4.00e-06
	$SiO2_{film}$	1.40	9.50e-07	1	1.00e-07	2.50e-07
Reference	$SIO2_{GE124}$	1.45	7.44e-07	1	0	1.00e-03

related to the insulation layer over the heater. As such, only two reasonable sets of data were captured for the Fecralloy grown MWNTs. Both samples measured were grown simultaneously using the best growth conditions established for this material. Their height was roughly $17\mu m$ and both were tested using a $22\mu m$ wide by $2.98mm$ long heater with an applied RMS power of 2.71mW.

While the raw data appears to be a very good dataset, containing very low noise and a steady decrease in impedance with increasing pressure, data fitting reveals some major problems. Figure 7.12 shows similar, single-curve,single-pressure data fit for the Fecralloy sample on the $22\mu m$ heater as with that presented earlier for the $45\mu m$ heater, Figure 7.10. Again, the black data and curve represent the reference surface thermal impedance and data fit, the red data and fit line represent the measured surface thermal impedance of the sample and reference in parallel, while the green points and curve are the calculated impedances for the sample alone. Looking at either the
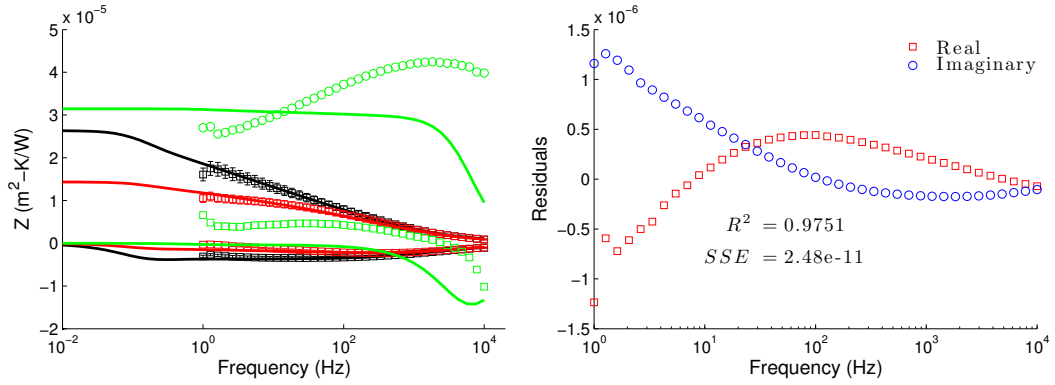
Figure 7.12: Example data fitting of a $17\mu m$ thick CNT forest sample grown on Fecralloy. The left plot shows the fit data, the black points and curves show the reference fused silica sample, the red data shows the measured surface thermal impedance, reference in parallel with the sample, and the green curves show the calculated thermal impedance of the sample alone. The right plot shows the residuals of the measured surface impedance.

calculated values for the sample and fit or the residuals makes it blatantly obvious that the fit is not good. Similar but much less drastic behavior was seen in the $45\mu m$ heater with silicon sample, where for low frequencies the slope of the real part of the sample impedance is positive and the value of the imaginary part of is above zero. These trends oppose the normal behavior of the surface thermal impedance model given rational values for the thermophysical properties. This behavior would suggest a negative thermal conductivity for the Fecralloy growth substrate. Figure 7.13 demonstrates a slightly improved fit using a negative thermal conductivity for Fecralloy and letting the fitting
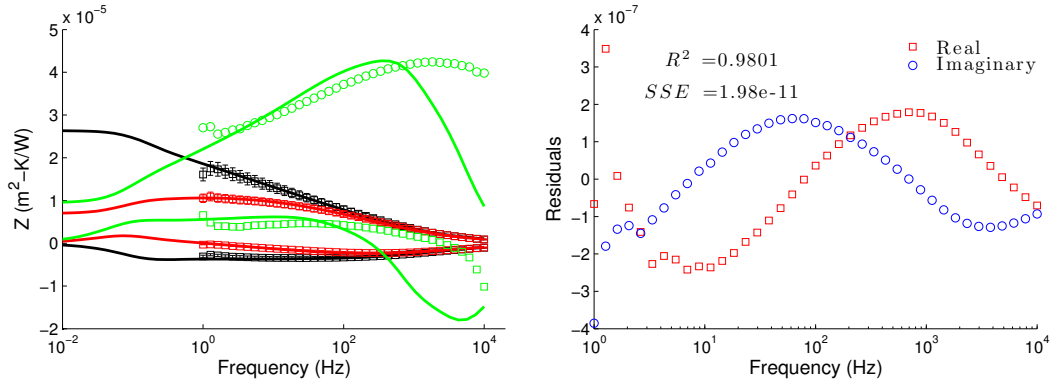
Figure 7.13: Example of the poor fit for the $22\mu m$ wide heater, where the thermal impedance model must be given negative substrate conductivities in order to approach a better fit for the sample. Likely caused by a parasitic reactance in the measurement circuit.

function attempt to fit this parameter. However, using a negative substrate thermal conductivity is irrational and the behavior probably better explained as a parasitic reactance either in the wheatstone bridge or heater. Some attempts to model this behavior have been made but no clear solution has been found. Unfortunately the processing of this data was postponed until after the experiments had been concluded and as such there was no experimental investigation into the parasitic behavior. Despite this clear divergence in the fit, the high frequency response is still expected to contain some useful information. For this reason, the Fecralloy data has been analyzed, although the results must be interpreted with some degree of caution.

Figure 7.14 plots the fit thermal contact resistance between the free ends of the

227

Table 7.5: Thermophysical properties used for Fecralloy sample data fitting. Bold items are fit parameters.

Layer	$\kappa(W/mK)$	$\alpha(m^2/s)$	ψ	Resistance (m^2K/W)	Height (m)
Fecralloy	16.0	4.82e-06	1	**$2.0e-06$**	9.00e-04
$CNT_{17\mu m}$	50.0	9.09e-05	1	**varied**	1.77e-05
$SiO2_{film}$	1.40	9.50e-07	1	1.00e-07	2.50e-07
$SIO2_{GE124-22um}$	1.48	6.17e-07	1	0	1.00e-03

Fecralloy grown CNTs to the opposing substrate as a function of pressure, $R_{OS\text{-}CNT}(P)$. Measurements were made for both the loading and unloading cycles, illustrating the hysteresis in the contact resistance. The larger error bars on this dataset is a result of the poor fit described earlier. As with the Silicon substrate samples, the fitting function fit the CNT-growth substrate contact resistance, $R_{CNT\text{-}GS}$ common to all pressures measurements, while fitting unique $R_{OS\text{-}CNT}$ to each pressure curve, as in Equation 7.24. $R_{CNT\text{-}GS}$ was found to be $2.0 \pm 55.3mm^2K/W$, this along with all of the static thermophysical properties used for the data fitting are listed in Table 7.5. Clearly the error associated with $R_{CNT\text{-}GS}$ supports that the model is insensitive to this fit parameter. Despite the large error in this contact resistance, it is still evident that $R_{CNT\text{-}GS}$ is much smaller for the Fecralloy sample than it is for the silicon sample, in effect lowering the entire TIM resistance. Additionally the free end contact, $R_{OS\text{-}CNT}(P)$, is nearly half that of the MWNTs grown on Silicon, for a similar pressure range. Again, $R_{OS\text{-}CNT}(P)$ was fit assuming a simple inverse pressure relation, resulting in an asymptotic contact
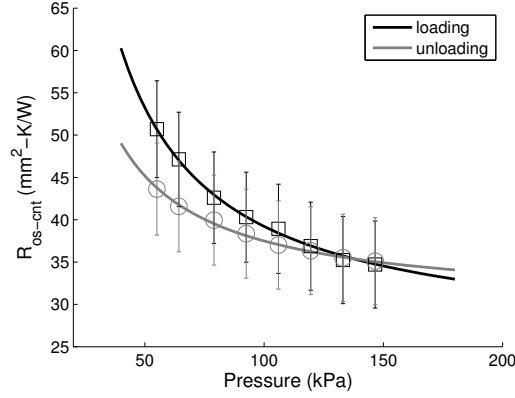
Figure 7.14: Free-end CNT contact resistance vs pressure for Fecralloy sample.

resistance of $25mm^2K/W$ for the loading curve and $30mm^2K/W$ for the unloading curve. The asymptotic behavior of both the loading and unloading curves should be consistent but the fitting has not been suitably constrained to reflect this. The observed hysteresis between loading and unloading curves is suspected to be a result of the van der Waals adhesive force of the free CNT tips, maintaining their adhesion to the opposing substrate during unloading.

7.6 Conclusion

The transient 3 omega thermal measurement technique has been adapted to characterize the thermal performance of carbon nanotube thermal interface materials. A multi-layer, surface thermal impedance model has been extended to parallel path heat diffusion to accurately model the experimental configuration of a TIM on mating substrate. Sensitivity analysis was performed to determine the experimental configurations

necessary for observing particular thermophysical properties. Several microfabricated 3 omega heaters were made on fused silica and tested to validate the technique. The 3ω measurement performance of the SiO2 compared well to the manufacturers datasheet, showing the value of the technique. These heaters on SiO2 then served as the mating substrate for CNT TIM testing. MWNTs grown on both silicon and fecralloy substrate were analyzed using a range of contact pressures. The contact resistances at the CNT-opposing substrate (CNT-OS) and growth substrate-CNT (GS-CNT) interfaces were fit to the thermal spectroscopy measurements. In the case of the silicon substrate growth, $R_{CNT\text{-}GS}$ was found to dominate the TIM resistance at $200 mm^2 K/W$, while $R_{OS\text{-}CNT}$ showed the expected inverse pressure relationship with values between $100\text{-}50 mm^2 K/W$. The Fecralloy grown MWNTs were found to perform much better with the contact resistance dominated by the free-ends and still exhibiting the inverse pressure relationship. The growth substrate to CNT resistance was found to be $\sim 2 mm^2 K/W$, while the mating substrate to CNT resistance ranged from $\sim 50 - 35 mm^2 K/W$ for pressures range of 50 - 150 kPa. These results compare favorably with other transient and steady-state measurements, in particular they compare very well to the DC measurements performed on similar samples in Chapters 5 and 6. Additionally these findings support the theory that substrate adhesion plays a vital role in the growth substrate to CNT resistance.

Chapter 8

In-situ observations of surface contact dynamics of CNT forests

8.1 Motivation

Quantifying the nature and extent of contact area for mating solid surfaces is important to a number of disciplines, yet it has been very difficult particularly at the micro or nano scale. Here we present a method to directly observe the nano-contact dynamics by using an electron transparent membrane as one of the two contacting surfaces, allowing the contacts to be visualized using a scanning electron microscope. This method presents a remarkably high contrast between contacting and non-contacting areas. The contrast mechanism is attributed to trapped charges at the material interface, producing a voltage contrast effect that enhances secondary electron emission. Both contact shape and area can be measured as a function of applied pressure. We demon-

strate the utility of this technique by observing the contact behavior of vertically aligned multiwalled carbon nanotube arrays and correlate this contact to their performance in thermal interface and dry adhesion applications.

8.2   Introduction

Knowledge of the true contact area between two surfaces is critical to a number of disciplines, particularly for thermal interface and dry adhesive applications [67, 83]. In the thermal interface field, a large thermal resistance is present as a result of the microscopic surface roughnesses and non-planar nature of the contacting materials. The surface roughness alone can significantly decrease the real contact area, in many cases reducing it to only a few percent of the apparent contact area. Uncertainty of the true surface area is part of what has impeded the progress in this field. Traditionally researchers have measured the contacts during loading, either directly using optical and interferometric techniques or indirectly through thermal and electrical conduction [125]. While interferometric techniques can provide high vertical resolution, their lateral resolution is diffraction limited. The thermal and electrical techniques are advantageous because they can be evaluated for both static and kinetic contacts. However, they give little information about the size, shape or composition of the contacts and can suffer from errors due to the presence of oxide films between contacts. There is a growing need for more advanced characterization techniques of such contacts, particularly at the nano-scale. Such techniques will help develop the next generation of materials.

To directly observe the contact mechanics with nano-scale lateral resolution, we've adapted a technique originally developed for environmental SEM that relies on the use of electron transparent membranes [126, 127, 128]. Rather than serve as a window into a different environment, these membranes can be forced against a surface revealing the areas of contact between the membrane and the opposing surface. Given the right membrane and beam conditions, this technique can provide a remarkably high contrast between areas with and without contact, down to the nanometer range.

This chapter describes the basic technique, the factors that influence resolution and image quality, the origin of contrast mechanism, and presents a case study using the method to characterize the contact mechanics of MWNTs. The data derived from the MWNT contact analysis is then compared to experimental results for thermal interface and van der Waals adhesion applications.

8.3 Experiment Setup

A custom fabricated, in situ, SEM load clamp was designed to perform the contact analysis (Fig. 8.1). This load clamp uses a pair of screws with springs to apply pressure to a copper gasket, which in turn pushes a low stress, electron translucent, atomically flat, Si_3N_4 membrane against a contacting sample. The opening in the copper gasket aligns with the Si_3N_4 membrane such that the electron beam enters and passes through the membrane. The electron beam rasters over the membrane in x and y directions, forming an image of the nano-contacts. Pressure between the membrane and

sample can be increased by tightening the screws, and is known quantitatively through calibration of the spring constant of the springs.
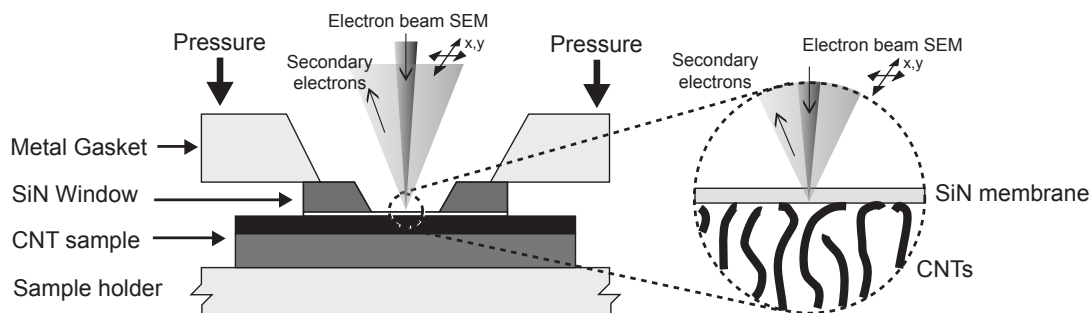
Figure 8.1: Cross section diagram showing in situ SEM load clamp for compressing an electron translucent membrane against a CNT sample for contact analysis.

Commercially available Si_3N_4 membranes of various thicknesses (15nm, 50nm) were purchased from Ted Pella, Inc. and 200nm membranes from Applied NanoStructures, Inc. Vertically aligned multi walled carbon nanotubes were grown via chemical vapor deposition on silicon substrates. To catalyze CNT growth, 10nm of Aluminum followed by 2.5nm of Iron were deposited onto the Si substrate via ion beam sputtering using a South Bay Technologies IBS/e. The growth was performed at 750°C in a quartz tube furnace, at atmospheric pressure using C_2H_4 feedstock gas and H_2 carrier gas flowing at 380 and 135 SCCM respectively. Scanning electron microscopy was performed using a Hitachi S-4800.

8.4   Results and Discussion

The procedure for imaging a sample is very straightforward and differs little from traditional SEM imaging. Once the membrane has been sufficiently compressed against a sample, to establish contact, the contact area can be viewed both optically, using a reflected mode brightfiled microscope, and via the SEM. The optical imaging is useful for ensuring contact has been established prior to SEM imaging. To demonstrate the utility of this method, the contacts developed by carbon nanotube forests against an opposing membrane were studied. Figure 8.2 (A) illustrates the tips of the CNT forest coming into contact with a 15nm thick membrane. The sections of CNTs that are in contact with the membrane have been highlighted red and correspond directly with the cropped SEM image floating above the 3D model. Figure 8.2 (B) shows a typical, un-modified SEM image from these CNT contact studies. The areas of contact show up as very well distinguished bright areas in contrast to the membrane and the CNT sections that are not in intimate contact. The physical interpretation of this contrast mechanism along with the factors that influence image quality, such as primary beam energy and membrane thickness are addressed in the following sections. The CNT contact evolution is then studied as a function of applied pressure and these results are compared to thermal interface and van der Waals adhesion studies.
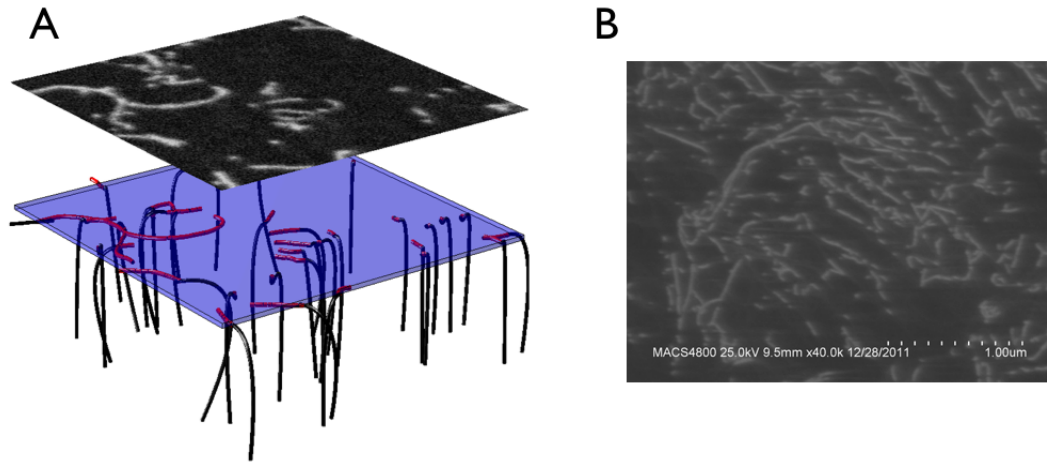
Figure 8.2: (A) 3D rendering of CNT forest making contact to a thin membrane. The section of CNTs in contact with the membrane are highlighted red. The same contact geometry was observed in the cropped SEM image hovering above the 3D model. (B) Unmodified Secondary Electron SEM image of CNT contacts to 15nm Si_3N_4 membrane imaged at 25KV.

8.4.1 Influence of beam energy and membrane thickness

The electron beam energy and the membrane thickness play an important role in the image formation. Together they govern the electron beam interaction volume, in turn setting the penetration depth, opacity of the membrane and the minimum attainable resolution. To investigate this further, several membrane thicknesses were imaged with varying acceleration voltage, after being pressed up against CNT forests. The image set in Figure 8.3 shows several SEM images taken with different acceleration voltages. All of the images are taken in the same spot of a single sample, where a

236

section of the membrane has broken, allowing simultaneous view of both the exposed CNT forest in the upper half of the image and the contacting CNTs below a 15nm Si_3N_4 membrane in the lower half. All of the images are registered to a small piece of debris in the lower right hand corner of the frame. From this image set it is clear that at higher acceleration voltages the membrane appears more translucent, making CNTs that are not in full contact with the membrane visible. At lower beam energies the contacts appear larger and more clearly distinguished from non-contacting CNTs. While there may be some broadening of the contact size due to inconsistent focusing between images, the difference between the 1keV and 25keV is too large to be explained by focus alone. The CNT widths as viewed through the nitride window were measured by hand for each acceleration voltage. It was found that the widths decrease from a maximum at 1keV of 33.5 +/- 3.7nm to a minimum at 25keV of 19.7 +/- 3.4nm. The beam interaction volume and beam broadening in the membrane is at least partially responsible for the increased size in the observed contacts.

In addition to acceleration voltage, the membrane thickness was also investigated as a variable in forming clear and accurate representations of the contacts. Thicker membranes are desirable due to their higher breaking pressure and decreased deformation for a given load. However, from these investigations it appears as though the increase in opacity with membrane thickness may offset the advantage of increased breaking pressure. While both the 50nm and 200nm membranes did produce images with some visible contacts, their features were inflated significantly, making it unclear whether individual CNTs were being image or larger agglomerates. Figure 8.4 shows

237
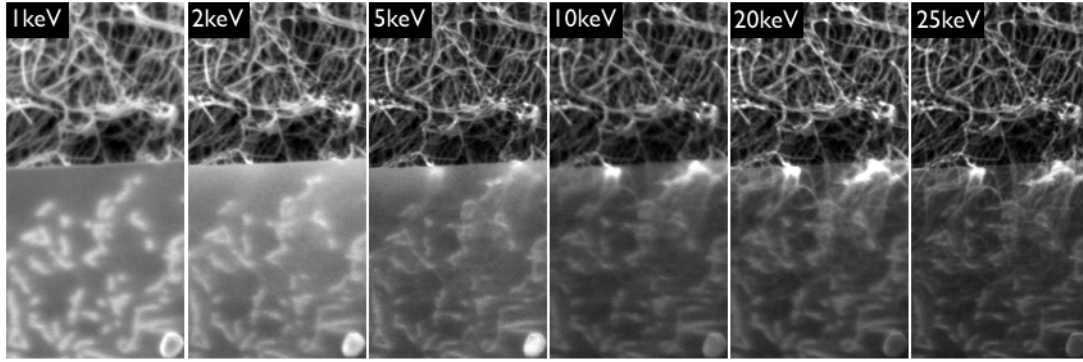
Figure 8.3: Image set of CNT forest partially covered (bottom half of image) by a 15nm thick Si_3N_4 membrane, demonstrating the importance of acceleration voltage in the image formation of the contacting surface. Each image width is one micron and the height is two microns.

the contacts formed under three different thickness membranes. The 15nm and 50nm membranes were imaged at 5keV while the 200nm membrane was imaged at 10keV due to charge accumulation at lower acceleration voltages. Fig. 8.4 (A), the 15nm membrane, clearly shows a number of CNTs making 'side-wall' contact to the membrane, with faint non-contacting CNTs below the surface. Fig. 8.4 (B) depicts the 50nm membrane with a more sparse distribution of predominantly 'tip-contacts', a clearly resolved piece of debris on the top surface of the membrane shows that the poor resolution of the contacts is not a result of focusing or astigmatism. The 200nm membrane of Fig. 8.4 (C) shows a dense distribution of contacts in which individual contact widths can no longer be distinguished due to blurring and dilation of the features through the thick membrane. This thicker membrane also suffered from charge inversion at lower accel-

eration voltages ($> \sim$ 5keV) similar to that seen by Li and others observing charging of CNT/polymer composites [129]. From these images it is clear that with increasing membrane thickness, the minimum observable feature size increases while the signal to noise ratio decreases. Although these thicker membranes are unable to reveal meaningful information about the nano-scale contacts, they may still have utility at the micro scale.
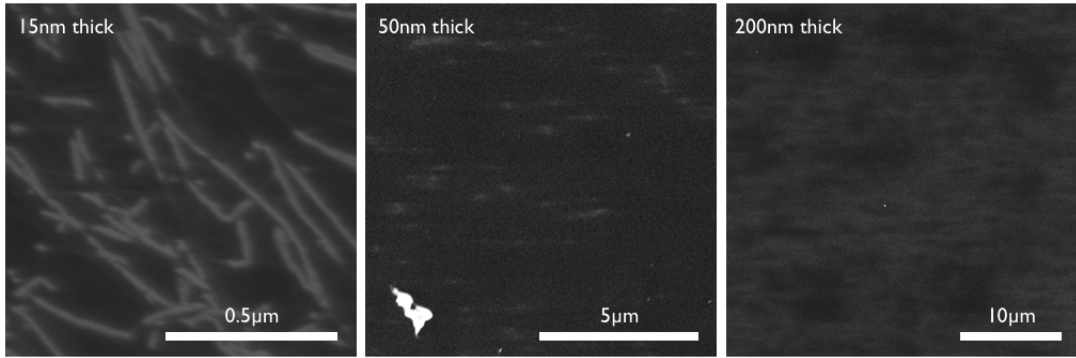

Figure 8.4: Three SEM micrographs showing different thickness membranes in contact with MWNT forests. The thicker membranes produce more blurry images with decreased resolving power and decreased signal to noise. The 15nm and 50nm were imaged with beam energy of 5keV while the 200nm membrane had to be imaged at 10keV due to charge accumulation at lower voltages.

The approach to quantifying the resolution limit is based on the effective signal producing volume. A simplified approximation to the interaction volume within a material is to use the Kanaya-Okayama range R_{KO} [130]. Developed to predict electron absorption, transmission and reflection in solid amorphous targets, R_{KO} represents

the electron penetration depth limit approximated by a sphere with its center at the maximum energy dissipation depth. It is defined as:

$$R_{KO} = \frac{0.0276 A E_0^{5/3}}{Z^{8/9} \rho} \tag{8.1}$$

where A is the atomic wight (g/mol), E_0 is the beam energy (keV), Z is the atomic number and ρ is the density (g/cm^3). However, this approach produces a gross overestimate of the beam size, one which both much larger than the thickness of the membrane and of the apparent resolution. For example, using the properties of silicon nitride and and an effective Z of 12.1, at 10keV $R_{KO} > 5\mu$m. The Kanaya-Okayama range may be sufficient for describing the interaction volume in thick solid targets but it's clearly not appropriate for thin membranes.

To more accurately evaluate the beam size as it exits the membrane, Monte Carlo (MC) simulations of electron beam interactions were performed using the *CASINO* software [131]. Simulations were performed on Si_3N_4 membranes of various thicknesses and across a range of primary beam energies, 0.5 - 29keV, with a primary beam diameter of 1nm. The trajectories of the electrons were analyzed, finding the location of those that traversed the membrane and calculating their radial distance from the center of the primary beam upon transmission. Two times the standard deviation of the beam radius was taken as the beam diameter and plotted in Figure 8.5. In addition to the Monte Carlo simulation data, lines approximating the beam diameter have been included on the plot, using the beam broadening equation described by Jonge and Ross [126]:

$$d \approx 6.1 \times 10^3 T^{3/2} \frac{Z}{E_0} \left(\frac{\rho}{A} \right)^{1/2} \qquad (8.2)$$

While the beam broadening equation shows fairly good agreement with the Monte Carlo simulations for high beam energies, it fails to predict the beam size when the range of the interaction is on the same order as the membrane thickness. This regime is particularly interesting to this work because it appears to offer greater contrast between the contacting and non-contacting surfaces, yet suffers from greater feature dilation. In this region the beam size initially increases with beam energy as the hemispherical tip of the beam protrudes out of the membrane. Figure 8.5 (A,B) show the cross sections of a few selected MC trajectories and electron exit scatter for the 15nm membrane. The initial beam broadening can be seen in these trajectories, between 0.9keV and where it reaches a maximum beam radius at 1.6keV. This corresponds to the energy at which the maximum width of the pear shaped interaction volume intersects the exit side of the membrane. In each membrane thickness, this maxima in beam size corresponds to roughly 70% electron transmission. At higher energies the beam narrows, following equation 8.2. The dashed line on the plot highlights the onset of beam transmission through the membrane and follows the asymptotic behavior of the beam size in this regime. This line follows $\propto E_0^{5/3}$ dependence similarly to the Bethe range [132] and hence the Kanaya-Okayama range described previously [130]. Lastly, the diameters of the contacts imaged in Figure 8.3 have been plotted after subtracting the mean diameter of the exposed CNTs, as determined by the image at 25keV without the membrane present. The data reduced in this way shows good agreement with the

simulation from 1-25keV

Figure 8.5 (D) shows the Monte Carlo simulation results for the transmission ratio of electrons for the three membrane thicknesses used. These plots support the observations of Figure 8.3 showing decreasing membrane opacity with increasing beam energy. Future experiments may try to image with beam energies of low to no transmission to help identify the origin of the contrast mechanism. The micrographs in Figure 8.4 for the two thicker membranes would appear to contradict the transmission behavior predicted by the MC simulations. However, it is likely that the membranes do not appear transparent due to the limited escape depth of the secondary electrons (SE). The SE escape depth for Si_3N_4 is $\lambda = 4nm$ [133] and the maximum escape depth, T $\approx$ 5λ. SEs generated deep within or below thick (>20nm) membranes may not reach the detector, leading to apparently opaque membranes. The fact that the contacts are still visible in these thick membranes is particularly interesting and may be understood by further study of the contrast mechanism.

8.4.2 Contrast mechanism

A number of research groups have used similar methods of SEM imaging through electron transparent membranes to view liquid or biological specimens [126, 127, 128]. This is a recently developed form of environmental SEM for samples that are incapable of withstanding the high vacuum of the SEM. These studies used backscattered electrons as their primary signal for image generation. They typically use Gold or Platinum colloids to stain the samples under investigation, offering high Z contrast

242
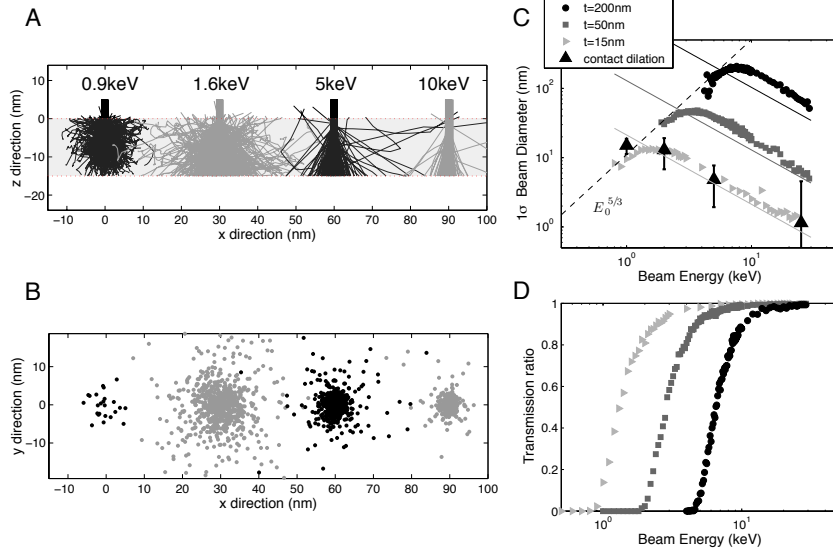
Figure 8.5: Plots of Monte Carlo (MC) simulation results for varying Si_3N_4 membrane thickness and acceleration voltage. (A) depicts a 2D cross section of selected MC trajectories for the 15nm nitride membrane, 1.6keV corresponds to the maximum beam broadening. (B) illustrates the electron scatter for the corresponding trajectories depicted in (A), as they exit the membrane. The exiting electron positions were used to calculate the beam diameters plotted in (C). The associated solid line depicts the beam broadening corresponding to each thickness from equation 8.2. The black dashed line marks the onset of transmission across the membrane and follows a $\propto E_0^{5/3}$ dependence. The black triangular data points with error bars are derived from image analysis of the contacts from Figure 8.3 and show the contact width dilation in good agreement with the beam broadening. (D) shows the MC data for the electron transmission ratio versus beam energy across each membrane.

to the water or biological material. Taking advantage of the Z contrast was not feasible in the current work due to the similarity in atomic number between the membrane, Si(14),N(7), and that of the CNTs, C(6). Coating the CNTs with a high Z material was not desired so as not to affect the contact mechanism. Therefore, all of the investigations here relied on secondary electron emission for image generation. Despite the lack of Z contrast, there is still a remarkably strong contrast between the membrane and the CNTs, particularly for the areas in intimate contact. The contrast between contacting and non-contacting areas indicates that it is not created by simple material contrast alone, rather some other mechanism related to the contact itself. This contrast has been identified as a form of voltage contrast (VC). Widely used in IC measurements, VC SEM has been observed as early as Oatley and Everhart [129] and generally refers to a phenomena whereby a change in surface potential leads to a change in brightness. VC has been identified in a number of previous CNT studies, it has been modulated via external potentials [134, 135] and has been observed to occur as a result of self charging from the electron beam current [85, 129, 136].

The present study relies on a completely passive VC mechanism, there are no external biases applied to the sample, substrate or membrane. The CNT forest is grounded through the specimen holder, thus removing any buildup of negative charge in the CNTs, although there is still the potential for the insulating nitride membrane to charge. This, along with the stark contrast between the contacting and non-contacting CNTs suggests a slightly different self charging mechanism than that proposed by Zhang et al. in which CNTs on an insulting substrate would charge negatively relative to

the positive substrate [136]. Here the difference in electric susceptibility χ between the CNT and the membrane is believed to create a potential well at the interface, capable of trapping negative charges [137]. This trapping mechanism is often seen in point defects caused by nano-inclusions, nonstoichiometry or doping, although it is also present in larger defects such as polycrystalline grain boundaries or dislocations. Recently others have attributed this trapping mechanism to charge contrast observed in CNT/polymer composites [129].

There are three distinct types of Voltage Contrast which rely on different physical mechanisms to produce a change in observed signal strength. VC type 1 is characterized as a change in SE yield due to a difference in energy of the primary electrons (PE) striking the surface. The difference in energy can be a result of a change in the acceleration voltage or from a surface potential. In order to have a significant influence on the PE energy, the surface potential must be comparable in magnitude to the PE energy, i.e. on the order of kilovolts. VC type 2 is characterized as a shift in the energy distribution of SE. This spectrum shift can be caused by a change in the surface potential which in turn changes the work function. However, large electric fields are required to appreciably change the work function [134]. VC type 3 is characterized as a deflection of the low energy ($< 50eV$) SE from an electric field. It is not clear from the present study what mechanism is responsible for the observed VC. However, we do know that the contrast is more stark at lower PE beam energies (indicative of type 1) and there still appears to be contrast for very thick membranes, much thicker than the SE escape depth. This suggests that the SE are being generated away from the contacts,

245

within the membrane. Either the contacts locally enhance the SE generation in the membrane VC type 1 or 2, or the contacts locally accelerate SE out of the membrane, VC type 3.

8.4.3 Pressure dependent contacts

The main purpose of this study is to be able to quantify the contact area and see its evolution as a function of applied pressure. The ultimate goal is to relate this area to other physical properties such as thermal contact resistance, electrical resistance or adhesive force and to help tailor materials to enhance such favorable properties. As a case study we observed the contact dynamics of MWNT forests and have related these measurements to both contact area predictions made from thermal resistance and van der Waals adhesion studies.

To begin, the MWNT sample is adhered to the substrate holder, the Si_3N_4 membrane and copper gasket are carefully brought into contact by equally tightening each spring compressing screw. Once the membrane is sufficiently close to contacting the sample, it is imaged in the SEM. The sample is imaged between each successive tightening of the screws. The force exerted by the screws was calibrated previously using a load cell and the apparent pressure is calculated using the entire area of the Si_3N_4 window. The pressure is expected to vary across the membrane surface especially in sections with greater or lesser intimate contact with the sample. A more rigorous method of quantifying the pressure is needed for future experiments and may involve measuring deflection of the membrane through optical interferometric or photogram-

metric techniques.

An example of a series of raw images are shown in Figure 8.6 (B,C and D) at different contacting pressures. After collection, these images are registered, background subtracted, intensity normalized and then cropped. Initial image analysis tests used simple thresholding to quantify the contact area, although this proved to be insufficient as small changes in threshold values resulted in large shifts in the measured area. As a result, a more robust filament tracking approach was applied using the *ImageJ* plugin *JFilament*. Originally developed for quantifying cytoskeletal structures, *JFilament* segments and tracks filaments using an open active contour method [138]. Currently this process is fairly laborious, requiring initial placement of the filaments for automatic stretching and tracking, although it offers more resilience and more detailed information about each segment. An example of the resulting image analysis can be seen in Figure 8.6 (A) where the filaments are highlighting the contacting CNTs. The complete line segment list can be saved as a series of points or a summary of the evolving filaments can be saved with length, tip and tail displacement data. Since the image analysis only fits lines to the filaments, the average contact width, $2\bar{a}_x$, has been calculated via van der Waals forces and elastic strain theory [139]. Bahadur et al. initially demonstrated this technique for Silicon nanowires and has since been illustrated by Cola et al. for MWNTs [32].

The van der Waals force for a nanowire of diameter D against a planar substrate can be calculated as described by V. Bahadur [139]:
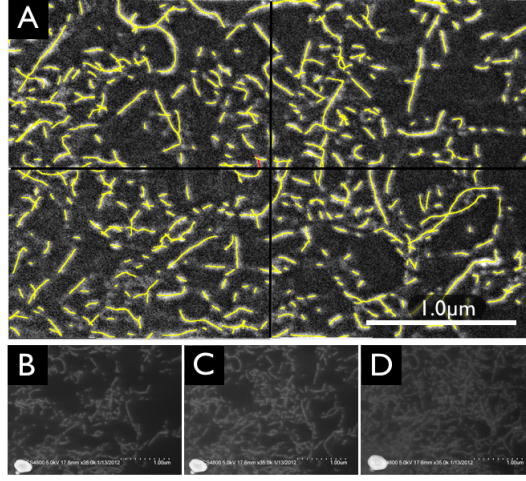
Figure 8.6: SEM images of contact pressure study. (A) shows the contacts highlighted after performing the snake image analysis. (B,C,D) show the raw images at various stages of contact.

$$F_{vdW} = -\frac{A}{pi} \sum_{i=1}^{n} \frac{\sqrt{(D - y_i)y_i}}{(y_i + l)^4} \Delta y_i \tag{8.3}$$

where A is the Hamaker constant l is the separation distance between nanowire and plane, in this case assumed to be the interlayer spacing of graphite, 0.335nm, $\Delta y_i = D/n$ is the interval for numerical integration and y_i is the center point for each interval. The Hamaker constant in vacuum between two dissimilar materials is calculated via $A_{12} = \sqrt{A_{11}A_{22}}$ and between a third material, such as H_20 - a thin layer of which is often present in ambient room conditions, via $A_{132} = (\sqrt{A_{11}}\sqrt{A_{33}})(\sqrt{A_{22}}\sqrt{A_{33}})$ [140]. A_{cnt} was found by Akita et al. to be equal to $60 \times 10^{-20} J$ [141], while $A_{Si_3N_4}$ was found in Ref. [142] and a variety of other metals were found in Ref. [140]. From this force,

248

the average contact width can be derived using the elastic strain theory outlined by Bahadur:

$$2\bar{a_x} = \left(\frac{16 F_{vdW} E_m D}{pi} \right)^{1/2} \tag{8.4}$$

where E_m is the effective modulus given by:

$$E_m = \frac{1}{2}\left[\frac{1 - \nu_s^2}{E_s} + \frac{1 - \nu_w^2}{E_w} \right] \tag{8.5}$$
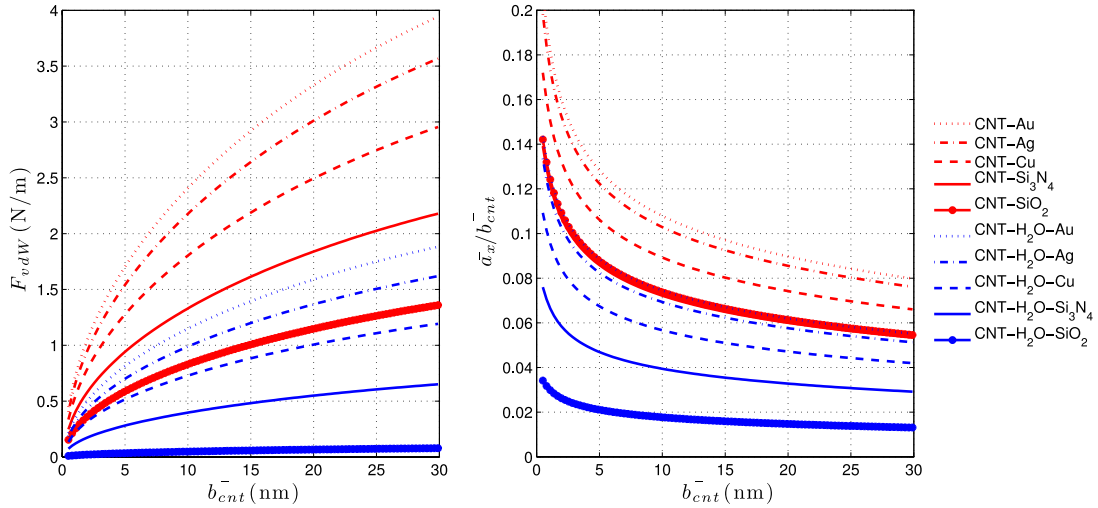
Figure 8.7: Van der Waals force F_{vdW} and normalized contact width $\bar{a_x}/\bar{b_{cnt}}$ versus CNT radius $\bar{b_{cnt}}$ for a variety of contacting substrate materials, with and without an interfacial water layer.

The Young's modulus in the radial direction was measured by Palaci to be $E_r = 30 \pm$ 10 GPa [143], very close to that of graphite along its c axis ($E_r = 36$GPa, $\nu = 0.012$)

[32]. The Young's modulus of Si_3N_4 has been reported to be between 151GPa [144] and 385GPa [145], and is highly sensitive to fabrication conditions. The Si_3N_4 values used for the elastic deformation calculations are ($E_s = 310$GPa, $\nu = 0.27$). These calculations give average contact widths that are typically less than 10% of the average CNT diameter, as can be seen in Figure 8.7. This suggests that either the previous beam broadening equations are not enough to explain the dilation of the observed contacts or, possibly more likely, that this technique does not have the resolving power to distinguish contact for segments that are in such close proximity to the membrane surface. Using the average contact width $\bar{a}_x$, the line segments produced from the image analysis, and the apparent contact area A, that of the analyzed SEM image, one can compute the real to apparent contact area as follows:

$$\frac{A_{r \cdot free-ends}}{A} = \frac{2\bar{a}_x}{A} \sum_i l_i \tag{8.6}$$

The results from the image set presented in Figure 8.6 are summarized in Figures 8.8 and 8.9. Figure 8.8 plots the real to nominal contact area as a function of applied pressure. The data is fit using the following approximation, $A_{r \cdot free-ends}/A \propto a/(1 + bP^{-1})$, where a and b are the fit parameters (a=0.005, b=145). This data is compared to an area ratio prediction for CNT contacts developed by Cola et al. using load displacement and elastic strain analysis [32]. Cola's theory fits thermal contact resistance versus pressure data for CNT forest, along with other forest attributes such as average diameter, height and volume ratio, to estimate the contact resistance and area ratio. Each of the gray curves in Figure 8.8 represents the contact established

250

for a unique CNT interface assembly, previously measured and analyzed by Cola and the affiliated group at Purdue University. These curves were reproduced using material properties and the equations described in Ref. [32]. While there is a fairly great range of area ratios, as attributed to variations in array density and compressibility by Cola, the values and trend obtained in this study match well with those predicted. Additionally Cola has demonstrated that the overall CNT resistance is dominated by the resistance at the van der Waals contact and will follow the contact area as:

$$R_{CNT} \approx \frac{R_{vdW} \cdot A}{A_{r \cdot free-ends}} \tag{8.7}$$

Given R_{vdW} found for molecular dynamics simulations of SWNT-SWNT contacts (0.1 mm$^2 \cdot$ K/W)[146] and typical values of CNT array thermal resistance (10-100 mm$^2 \cdot$ K/W), the area ratios here support this relation.

The inset of Figure 8.8 shows an added level of detail over the simple area analysis, that is made possible by the direct observation technique. Here the contact area has been evaluated based on the filament length. Contacts that have an aspect ratio of two or less ($l < 60nm$) are assumed to be 'tip' contacts, whereas those that are greater than two are assumed to be 'side wall' contact. The fits show that at very low pressures the area from these two contact mechanisms will converge and tip contact may dominate. Additionally it shows that the tip contact area saturates more quickly than the side wall contact. This behavior is expected as increased pressure will cause CNTs to buckle and slip, going from tip to side wall contact in the process. New CNTs below the top canopy can then make tip contact as the forest compresses and the process

repeats up to some saturation level. Additional data like this may help identify material

traits that are critical in tailoring the desired physical properties.
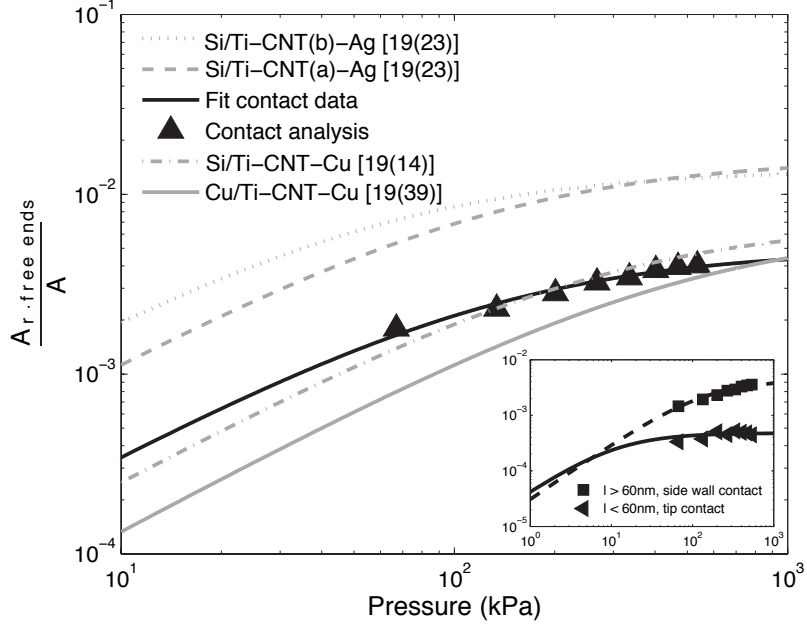

Figure 8.8: Ratio of real to apparent contact area at the MWNT tip/opposing substrate interface. The solid black line fits the triangular data points found using the contact analysis described by this study, while the gray lines show the predicted area ratios using load displacement and elastic strain analysis from Cola et al. [32]. The inset shows the contacts divided into those that have an aspect ratio less than or greater than two. Those that are less than two are assumed to be 'tip' contact while those that are greater than two are 'side wall' contact.

Figure 8.9 shows the areal density of contacts compared to the areal density of the CNT roots, all of which are assumed to be in contact with the substrate. The

predicted CNT root areal density is determined by measuring the bulk forest density ρ_f, the average CNT radius b_{CNT}^{-} and using the bulk density of graphite $\rho_{graphite}$,

$$\frac{N}{A} = \frac{\rho_f}{\rho_{graphite} \pi b_{CNT}^2}$$ (8.8)

This shows that the number of contacting tips is roughly one tenth the total number of CNTs. These measurements are supported by observations in Figure 8.3, where a number of non-contacting CNTs become visible as the membrane becomes more transparent at high acceleration voltage. It is noteworthy, in Figure 8.9, that the number of contacts saturates with pressure at a number well below the number of CNTs present. This suggests that entanglement of the forest will prevent all CNTs from directly contacting the surface. Additionally one may infer that the number of contacts may not always increase with CNT density, rather there may be some optimal density to maximize the number of contacts.

Similarly to thermal contact resistance, the study of van der Waals adhesion of CNT forests is a well suited to this contact analysis. A number of research groups have studied the van der Waals adhesion of CNT forests for their use as synthetic 'dry' adhesives, similar to gecko's feet [147, 148, 149]. Here they've seen significant adhesion strengths (>11N/cm^2), greater than natural gecko feet, yet still below the theoretically predicted values [147]. As suggested in the previous studies, falling short of the theory is likely due to incomplete contact between the CNTs and the mating substrate.

Zhao estimated a CNT areal density of 10^{10}-10^{11} tubes/cm^2, assuming that all tubes are in contact with a SiO$_2$ surface, it should be possible to generate in excess
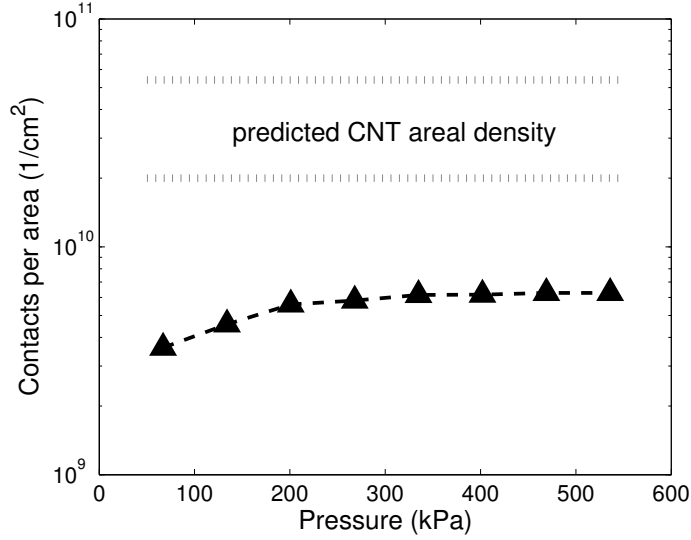
Figure 8.9: The contact areal density as a function of applied pressure, compared to the predicted CNT root areal density. Roughly one in ten CNTs make contact with the mating surface.

of $500 \ N/cm^2$. Similar analysis was performed using the contact lengths established in this study and using the same data set as portrayed in Figure 8.6. With a dry interface between the CNTs and SiO2, this data supports the theoretical adhesive strengths suggested by Zhao. However, the presence of a condensed water layer, as may form in ambient condition [139], results in values much closer to those found experimentally. The summary of these adhesion strengths are plotted in Figure 8.10.

Additionally, it is important to note that this contact analysis was performed on a very small section of the CNT array and as a result may not represent the true statistical variation of the entire forest. There is likely a distribution in the nature and

extent of the contacts at a number of different length scales. Imaging larger sections, with comparable resolution, would lead to more accurate representations of the forest.
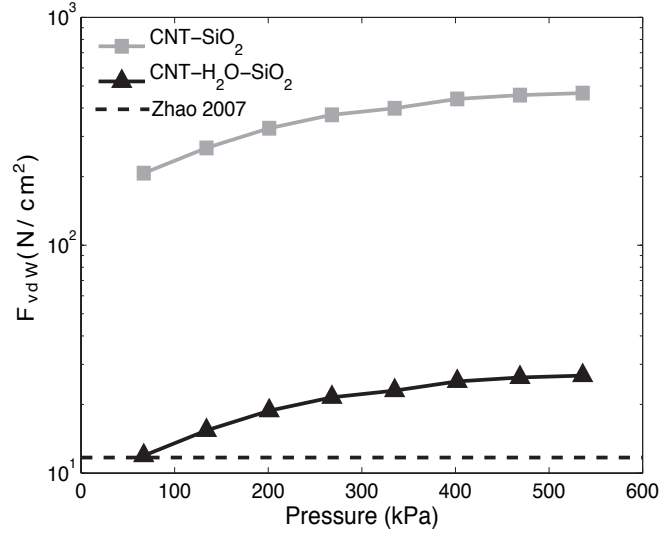

Figure 8.10: Adhesion strength of CNT contacts as determined from contact analysis. The gray square points depict the results for a dry CNT-SiO$_2$ interface, while the black triangles show the CNT-SiO$_2$ in a water environment, producing results very similar to experimental adhesive strengths found by Zhao et al.

Both of these applications, the thermal interface and the dry van der Waals adhesive, rely heavily on the real contact area established and to a lesser extent on the total number of contacts. It is clear that in order to improve their performance a greater fill factor or contact fraction is necessary. This may be achieved from a change in areal density of CNTs, an increase in compressibility, an increase in conformability of the substrate, or a more planar top surface. The effectiveness of these different approaches

may be better realized using a direct observation technique such as the one described here.

8.5   Conclusions

A new technique for observing nano sized contacts has been established using a modification to a previously established ESEM method. Contacts can be established and imaged through electron transparent membranes using an SEM. The remarkably high contrast observed, despite the lack of Z contrast, has been attributed to a voltage contrast mechanism established by trapped charges from a susceptibility gradient between the two materials. The resolution limits have been studied by way of electron beam interactions and the use of Monte Carlo simulations. It has been shown that with sufficiently thin membranes, nanometer resolution can be obtained. The utility of the technique is illustrated by observing the contact behavior of MWNTs. The real to apparent contact area measured has been compared to predictions made using load displacement and elastic strain analysis. It has been shown that the real contact area is less than 1/100th the apparent contact area even at moderate pressures and that the number of contacting CNTs is approximately 1/10th the total number of CNTs. These results confirm experimental measurement values for thermal interface resistance and van der Waals adhesion strengths.

Chapter 9

Conclusions and future work

This dissertation focuses on the problem related to scaling up the remarkable properties of the CNT to the macroscopic world. This includes scaling up the production techniques as well developing new CNT assemblies to leverage their extraordinary electrical and thermal conduction. Early work focused on the electrical conductor problem, attempting to make macroscopic, continuous wires from aligning CNT bundles using an electrospinning approach. Later work took a slight tack from the wire-making, focusing on the thermal conduction problem and attempting to use the inherent vertically aligning CNT forests, generated via chemical vapor deposition growth, to serve as a highly conducting thermal interface material. The thermal interface work also prompted the work related to scaling up the synthesis, involving the creation of a large scale CVD chamber.

The challenges of scaling up the growth process is addressed by the design, construction and testing for a four inch diameter substrate, pilot production scale,

CVD chamber. The main design optimization was placed on the production of highly uniform height and quality across the growth area. Initial tests were performed on an experimental scale hot-plate CVD chamber to identify potential design flaws. A custom design was implemented based on a dual zone hot-plate and heated shower-head. A number of implementation obstacles were mitigated, resulting in a well functioning system capable of producing highly uniform CNT growth across a four inch wafer. This system was used for the production of other CNT assemblies, designed to harness the electrical and thermal conductivity of the MWNTs.

9.1   Electrospinning CNT composites

To scale up the electron transport properties of the CNT requires the production of semi-continuous CNT wires. Due to their limited synthesis length, strong van der Waals adhesion, and highly isotropic nature, producing assemblies of such wires that perform similarly to their individual counterpart has proved challenging. The research presented here attempted to solve the problem using the electric/flow-field orientation developed during electrospinning. Micron sized, MWNT shell-PMMA core, composite fibers were prepared via a coaxial electrospinning technique. Two point electrical measurements were performed on short segments of MWNT cores following thermal degradation of the shell, showing conductivities up to two orders of magnitude higher than homogeneous MWNT/polymer composite fibers. The interaction of the polymer free core on the shell was investigated through the use of the Hansen's solubility pa-

rameters with the goal of promoting alignment, packing density, and continuity of the core.

Four core shell solution interaction regimes were explored based on their miscibility and the core solutions solvency of the shell polymer. Immiscible-solvent pairs produced the best bundled MWNT cores, though this regime had the most variation in fiber morphology, producing hollow cores, bundled cores, porous shells, and other fiber artifacts. Miscible-solvent pairs were also found to produce reasonable coaxial fibers with well ordered bundles. However, miscible-nonsolvent solutions lead to immediate coagulation of the shell and immiscible-nonsolvent pairs lead to predominantly hollow cores.

While the ultimate fiber morphology was not achieved, there is still promise for increased nanotube alignment and packing density with decreased fiber diameter. The ultimate limiting factor to this technique and other solution based CNT fiber making techniques appears to be the quality of the CNT dispersion. It is speculated that the continuity and alignment of the MWNT core could be drastically increased if a suitable CNT dispersion in the ones to tens of a weight percent were achieved.

9.2 CNT thermal interface materials

Vertically aligned MWNT forests have been investigated for a several years for their potential use as high performance thermal interface materials. Yet despite the remarkable thermal conductivity of individual CNTs and the apparently high per-

formance of vertically oriented arrays, their implementation into commercial systems has not been realized. The work here investigates their use in macroscopic thermal management applications, shedding light onto their variable performance, the factors that influence their performance and in developing new metrology tools for helping the further development of this technology.

Initial work investigated the thermal interface performance of MWNT-Silicon-MWNT assemblies using a DC, 1D reference bar thermal measurement technique. Preliminary characterization of samples revealed a significant discrepancy between the literature results and those reported here. This prompted a detailed investigation into the 1D reference bar thermal measurement, resulting in several improvements to the overall accuracy and precision. The discrepancy also motivated a higher level of scrutiny of the sample. In an attempt to control only MWNT density, a micelle template technique for accurately controlling the catalyst was pursued. While this catalyst preparation technique showed some promise, the resulting MWNTs were of too low density to form vertically aligned arrays, as a consequence no thermal characterization was performed on these samples. In lieu of the micelle controlled density study, a number of array properties were characterized as a function of growth time and temperature for MWNTs grown from sputter deposited catalyst. These studies found dramatic changes in not only height but array density and crystallinity. While not showing a clear Fourier dependence on array hight, a more complex thermal model was developed to explain the measured resistance as a function of array height and density. Based on Euler buckling, the thermal model finds that below a critical buckling pressure, the thermal resistance

decreases with ρ/L, while above this threshold the resistance decreases with L/ρ.

Self catalyzing Fecralloy substrates were investigated as a growth substrate for MWNT-metal foil-MWNT TIMs due to their malleability, ease of production, and increased CNT adhesion. Fecralloy was used without any additional catalyst and with minimal surface preparation to grow double-sided MWNT TIM assemblies. The growth behavior was studied with respect to the array morphologies, i.e. array height, density, crystallinity, and diameter distribution. The contact resistance of dozens of such samples were evaluated using a DC, 1D reference bar, thermal conductivity measurement system under vacuum. A few samples were used for pressure dependent and temperature dependent thermal resistance measurements. The temperature dependent measurements offer insight into the interfacial phonon conduction physics and are found to agree with other temperature dependent studies, suggesting inelastic scattering at the MWNT-Cu interface. Both the surface roughness of the Cu measurement bars and that of the substrate is found to influence the contact resistance, in both cases smoother surfaces reduced the resistance. Due to the challenges associated with deliberately controlling a single array morphology, a statistical approach was used for identifying the influences of the multivariate array morphology on contact resistance. Showing the strongest correlation with array height, following a $R \sim L^{-0.5}$, contradicting Fourier's law. However, this is likely a result of the mechanical compliance rather than a ballistic conduction mechanism. Finally, several attempts were made at modeling the relationship between the measured array morphologies and the contact resistance. However, the empirical relations found in the exploratory data analysis are better at describing the sample

dynamics. These drop-in-place MWNT/foil TIMs were found to have a minimum thermal resistance of 64mm^{2}K/W, nearly half that of the best performing MWNT/Silicon samples in this study. The improved performance is attributed to an increase in adhesion which was subsequently corroborated by the development of a transient thermal interface measurement apparatus.

The transient 3 omega thermal measurement technique has been adapted to characterize the thermal performance of CNT TIMs. A multi-layer, surface thermal impedance model has been extended to parallel path heat diffusion to accurately model the experimental configuration of a TIM on mating substrate. Sensitivity analysis was performed to determine the experimental configurations necessary for observing particular thermophysical properties. Several microfabricated 3 omega heaters were made on fused silica and tested to validate the technique. The 3ω measurement performance of the SiO2 compared well to the manufacturers datasheet, showing the value of the technique. These heaters on SiO2 then served as the mating substrate for CNT TIM testing. MWNTs grown on both silicon and fecralloy substrate were analyzed using a range of contact pressures. The contact resistances at the CNT-opposing substrate (CNT-OS) and growth substrate-CNT (GS-CNT) interfaces were fit to the thermal spectroscopy measurements. In the case of the silicon substrate growth, $R_{CNT\text{-}GS}$ was found to dominate the TIM resistance at $200mm^2K/W$, while $R_{OS\text{-}CNT}$ showed the expected inverse pressure relationship with values between 100-50mm^2K/W. The Fecralloy grown MWNTs were found to perform much better with the contact resistance dominated by the free-ends and still exhibiting the inverse pressure relationship. The

growth substrate to CNT resistance was found to be $\sim 2mm^2/W$, while the mating substrate to CNT resistance ranged from $\sim 50 - 35mm^2K/W$ for pressures range of 50 - 150 kPa, showing good agreement with the samples characterized using the 1D reference bar technique.

To better understand the mechanisms limiting the thermal contact resistance of CNT TIMs, a new technique for observing nano sized contacts has been established using a modification to a previously established ESEM method. Contacts can be established and imaged through electron transparent membranes using an SEM. The remarkably high contrast observed, despite the lack of Z contrast, has been attributed to a voltage contrast mechanism established by trapped charges from a susceptibility gradient between the two materials. The resolution limits have been studied by way of electron beam interactions and the use of Monte Carlo simulations. It has been shown that with sufficiently thin membranes, nanometer resolution can be obtained. The utility of the technique is illustrated by observing the contact behavior of MWNTs. The real to apparent area measured has been compared to predictions made using load displacement and elastic strain analysis. It has been shown that the real contact area is less than 1/100th the apparent contact area even at moderate pressures and that the number of contacting CNTs is approximately 1/10th the total number of CNTs. These results confirm experimental measurement values for thermal interface resistance and van der Waals adhesion strengths.

To fully understand the factors that influence CNT TIM performance allowing for optimization and their eventual use in commercial products requires a level of

scrutiny not yet realized. The ultimate limiting factor in the thermal resistance of these systems is that of the free end contact to mating substrate. This contact resistance is proportional to the real contact area (sum of all point or line contacts of each CNT in contact). The number of contacts and or length of line contacts is largely dependent upon the mechanical and topological properties of the CNT forest. Better understanding of the forests mechanical compliance is critical to developing high performance TIMs. Better systematic studies of the array morphologies coupled with in-situ mechanical compliance and surface contact area analysis during thermal testing are required to fully understand and optimize the array for minimized contact resistance.

Appendix A

Appendix

A.1 Hot-plate calculations

Goals:

- Maximize heating uniformity across heater plate

- Reach a minimum temperature of 750°

A.1.0.1 Maximize heating uniformity

Since the power emitted from a joule heater is proportional to the length of the wire, we want to make the surface area per unit wire, constant across the hot plate. This is easy given a square geometry but becomes slightly more difficult with the circular hot-plate. We want Power/Area = constant

$$P = i^2 R \tag{A.1}$$

$$R = \rho \frac{L_{wire}}{A_{wire}}, \tag{A.2}$$

where ρ and A_{wire} are constant. Therefore:

$$\frac{L_{wire}}{Area} = constant \tag{A.3}$$

$$\frac{2\pi ra}{ra22 - ra12} = constant \tag{A.4}$$

which contains one equation, but two unknowns, need another condition. The area on each side of the wire, i.e. A1 and A2, should be equal.

$$A1 = A2 \tag{A.5}$$

Given these two equations, two unknowns and the starting point that the minimum dimension between two adjacent wires should be 7.63mm $\sim$ 8.0mm due to surface arching between wires (note: this is also related to the applied voltage), we can work our way backwards from the, finding out the constant for L_{wire}/Area, then finding the dimensions for section A and working out B, C, etc. As it turns out, the radii dont differ considerably after section B...

A.1.0.2 Reach a minimum temperature of 750°C

Temperature estimated using Stephan-Boltzmanns (SB) law for radiation emitted from a black body:

$$\sigma T^4 = \frac{P}{S}, \tag{A.6}$$

where σ is the SB coefficient, $5.67x10^{-12}$ [W/cm^{2}K], P is power emitted, and S is the surface area. Rearranging terms leads to:

$$P = \sigma S T^4 \tag{A.7}$$

Since we're breaking the heater up into two elements, one containing the first 2in in radius and the second extending from 2in to 2.75in, we can calculate the power emitted for each section assuming our target temperature of 750°C. Given these power values we can estimate the current needed given a fixed voltage, a fixed wire length, and a fixed wire resistance.

Were using Omegas NIC80-020-188 wire which has an R = 3.574 ohm/in = 1.407 ohm/cm.

A1: 0-2in

P1 = (5.67e-12)(pi(2in*2.54cm/1in)2)(750C + 273)4 = 503W

L1_total \sim ra+rb+rc+rd = 0.4168 + 0.8336 + 1.2505 + 1.6673 = 4.1682in

R1_total = L1_total * 3.574 ohm/in = 4.1682in * 3.574 ohm/in = 14.897 ohm

P = i2R => i = sqrt(P/R) i1 = sqrt(503W/14.897ohm) = 5.81A

```
V=iR V1 = 5.81A* 14.897ohm = 86.55V
```

A2: 2-2.75in

```
P1 = (5.67e-12)(pi(2in*2.54cm/1in - 2.75in*2.54cm/1in)2)(750C + 273)4 = 448W

L2_total ~ re+rf = 2.0841 + 2.501 = 4.5851in

R2_total = L2_total * 3.574 ohm/in = 4.5851in * 3.574 ohm/in = 16.887 ohm

i1 = sqrt(448W/16.887ohm) = 5.15A

V1 = 5.15A* 16.887ohm = 86.97V
```

These voltages tie back into the geometry of the design, and should be within the surface breakdown voltage of the ceramic.

A.2   Code

A.2.1   3 omega data analysis

Main program

```
1  %testing  stackImpedance  for  multilayer
   clear;
3  tic


5  %% ——————————————— heater  properties ———————————————
   h=heater('heater_22');
```

```matlab
7
%% ———————————————————— material properties
         ————————————————
9 material_prop01;


11 %% ————————————————— Loading data ——————————————————————
   %22 micron heater files
13 file_list = {'1303','1304','1305','1306','1307','1308','1309','1310',
   '1311','1312','1313','1314','1315','1316','1317','1318'};
15

   pressure = [4.1285, 4.8195, 5.9252, 6.9388, 7.9523, 8.9658, 9.9794,
17    10.9929, 10.9929, 9.9794, 8.9658, 7.9523, 6.9388, 5.9252,
      4.8195, 4.1285]./7.5e−5;    % Pa, N/m^2
19

   meas_ref=measurement('1320',h);
21

   for i = 1:length(file_list);
23      file_list{i};
        meas(i)=measurement(file_list{i}, h);     % passing a file list
25    % with measurement data and a heater object to each measurement
   end
27 start=1;


29 % load layers in material stack
   layers(1) = layer('SiO2_GE124_22um',−1);
31 layers(2) = layer('Fecralloy',1);
```

269

```matlab
layers(3) = layer('CNT_22um',2);
layers(4) = layer('fSiO2',3);


% Fit coefficient constructor arrays
D = [0,0,0,0,0];
E = [1,0,0,1,0;
     0,0,0,2,0;
     0,0,0,0,0];


saveDir='./22um_fits/11/';
saveName = '22um_fit';


%% ---------------------------- function definitions ------------------------


[c,lw_bds,up_bds]=material_stack.fit_coefficient_constructor(layers,D,E,
    meas);
for i=1:length(meas(:));
    meas(i).my_index = i;
end


%% ---------------------------- fit methods
   ------------------------------


chi2=@(c) fit_fn.reduced_chi2(layers,D,E,meas,c,start,h);


problem = createOptimProblem('fmincon', ...
```

```
                                    'objective', chi2, ...
57                                  'x0', c, ...
                                    'lb', lw_bds, ...
59                                  'ub', up_bds, ...
                                    'options',optimset( ...
61                                  'Display','iter','TolFun',1e-8,'TolX',
            1e-8,'MaxIter',200,'MaxFunEvals',8000))

63

   ms = MultiStart('StartPointsToRun','bounds');
65 [cfit fval eflag output manymins] = run(ms, problem, 1)


67 %% ——————————————————————— error analysis
        ———————————————————

   sig = fit_fn.fit_parameter_error(layers,D,E,meas,cfit,start,h)
69

   %% ——————————————————— plotting results ———————————————————
71
```

./chapters/appendix/3omega/fitting3omega.m

Model fitting fuctions

```
   classdef fit_fn
2      %   class definition for 3 omega chi squared fitting and model
       %
```

```matlab
4
        methods (Static)
6           % reduced_chi2
            function chi2 = reduced_chi2(layers, D, E, meas, c, start, heater)
8               value = 0;
                total_elements = 0;
10              for i=1:length(meas(:));
                    tmp_f_eval = fit_fn.model(material_stack(layers,D,E,meas,c
                        ,i),meas(i).x(meas(i).subset),heater);
12                  value = value + sum(((meas(i).Zr(meas(i).subset)'-real(
                        tmp_f_eval))./meas(i).sig_Zr(meas(i).subset)').^2)...
                        + sum(((meas(i).Zi(meas(i).subset)'-imag(tmp_f_eval)
                            )./meas(i).sig_Zr(meas(i).subset)').^2);
14                  total_elements = total_elements + 2*numel(meas(i).x(meas(i
                        ).subset));
                end
16              chi2 = value ./ (total_elements-length(c));
            end
18

            % chi2
20          function chi2 = chi2(layers, D, E, meas, c, start, heater)
                value = 0;
22              for i=1:length(meas);
                    tmp_f_eval = fit_fn.model(material_stack(layers,D,E,meas,c
                        ,i),meas(i).x(meas(i).subset),heater);
24                  value = value + sum(((meas(i).Zr(meas(i).subset)'-real(
```

```matlab
                        tmp_f_eval ))./ meas ( i ). sig_Zr ( meas ( i ). subset ) ').^2) ...
                            + sum ((( meas ( i ). Zi ( meas ( i ). subset ) '-imag (
                                tmp_f_eval ))./ meas ( i ). sig_Zr ( meas ( i ).
                                subset ) ').^2);
            end
            chi2 = value ;
        end


        % SSE
        function SSE = SSE ( layers , D, E, meas , c, start , heater )
            SSE=0;
            for i =1:length ( meas )
                tmp = ( fit_fn . model ( material_stack ( layers ,D,E, meas ,c,i ) ,
                    meas ( i ). x( meas ( i ). subset ), heater ));
                SSE = SSE+sum (( meas ( i ). Zr ( meas ( i ). subset ) ' - real ( tmp ))
                    .^2) ...
                    +sum (( meas ( i ). Zi ( meas ( i ). subset ) ' - imag ( tmp )).^2);
            end
        end

        % TSS - Total Sum of Squares
        function TSS = TSS ( meas , start )
            TSS=0;
            for i =1:length ( meas )
                TSS = TSS+sum ((( meas ( i ). Zr ( meas ( i ). subset ) ' - mean (( meas ( i
```

273

```matlab
                       ).Zr(meas(i).subset)))).^2)...
46                      +sum(((meas(i).Zi(meas(i).subset))' - mean((meas(i).Zi
                          (meas(i).subset)))).^2));
                end
48          end


50          % Rsquared - 1-SSE/TSS
            function R2 = Rsquared(layers, D, E, meas, c, start, heater)
52              R2 = 1-fit_fn.SSE(layers, D, E, meas, c, start, heater)/fit_fn
                    .TSS(meas,start);
            end
54


56          % plot_residuals
            function res = plot_residuals(layers, D, E, meas, c,start,heater)
58              %figure();
                %clf;
60              hold on;
                for i=1:length(meas)
62                  tmp = (fit_fn.model(material_stack(layers,D,E,meas,c,i),
                        meas(i).x(meas(i).subset),heater));
                    res(:,i) = ((meas(i).Zr(meas(i).subset)' - real(tmp))) +1i
                        *((meas(i).Zi(meas(i).subset)' - imag(tmp)));
64                  semilogx(meas(i).x(meas(i).subset),((meas(i).Zr(meas(i).
                        subset)' - real(tmp))),'rs');
                    semilogx(meas(i).x(meas(i).subset),((meas(i).Zi(meas(i).
```

```
                       subset ) ' − imag ( tmp ) ) ) , 'bo ' ) ;

66            end

              %ylim ( [ 0 , ( mean ( res )+.05∗std ( res ) ) ] )

68            set ( gca , 'xscale ' , 'log ' ) ;

        end

70

        % fit_parameter_error

72      function  sig = fit_parameter_error ( layers , D, E, meas , c , start ,
            heater )

            Fs=@( c )  ( fit_fn . f_fit ( layers , D, E, meas , c , start , heater ) ) ;

74          J = jacobianest ( Fs , c ) ;

            A=J . '∗ J ;

76          Ai=inv (A) ;

78          SSE=fit_fn .SSE( layers ,D,E, meas , c , start , heater ) ;

80          N_data_pts = 0;

            for  i =1: length ( meas )

82              N_data_pts = N_data_pts + numel ( meas ( i ) . Zr ( meas ( i ) . subset )
                    ) + numel ( meas ( i ) . Zi ( meas ( i ) . subset ) ) ;

            end

84

            tsig=sqrt (Ai .∗SSE . / ( N_data_pts−length ( c ) )  ) ;

86          sig = diag ( tsig ) ';

        end

88
```

275

```matlab
            % f_fit

            function out = f_fit(layers, D, E, meas, c, start, heater)


                for i=1:length(meas);
                    if i == 1
                        out = [real(fit_fn.model(material_stack(layers,D,E,
                            meas,c,i),meas(i).x(meas(i).subset),heater)');...
                        imag(fit_fn.model(material_stack(layers,D,E,meas,c,i),
                            meas(i).x(meas(i).subset),heater)')];
                    else
                    out = [out; [real(fit_fn.model(material_stack(layers,D,E,
                        meas,c,i),meas(i).x(meas(i).subset),heater)');...
                        imag(fit_fn.model(material_stack(layers,D,E,meas,c,i),
                            meas(i).x(meas(i).subset),heater)')]];
                    end
                end


            end


        % The model
        function [value] = model(stack,x,heater)
            if isempty(stack.A)
                value = fit_fn.modelB(stack,x,heater);
            elseif isempty(stack.B)
                value = fit_fn.modelA(stack,x,heater);
            else
```

276

```matlab
                value = ((1./stackImp(stack.A, x, heater.b, 2)...
                +1./stackImp(stack.B, x, heater.b, 2)).^-1);

                end
        end


        function [value] = modelA(stack,x,heater)
                value = stackImp(stack.A, x, heater.b, 2);
        end


        function [value] = modelB(stack,x,heater)
                value = stackImp(stack.B, x, heater.b, 2);
        end
    end
end
```

./chapters/appendix/3omega/fit_fn.m

Measurement class

```matlab
classdef measurement
    % Class to represent a measurement


    properties
        base_file   % ex 1320, from with the real, 1320.0 and imaginery,
            1320.1, parts are pulled
        description % first line of the Regular data file (ie. the
```

```matlab
                commented line )

            x
8           v_3w          % real part of 3 omega voltage
            phase
10          imag_v_3w    % imaginary part of 3 omega voltage
            Zi            % thermal surface impedence, imaginary part
12          Zr            % thermal surface impedence, real part
            Zp
14          sig_Zi        % standard deviation of thermal surface impedence,
                imaginary part
            sig_Zr        % standard deviation of thermal surface impedence,
                imaginary part
16          my_index
            steps
18          Vs
            subset
20      end


22      methods
            function obj=measurement(base_file, heater)
24              obj.base_file = base_file;
                R_file = strcat(obj.base_file,'.0');
26              I_file = strcat(obj.base_file,'.1');
                obj.x=1*(logspace(log10(1),log10(10000),length(load(R_file))))
                    ';
28              tmp = find(obj.x <= 1);
```

278

```matlab
                 obj.subset = [tmp(end):length(obj.x)];

30               obj.v_3w = load(R_file);

                 obj.phase = load(I_file);

32               obj.imag_v_3w = obj.v_3w.*tand(obj.phase);

                 [obj.Zi,obj.sig_Zi,p] = V2Z_Bridge02(100, 100, heater.R0,
                     heater.R0, heater.Vs, heater.length, heater.b, heater.alpha
                     , obj.imag_v_3w);

34               [obj.Zr,obj.sig_Zr,p] = V2Z_Bridge02(100, 100, heater.R0,
                     heater.R0, heater.Vs, heater.length, heater.b, heater.alpha
                     , obj.v_3w);

                 obj.Zp = ((obj.Zr+1i*obj.Zi).^-1 + 1i*4*pi.*obj.x*heater.
                     thickness*heater.rho*heater.C).^-1;

36               material_prop01;

            end

38      end

end
```

./chapters/appendix/3omega/measurement.m

Material stack class

```matlab
1 classdef material_stack
     %UNTITLED8 Summary of this class goes here
3    %   Detailed explanation goes here


5    properties
```

```matlab
            A
            B
        end

        methods (Static)
            function [c,lw_bds,up_bds] = fit_coefficient_constructor(layers,D,
                E,meas)
                layerIndex = [layers.index];
                [sortedLayers, index] = sort(layerIndex);
                positiveIndex = find(sortedLayers > 0);
                negativeIndex = find(sortedLayers < 0);


                F=[D;E];
                F1i = length(find(F == 1));
                %sprintf('%d experimental variables',F1i)
                F2i = length(find(F == 2))*length(meas);
                %sprintf('%d experimental variables',F2i)


                c=zeros(1,(F1i+F2i));
                lw_bds=zeros(1,(F1i+F2i));
                up_bds=zeros(1,(F1i+F2i));



                if length(F(:,1)) ~= length(layers)
                    sprintf('error: layers dont match input constructor matrix
                        length')
```

```matlab
            end

            c1i = 1;
            c2i = 1;


            for i = 1:2
                for j = 1:length(index)
                    for k = 1:5
                        if F(j,k) == i
                            switch i
                                case 1
                                    switch k
                                        case 1
                                            c(c1i) = layers(index(j)).
                                                kappa;
                                            lw_bds(c1i) = layers(index(j))
                                                .kappa/10;
                                            up_bds(c1i) = layers(index(j))
                                                .kappa*10;
                                            c1i=c1i+1;
                                        case 2
                                            c(c1i) = layers(index(j)).
                                                alpha;
                                            lw_bds(c1i) = layers(index(j))
                                                .alpha/10;
                                            up_bds(c1i) = layers(index(j))
```

```
                                    . alpha *10;
51                              c1i=c1i+1;
                            case 3
53                              c(c1i) = layers(index(j)).psi;
                                lw_bds(c1i) = layers(index(j))
                                    .psi/10;
55                              up_bds(c1i) = layers(index(j))
                                    .psi*10;
                                c1i=c1i+1;
57                          case 4
                                c(c1i) = layers(index(j)).R;
59                              lw_bds(c1i) = layers(index(j))
                                    .R/100;
                                up_bds(c1i) = layers(index(j))
                                    .R*100;
61                              c1i=c1i+1;
                            case 5
63                              c(c1i) = layers(index(j)).H;
                                lw_bds(c1i) = layers(index(j))
                                    .H/10;
65                              up_bds(c1i) = layers(index(j))
                                    .H*10;
                                c1i=c1i+1;
67                      end


69                  case 2
```

```matlab
        for l=1:length(meas)
            switch k
                case 1
                    c((c1i-1)+(c2i-1)*length(
                        meas)+l) = layers(index
                        (j)).kappa;
                    lw_bds((c1i-1)+(c2i-1)*
                        length(meas)+l) =
                        layers(index(j)).kappa
                        /10;
                    up_bds((c1i-1)+(c2i-1)*
                        length(meas)+l) =
                        layers(index(j)).kappa
                        *10;
                case 2
                    c((c1i-1)+(c2i-1)*length(
                        meas)+l) = layers(index
                        (j)).alpha;
                    lw_bds((c1i-1)+(c2i-1)*
                        length(meas)+l) =
                        layers(index(j)).alpha
                        /10;
                    up_bds((c1i-1)+(c2i-1)*
                        length(meas)+l) =
                        layers(index(j)).alpha
                        *10;
```

```matlab
            case 3
                c((c1i-1)+(c2i-1)*length(
                    meas)+l) = layers(index
                    (j)).psi;
                lw_bds((c1i-1)+(c2i-1)*
                    length(meas)+l) =
                    layers(index(j)).psi
                    /10;
                up_bds((c1i-1)+(c2i-1)*
                    length(meas)+l) =
                    layers(index(j)).psi
                    *10;
            case 4
                c((c1i-1)+(c2i-1)*length(
                    meas)+l) = layers(index
                    (j)).R;
                lw_bds((c1i-1)+(c2i-1)*
                    length(meas)+l) =
                    layers(index(j)).R/10;
                up_bds((c1i-1)+(c2i-1)*
                    length(meas)+l) =
                    layers(index(j)).R*10;
            case 5
                c((c1i-1)+(c2i-1)*length(
                    meas)+l) = layers(index
                    (j)).H;
```

```matlab
                                                lw_bds((c1i-1)+(c2i-1)*
                                                    length(meas)+l) = ...
                                                    layers(index(j)).H/10;
                                                up_bds((c1i-1)+(c2i-1)*
                                                    length(meas)+l) = ...
                                                    layers(index(j)).H*10;
                                            end
                                        end
                                c2i=c2i+1;
                                    end
                            end
                        end
                    end
                end
            end


    end


    methods
        function obj = material_stack(layers,D,E, meas,c, measIndex);
            layerIndex = [layers.index];
            [sortedLayers, index] = sort(layerIndex);
            positiveIndex = find(sortedLayers > 0);
            negativeIndex = find(sortedLayers < 0);

```

```matlab
            F=[D;E];
            %F1i = length(find(F == 1));
            %sprintf('%d experimental variables',F1i)
            %F2i = length(find(F == 2))*length(meas);
            %sprintf('%d experimental variables',F2i)

            if length(F(:,1)) ~= length(layers)
                sprintf('error: layers dont match input constructor matrix
                    length')
            end

            %if length(positiveIndex) > 0
            C=zeros(length(sortedLayers), 5);
            c1i = 1;
            c2i = 1;

            for i = 0:2
                for j = 1:length(index)
                    for k = 1:5
                        if F(j,k) == i
                            switch i
                                case 0
                                    switch k
                                        case 1
                                            C(j,k) = layers(index(j)).
                                                kappa;
```

```matlab
                                        case 2
                                            C(j,k) = layers(index(j)).
                                                alpha;
                                        case 3
                                            C(j,k) = layers(index(j)).psi;
                                        case 4
                                            C(j,k) = layers(index(j)).R;
                                        case 5
                                            C(j,k) = layers(index(j)).H;
                                    end
                                case 1
                                    C(j,k) = c(c1i);
                                    c1i=c1i+1;
                                case 2
                                    C(j,k) = c(c2i*measIndex + (c1i-1));
                                    c2i=c2i+1;
                                end
                            end
                        end
                    end
                end


            obj.A=C(negativeIndex,:);
            obj.B=C(positiveIndex,:);

        end
```

```
161          end


163  end
```

./chapters/appendix/3omega/material_stack.m

Layer class

```
     classdef layer
2          % class to define a material layer in 3 omega measurement


4            properties
                 file
6                name
                 index
8                kappa          % thermal conductivity (W/mK)
                 alpha          % thermal diffusivity (m^2/s)
10               psi            % thermal isotropy in−plane to cross−plane (unitless)
                 R              % thermal boundary resistance (m^2−K/W)
12               H              % height (m)
                 rho            % density (kg/m^3)
14               c              % specific heat capacity (J/kg−K)
                 s              % volumetric heat capacity (J/m^3−K)
16  % bounds
                 b_kappa
18               b_alpha
```

```matlab
            b_psi

20          b_R

            b_H

22

        end

24

        methods

26          function obj=layer(file, index)

                obj.file=file;

28              obj.index = index;

                eval(file, ';');

30              obj.name = material_type;

                obj.rho = rho;

32              obj.kappa = kappa;

                obj.c = c;

34              obj.alpha = obj.kappa/(obj.rho*obj.c);

                obj.psi = mpsi;

36              obj.R = R;

                obj.H = H;

38              obj.s = obj.c*obj.rho;

                % bounds

40              obj.b_kappa=[obj.kappa/10, obj.kappa*10];

                obj.b_alpha=[obj.alpha/10, obj.alpha*10];

42              obj.b_psi=[obj.psi/10, obj.psi*10];

                obj.b_R=[obj.R/10, obj.R*10];

44              obj.b_H=[obj.H/10, obj.H*10];
```

289

```
            end
46      end


48 end
```

./chapters/appendix/3omega/layer.m

heater data

```
1 %% ———————————————————— heater properties ————————————————————

%Heater details

3 heater_width=22e−6;

b=heater_width/2;

5 %H=2nm Cr, 150nmPd, 100nm SiO2

heater_thickness = 150e−9;

7 %heater_thickness = 300e−9;

H_e = heater_thickness;

9 heater_length = 2983e−6;

heater_area = heater_width*heater_length;

11 R0=136.9;


13 TCR = [−18.8  130.7;

      4.7  134.4;

15      20.9   136.9;

      56.8   142.1;

17      75.5   144.8];
```

```matlab
[alpha ,S1]=polyfit(TCR(: ,1) ,TCR(: ,2) ,1);


% reference fit
alphafit_sio2 = 7.28e-07;
kfit_sio2 = 1.56;


%supply voltage
Vs = 1.5;


% heater material Palladium
rho = 12.023e3;  %g/cm^3 *1kg/1000g *(100cm/1m)^3 kg/m^3
kappa = 71.8e0;     %W/m-K
cm = 25.98;                 %J mol?1 K?1
at = 106.42e-3;                 %kg/mol
C = cm/at;  %J/kg-K
alpha = k_sio2/(rho_sio2*c_sio2); % (m^2/s)
```

./chapters/appendix/3omega/heater_22.m

CNT data

```matlab
%CNT
material_type = 'CNT_22um';
rho = 0.151 * (100)^3/1000;    %kg/m^3 this is taken from the mean of all
    FeCr data.
```

291

```matlab
4  kappa = 50;              % this value is taking air into account

   s = 550*1000;      %KJ/m^3-K * 1000 J/m^3-K      volumetric heat capacity

6  c = (s/rho);

   %alphae_cnt = ke_cnt/(rho_cnt*c_cnt); % (m^2/s)

8  alpha = kappa/s; % (m^2/s)

   R = 2e-5;

10 H = 17.7e-6;

   mpsi = 1;
```

./chapters/appendix/3omega/CNT_22um.m

Fecralloy data

```matlab
1  %Fecralloy

   material_type = 'Fecralloy';

3  rho = 7.22 * (100)^3/1000;   %kg/m^3

   kappa = 16e0;      %W/m-K

5  c = 0.460*1000;   %J/kg-K

   %alpha = k_FeCr/(rho_FeCr*c_FeCr); % (m^2/s)

7  mpsi = 1;

   R = 2e-5;

9  H = 0.9e-3;
```

./chapters/appendix/3omega/Fecralloy.m

Thin film SiO2 data

```
1  %GE sputtered quartz, film
   material_type = 'SiO2$_{film}$';
3  rho = 2.2e3;  %kg/m^3
   kappa = 1.4e0;      %W/m-K
5  c = 670;  %J/Kg-K              specific heat capacity
   alpha = kappa/(rho*c); % (m^2/s)
7  mpsi = 1;
   R = 1e-7;
9  H = 250e-9;
```

./chapters/appendix/3omega/fsio2.m

Bulk SiO2 data

```
1  %GE 124 quartz
   material_type = 'SIO2$_{GE124-22um}$';
3  rho = 2.2e3;                      %kg/m^3
   kappa = 1.4767e0;                 %W/m-K
5  alpha = 6.1676e-7;                %m^2/s
   %alpha = kappa/(rho*c);           %m^2/s
7  c=kappa/(rho*alpha);
   mpsi = 1;
9  R = 0;
   H = 1e-3;
```

Silicon data

```matlab
% material properties for Si
material_type = 'Silicon';
rho = 2.329 * (100)^3/1000; % (g/cm^3) * (100)^3/1000 = (kg/m^3)
kappa = 149; % (W/mK)
c = 0.7 * 1000; % (J/kg-K)
%alpha = kappa/(rho*c); % (m^2/s)
mpsi = 1e0;
R = 2e-5;       % I assume units of m^2-K/W ie 10mm^2-K/W = 1e-5m^2-K/W
H = 500e-6;
```

./chapters/appendix/3omega/Si.m

A.2.2   CNT contact width via $\mathbf{F}_{vdW}$ and elastic strain theory

This is a simple matlab script to calculate the contact width of a CNT lying against a plane surface. It is based off the work done by Bahadur [139] using elastic strain theory and van der Waals forces to calculate the contact width 'ax'. It requires an array containing the CNT diameter, the equilibrium spacing between CNT and surface, and the substrate material type defined by an integer, 1 through 12 corresponding to the material combinations listed in the case statements below.

```matlab
% function to compute the contact area of a CNT given the diameter
    equilibrium
% spacing between the two bjects and the surface materials upon which it's
% lying.


% compute the Van der Waals force of a nanowire on a plane following the
% equations outlined in Bahadur:2005 and the values from Cola:2009,
% Visser:1989 and Bergstrom:1997us


function [Fvdw, ax] = ax_bcnt(params)
% params = [diameter equilibrium_spacing material_type];


%D = 10e-9;       %D is the diameter of the nanowire
%l = 0.335e-9;   %l is the equilibrium spacing between the two objects


D = params(1);
l = params(2);


A_cnt = 60e-20;       %A is the Hamaker constant in this case between a CNT
    and metal Akita:2000tm


A_Au_Au = (3/(4*pi)*14.3)*1.602e-19;     %Visser:1989
A_Au_H2O = (3/(4*pi)*9.85)*1.602e-19;    %Visser:1989
A_Si_Si = (3/(4*pi)*6.76)*1.602e-19;     %Visser:1989
A_Si_H2O = (3/(4*pi)*3.49)*1.602e-19;    %Visser:1989
A_Cu_Cu = (3/(4*pi)*8.03)*1.602e-19;     %Visser:1989
```

```matlab
25   A_Cu_H2O = (3/(4*pi)*4.68)*1.602e−19;   %Visser:1989

     A_H2O_H2O = (3/(4*pi)*1.43)*1.602e−19;  %Visser:1989

27   A_Si3N4_Si3N4 = 16.7e−20;          % Bergstrom:1997us

     A_Si3N4_H2O_SI3N4 = 4.85e−20;     % Bergstrom:1997us

29   A_Diamond_air_Si3N4 = 22.0e−20;   % Bergstrom:1997us

     A_Diamond_H2O_Si3N4 = 7.94e−20;   % Bergstrom:1997us

31   A_Ag_Ag = (3/(4*pi)*11.7)*1.602e−19;     %Visser:1989

     A_SiO2_SiO2 = 6.5e−20;               % Israelachvili:2011ug

33

     switch params(3)

35       case 1

             %A_cnt_Si3N4

37           A_xy = sqrt(A_cnt*A_Si3N4_Si3N4);

             Es = 310e9;

39           Vs = 0.27;

         case 2

41           %A_cnt_H2O_Si3N4

             A_xy = (sqrt(A_cnt)−sqrt(A_H2O_H2O))*(sqrt(A_Si3N4_Si3N4)−sqrt(
                 A_H2O_H2O));

43           Es = 310e9;

             Vs = 0.27;

45       case 3

             %A_cnt_Cu

47           A_xy = sqrt(A_cnt*A_Cu_Cu);

             Es = 128e9;     % wiki

49           Vs = 0.34;       % wiki
```

296

```matlab
    case 4
        %A_cnt_H2O_Cu
        A_xy = (sqrt(A_cnt)-sqrt(A_H2O_H2O))*(sqrt(A_Cu_Cu)-sqrt(A_H2O_H2O
            ));
        Es = 128e9;      % wiki
        Vs = 0.34;       % wiki
    case 5
        %A_cnt_Si
        A_xy = sqrt(A_cnt*A_Si_Si);
        Es = 188e9;      % wiki
        Vs = 0.28;       % wiki
    case 6
        %A_cnt_H2O_Si
        A_xy = (sqrt(A_cnt)-sqrt(A_H2O_H2O))*(sqrt(A_Si_Si)-sqrt(A_H2O_H2O
            ));
        Es = 188e9;      % wiki
        Vs = 0.28;       % wiki
    case 7
        %A_cnt_Au
        A_xy = sqrt(A_cnt*A_Au_Au);
        Es = 79e9;       % wiki
        Vs = 0.44;       % wiki
    case 8
        %A_cnt_H2O_Au
        A_xy = (sqrt(A_cnt)-sqrt(A_H2O_H2O))*(sqrt(A_Au_Au)-sqrt(A_H2O_H2O
            ));
```

```matlab
73          Es = 79e9;        % wiki
            Vs = 0.44;        % wiki
75      case 9
            %A_cnt_Ag
77          A_xy = sqrt(A_cnt*A_Ag_Ag);
            Es = 83e9;        % wiki
79          Vs = 0.37;        % wiki
        case 10
81          %A_cnt_H2O_Ag
            A_xy = (sqrt(A_cnt)-sqrt(A_H2O_H2O))*(sqrt(A_Ag_Ag)-sqrt(A_H2O_H2O
                ));
83      case 11
            %A_cnt_SiO2
85          A_xy = sqrt(A_cnt*A_SiO2_SiO2);
            Es = 41e9;        % http://accuratus.com/fused.html
87          Vs = 0.17;        % http://accuratus.com/fused.html
        case 12
89          %A_cnt_H2O_SiO2
            A_xy = (sqrt(A_cnt)-sqrt(A_H2O_H2O))*(sqrt(A_SiO2_SiO2)-sqrt(
                A_H2O_H2O));
91          Es = 41e9;        % http://accuratus.com/fused.html
            Vs = 0.17;        % http://accuratus.com/fused.html
93 end


95 n = 1000;        %number of intervals in numerical integration
```

```matlab
97  yi = 0:D/n:D;

    f = sqrt((D-yi).*yi)./(yi+l).^4;
99  F = trapz(yi,f);


101 %Es = 310e9;

    Ew = 36e9;
103 %Vs = 0.27;

    Vw = 0.012;
105 Em = 1/2*(((1-Vs^2)/Es)+((1-Vw^2)/Ew));


107 Fvdw = A_xy/pi*F;

    b = 1/2*((16*Fvdw*Em*D)./pi).^(1/2);   %b is half the contact width

109
    ax = b/D;
```

./chapters/appendix/ax_bcnt.m

299

Bibliography

[1] R. Saito, G. Dresselhaus, and M. Dresselhaus, *Physical Properties of Carbon Nanotubes*, Carbon, **38** (2000).

[2] R. H. Baughman, *CHEMISTRY: Dangerously Seeking Linear Carbon*, Science, **312**, pp. 1009–1110 (2006).

[3] R. R. Tykwinski, W. Chalifoux, S. Eisler, A. Lucotti, M. Tommasini, D. Fazzi, M. Del Zoppo, and G. Zerbi, *Toward carbyne: Synthesis and stability of really long polyynes*, Pure and Applied Chemistry, **82**, pp. 891–904 (2010).

[4] K. S. Novoselov, *Electric Field Effect in Atomically Thin Carbon Films*, Science, **306**, pp. 666–669 (2004).

[5] A. K. Geim and K. S. Novoselov, *The rise of graphene*, nature materials, **6**, pp. 183–191 (2007).

[6] A. A. Balandin, S. Ghosh, W. Bao, I. Calizo, D. Teweldebrhan, F. Miao, and C. N. Lau, *Superior Thermal Conductivity of Single-Layer Graphene*, Nano Letters, **8**, pp. 902–907 (2008).

[7] H. W. Kroto, J. R. Heath, S. C. O'Brien, R. F. Curl, and R. E. Smalley, *C60: Buckminsterfullerene*, Nature, **318**, pp. 162–163 (1985).

[8] J. Li, C. Alan, and B. Cruden, *Encyclopedia of Nanoscience and Nanotechnology: Vertically Aligned Carbon Nanostructures*, volume 25, American Scientific Publishers, 1 edition (2011).

[9] M. S. Dresselhaus and P. C. Eklund, *Phonons in carbon nanotubes*, Advances in Physics, **49**, pp. 705–814 (2000).

[10] J. Hone, *Phonons and thermal properties of carbon nanotubes*, Carbon Nanotubes, **80**, pp. 273–286 (2001).

[11] *Armchair Quantum Wire project*, <http://aqw.smalley.rice.edu/>.

[12] M. Yu, B. Files, and R. Ruoff, *Tensile Loading of Ropes of Single Wall Carbon Nanotubes and their Mechanical Properties*, Physical Review Letters, **84**, pp. 5552–5555 (2000).

[13] G. Demczyk, M. Wang, J. Cumings, M. Hetman, W. Han, A. Zettl, and R. Ritchie, *Direct mechanical measurement of the tensile strength and elastic modulus of multiwalled carbon nanotubes*, Materials Science and Engineering, **334**, pp. 173–178 (2002).

[14] Wikipedia, *Carbon Nanotube* (published Dec. 8, 2008; last accessed Dec. 8, 2008), <http://en.wikipedia.org/wiki/Carbon_nanotube.

[15] Y.-L. Li, *Direct Spinning of Carbon Nanotube Fibers from Chemical Vapor Deposition Synthesis*, Science, **304**, pp. 276–278 (2004).

[16] M. Zhang, K. Atkinson, and R. Baughman, *Multifunctional Carbon Nanotube Yarns by Downsizing an Ancient Technology*, Science, **306**, pp. 1358–1361 (2004).

[17] X. Zhang, Q. Li, T. G. Holesinger, P. N. Arendt, J. Huang, P. D. Kirven, T. G. Clapp, R. F. Depaula, X. Liao, Y. Zhao, L. Zheng, D. E. Peterson, and Y. Zhu, *Ultrastrong, Stiff, and Lightweight Carbon-Nanotube Fibers*, Advanced Materials, **19**, pp. 4198–4201 (2007).

[18] M. Zhang, S. Fang, A. Zakhidov, S. Lee, A. Aliev, C. Williams, K. Atkinson, and R. Baughman, *Strong, Transparent, Multifunctional, Carbon Nanotube Sheets*, Science, **309**, pp. 1215–1219 (2005).

[19] L. Ericson, H. Fan, H. Peng, V. Davis, , W. zhou, J. Sulpizio, Y. Wang, R. Booker, J. Vavro, C. Guthy, , A. Nicholas, , G. Parra-Vasquez, M. Kim, , S. Ramesh, R. Saini, C. Kittrell, L. G, H. Schmidt, W. Adams, W. Billups, M. Pasquali, W. Hwang, R. Hauge, J. Fischer, and R. Smalley, *Macroscopic, Neat, Single-Walled Carbon Nanotube Fibers*, Science, **305**, pp. 1447–1450 (2004).

[20] B. Vigolo, A. Penicaud, C. Coulon, C. Sauder, R. Pailler, C. Journet, P. Bernier, and P. Poulin, *Macroscopic Fibers and Ribbons of Oriented Carbon Nanotubes*, Science, **290**, pp. 1331–1334 (2000).

[21] C. H. Liu, H. Huang, Y. Wu, and S. S. Fan, *Thermal conductivity improvement*

of silicone elastomer with carbon nanotube loading, Applied Physics Letters, **84**, p. 4248 (2004).

[22] T. Tong, Y. Zhao, L. Delzeit, and A. Kashani, *Dense vertically aligned multi-walled carbon nanotube arrays as thermal interface materials*, IEEE Transactions on Components and Packaging . . . , **30**, pp. 92–99 (2007).

[23] B. Cola, J. Xu, C. Cheng, X. XU, T. Fisher, and H. Hu, *Photoacoustic character-ization of carbon nanotube array thermal interfaces*, Journal of Applied Physics, **101**, p. 054,313 (2007).

[24] J. Xu and T. Fisher, *Enhanced Thermal Contact Conductance Using Carbon Nan-otube Array Interfaces*, IEEE Transactions on Components and Packaging . . . (2006).

[25] J. Xu and T. Fisher, *Enhancement of thermal interface materials with carbon nanotube arrays*, International Journal of Heat and Mass Transfer, **49**, pp. 1658–1666 (2006).

[26] B. Cola, P. Amama, X. XU, and T. Fisher, *Effects of growth temperature on car-bon nanotube array thermal interfaces*, Journal of Heat Transfer, **130**, p. 114,503 (2008).

[27] B. Cola, S. L. Hodson, X. XU, and T. S. Fisher, *Carbon nanotube array ther-mal interfaces enhanced with paraffin wax*, ASME 2008 Heat Transfer Summer Conference (2008).

[28] R. Cross, B. A. Cola, T. Fisher, X. Xu, K. Gall, and S. Graham, *A metallization and bonding approach for high performance carbon nanotube thermal interface materials*, Nanotechnology, **21**, p. 445,705 (2010).

[29] S. Aradhya, S. Garimella, and T. Fisher, *Electrothermally bonded carbon nanotube interfaces*, Thermal and Thermomechanical Phenomena in Electronic Systems, 2008. ITHERM 2008. 11th Intersociety Conference on, pp. 1071–1077.

[30] B. Cola, X. XU, and T. Fisher, *Increased real contact in thermal interfaces: A carbon nanotube/foil material*, Applied Physics Letters, **90**, p. 093,513 (2007).

[31] B. Cola, X. XU, and T. S. Fisher, *Aluminum Foil/Carbon Nanotube Thermal Interface Materials*, Proceedings of ASME/JSME Thermal Engineering Summer Heat Transfer, Vancouver, BC, Canada, **2**, pp. 901–903 (2007).

[32] B. A. Cola, J. Xu, and T. S. Fisher, *Contact mechanics and thermal conductance of carbon nanotube array interfaces*, International Journal of Heat and Mass Transfer, **52**, pp. 3490–3503 (2009).

[33] S. Iijima, *Helical microtubules of graphitic carbon*, Nature, **354**, pp. 56–58 (1991).

[34] M. Dresselhaus, *Carbon Nanotubes: Synthesis, Structure, Properties, and Applications*, Berlin ; New York : Springer, 2001 (2001).

[35] T. Guo, P. Nikolaev, A. Thess, D. T. Colbert, and R. E. Smalley, *Catalytic growth of single-walled manotubes by laser vaporization*, Chemical Physics Letters, **243**, pp. 49–54 (1995).

[36] R. L. Vander Wal, G. M. Berger, and L. J. Hall, *Single-Walled Carbon Nanotube Synthesis via a Multi-stage Flame Configuration*, J Phys Chem B, **106**, pp. 3564–3567 (2002).

[37] G. Pirio, P. Legagneux, D. Pribat, K. Teo, M. Chhowalla, G. Amaratunga, and W. I. Milne, *Fabrication and electrical characteristics of carbon nanotube field emission microcathodes with an integrated gate electrode*, Nanotechnology, **13**, p. 1 (2001).

[38] B. A. Cruden and A. M. Cassell, *Vertically oriented carbon nanofiber based nano-electromechanical switch*, IEEE Transactions On Nanotechnology, **5**, pp. 350–355.

[39] S. M. Kim, C. L. Pint, P. B. Amama, D. N. Zakharov, R. H. Hauge, B. Maruyama, and E. A. Stach, *Evolution in Catalyst Morphology Leads to Carbon Nanotube Growth Termination*, The Journal of Physical Chemistry Letters, **1**, pp. 918–922 (2010).

[40] R. Bhowmick, *Kinetics of carbon nanotube growth with application in hydrogen storage*, Ph.D. thesis, Stanford University (2011).

[41] X. Liu, T. P. Bigioni, Y. Xu, A. M. Cassell, and B. A. Cruden, *Vertically aligned dense carbon nanotube growth with diameter control by block copolymer micelle catalyst templates*, The Journal of Physical Chemistry B, **110**, pp. 20,102–20,106 (2006).

[42] L. Delzeit, I. McAninch, B. A. Cruden, D. Hash, B. Chen, J. Han, and M. Meyyap-

pan, *Growth of multiwall carbon nanotubes in an inductively coupled plasma reactor*, Journal of Applied Physics, **91**, p. 6027 (2002).

[43] B. Sundaray, V. Subramanian, T. Natarajan, and K. Krishnamurthy, *Electrical conductivity of a single electrospun fiber of poly (methyl methacrylate) and multiwalled ...*, Applied Physics Letters, **88**, pp. 143,114–143,117 (2006).

[44] G. Wang, Z. Tan, X. Liu, S. Chawda, J.-S. Koo, V. Samuilov, and M. Dudley, *Conducting MWNT/poly(vinyl acetate) composite nanofibres by electrospinning*, Nanotechnology, **17**, pp. 5829–5835 (2006).

[45] L. Liu, D. Tasis, M. Prato, and H. Wagner, *Tensile Mechanics of Electrospun Multiwalled Nanotube/Poly (methyl methacrylate) Nanofibers**, Advanced Materials, **19**, pp. 1228–1233 (2007).

[46] F. Ko, Y. Gogotsi, A. Ali, N. Naguib, H. Ye, and G. Yang, *Electrospinning of Continuous Carbon Nanotube-Filled Nanofiber Yarns**, J. Am. Chem. Soc, **15**, pp. 1161–1165 (2002).

[47] J. Liu, T. Wang, T. Uchida, and S. Kumar, *Carbon nanotube core-polymer shell nanofibers*, Journal of Applied Polymer Science, **96**, pp. 1992–1995 (2005).

[48] H. Hou, J. Ge, J. Zeng, Q. Li, D. Reneker, and A. Greiner, *Electrospun polyacrylonitrile nanofibers containing a high concentration of well-aligned multiwall ...*, Chem. Mater, **17**, pp. 967–973 (2005).

306

[49] E. Malone and H. Lipson, *Fab@Home: the personal desktop fabricator kit*, Rapid Prototyping Journal, **13**, pp. 245–255 (2007).

[50] S. Reznik, A. Yarin, E. Zussman, and L. Bercovici, *Evolution of a compound droplet attached to a core-shell nozzle under the action of a strong . . .* , Physics of Fluids, **18**, pp. 062,101–062,114 (2006).

[51] O. Guise, J. Ahner, M. Jung, and P. Goughnour, *Reproducible electrochemical etching of tungsten probe tips*, Nano Letters, **2**, pp. 191–193 (2002).

[52] T. Song, Y. Zhang, T. Zhou, C. Lim, S. Ramakrishna, and B. Liu, *Encapsulation of self-assembled FePt magnetic nanoparticles in PCL nanofibers by coaxial electrospinning*, Chemical Physics Letters, **415**, pp. 317–322 (2005).

[53] D. W. v. D. W. Krevelen, *Properties of polymers : their correlation with chemical structure, their numerical estimation and prediction from additive group contributions / by D.W. van Krevelen.*, Elsevier (1990).

[54] M. Hansen, Charles, *Hansen solubility parameters*, Boca Raton: CRC Press (2007).

[55] A. L. Yarin, E. Zussman, J. H. Wendorff, and A. Greiner, *Material encapsulation and transport in core?shell micro/nanofibers, polymer and carbon nanotubes and micro/nanochannels*, Journal of Materials Chemistry, **17**, pp. 2585–2599 (2007).

[56] M. Bognitzki, W. Czado, T. Frese, and A. Schaper, *Nanostructured Fibers via Electrospinning*, Advanced Materials, **13**, pp. 70–72 (2001).

[57] E. Zussman, A. Yarin, A. Bazilevsky, and R. Avrahami, *Electrospun Polyacrylonitrile/Poly (methyl methacrylate)-Derived Turbostratic Carbon Micro-/ . . .* , Advanced Materials, **18**, pp. 348–353 (2006).

[58] H. Ham, Y. Choi, and I. Chung, *An explanation of dispersion states of single-walled carbon nanotubes in solvents and aqueous surfactant solutions using solubility parameters*, Journal of Colloid and Interface Science, **286**, pp. 216–223 (2005).

[59] M. Dresselhaus, G. Dresselhaus, R. Saito, and A. Jorio, *Raman spectroscopy of carbon nanotubes*, Physics Reports, **409**, pp. 47–99 (2005).

[60] A. Matsushita, Y. Ren, K. Matsukawa, H. Inoue, Y. Minami, I. Noda, and Y. Ozaki, *Two-dimensional Fourier-transform Raman and near-infrared correlation spectroscopy studies of poly (. . .* , Vibrational Spectroscopy, **24**, pp. 171–180 (2000).

[61] P. Temple and C. Hathaway, *Multiphonon Raman Spectrum of Silicon*, Physical Review B, **7**, pp. 3685–3697 (1973).

[62] C. Thompson, G. Chase, A. Yarin, and D. Reneker, *Effects of parameters on nanofiber diameter determined from electrospinning model*, Polymer, **48**, pp. 6913–6922 (2007).

[63] D. Li and Y. Xia, *Electrospinning of Nanofibers: Reinventing the Wheel?*, Advanced Materials, **16**, pp. 1151–1170 (2004).

[64] P. Ajayan, M. Terrones, A. de la Guardia, and V. Huc, *Nanotubes in a Flash-Ignition and Reconstruction*, Science, **296**, p. 705 (2002).

[65] B. Panchapakesan, S. Lu, K. Sivakumar, K. Taker, G. Cesarone, and E. Wickstrom, *Single-wall carbon nanotube nanobomb agents for killing breast cancer cells*, NanoBioTechnology, **1**, pp. 133–139 (2005).

[66] *International technology roadmap for semiconductors*, online (last accessed Oct. 23, 2012), <http://www.itrs.net/Links/2010ITRS/Home2010.htm>.

[67] C. Madhusudana, *Thermal Contact Conductance*, Springer-Verlag (1996).

[68] D. Cahill, W. Ford, K. Goodson, G. Mahan, A. Majumdar, H. Maris, R. Merlin, and S. Phillpot, *Nanoscale thermal transport*, Journal of Applied Physics, **93**, p. 793 (2003).

[69] H.-K. Lyeo and D. Cahill, *Thermal conductance of interfaces between highly dissimilar materials*, Physical Review B, **73**, p. 144,301 (2006).

[70] B. Gundrum, D. Cahill, and R. Averback, *Thermal conductance of metal-metal interfaces*, Physical Review B, **72**, p. 245,426 (2005).

[71] C. J. M. Lasance, *The urgent need for widely-accepted test methods for thermal interface materials*, pp. 123–128 (2003).

[72] X. Liu, Y. Zhang, A. Cassell, and B. Cruden, *Implications of catalyst control for carbon nanotube based thermal interface materials*, Journal of Applied Physics, **104**, p. 084,310 (2008).

[73] Y. Gao, T. Kodama, Y. Won, S. Dogbe, L. Pan, and K. E. Goodson, *Impact of nanotube density and alignment on the elastic modulus near the top and base surfaces of aligned multi-walled carbon nanotube films*, Carbon, **50**, pp. 3789–3798 (2012).

[74] Y. Won, Y. Gao, M. A. Panzer, S. Dogbe, L. Pan, T. W. Kenny, and K. E. Goodson, *Mechanical characterization of aligned multi-walled carbon nanotube films using microfabricated resonators*, Carbon, **50**, pp. 347–355 (2012).

[75] P. Wesling, *13th IEEE InterSociety Conference on Thermal Phenomena in Electronic Systems*, Technical report (2012).

[76] J. Yu, A. Yee, and R. Schwall, *Thermal conductance of Cu/Cu and Cu/Si interfaces from 85 K to 300 K*, Cryogenics, **32**, pp. 610–615 (1992).

[77] J. Wolberg, *Data analysis using the method of least squares: extracting the most information from experiments*, Springer, 1 edition (2006).

[78] P. Misra and J. Nagaraju, *Thermal gap conductance at low contact pressures (<1MPa): Effect of gold plating and plating thickness*, International Journal of Heat and Mass Transfer, **53**, pp. 5373–5379 (2010).

[79] M. A. Panzer, H. M. Duong, J. Okawa, J. Shiomi, B. L. Wardle, S. Maruyama, and K. E. Goodson, *Temperature-Dependent Phonon Conduction and Nanotube Engagement in Metalized Single Wall Carbon Nanotube Films*, Nano Letters, pp. A–F (2010).

[80] R. Bennett, G. Xiong, Z. Ren, and R. Cohen, *Using block copolymer micellar thin films as templates for the production of catalysts for carbon nanotube growth*, Chemistry of materials, **16**, pp. 5589–5595 (2004).

[81] R. D. Bennett, A. J. Hart, and R. E. Cohen, *Controlling the Morphology of Carbon Nanotube Films by Varying the Areal Density of Catalyst Nanoclusters Using Block-Copolymer Micellar Thin Films*, Advanced Materials, **18**, pp. 2274–2279 (2006).

[82] X. Liu, T. Bigioni, Y. Xu, A. Cassell, and B. Cruden, *Vertically aligned dense carbon nanotube growth with diameter control by block copolymer micelle catalyst templates*, The Journal of Physical Chemistry B, **110**, pp. 20,102–20,106 (2006).

[83] J. Israelachvili, *Intermolecular and Surface Forces* (2011).

[84] R. Bennett, A. Miller, N. Kohen, P. Hammond, D. Irvine, and R. Cohen, *Strategies for controlling the planar arrangement of block copolymer micelles and inorganic nanoclusters*, Macromolecules, **38**, pp. 10,728–10,735 (2005).

[85] T. Brintlinger, Y. Chen, T. Dürkop, E. Cobas, M. Fuhrer, J. Barry, and J. Melngailis, *Rapid imaging of nanotubes on insulating substrates*, Applied Physics Letters, **81**, p. 2454 (2002).

[86] S. Pal, S. Talapatra, S. Kar, L. Ci, R. Vajtai, T. Borca-Tasciuc, L. Schadler, and P. Ajayan, *Time and temperature dependence of multi-walled carbon nanotube growth on Inconel 600*, Nanotechnology, **19**, p. 045,610 (2008).

[87] K. Zhang, Y. Chai, M. Yuen, and D. Xiao, *Carbon nanotube thermal interface material for high-brightness light-emitting-diode cooling*, Nanotechnology (2008).

[88] Y. Zhang, Y. Xu, and E. Suhir, *Effect of rapid thermal annealing (RTA) on thermal properties of carbon nanofibre (CNF) arrays*, Journal of Physics D: Applied Physics, **39**, p. 4878 (2006).

[89] Z. Gao, K. Zhang, and M. Yuen, *Fabrication of carbon nanotube thermal interface material on aluminium alloy substrates*, pp. 1401–1408 (2010).

[90] J. Gaillard, M. Skove, and A. M. Rao, *Mechanical properties of chemical vapor deposition-grown multiwalled carbon nanotubes*, Applied Physics Letters, **86**, p. 233,109 (2005).

[91] P. Kim, L. Shi, A. Majumdar, and P. McEuen, *Thermal transport measurements of individual multiwalled nanotubes*, Physical Review Letters, **87**, p. 215,502 (2001).

[92] M. Fujii, X. Zhang, H. Xie, H. Ago, K. Takahashi, T. Ikuta, H. Abe, and T. Shimizu, *Measuring the thermal conductivity of a single carbon nanotube*, Physical Review Letters, **95**, p. 65,502 (2005).

[93] S. Pal, Y. Son, T. Borca-Tasciuc, and D. Borca, *Thermal and electrical transport along MWCNT arrays grown on Inconel substrates*, Journal of Materials Research (2008).

[94] J. Xu and T. Fisher, *Enhanced thermal contact conductance using carbon nanotube*

arrays, Thermal and Thermomechanical Phenomena in Electronic Systems, 2004. ITHERM'04. The Ninth Intersociety Conference on, **2**, pp. 549–555 Vol. 2 (2004).

[95] S. Talapatra, S. Kar, S. Pal, R. Vajtai, L. Ci, P. Victor, M. Shaijumon, S. Kaur, O. Nalamasu, and P. Ajayan, *Direct growth of aligned carbon nanotubes on bulk metals*, Nature nanotechnology, **1**, pp. 112–116 (2006).

[96] T. Hiraoka, T. Yamada, K. Hata, D. N. Futaba, H. Kurachi, S. Uemura, M. Yumura, and S. Iijima, *Synthesis of Single- and Double-Walled Carbon Nanotube Forests on Conducting Metal Foils*, J. Am. Chem. Soc, **128**, pp. 13,338–13,339 (2006).

[97] L. Camilli, M. Scarselli, S. Del Gobbo, P. Castrucci, F. Nanni, E. Gautron, S. Lefrant, and M. De Crescenzi, *The synthesis and characterization of carbon nanotubes grown by chemical vapor deposition using a stainless steel catalyst*, Carbon, **49**, pp. 3307–3315 (2011).

[98] D. L. Niemann, J. Silan, J. L. Killian, K. R. Schwanfelder, M. Rahman, M. Meyyappan, and C. V. Nguyen, *Carbon Nanotube Field Emission Devices with Integrated Gate for High Current Applications*, pp. 456–459 (2008).

[99] M. Oye, S. Yim, A. Fu, K. Schwanfelder, M. Meyyappan, and C. Nguyen, *Surface Smoothness Effect for the Direct Growth of Carbon Nanotubes on Bulk FeCrAl Metal Substrates*, Journal of Nanoscience and Nanotechnology, **10**, p. 4082 (2010).

[100] C. Masarapu and B. Wei, *Direct Growth of Aligned Multiwalled Carbon Nanotubes on Treated Stainless Steel Substrates*, Langmuir, **23**, pp. 9046–9049 (2007).

[101] E. Pop, D. Mann, Q. Wang, K. Goodson, and H. Dai, *Thermal conductance of an individual single-wall carbon nanotube above room temperature*, Nano Letters, **6**, pp. 96–100 (2005).

[102] A. Cassell, B. Cruden, Q. Ngo, and J. Li, *Thermal Contact Resistance and Thermal Conductivity of a Carbon Nanofiber*, Journal of Heat Transfer, **128**, pp. 234–239 (2006).

[103] J. L. Abot, V. Raghavan, G. Li, and E. L. Thomas, *Effect of Interface, Height and Density of Long Vertically Aligned Carbon Nanotube Arrays on Their Thermal Conductivity: An Experimental Study*, Journal of Nanoscience and Nanotechnology, **11**, pp. 115–124 (2011).

[104] H. Xie, A. Cai, and X. Wang, *Thermal diffusivity and conductivity of multiwalled carbon nanotube arrays*, Physics Letters A, **369**, pp. 120–123 (2007).

[105] X. Hu, A. Padilla, J. Xu, and T. Fisher, *3-omega measurements of vertically oriented carbon nanotubes on silicon*, Journal of Heat Transfer, **128**, pp. 1109–1113 (2006).

[106] R.-S. Chu, Y. Zhao, C. P. T. Grigoropoulos, and T. P. in Electronic Systems ITherm 2012 13th IEEE Intersociety Conference on, *Effect of copper surface roughness on thermal conductance of copper/carbon nanotube array interface*, in *Ther-*

mal and Thermomechanical Phenomena in Electronic Systems (ITherm), 2012 13th IEEE Intersociety Conference on.

[107] C. Chang, D. Okawa, H. Garcia, A. Majumdar, and A. Zettl, *Breakdown of Fourier's Law in Nanotube Thermal Conductors*, Physical Review Letters, **101**, p. 075,903 (2008).

[108] P. M. Norris, J. L. Smoyer, J. C. Duda, and P. E. Hopkins, *Prediction and Measurement of Thermal Transport Across Interfaces Between Isotropic Solids and Graphitic Materials*, Transactions of the ASME-C-Journal of HeatTransfer, **134**, p. 20,910 (2012).

[109] N. Birge and S. Nagel, *Widefrequency specific heat spectrometer*, Review of Scientific Instruments, **58**, pp. 1464–1470 (1987).

[110] I. Moon, Y. Jeong, and S. Kwun, *The 3ω technique for measuring dynamic specific heat and thermal conductivity of a liquid or solid*, Review of Scientific Instruments, **67**, pp. 29–35 (1996).

[111] S. Choi, J. Kim, and D. Kim, *3ω method to measure thermal properties of electrically conducting small-volume liquid*, Review of Scientific Instruments, **78**, p. 084,902 (2007).

[112] B. W. Olson, S. Graham, and K. Chen, *A practical extension of the 3ω method to multilayer structures*, Review of Scientific Instruments, **76**, p. 053,901 (2005).

[113] D. Cahill, *Thermal conductivity measurement from 30 to 750 K: the 3ω method*, Review of Scientific Instruments, **61**, pp. 802–808 (1990).

[114] T. Yamane, N. Nagai, S. Katayama, and M. Todoki, *Measurement of thermal conductivity of silicon dioxide thin films using a 3ω method*, Journal of Applied Physics, **91**, p. 9772 (2002).

[115] D. Cahill and R. Pohl, *Thermal conductivity of amorphous solids above the plateau*, Physical Review B, **35**, p. 4067 (1987).

[116] N. Birge and S. Nagel, *Specific-heat spectroscopy of the glass transition*, Physical Review Letters, **54**, p. 2674 (1985).

[117] H. S. Carslaw and J. C. Jaeger, *Conduction of heat in solids*, Clarendon Press, 2 edition (1986).

[118] T. Borca-Tasciuc and A. Kumar, *Data reduction in 3ω method for thin-film thermal conductivity determination*, Review of Scientific Instruments (2001).

[119] D. Cahill, M. Katiyar, and J. Abelson, *Thermal conductivity of a-Si: H thin films*, Physical Review B, **50**, p. 6077 (1994).

[120] G. Chen, S. Zhou, D.-Y. Yao, C. Kim, X. Zheng, Z. Liu, and K. Wang, *Heat conduction in alloy-based superlattices*, in *Thermoelectrics, 1998. Proceedings ICT 98. XVII International Conference on*, pp. 202–205 (1998).

[121] J. Kim, A. Feldman, and D. Novotny, *Application of the three omega thermal con-*

ductivity measurement method to a film on a substrate of finite thickness, Journal of Applied Physics, **86**, p. 3959 (1999).

[122] D. Jung, T. Kwon, D. Bae, I. Moon, and Y. Jeong, *Fully automated dynamic calorimeter*, Measurement Science and Technology, **3**, p. 475 (1992).

[123] S.-M. Lee, *Thermal conductivity measurement of fluids using the 3ω method*, Review of Scientific Instruments, **80**, p. 024,901 (2009).

[124] Z. L. Wang, Q. Li, and D. W. Tang, *Experimental Reconstruction of Thermal Parameters in CNT Array Multilayer Structure*, International Journal of Thermophysics, **32**, pp. 1013–1024 (2011).

[125] K. Woo and T. Thomas, *Contact of rough surfaces: a review of experimental work*, Wear, **58**, pp. 331–340 (1980).

[126] N. de Jonge and F. Ross, *Electron microscopy of specimens in liquid*, Nature nanotechnology, **6**, pp. 695–704 (2011).

[127] S. Thiberge, O. Zik, and E. Moses, *An apparatus for imaging liquids, cells, and other wet samples in the scanning electron microscopy*, Review of Scientific Instruments, **75**, p. 2280 (2004).

[128] H. Nishiyama, M. Suga, T. Ogura, Y. Maruyama, M. Koizumi, K. Mio, S. Kitamura, and C. Sato, *Atmospheric scanning electron microscope observes cells and tissues in open medium through silicon nitride film*, Journal of Structural Biology, **169**, pp. 438–449 (2010).

[129] W. Li, S. T. Buschhorn, K. Schulte, and W. Bauhofer, *The imaging mechanism, imaging depth, and parameters influencing the visibility of carbon nanotubes in a polymer matrix using an SEM*, Carbon, **49**, pp. 1955–1964 (2011).

[130] K. Kanaya and S. Okayama, *Penetration and energy-loss theory of electrons in solid targets*, Journal of Physics D: Applied Physics, **5**, p. 43 (1972).

[131] D. Drouin, A. Couture, D. Joly, X. Tastet, V. Aimez, and R. Gauvin, *CASINO V2. 42—A Fast and Easytouse Modeling Tool for Scanning Electron Microscopy and Microanalysis Users*, Scanning, **29**, pp. 92–101 (2007).

[132] D. Joy and C. Joy, *Low voltage scanning electron microscopy*, Micron, **27**, pp. 247–263 (1996).

[133] J. Fijol, A. Then, G. Tasker, and R. Soave, *Secondary electron yield of SiO_2 and Si_3N_4 thin films for continuous dynode electron multipliers*, Applied Surface Science, **48**, pp. 464–471 (1991).

[134] S. Jesse, M. A. Guillorn, I. N. Ivanov, A. A. Puretzky, J. Y. Howe, P. F. Britt, and D. B. Geohegan, *In situ electric-field-induced contrast imaging of electronic transport pathways in nanotube-polymer composites*, Applied Physics Letters, **89**, p. 013,114 (2006).

[135] A. Vijayaraghavan, S. Blatt, C. Marquardt, S. Dehm, R. Wahi, F. Hennrich, and R. Krupke, *Imaging electronic structure of carbon nanotubes by voltage-contrast scanning electron microscopy*, Nano Research, **1**, pp. 321–332 (2008).

[136] R. Y. Zhang, Y. Wei, L. A. Nagahara, I. Amlani, and R. K. Tsui, *The contrast mechanism in low voltage scanning electron microscopy of single-walled carbon nanotubes*, Nanotechnology, **17**, pp. 272–276 (2006).

[137] J. Cazaux, *The electric image effects at dielectric surfaces*, Dielectrics and Electrical Insulation, IEEE Transactions on, **3**, pp. 75–79 (1996).

[138] M. Smith, H. Li, T. Shen, X. Huang, E. Yusuf, and D. Vavylonis, *Segmentation and tracking of cytoskeletal filaments using open active contours*, Cytoskeleton, **67**, pp. 693–705 (2010).

[139] V. Bahadur, J. Xu, Y. Liu, and T. S. Fisher, *Thermal Resistance of Nanowire-Plane Interfaces*, Journal of Heat Transfer, **127**, p. 664 (2005).

[140] J. Visser, *Van der Waals and other cohesive forces affecting powder fluidization*, Powder Technology, **58**, pp. 1–10 (1989).

[141] S. Akita, H. Nishijima, and Y. Nakayama, *Influence of stiffness of carbon-nanotube probes in atomic force microscopy*, Journal of Physics D: Applied Physics, **33**, p. 2673 (2000).

[142] L. Bergström, *Hamaker constants of inorganic materials*, Advances in Colloid and Interface Science, **70**, pp. 125–169 (1997).

[143] I. Palaci, S. Fedrigo, H. Brune, C. Klinke, M. Chen, and E. Riedo, *Radial Elasticity of Multiwalled Carbon Nanotubes*, Physical Review Letters, **94** (2005).

[144] D. Maier-Schneider, A. Köprülülü, S. Holm, and E. Obermeier, *Elastic properties and microstructure of LPCVD polysilicon films*, Journal of Micromechanics and Microengineering, **6**, p. 436 (1996).

[145] K. Bhat, *Silicon Micromachined Pressure Sensors*, Journal of the Indian Institute of Science, **87**, pp. 115–131 (2007).

[146] H. Zhong and J. Lukes, *Interfacial thermal resistance between carbon nanotubes: Molecular dynamics simulations and analytical thermal modeling*, Physical Review B, **74** (2006).

[147] Y. Zhao, T. Tong, L. Delzeit, A. Kashani, M. Meyyappan, and A. Majumdar, *Interfacial energy and strength of multiwalled-carbon-nanotube-based dry adhesive*, Journal of Vacuum Science & Technology B: Microelectronics and Nanometer Structures, **24**, p. 331 (2006).

[148] L. Ge, S. Sethi, L. Ci, P. Ajayan, and A. Dhinojwala, *Carbon nanotube-based synthetic gecko tapes*, Proceedings of the National Academy of Sciences, **104**, p. 10,792 (2007).

[149] S. Sethi, L. Ge, L. Ci, P. Ajayan, and A. Dhinojwala, *Gecko-inspired carbon nanotube-based self-cleaning adhesives*, Nano Letters, **8**, pp. 822–825 (2008).